

UNIVERSIDADE FEDERAL DE SANTA CATARINA  
DEPARTAMENTO DE ENGENHARIA MECÂNICA  
PROGRAMA DE PÓS-GRADUAÇÃO EM ENGENHARIA MECÂNICA

**A STUDY OF SQUEAL NOISE IN A DISC BRAKE SYSTEM AND  
INFLUENCE OF RUBBER COATED SHIMS ON SYSTEM  
DAMPING**

Thesis submitted to the Department of Mechanical Engineering  
in partial fulfillment of the requirements for the degree of  
Doctor in Mechanical Engineering

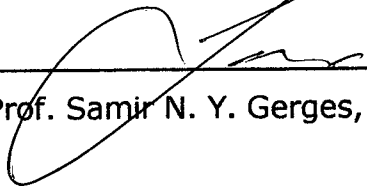
Eng. Alessandro M. Balvedi, M. Eng.

Florianópolis, November / 2002

ESTUDO DO RUÍDO DE ALTA FREQUÊNCIA EM FREIOS A DISCO E  
DA INFLUÊNCIA DE LÂMINAS DE REVESTIMENTO NO  
AMORTECIMENTO DO SISTEMA

Eng. Alessandro M. Balvedi, M. Eng.

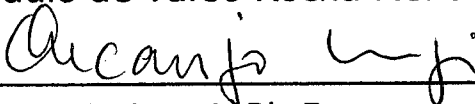
Professor Orientador

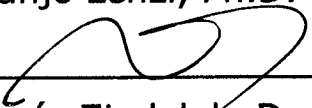
  
\_\_\_\_\_  
Prof. Samir N. Y. Gerges, Ph. D. (UFSC)

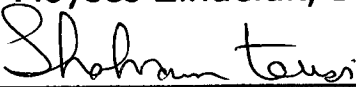
Banca Examinadora

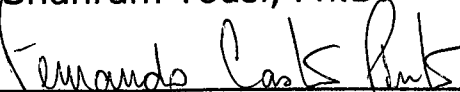
  
\_\_\_\_\_  
Prof. Samir Nagi Yousri Gerges, Ph.D.

  
\_\_\_\_\_  
Prof. Paulo de Tarso Rocha Mendonça, Ph.D.

  
\_\_\_\_\_  
Prof. Arcanjo Lenzi, Ph.D.

  
\_\_\_\_\_  
Prof. Moysés Zindeluk, Dr. Eng.

  
\_\_\_\_\_  
Dr. Shahram Tousi, Ph.D.

  
\_\_\_\_\_  
Dr. Fernando Augusto de N. Castro Pinto, Dr. Ing.

## **ACKNOWLEDGEMENTS**

I wish to express my gratitude to my major advisors, Professor Samir N.Y. Gerges and Mr. Ahid Nashif, for their friendship, patience, guidance and assistance through this journey. The lessons they taught were not only about Noise and Vibration, but also about life.

I am also grateful to Dr. Shahram Tousi, for his support and specially friendship during this research.

My thanks are extended to Material Sciences Corporation, which provided the resources and means for this research.

Thanks to Mr. Andrew Winkley and Ms. Siobhan Wiese, for the correction in the english language of this thesis. "Vielleicht wird es nächst mal auf Deutsch!"

I am indebted with my mother, who never failed in giving me love, support and guidance for life, being always my safe port.

My beloved Carina, whose love and dedication have made me a better person.

I am also in debit with many other persons that mentioning would not be possible in such few pages. Hopefully, future will reserve many successful moments in our lives to give us opportunity to share with those here unfairly not mentioned.

## TABLE OF CONTENTS

LIST OF FIGURES	VI
LIST OF TABLES	XI
NOMENCLATURE	XII
ABSTRACT	XIV
1. INTRODUCTION	1
1.1 Brake Components	2
1.2 Objectives	4
1.3 Research Description	4
2. LITERATURE REVIEW	8
2.1 Viscoelastic Materials	8
2.1.1 Measurement and Data Presentation of the Dynamic Properties	9
2.1.2 Viscoelastic Materials Applied in Multi-layer Structures	11
2.1.2.1 Methods for Measuring Dynamic Properties	12
2.1.2.2 Numerical Models	13
2.2 Dynamics of Brake Systems	16
2.2.1 Numerical/Analytical Models	16
2.2.2 Experimental Tools	21
3. VISCOELASTIC MATERIALS AND LAMINATES: CHARACTERIZATION AND DAMPING MECHANISMS	25
3.1 Laminates with Viscoelastic Materials	25
3.1.1 Shear Damping	25
3.1.2 Extensional Damping	28
3.1.3 Damping Due to Thickness Deformation	28
3.2 Behavior Characterization of Viscoelastic Materials	29
3.2.1 Dynamic Young's Modulus	30
3.2.2 Influence of Temperature	31
3.2.3 Influence of Frequency	32
3.2.4 Frequency-Temperature Superposition Principle	33

3.2.5	Measurement of Young's Modulus and Loss Factor	36
3.2.5.1	Dynamic Properties of Rubber Coat RC1	41
3.2.5.2	Dynamic Properties of Pressure Sensitive Adhesive PSA	49
3.2.5.3	Dynamic Properties of Rubber Coat RC2	52
4.	DYNAMICS OF THE BRAKE SYSTEM	54
4.1	Squeal Mechanism	54
4.2	Modal Coupling in a 2 Degrees-of-Freedom Model	57
4.3	Squeal Mechanism in the Brake System	65
4.4	Dynamometer Results of Baseline	67
4.5	Component Modal Analysis	70
4.5.1	Pad Modal Analysis	70
4.5.2	Rotor Modal Analysis	74
4.5.3	Caliper Modal Analysis	81
4.6	Analysis of Assembly Brake System	84
5.	SOUND INTENSITY AND ACOUSTICAL MEASUREMENTS	100
5.1	Sound Intensity	100
5.1.1	Source of Errors and Probe Calibration	103
5.1.1.1	Errors Due to the Finite Difference Approximation	103
5.1.1.2	Microphones Phase Mismatch	104
5.1.1.3	Phase Mismatch Evaluation	104
5.1.1.4	Intensity Calibration	106
5.2	Sound Intensity Results	107
5.3	Measurements of Sound Pressure Level	114
6.	EFFECT OF TEMPERATURE ON THE DYNAMICS OF THE BRAKE SYSTEM: RUBBER COAT MECHANISM	120
6.1	Effects of Temperature on the System Dynamics	120
6.1.1	Damping Mechanism of Rubber Coats	124
6.2	Analytical Model	133
7.	DYNAMOMETER TESTS	142
8.	CONCLUSIONS AND RECOMMENDATIONS	155

LIST OF REFERENCES	159
APPENDICES	
Appendix 1 – Equations of Motion for the Modal Coupling Model and Implementation in Mathcad	163
Appendix 2 – Equations of Motion of the 2 Degrees-of-Freedom System Used for Parametric Analysis of Rubber Coat Damping Mechanism and Implementation in Matlab	167

## LIST OF FIGURES

- Figure 1.1 - Brake components
- Figure 1.2 - Caliper disassembled and detail of a pad with shim
- Figure 1.3 - Example of shim configurations usually applied on brake pads
- Figure 1.4 - Shim configurations analyzed
- Figure 2.1 - Effect of temperature on Young's storage modulus  $E$  and loss factor  $\eta$
- Figure 2.2 - Ring configurations analyzed by Lu et al (source: ref. [24])
- Figure 2.3 - Model of a brake system by Kung et al. (source: ref. [32])
- Figure 2.4 - Root locus graph of the complex eigenvalue of 2500 Hz in terms of the friction coefficient (source: ref. [32])
- Figure 2.5 - Pin-on-disc system analyzed by Tuchinda et al. (Source: Ref. [34])
- Figure 3.1 - Shear damping: Configuration in its initial and deformed state (source: ref. [6])
- Figure 3.2 - Extensional or unconstrained layer damping
- Figure 3.3 - Damping due to thickness deformation
- Figure 3.4 - Complex Young's modulus
- Figure 3.5 - Effect of temperature on Young's storage modulus and loss factor
- Figure 3.6 - Effect of frequency on the Young's storage modulus
- Figure 3.7 - Effect of frequency on the loss factor
- Figure 3.8 - Loss factor vs. temperature and frequency and Young's storage modulus vs. temperature and frequency (source: ref. [5])
- Figure 3.9 - Resonance method
- Figure 3.10- Diagram of a typical laboratory test-rig for beam tests
- Figure 3.11- Effect of magnetic pull on FRF
- Figure 3.12- Setup for beam test
- Figure 3.13- Waterfall: FRF response/excitation as a function of temperature
- Figure 3.14- Loss factor vs. temperature and storage shear modulus vs. temperature for RC1
- Figure 3.15- Nomogram of rubber coat RC1
- Figure 3.16- Loss modulus vs. storage modulus for RC1

- Figure 3.17- Loss factor vs. storage modulus for RC1
- Figure 3.18- Analytical curves for loss factor vs. frequency
- Figure 3.19- Analytical curves for storage modulus vs. frequency
- Figure 3.20- Analytical curves for loss factor and storage modulus vs. temperature
- Figure 3.21- Nomogram of pressure sensitive adhesive PSA
- Figure 3.22- Loss factor vs. storage modulus for PSA
- Figure 3.23- Loss modulus vs. storage modulus for PSA
- Figure 3.24- RC2 shim configuration and cross section
- Figure 3.25- Nomogram of rubber coat RC2
- Figure 4.1 - Graphic illustration of dry and viscous friction force as a function of sliding velocity
- Figure 4.2 - 2 degrees-of-freedom model
- Figure 4.3 - System displacement vs. time for  $\mu=0.1$
- Figure 4.4 - System displacement vs. time for  $\mu=0.3$
- Figure 4.5 - System displacement vs. time for  $\mu=0.4$
- Figure 4.6 - System displacement vs. time for  $\mu=0.5$
- Figure 4.7 - Modal coupling: Imaginary part of system modes vs. friction coefficient
- Figure 4.8 - Root locus plot of the complex roots of the characteristic equation
- Figure 4.9 - Values of  $b^2$  and  $4ac$  for the 2 DOF model, indicating the instability range
- Figure 4.10- System displacement vs. time for  $K_1=600\text{N/m}$  and  $K_2=1000(1+0.1i)\text{N/m}$
- Figure 4.11- System displacement vs. time for  $K_1=600(1+0.1i)\text{N/m}$  and  $K_2=1000(1+0.2i)\text{N/m}$
- Figure 4.12- System displacement vs. time for  $K_1=600(1+0.2i)\text{N/m}$  and  $K_2=1000(1+0.2i)\text{N/m}$
- Figure 4.13- Coupling between modes of vibration of rotor and pad.
- Figure 4.14- Influence of temperature and pressure on rotor and pad modes
- Figure 4.15- Sketch of a typical inertia dynamometer for brake systems
- Figure 4.16- Percentage of noise occurrence ( $>70\text{dB}$ ) vs. pressure and temperature
- Figure 4.17- Noise occurrence distribution as function of frequency
- Figure 4.18- Mesh of the pad



- Figure 4.19- Vibration modes of the pad
- Figure 4.20- Synthesized curve (blue) and sum of the 40 FRFs (red)
- Figure 4.21- Modal analysis of rotor and its mesh
- Figure 4.22- FRF for point 60z/60z (point frequency response function)
- Figure 4.23- Examples of bending modes of the rotor
- Figure 4.24- Radial and twisting modes of the rotor in the frequency range from 6500 to 9000Hz
- Figure 4.25- Stability diagram from 6300 to 8340 Hz (1024 lines)
- Figure 4.26- Resonant modes for rotor and pad
- Figure 4.27- FRF of a pad simply resting on a table and under pressure
- Figure 4.28- Mode shapes of the caliper and example FRF example
- Figure 4.29- Sketch and photo of test setup for measurement of system FRF as a function of pressure
- Figure 4.30- FRFs for Baseline: Accelerometers located at rotor and pad
- Figure 4.31- System loss factor and resonance vs. lining pressure for Baseline
- Figure 4.32- Frequency response of brake system: Baseline at  $8.6e5N/m^2$
- Figure 4.33- Mode shapes of the rotor lap under pressure ( $8.6e5N/m^2$ )
- Figure 4.34- System loss factor for Baseline and Shim 6 and description of Shim configuration 6
- Figure 4.35- FRFs for Shim 6: Accelerometers located at rotor and pad
- Figure 4.36- Loss factor for the pad using different shim configurations under various temperature conditions for the 3<sup>rd</sup> bending mode
- Figure 4.37- System loss factor for the shim configurations
- Figure 4.38- System loss factor for some of the shim configurations
- Figure 4.39- System resonance as a function of lining pressure
- Figure 4.40- Waterfalls of FRFs for the shim configurations
- Figure 5.1 - Different probe configurations
- Figure 5.2 - Example of error due to the finite difference approximation
- Figure 5.3 - Sound intensity calibrator (closed coupler volume)
- Figure 5.4 - P-I Index for analyzer and intensity instrumentation
- Figure 5.5 - Background noise. 1/3 octave band and constant band

- Figure 5.6 - Pads with patch actuators
- Figure 5.7 - Test setup used for the sound intensity measurements
- Figure 5.8 - Sound intensity maps of the exposed rotor lap as a function of lining pressure
- Figure 5.9 - Pi-Index for the analyzer, for the intensity probe and at point 53 (lining pressures of  $13.8 \times 10^5$  and  $20.7 \text{ N/m}^2$ )
- Figure 5.10- Test setup for measurements of sound pressure level
- Figure 5.11- FRF of microphone autospectrum and excitation signal.
- Figure 5.12- Measurements of FRF microphone autospectrum/excitation signal, for Baseline and Shim 2(RC1)
- Figure 5.13- Resonance frequency as a function of pressure for the pad configurations
- Figure 5.14- Contour plots of Baseline, Shim 2 and Shim 6
- Figure 5.15- FRF Microphone autospectrum/excitation signal: Frequency range of 7700 to 8500Hz
- Figure 6.1 - Pictures of the setup for measurements of the brake system under temperature
- Figure 6.2 - Modal loss factor vs. temperature for the brake system for different breaking pressures
- Figure 6.3 - Measurement of the pad friction material dynamic properties
- Figure 6.4 - Deformation of the caliper fingers necessary for shear damping to occur in the rubber coat layer
- Figure 6.5 - Constrained layer damping treatment and rubber coat under caliper: No shearing occurs at the rubber coat under the caliper
- Figure 6.6 - Wavelength dependency on shear deformation
- Figure 6.7 - Modal loss factor vs. temperature for the brake system with Shims 2, 4 and 5
- Figure 6.8 - Effects of static pre-load on the loss factor and storage modulus
- Figure 6.9 - Brake system resonance frequency vs. temperature
- Figure 6.10- Waterfall and contour plot of FRFs for the shim configurations
- Figure 6.11- 2 degrees-of-freedom model

Figure 6.12- Area of rubber coat in contact with caliper fingers

Figure 6.13- Determination of component modal parameters

Figure 6.14- 2DOF model: Loss factor vs. temperature

Figure 6.15- 2DOF model: Loss factor for different values for the modal parameters of the brake components

Figure 6.16- Example of FRF calculated by the 2DOF model

Figure 6.17- Loss factor vs. temperature for different rubber coat RC1 thicknesses

Figure 7.1 - Inertia dynamometer

Figure 7.2 - Dynamometer results for Baseline

Figure 7.3 - Dynamometer results for Shim 1 (RC1+PSA)

Figure 7.4 - Dynamometer results for Shim 2 (RC1)

Figure 7.5 - Dynamometer results for Shim 3 (PSA)

Figure 7.6 - Graphs and waterfalls of the dynamometer tests measured under the conditions of squeal noise and quiet system

---

## LIST OF TABLES

- Table 1.1 - Thickness of shim layers
- Table 4.1 - Resume of dynamometer test for baseline
- Table 4.2 - Modal parameter for the pad
- Table 4.3 - Modal parameters for the bending modes of the rotor
- Table 4.4 - Estimated resonances and loss factor of caliper modes
- Table 5.1 - Modal parameters of pads with and without patch actuators
- Table 6.1 - Loss Factor & Shear Modulus x Temperature for RC1
- Table 7.1 - Summary of the dynamometer results for the shim configurations

## NOMENCLATURE

A	area
C	damping matrix
$C_1, C_2$	constants of WLF equation
$C_3$	constant of Arrhenius equation
$C_n$	coefficient for mode $n$ , of clamped-free (uniform) beam
D	energy dissipated per radian (Chapter 6)
$E, E'$	storage Young's modulus
$E''$	loss Young's modulus
$E^*$	complex Young's modulus
$E_0$	minimum value measured for Young's modulus
$E_\infty$	maximum value measured for Young's modulus
$f$	frequency
$f_n$	natural frequency or resonance frequency for mode $n$
$f_s$	resonance frequency for mode $s$ of composite beam
$f_f$	friction force between pad and rotor
$g$	shear parameter
G	shear modulus
$G_{AB}$	cross spectrum between microphones A and B (Chapter 5)
H	thickness
I	second moment of area
$\vec{I}$	intensity vector (Chapter 5)
k	wavenumber
K	stiffness matrix (Chapter 2)
K	spring stiffness (Chapter 6)
$K_i$	$E_i \cdot H_i$
$K_1, K_2$	spring stiffness (Chapter 4)
$K_{RC}$	Stiffness of the rubber coat layer (Chapter 6)
l	length
M	mass or mass matrix
N	normal force
p	sound pressure (Chapter 5)

---

Q	amplification factor (Chapter 6)
$s_i$	roots of the characteristic equation
t	thickness (Chapter 6)
T	temperature
$T_0$	reference temperature (temperature where loss factor is maximum)
$T_A$	activation temperature
$T_g$	temperature where loss modulus is maximum
u	displacement
$\vec{u}$	particle velocity (Chapter 5)
V	velocity (Chapter 4)
V	elastic strain energy (Chapter 2)
$V_r$	relative sliding velocity
$\alpha_T$	shift factor
$\beta$	rate of variation of Young's modulus with frequency (exponent)
$\beta_2$	loss factor of viscoelastic material
$\delta$	angle between storage and loss modulus
$\Delta f$	half-power bandwidth
$\Delta r$	distance between microphones (Chapter 5)
$\varepsilon$	strain
$\eta$	loss factor
$\lambda$	wavelength (Chapters 2, 3, 5 and 6)
$\lambda_1, \lambda_2$	eigenvalues (Chapter 4)
$\mu$	dynamic friction coefficient
$\Omega$	rotational speed
$\rho$	density;
$\rho$	air density (Chapter 5)
$\sigma$	stress
$\omega$	frequency (radians)

## ABSTRACT

Brake squeal noise is an ongoing problem for the automotive industry. Squeal is perceived by consumers as both annoying and an indication of a problem with the braking system. These perceptions dramatically affect quality and satisfaction ratings as well as warranty costs.

Squeal noise is believed to be the result of the modal coupling of two vibration modes of the brake components such as pads, rotor and caliper. Among the methods that have been used to control squeal noise, increasing the system damping has shown to be very effective. The most commonly used method to increase system damping consists of applying a shim to the back of the brake pad, so that the vibration energy is dissipated. The shim structure consists of a sandwiched composite of constrained-layer material with outer metal skins and inner viscoelastic polymer core.

In some shim configurations, a rubber coating is applied over the outer metal skin (constraining layer) in order to improve the damping characteristics of the brake system. The main goal of this thesis is to investigate the influence of such elastomer coatings in the overall damping introduced by the brake shims. In order to achieve that, a series of steps toward the understanding of the squeal mechanism were taken.

First, the damping mechanisms of viscoelastic materials are depicted. In brake shims, such mechanisms depends on whether a constraining metal layer is present or not, besides the geometric parameters of the viscoelastic layer. Measurements of the dynamic properties of the viscoelastic materials used in this thesis are presented and discussed.

Second, the squeal mechanism in the brake system is discussed. A 2 degrees-of-freedom model is used to study the modal coupling mechanism and the influence of adding damping to the unstable modes on the dynamic response of the system. Modal analysis of the brake components is performed and the coupling modes pinpointed. Next, modal parameters of the critical mode of the assembly brake system are tracked as function of lining pressure and temperature. The system remained in a static condition, in an attempt to keep the same boundary conditions to the whole measurements as well as to allow some parametric analysis. In order to achieve that, a series of techniques were applied and improved. Frequency responses, sound intensity maps and acoustical measurements were applied to gain insight the squeal mechanism.

Finally, the damping mechanism of rubber coating is discussed. The influence of the modal parameters of the brake components in such damping mechanism is also explained by a 2 degrees-of-freedom system. The thesis is finalized with dynamometer results for the brake system with the different shim configurations.

Some of the main conclusions of this research are:

- . The condition for the squeal noise occurrence, in the brake system under analysis, relies on a modal coupling between a bending mode of the rotor and a bending mode of the pad. In this case, rotor and pad vibrates in-phase, with the same frequency and mode shape, and the frictional damping is lost.
- . During squeal conditions, the anti-nodes of the rotor mode related to the squeal frequency are fixed on space, i.e., they no longer rotate, remaining in the same position along the rotor diameter.
- . The damping mechanism of rubber coating was found to be the dynamic compression/relaxation of the elastomer in its thickness direction. The amplitude of such deformations is function of the dynamic properties of the elastomer as well as the modal parameter of the brake components.
- . Squeal noise occurs in a discrete tone, indicating the dependency of the coupling of the brake components modes on the determination of the squeal frequency.

**Keywords:** Squeal Noise, Vibration, Damping, Brake Shims, Rubber Coating.



# CHAPTER 1

## INTRODUCTION

In recent years, brake systems have become one of the key issues in the rating of vehicle noise and vibration. With powertrain noise contribution to the overall noise inside the passenger chamber sometimes as low as 50 dB, sources like brake, tires and suspension play an important role.

The dynamic behavior of disc brakes is still not well understood and the efforts deployed to design quieter brakes and diagnose NVH (noise, vibration and harshness) problems have increased substantially.

Brake noise can basically be classified in low and high frequency noise. Low frequency noise, also known as moan, has been determined to be audible vibrations below 1000 Hz. As well as the brake system by itself, the dynamics of the vehicle suspension play an important role in generating moan. Brake noise above 1000 Hz is usually known as squeal. In this case, the dynamics of the individual components of the brake system are responsible for noise generation.

Brake squeal is one of the major contributors to the noise related warranty costs of the automotive industry. Although it is not a safety-related issue, it is perceived by the passengers as annoying and even as a brake performance problem.

Among many hypotheses to explain squeal noise generation, primarily two types of mechanisms have been addressed [1,2]. One is the "stick-slip" mechanism, also described as a "negative damping", causing self-excited vibrations. The second is related to the coupling between two brake system modes. Two modes of vibration geometrically "matched" (same wavelength) with close resonances can induce high amplitudes of vibration in the brake components. A combination of these two aforementioned mechanisms has led to the most widely accepted theory.

In a general view, squeal noise is a phenomenon resulting from the vibration caused by a change in the coefficient of friction between the rotor and the disc pads. During braking, the friction coefficient between rotor and pads does not remain constant. Variation of the friction coefficient can lead to instability of some modes of vibration and to the coupling between two vibration modes. At this moment, the system is not able to

dissipate part of the energy introduced by the friction between rotor and pads. The consequence is an increase in the amplitude of the vibration of the rotor.

In this case, lining pressure and temperature are very critical factors in the characterization of component dynamic properties, especially pads.

Of the various methods that have been developed to control squeal noise, increasing the damping in the system has been found to be one of the most successful [3]. Viscoelastic materials in multi-layers have been used for this purpose. These configurations consist of metal and viscoelastic layers bonded or attached to the brake pads.

In order to understand this mechanism, it is useful at this point to give a brief description of the brake parts used in this research and how damping can be added.

## 1.1 BRAKE COMPONENTS

The components of the brake system used in this research were rotor, pads, caliper and knuckle. Figures 1.1 and 1.2 are photographs of these parts.

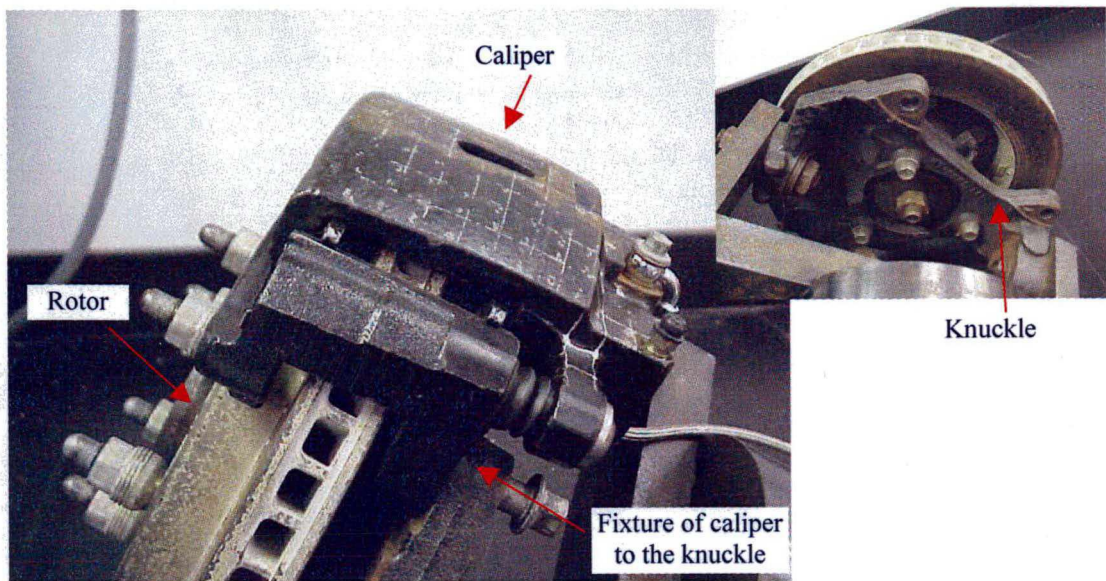


Figure 1.1 – Brake components. Main picture shows the rotor and caliper (with pads inside). The knuckle can be seen in the detail.

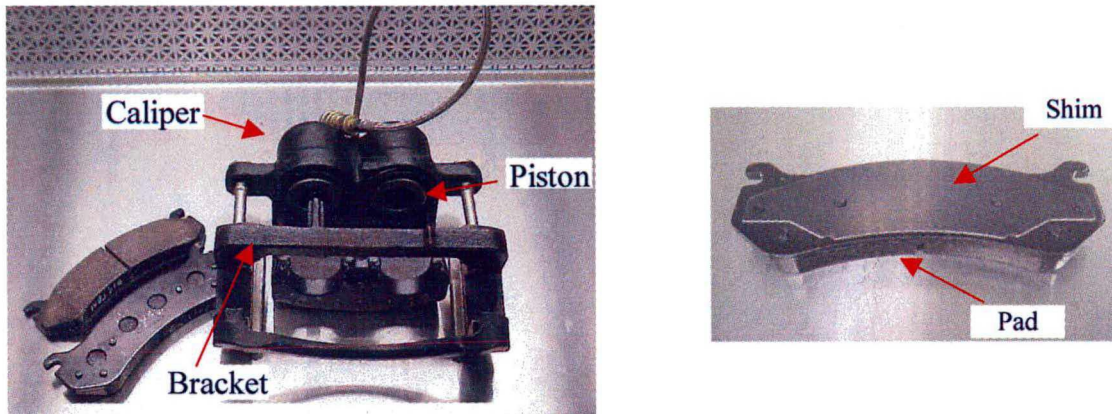


Figure 1.2 – Caliper disassembled and detail of a pad with shim

Two parts compose the caliper: caliper housing and bracket. The pad in contact with the piston(s) inside the caliper body is pushed against the rotor. The other pad is also pushed but only after the contact between the first pad and the rotor. The bracket is screwed to the knuckle, which is attached to the vehicle body/suspension.

Multi-layer laminates, also known as *shims*, are bonded or mechanically attached to the pads in order to increase the system damping. The usual configurations consist of one or more layers of viscoelastic materials constrained between two metal layers. Two examples of shim configurations are presented in Figure 1.3. In the first example, the shim composed by a viscoelastic material constrained between two metal sheets is bonded to the pad through another viscoelastic adhesive. This bonding viscoelastic adhesive is itself a constrained layer between the metal sheet and the pad back plate. An adhesive viscoelastic layer, a metal layer and a rubber coat constitute the second example.

The shim configuration and the dynamic properties of its materials determine the damping added to the system and, as a consequence, the stable/unstable dynamic condition. As will be discussed in Chapter 3, the viscoelastic constrained layer is usually the best configuration to improve structural damping.

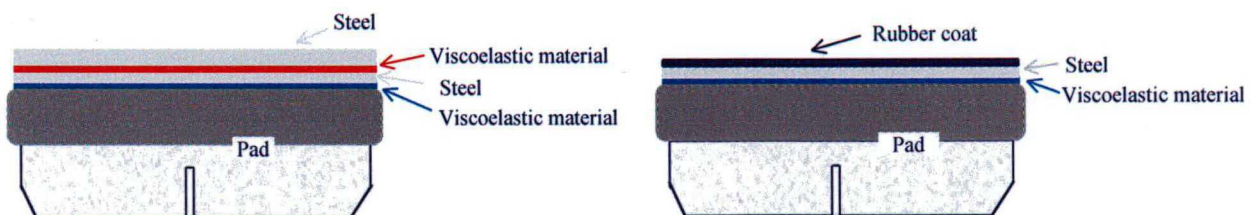


Figure 1.3 – Example of shim configurations usually applied on brake pads

## 1.2 OBJECTIVES

As previously stated, constrained layers have been used as an effective configuration for shims. Nevertheless, dynamometer results and market experience have shown that using rubber coatings (see Figure 1.3) can also help to increase the system damping in some situations.

While the damping mechanism of constrained layers in brakes is already known, the same cannot be said for exposed viscoelastic materials, like rubber coats. Besides the damping mechanism, the contribution of the rubber coating to the overall system damping also remains unknown. As can be seen in Figure 1.3, rubber coat is used along with constrained layers. Therefore, the aim of the research reported in this thesis was to figure out the damping mechanism and quantify the contribution of rubber coats to brake system damping. In order to achieve this, techniques for measuring brake system damping were improved and new methodologies were developed to gain insight into the squeal mechanism.

The main contributions of this research can be resumed as follows:

- 1) Development and improvement of experimental methods to quantify loss factor and evaluate brake shim performance in brake systems;
- 2) Application of the Sound Intensity technique to gain insight into the squeal generation mechanism;
- 3) Understanding the damping mechanism of rubber coats used in brake shims.

## 1.3 RESEARCH DESCRIPTION

A total of six shim configurations were used. The basic configuration was a shim already applied in industry, composed of a viscoelastic adhesive, from here on called PSA (Pressure Sensitive Adhesive), a steel layer and a rubber coat, from here on called RC1 (Rubber Coat 1). A graphical description of each configuration and their denominations are presented in Figure 1.4.

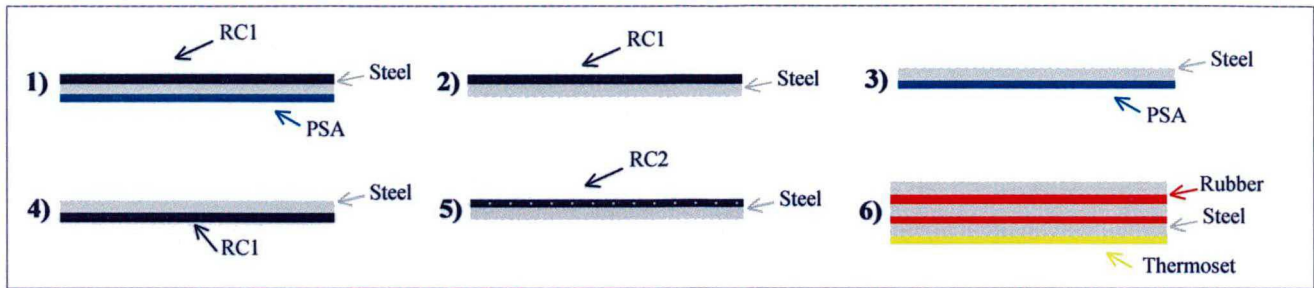


Figure 1.4 – Shim configurations analyzed

The first configuration was the basic one. The PSA is a room-temperature-bonded adhesive and works as a constrained-layer. In configurations 2 and 3 the rubber coat RC1 and the PSA were evaluated individually. Configuration 4 also used RC1, but as a constrained layer instead of as a coating. Configuration 5 used a rubber coat, from here on named RC2, with different dynamic properties to those of RC1, as will be seen in Chapter 3. It must be mentioned that in the cases of configurations 2, 4 and 5, the shims were bonded to the pads by a structural adhesive (high stiffness and low damping) in order to take into account only the influence of the rubber layers RC1 and RC2 on the system damping. Configuration 6 is another commercial shim and the maximum loss factor was found to be around 25° C. Its performance was used as a reference in some measurements at room temperature. Table 1.1 shows the thickness of each layer for the six configurations.

Table 1.1 – Thickness of shim layers

		Density (Kg/m <sup>3</sup> )	Thickness (mm)			Density (Kg/m <sup>3</sup> )	Thickness (mm)
Shim 1	RC1	1298	0.102	Shim 5	RC2	996	0.150
	Steel	7800	0.762		Steel	7800	0.500
	PSA	939	0.055	Shim 6	Rubber layer (each)	---	0.0254
Shims 2 and 4	RC1	1298	0.102		Steel layer (each)	---	0.267
	Steel	7800	0.762		Thermoset	---	---
Shim 3	Steel	7800	0.762			---	---
	PSA	939	0.055	---		---	

This thesis begins by presenting in Chapter 2, a non-exhaustive literature review related to the issues involved in the research. Regarding viscoelastic materials, the subjects covered are the characterization (influence of some parameters on the dynamic behavior, measurement techniques and analytical modeling), use of viscoelastic materials in laminates and methods for measuring the loss factor of such structures. Many articles have been published reporting the efforts to understand brake NVH issues and some of them are also covered in the review. Numerical methods for analysis of brake dynamic stability and experimental methods to provide insight into squeal mechanisms are some of the topics mentioned.

In order to evaluate the performance of different shims, it becomes necessary to quantify the dynamic properties of their viscoelastic materials. In this way, Chapter 3 presents a general description of the dynamic behavior of viscoelastic materials and their application in multi-layers. The measured properties for RC1, PSA and RC2 are also shown.

Chapter 4 discusses the dynamics of the brake system used in this research. At first, the squeal noise mechanism is broken down and a simple analytical model is used to exemplify the modal coupling phenomenon and how damping affects it.

Modal analysis of the individual brake components is performed in order to pinpoint the modes responsible for squeal generation.

After determining the critical modes, the technique to measure brake system damping as a function of line pressure is explained and the results for each shim configuration are discussed.

One of the conditions necessary for the occurrence of squeal noise in brake systems is related to the relative position of the rotor and pad critical mode shapes. This condition, addressed in some articles [3,4], is discussed in Chapter 4. In Chapter 5, the Sound Intensity technique is applied to verify the occurrence of this condition. The methodology is based on a brake system static condition and patch actuators inside the pads were used to simulate the excitation force due to friction between rotor and pads.

Once the dynamics of the brake system and the performance of each shim as a function of pressure had been investigated (Chapter 4), the same analysis was made as a function of system temperature, for specific line pressures. The results are shown in Chapter 6.

Chapter 6 also presents an analytical model built to explain the damping mechanism of the rubber coats in the brake system, based on the results obtained in Chapters 4 and 6.

The input data of this model are the modal parameters of the caliper, rotor and pad. It must be noted that this model does not aim to predict the dynamic behavior of the brake system but to explain how the rubber coat adds damping to it.

Validation of the conclusions is made through dynamometer tests, shown in Chapter 7. The percentage of noise occurrence, as a function of pressure and temperature, is presented for tests performed on the baseline (pad without shim), RC1, PSA and RC1+PSA (configuration 1 on Figure 1.4).

Finally, Chapter 8 contains the final conclusions and suggests topics for further researches.

## CHAPTER 2

### LITERATURE REVIEW

This chapter presents a literature review on the dynamic characterization of viscoelastic materials, their application in multi-layers and also research with regards to noise and vibration in brake systems. As will be seen, there is a research gap between the two main subjects: multi-layers with viscoelastic materials for NVH and the dynamics of brake systems. Few papers dealing with the application of multi-layers for noise and vibration control in brake systems are available. This review is, therefore, divided into the two main subjects mentioned above.

#### 2.1 VISCOELASTIC MATERIALS

The widespread use of viscoelastic materials results largely from their versatile mechanical properties. The properties of viscoelastic materials are strongly dependent on temperature and time (or frequency). Descriptions of the effects of these variables can be found in references [5], [6], [7] and [8]. Actually, this dependence exists in every kind of material but it becomes very apparent in polymers. This behavior, although seeming, in principle, to be a shortcoming, should be considered as advantageous, since it allows a certain amount of flexibility in the design of materials for noise and vibration control.

According to Ungar [5] and Nashif et al. [6], [7], Young's storage modulus (or storage modulus) has the characteristic of decreasing with the increasing in temperature, while the loss factor reaches its maximum value at the so called transition temperature, as illustrated in Figure 2.1. It can be seen that the dynamic properties of the material change at a much higher rate in the transition region. For instance, Nielsen [8] mentions that the storage modulus may decrease by a factor of over 10000 as the temperature is raised through the transition region.



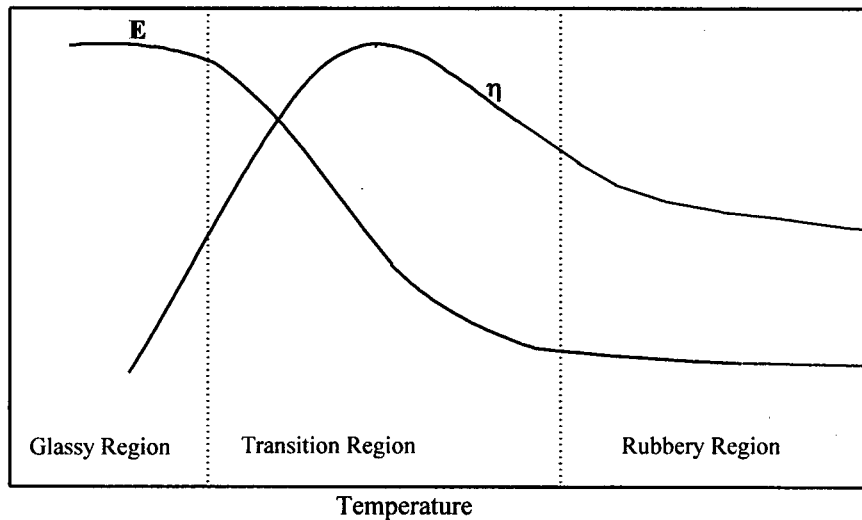


Figure 2.1 – Effect of temperature on Young's storage modulus,  $E$ , and loss factor  $\eta$

Frequency can have different effects, depending on the temperature region studied. In general, the loss factor tends to be proportional to frequency in the rubbery region, reach its maximum value in the transition region and tends to be inversely proportional to frequency in the glassy region. The storage modulus increases with the increase in frequency, independent of temperature, although the increase rate is higher in the transition region. A more detailed discussion of these effects is given in Chapter 3. Other parameters, such as static pre-load, cyclical deformations and fillers also affect the behavior of viscoelastic materials, but at a lower level. Explanations and examples of these effects are found in references [6], [7] and [8].

### 2.1.1 Measurement and Data Presentation of the Dynamic Properties

Obtaining information about the dynamic behavior of viscoelastic materials requires experimental methods. In 1972, Jones [9] presented an article mentioning the resonance method for measuring Young's modulus and loss factor. This method consists of measuring the dynamic properties of a one degree-of freedom system, where the material sample acts as the spring element. By varying the temperature and the mass over the material sample, the dynamic properties can be measured over a range of frequency (resonance of the system) and temperature. Alternatively, a shear configuration can be used to measure the specimen's shear modulus. In his article, Jones also explained a particular method for measuring these properties when the viscoelastic material is

available only in very thin layers, such as strips bonded on aluminum foils. The technique is based on the comparison of data with values determined for the same configuration, but using other viscoelastic material with known properties.

In another article from 1974, Jones [10] discussed the resonance method and applied it, along with the beam method, to determine the curves of viscoelastic materials used for vibration control. The author also made use of the “frequency-temperature superposition principle” to represent the data in a single graph.

In 1995, Gade et al. [11] published an article with a summary of the resonance method, presenting its theory and mathematical basis, as well as experimental results obtained using such a method. The authors also mentioned a non-resonant method, which allows one to obtain the dynamic properties of the sample from the real and imaginary part of the frequency response spectra (specifically Force / Displacement) as a continuous function of frequency.

The American Society for Testing and Materials (ASTM) standard E-756-98 [12], originally published in 1980, standardized the beam method, also known as the Oberst test, for measuring the dynamic properties of viscoelastic materials submitted to tension/compression or shear stress. The beam method is based on the equations developed by Ross, Ungar and Kerwin [13] and currently is probably the most used method. ASTM E-756-98 also mentions other methods for evaluating the performance of damping materials, dividing them into two categories: those whose purpose is to rank the performance of damping materials for a defined structure and those whose purpose is to measure the properties of the damping material alone.

Representing the effects of temperature and frequency on the dynamic behavior of viscoelastic materials in a single graph is extremely useful. These graphs, called *nomograms*, are created using the frequency-temperature superposition principle, based on the works of William, Landel and Ferry [14]. Explanation of this principle is found in references [6], [7] and [10]. In the updated edition, ASTM E756-98 [12] also explains the data presentation using “reduced-frequency nomograms”, summarizing how a nomogram can be generated and how material properties can be read from it. The frequency-temperature superposition principle is based on the fact that low frequencies are equivalent to high temperatures. In this way, it is possible to reduce data generated at different temperatures into one curve, provided that a correct shift factor for each temperature is determined.

### 2.1.2 Viscoelastic Materials Applied in Multi-layer Structures

With regards to the study of viscoelastic materials applied in multi-layer structures, a contribution was made by the work developed in 1959 by Kerwin, Ross and Ungar [13]. In this paper, Kerwin et al. introduced the equations to calculate the loss factor of metal/viscoelastic/metal beams. Comparisons with experimental results were presented, including the use of spacers between the layers. According to the authors, for constrained layer configurations, the major damping mechanism is the shearing of the viscoelastic layer. The authors also considered the case where there was no constraining layer (upper metal face) and concluded that, for this configuration, the major mechanism of energy dissipation is the strain due to normal stresses at the viscoelastic layer. The mathematical approach was based on some considerations, described in Chapter 3. The general solution was an intricate relation between structure geometry, properties of the materials and wavenumber (or wavelength). In order to simplify the equations for the composite loss factor and bending stiffness, the authors assumed that the thickness of the viscoelastic layers and the constraining layer (metal upper face) were much smaller than the thickness of the base plate (metal lower face). In later references [6], [15], the considerations related to thickness were no longer applied and the equations for the loss factor and bending stiffness were presented for a general case. In addition, approximations for other boundary conditions were taken into account, depending on the vibration mode of the configuration. In this direction of considering other boundary conditions, Mead [16] published a paper discussing the effects of other support configurations, such as supports that allowed transversal displacement of a plate, but prevented rotation, supports riveted to the plate, allowing rotation, and supports riveted to the plate but preventing rotation.

Continuing the studies of multi-layer laminates, Ungar et al. [17] published, in 1962, an article establishing the definition of the loss factor in these configurations in energy terms. The authors considered the laminates as composed of viscoelastic springs. In this manner, the loss factor of the configuration could be interpreted as being a weighted average of the loss factors of the respective springs.

In 1964, these same authors published a study showing the influence of longitudinal damping (along the thickness) in multi-layer systems [18]. This damping mechanism occurs in configurations whose layer of viscoelastic material is thick and has a low Young's modulus. It is related to the dissipation of energy due to movement of the viscoelastic material along its thickness. According to the authors, this mechanism can

show damping peaks in the resonances, which occur when the thickness of the viscoelastic layer is a multiple number of  $\frac{1}{2}$  or  $\frac{1}{4}$  of the wavelength, according to whether the configuration has a constraining layer (metal upper face) or not.

In 1999 Danilov et al. [19] presented experimental results for the loss factor and Young's modulus of two multi-layer configurations, discussing the frequency ranges where damping by shear, by normal strain and by strain through the material thickness occurred. Using samples with a viscoelastic layer between 2 and 13 mm, the authors showed that damping by deformations through the thickness tends to occur in higher frequencies.

#### 2.1.2.1 Methods for Measuring Dynamic Properties

Experimental methods for measuring the dynamic properties of multi-layer systems are the same as those used for general structures. References to these methods can widely be found in the literature, such as in references [5], [6], [8] and [20]. Reference [20] presents a synthesis of three methods usually applied: the input power method, the decay method and the bandwidth method.

The input power method can provide good results for frequency bands but is strongly dependent of an accurate measurement of the parameters involved. In this method, loss factor is calculated by the relation between the power dissipated by the system, calculated from the spectrum of the input force and the Frequency Response Function (FRF) mobility, and the total energy introduced, given by the product of system mass and the square of the vibration velocity.

The decay method is based on the measurement of the reverberation time and generally presents lower results than the former method, since the reverberation time in each frequency band is usually dominated by the lower damping modes.

The bandwidth method is the measurement of the bandwidth at 3 dB under the resonance peak and is widely used to estimate loss factor. In structures with low damping, bands larger than 3dB can be used where the analyzer resolution is not sufficient [6]. For instance, a 20dB bandwidth will give a value ten times the real loss factor.

In 1985, Brown and Norton [21] published an article discussing the advantages and disadvantages of methods for measuring modal density and loss factor in structures. The authors concluded that, for each type of excitation, there is a more precise way of calculating the dissipated power. The authors also stated that on very lightly damped structures, the decay method, using non-contact transducers, provides better results than the input power method.

In their book, Heckl et al. [22] present a discussion about the methods for measuring the complex Young's modulus and, as a consequence, the loss factor. The authors divided the methods in two categories: One containing the methods such as the stress-strain curve, mechanical impedance, vibration decay and the resonance method, and the other category with the methods used for measuring the properties of beams, such as the half-power bandwidth method and the decay time.

### 2.1.2.2 Numerical Models

Since the 1970's numerical methods began to be applied in the analysis of the dynamic behavior of multi-layer systems. In 1979, Lu et al. [23] compared experimental and numerical results of frequency response functions of plates composed by metal/viscoelastic/metal. The authors compared impedance curves with results obtained by the finite element method. The effects of frequency on Young's modulus and loss factor of the viscoelastic material were considered according to the equations:

$$G = 102.39 \cdot 10^4 \cdot f^{0.625} \quad \text{and} \quad \beta_2 = 1.6274 \cdot f^{-0.072} \quad (2.1)$$

where

G is the shear modulus;

$\beta_2$  is the loss factor of the viscoelastic layer.

For the plate models, isoparametric solid elements of eight nodes were used for the viscoelastic layer. For the metal layers, four-node plate elements were considered.

In 1980 the same authors compared numerical and experimental impedance results for beams and multi-layer rings [24]. The beam model used membrane elements for the viscoelastic layer and beam elements for the metal layers. For the ring model, two configurations were analyzed, as shown in Figure 2.2. The authors highlighted the necessity to simulate a Frequency Response Function, since the dynamic properties of the viscoelastic material are dependent on frequency.

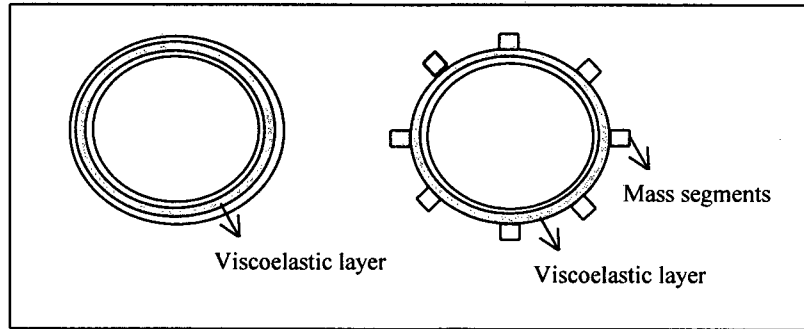


Figure 2.2 – Ring configurations analyzed by Lu et al (source: ref. [24])

In 1984, Lu et al. [25] analyzed the same plate models mentioned in reference [23], using viscoelastic beam elements instead of isoparametric solid elements to simulate the viscoelastic layer. The structural damping for these beams could be specified to simulate the shear and extensional damping provided by the thin viscoelastic layer.

In 1995, Mignery [26] presented a finite element model for prediction of the damping characteristics of composite laminates (metal/viscoelastic/metal). This model had two differences in relation to that described by Lu et al., in 1979 [23]. The first difference was the use of spring elements to represent the viscoelastic layer and shell elements for the metal layers. Each element of the viscoelastic layer was represented by three springs: one spring with extensional stiffness in direction  $z$  and two springs with shear stiffness in directions  $x$  and  $y$ . The second difference was the utilization of an energy method to calculate the loss factor of the configuration. In the Modal Strain Energy Method (MSEM), developed by Ungar [6], the loss factor of a multi-layer can be calculated by

$$\frac{\eta_s^r}{\eta_c} = \frac{V_c^r}{V_s^r} = \frac{\sum_{i=1}^n (SE)_c^i}{\sum_{j=1}^m (SE)_s^j} \quad (2.2)$$

where

$\eta_s^r$  is the loss factor of the configuration for the  $r_{th}$  mode;

$\eta_c$  is the loss factor for the viscoelastic material;

$V_c^r$  is the elastic strain energy stored in the viscoelastic material when the structure is deformed in its  $r_{th}$  mode;

$V_s^r$  is the elastic strain energy stored in the configuration when it is deformed in its  $r_{th}$  mode.

The third term in Equation 2.2 establish that the strain energy is calculated by the ratio between the sum of the strain energy in the  $n$  elements of the viscoelastic layer and the sum of the strain energy in the  $m$  elements of the whole configuration. Therefore, the loss factor of the configuration is calculated from the following interactive process:

- 1) The resonant frequency of the structure is first presumed ;
- 2) Young's modulus and loss factor of the viscoelastic layer is calculated for the assumed frequency, using known equations for the material (obtained experimentally and through nomograms, according to references [6], [7] and [10]);
- 3) The real part of Young's modulus is then used in the finite element model to determine the natural frequency for the mode in sight. If the calculated natural frequency is different from the frequency initially assumed in step 1, the Young's modulus is adjusted until the assumed and calculated natural frequencies are the same.

In 1997 Mignery et al. [27] compared numerical results from two models: elastic and viscoelastic. The elastic model considered solid elements for the viscoelastic layer and the loss factor of the configuration was calculated through the Modal Strain Energy Method (MSEM). The advantage of this elastic model was the processing time, since the stiffness of the viscoelastic material was a real number. The disadvantages were the amount of effort to obtain the results by the MSEM and the necessity of choosing a Young's modulus value representative of the frequency range for frequency response functions. In the viscoelastic model, beam elements and a complex Young's modulus were used for the viscoelastic layer. The natural frequencies and the respective loss factors were determined through a forced response simulation and the properties of the viscoelastic layer (as a function of frequency) were set as input data. The main disadvantage of this model was the slower computer execution time. The authors simulated some configurations and concluded that, in general, the two models predict natural frequencies well, but the elastic model overestimates the loss factor, in contrast with the viscoelastic model, that tends to underestimate the loss factor.

## 2.2 DYNAMICS OF BRAKE SYSTEMS

The dynamics of brake systems has been the subject of much research involving NVH techniques, such as modal analysis, operational deflection shapes and analytical/numerical models. The finite element method has been used extensively to simulate squeal noise generation in brake systems. More recently, complex eigenvalue analysis has helped brake engineers to pinpoint system parameter combinations under which squeal noise occurs. Other experimental tools aiding the brake design community are modal analysis, operational deflection shape (ODS), scanning laser and advanced holography systems that provide insight to rotor modes of vibration during the squeal event.

### 2.2.1 Numerical/Analytical Models

As mentioned above, in the last few years, numerical tools and analytical models have been used in order to understand and predict the dynamic behavior of brake systems.

In 1998, Dihua and Dongying [28] studied a squealing disc brake using the finite element method. Based on a system model, analysis was performed to find which structure components affected the squeal phenomenon significantly. The authors emphasized that the number of unstable modes obtained from the numerical model is greater than the result from field tests and indicated two reasons: the friction coefficient  $\mu$  used in the model was constant, while it is not constant in practice, and can lead to the tendency of reducing instability; the second factor is that damping was not considered in the model.

In one of the few papers involving the influence of damping on the dynamics of brake components, in 1999, Nashif and Mignery [29] analyzed the application of multi-layer systems in brake pads. A finite element model of a brake pad with a multi-layer shim was developed. Three layers of viscoelastic material and three layers of steel composed the shim. The properties of each viscoelastic layer, as a function of temperature and frequency, were taken into account. Numerical results for the first three bending modes of the configuration were compared with experimental measurements. The authors concluded that the damping and natural frequencies of the shim/shoe/lining assembly showed a similar temperature variation as the viscoelastic laminates, but experimental



data showed, at high temperatures, more damping than that predicted by the finite element analysis. According to the authors, this might be due to the inability of the damper adhesive model to accurately describe the material dynamic behavior in its rubbery region.

Hamabe et al. [30] used a finite element model to study squeal noise in a drum brake system. The first part of their article dealt with the explanation of the instability phenomenon, using a two degrees-of-freedom system. The authors showed how the variation in the friction coefficient affects the instability of the model. The instability is evaluated considering the signal of the real part of the eigenvalues. This two degree-of-freedom model is also used in Chapter 4 of this thesis to explain the instability phenomenon, but as well as the variation of the friction coefficient, the influence of damping is considered and graphics with the system displacement with time are presented. In the second part, the authors evaluated the drum brake by the finite element method and compared the results with experimental tests. In the case of drum brakes, squeal usually occurs due to coupling of bending modes of the rotor cheek, in the radial direction, contrary to transversal bending modes in disc brake systems.

Liu and Pfeifer [31], in 2000, presented a model for finite element analysis, trying to incorporate the effects of the pad/rotor coupling. The pad model was validated comparing the natural frequencies and vibration modes obtained numerically and experimentally. After validating the pad model, the vibration modes and displacement patterns were used as the input data (loading) for the numerical model of the rotor. In this way, the authors aimed to model the geometric coupling between the two structures and simulate the effects of different pad geometries in the dynamic response of the rotor.

Also in 2000, Kung et al. [32] presented a model for analysis by the finite element method of a brake system containing the pads, caliper and rotor, as illustrated in Figure 2.3. The authors performed a complex eigenvalue analysis and the potential for occurrence of squeal noise was evaluated by the instability of a given system mode. The dynamic equation of the brake system was given by

$$M \ddot{u} + C \dot{u} + Ku = f_f \quad (2.3)$$

where

M is the matrix of mass, C is the matrix of damping and K is the system matrix of stiffness;

u is the displacement;

$f_f$  is the vector of friction forces between pads and rotor.

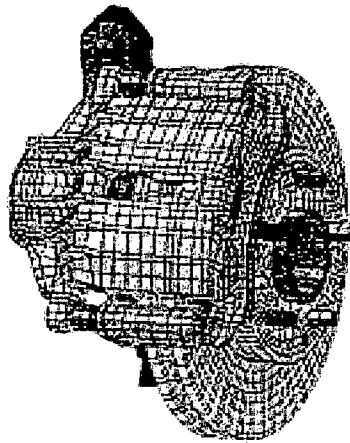


Figure 2.3 – Model of a brake system by Kung et al. (source: ref. [32])

The friction forces  $f_f$  were modeled as a set of springs, that is,  $f_f = K_f \cdot u$ , and the Equation 2.3 became

$$M \ddot{u} + C \dot{u} + [K - K_f]u = 0 \quad (2.4)$$

An algorithm for complex eigenvalues was used to solve the above equation, since the matrix  $[K - K_f]$  was not symmetrical. According to the authors, eigenvalues with a positive real part are related to unstable modes and always arise in conjugated pairs. In this case, when the matrix  $C$  is negligible, both roots of one conjugated complex pair have the same imaginary value and real value with opposite signals. Experimental results were compared with simulated modal analysis. After validating the model, simulations were performed in order to obtain the stability results of certain modes in terms of the friction coefficient. Figure 2.4 shows an example of the graphs, also known as *root locus plots*, obtained by the authors.

In another study, Kung et al. [1] analyzed a brake system also using a complex eigenvalue analysis to determine the unstable modes of the configuration. Software based on the Modal Assurance Criteria was used to find the participation of the modes of each component in such unstable modes. The authors suggested that, by knowing the unstable modes and the participation of each component on these modes, it is possible to optimize the design of the components to uncouple the vibration modes.

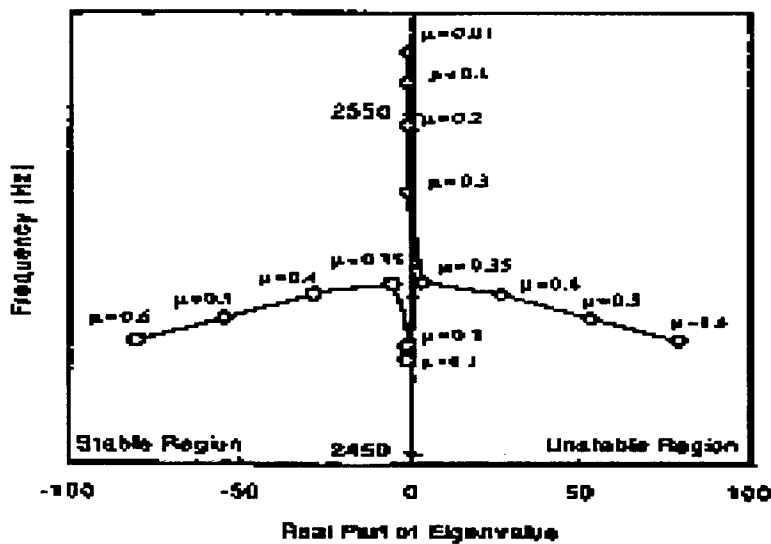


Figure 2.4 – Root locus plot of the complex eigenvalues of 2500 Hz in terms of the friction coefficient (source: ref. [32])

An approach to model the friction interaction at the rotor/pad interface was purposed by Blaschke et al. [2], using the finite element method to analyze the friction-induced vibration of brake systems. The pad was represented by a three degrees-of-freedom system while the rotor was modeled as a two degrees-of-freedom system. The basic dynamic equations for this system were developed and implemented in a finite element model. As in former papers, a complex eigenvalue analysis algorithm was used to predict the unstable modes of the brake system models studied. From the results, the authors concluded that the friction coupling makes both the mass and the stiffness matrices non-symmetric, which causes the eigenvalue solution to be complex, as mentioned also in references [1] and [32]. Furthermore, complex eigenvalue analysis predicts more unstable modes than the number of squeal frequencies in practice. The same conclusion was also mentioned by Dihua and Dongying [28], in 1998.

Still in 2000, Ouyang at al. [33] investigated the dynamics of a brake system, deriving equations to simulate the rotation of the rotor and the friction force between rotor and the set pad/caliper. Two finite element models were developed: the first model simulated the coupling between rotor and pad; the second model aimed to simulate the dynamic behavior of the entire configuration. The rotor model was based on Kirchoff's plate theory and the parameters/boundary conditions were adjusted so that natural frequencies obtained numerically were equal to the frequencies obtained by experimental modal

analysis. After the model was adjusted, the authors varied the parameters of the configuration and simulated the stable and unstable regions, according to the definition described in references [31] and [32]. The main conclusions reached were: The friction force is the most important parameter in the destabilization of the system and the unstable regions can be reduced substantially by damping the rotor and/or pads. The authors also concluded that increasing or decreasing the stiffness of the rotor or the pads may increase or decrease the unstable regions, it not being possible to estimate a tendency for this parameter.

In 2001 Tuchinda et al. [34] made a study using a pin-on-disc analytical model to simulate how squeal noise can be generated in vehicle disc brakes. The pin-on-disc system was modeled as a flexible beam in contact with a flexible disc. The response of each component was expressed as a sum of its normal modes, leading to a multi-degree-of-freedom model. The pin was fully clamped at the inner end and free at the outer rim, as shown in Figure 2.5.

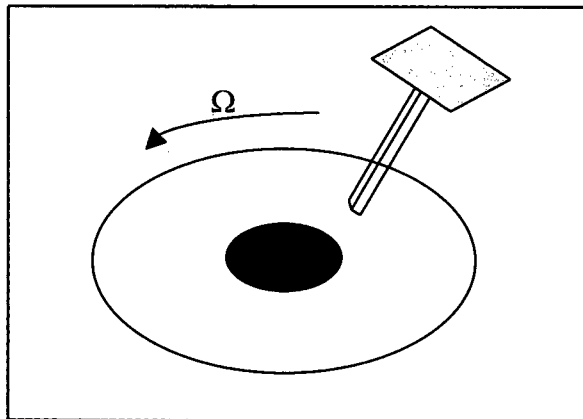


Figure 2.5 - Pin-on-disc system analyzed by Tuchinda et al. (Source: Ref. [34])

Axial and transversal modes were modeled for the pin, while only out-of-plane modes were allowed for the disc. The authors developed the equations of motion for each component and assumed that the only effect of the disc rotation is to create the frictional force. As a result, the disc was assumed static and the friction force was placed in the model as a Coulomb-type. No damping was considered. The results showed the effect of coupling of modes of vibration as a function of the friction coefficient. A different characteristic was noted in this model: At higher coefficient of friction values, the locked-in modes separated into two stable modes again and instability ceased to exist. This characteristic, termed by the authors as “mode lock-out”, had not been previously observed in the model described by Hamabe et al. [30].

## 2.2.2 Experimental Tools

The development of new analysis tools and experimental techniques has also helped engineers and brake system designers to understand the brake squeal mechanism and to optimize solutions.

In 1996, Noriyuki et al. [35] suggested an experimental method for measuring brake component frequency response during brake application, by oscillating the caliper with the friction surface condition stabilized. With the disc brake mounted on a brake dynamometer, the rotor was allowed to rotate at a constant speed. A random excitation was applied to the caliper by a shaker and the caliper frequency response was measured. Since the structural stiffness of the shoe material dramatically changes with lining pressure, the main issue for the method was to keep the friction surface condition stabilized. To secure the coherence, the authors fitted acrylic tips on the friction material contact area at each pressure-application position, corresponding to the pistons. With this method, an attempt was made to control the friction conditions. The size of the acrylic tips was varied in order to simulate different friction coefficients. A frequency response between the acceleration measured in the caliper and the excitation force applied by the shaker was measured for different tip sizes and the squeal was evaluated considering the peak height of each measurement.

Squeal noise has also been a critical issue in drum brake systems, as described by Hulten et al [36], in 1997. This paper brings an in-depth discussion about squeal noise in drum brakes. After discussing the theoretical background, the authors presented results of Operational Deflection Shapes (ODS) for a drum brake system. Measurements were taken for the brake shoe, brake drum and for the complete brake system. One of the main conclusions of the authors was that, for the brake system investigated, the waves of the drum and the shoes moved in phase at every angular position, i.e., points on a line through the drum center moved in phase, although the amplitude of the drum was larger than that of the shoes. This in-phase movement of the brake components was the result of coupling of modes with the same wavelength. With the drum and shoes vibrating in phase, the damping due to friction was lost.

In 1999, Fieldhouse [4] presented a paper suggesting a method to predict squeal noise frequencies in brake systems, considering the pad geometry and the diametrical modes of the rotor. According to the author, the set caliper/pads is capable of holding only an integer number of antinodes of the rotor mode under it. Under pressure, these antinodes under the caliper/pads are compressed, as consequence, expanding the antinodes to outside the set caliper/pads. In this situation, squeal noise will occur. It was also confirmed that the expansion of the antinodes outside the pads was also related to the fact that squeal noise frequency is usually found to be lower than rotor resonances in a free-free boundary condition. At higher pressure, the set caliper/pads cannot hold the antinodes, and the antinodes outside are compressed, making the system quiet. Fieldhouse employed the holographic interferometry technique to investigate the system. The author also concluded that, when determining the wavelength of the pad mode, the effective pad length to be considered as interacting with the rotor mode is between 80 to 100% of the total length.

Fieldhouse et al. [37] also used the holographic interferometer technique, in 2000, to measure operational deflection shapes of a brake system. The paper focused on the potential for using the laser holography in order to represent the motion of disc brake systems.

Also in 2000, Marchi et al. [38] presented an overview of four examples of holographic interferometry applications in brake vibration and NVH analysis. The first two examples were studies of brake roughness vibration in a rear drum brake system and a front disc brake system. The third and fourth examples were studies of brake squeal. The authors mentioned that, specifically for the squeal cases, the technique allows a better visualization of the mode shapes of rotor and pads. In the case studied, the 5<sup>th</sup> bending mode of the rotor was seen during brake squeal occurrence.

According to Chen et al. [39], not only out-of-plane modes can generate squeal noise, but in-plane modes too. The authors studied in-plane modes/friction processes and their contribution to disc brake squeal using pulsed laser interferometry to acquire the Operational Deflection Shapes (ODS) of a disc when it was squealing. The authors suggested that the coupling between in-plane modes and out-of-plane modes of the rotor could lead to squeal. According to this suggestion, the in-plane modes tend to control the squeal frequency, and the out-of-plane modes are efficient in generating noise.

The authors concluded, based on their measurements, that the out-of-plane mode with a higher resonant frequency adjacent to an in-plane mode tends to be the one that has the same vibration pattern as the squeal deflection shape.

The sound intensity technique and laser vibrometry were used by Cunefare and Rye [40] in experimental investigations of methods for disc brake squeal source localization. The sound intensity method was used to locate regions of airborne noise in the near field of a brake system mounted in a dynamometer. Scanning laser vibrometry was used to further investigate the vibration behavior of the suspected area and to normalize the intensity measurements: since the squeal occurrence could not be maintained for the whole time necessary for the intensity measurements, surface velocity was used in order to normalize the intensity levels. In this way, the assumption was that the vibration velocity of a reference point should be linearly correlated to the sound intensity measured. Coherence between sound pressure and surface velocity was also calculated to support the author's conclusion that there was a direct relationship between the acoustic measurements and the reference vibration. Finally, the authors concluded that, for the brake system studied, brake pad vibration (more specifically, pad tip vibration, or flutter) was the squeal source.

Some efforts have also been spent in developing test-rigs to better control squeal occurrence in brake systems. Following this path, Terrel et al. [41] developed a dynamometer, designed and constructed to study brake squeal at a system level. In their paper, the characteristics of the dynamometer are described. The ODS of a caliper and pad set, measured with an array of accelerometers, during squeal occurrence was also presented.

Finally, in 2001, Blaschke et al. [42] presented a general discussion about noise and vibration in brake systems, based on the research already published. Blaschke et al., according to the literature, classified the NVH issues in three fields: brake judder, low frequency brake noise and brake squeal noise. In this paper, the authors discussed the different mechanisms of noise and vibration generation, as well as the experimental and numerical tools used for analysis. Brake judder refers to the sensation of vibration by the driver or passenger during braking and is usually associated with the dynamic behavior of the steering wheel and floor-pan vibration ranging, from 5 to 35 Hz. Low frequency brake noise in automotive brakes refers to frequencies below 1000 Hz and usually involves the whole body motion. Therefore, in general, low frequency noise in brakes cannot be solved or investigated without integrating suspension or more vehicle components. Brake squeal

noise usually is above 2000 Hz and is related to the dynamics of the brake components. According to the authors, squeal can occur anytime throughout the history of the vehicle usage, which can be further broken down into break-in stage (first 5000 km), bedded-in stage (5000 to 25000 km) or worn-out stage (above 25000 km), but still within warranty period. Therefore, although not being a safety-related issue, squeal noise is one of the major contributors to brake warranty cost.



# VISCOELASTIC MATERIALS AND LAMINATES CHARACTERIZATION AND DAMPING MECHANISMS

Multi-layer laminates are well-known solutions for brake squeal and are widely applied by the vehicle industry. Selection of the configuration and especially the materials to be used strongly rely on the conditions of squeal occurrence for each brake system. Squeal is dependent on lining pressure and temperature. The design of an adequate shim becomes a critical issue, since the dynamic properties of viscoelastic materials (specifically for the scope of this work, Young's modulus and loss factor) are dependent on temperature and frequency.

### 3.1 LAMINATES WITH VISCOELASTIC MATERIALS

The theory of viscoelastic materials states that, if a viscoelastic material is submitted to mechanical deformations, part of the energy will be converted into heat. This phenomenon of internal dissipation of energy can be quantitatively measured by the **loss factor**, the ratio of the average energy dissipated per radian to the energy in the system.

If this material is applied to a rigid structure (like a metallic surface) and this configuration is subjected to resonant vibrations, the viscoelastic layer will deform and convert part of the energy into heat and, as a consequence, reduce the vibration amplitude.

Viscoelastic materials applied along with metal layers in laminates can dissipate energy basically by three mechanisms, according to the configuration of the system: shear damping, extensional damping (due to strain along the length of the configuration) and damping due to thickness deformation of the viscoelastic layer.

#### 3.1.1 Shear Damping

Shear damping is the dissipation mechanism that occurs when a layer of viscoelastic material is placed between two metallic layers with a higher Young's modulus (Figure 3.1). This dissipation mechanism has usually the best effectiveness among the three previously

mentioned, however, this characteristic is compensated by the greater complexity in the analysis and application [6].

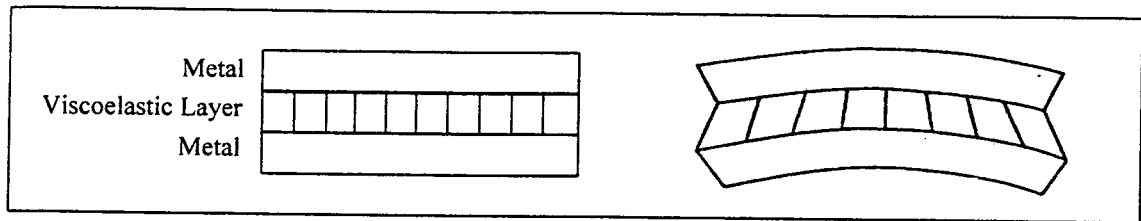


Figure 3.1 – Shear damping: Configuration in its initial and deformed state

(source: ref. [6])

Whenever the structure is subjected to a cyclical deformation, the metal layer will constrain the viscoelastic material and force it to shear. The presence of the viscoelastic layer changes the flexural rigidity of the structure in a manner that depends on the dimensions of the three layers and the Young's moduli.

The shear damping theory was initially developed by Kerwin, Ungar and Ross [13] for a three-layer configuration. The analytical solution considered the following assumptions:

- 1) Uni-dimensional wave propagation;
- 2) Sinusoidal modes of vibration;
- 3) It was assumed that the three layers shared the same movement (coupling between layers);
- 4) All the laminates were subjected to the same lateral displacements. This means that the shear strain of the viscoelastic layer was proportional to the flexural angle;
- 5)  $K_2 \ll K_1$ , where  $K_i = E_i H_i$ ,  $E_i$  and  $H_i$  being respectively the Young's modulus and the thickness of the  $i$ th layer;

The equation for the flexural stiffness of the configuration is given by ([6], [13] and [15]):

$$EI = \frac{E_1 H_1^3}{12} + \frac{E_2 H_2^3}{12} + \frac{E_3 H_3^3}{12} + E_1 H_1 D^2 + E_2 H_2 (H_{21} - D)^2 + E_3 H_3 (H_{31} - D)^2 - \left[ \frac{E_2 H_2^2}{12} + \frac{E_2 H_2}{2} (H_{21} - D) + E_3 H_3 (H_{31} - D) \right] \frac{H_{31} - D}{1 + g} \quad (3.1)$$

where

$$D = \frac{E_2 H_2 \left( H_{21} - \frac{H_{31}}{2} + g(E_2 H_2 H_{21} + E_3 H_3 H_{31}) \right)}{E_1 H_1 + \frac{E_2 H_2}{2} + g(E_1 H_1 + E_2 H_2 + E_3 H_3)}$$

$$H_{31} = \frac{H_1 + H_3}{2} + H_2 \quad H_{21} = \frac{H_1 + H_2}{2}$$

$$g = \frac{G_2}{E_3 H_3 H_2 k^2}$$

$E$  is the Young's modulus;

$G_2$  is the Shear modulus of the viscoelastic layer;

$I$  is the second moment of area;

$H_i$  is the thickness of the  $i_{th}$  layer;

$k^2$  is the wavenumber;

$g$  is the shear parameter.

If one has computational tools available that can handle complex numbers, one can insert complex values for any or all of the quantities  $E_1$ ,  $E_2$ ,  $E_3$  and particularly  $G_2$ . Hence, one can calculate a complex flexural stiffness  $EI(1+i\eta)$ , where  $\eta$  is the loss factor of the configuration.

One can also note that the behavior of the configuration depends most strongly on the shear parameter  $g$ , which combines the effect of the viscoelastic layer ( $G_2$  and  $H_2$ ) with the wavelength of the mode of vibration (since  $k^2 = 2\pi/\lambda$ ). At low temperatures, where  $G_2$  tends to high values, both metal and the constrained layer become rigidly coupled and little shear deformation occurs in the middle layer, dissipating little energy. At high temperature, the viscoelastic material becomes very soft and, even though the shear deformation in the constrained layer is high, the shear modulus  $G_2$  is low, again reducing the energy dissipation. Between the two extremes, the configuration possesses an optimum value of  $g$ , so that the energy dissipation for the constrained layer goes through a maximum.

Graphs demonstrating the influence of certain parameters, such as thickness ratios, shear modulus and wavelength on the dynamic properties of three-layer composites are found in numerous references, such as [6], [7], [13], [15] and [43].

### 3.1.2 Extensional Damping

The mechanism of energy dissipation in an unconstrained layer of viscoelastic material is the deformation of the viscoelastic layer during each cycle of flexural vibration [43]. In analyzing this type of treatment, it is usually appropriate to assume that normal lines through the undeformed neutral plane of the structure remain straight and normal to the deformed neutral plane, as shown in Figure 3.2.

The mathematical model of this mechanism may be derived from the shear damping equations, considering  $H_3 = 0$ , or from the bending wave equation for beams (Euler-Bernoulli equation). It is important to point out that, in the extensional damping mechanism, the loss factor of the configuration, unlike in the shear damping mechanism, is not dependent on the wavenumber (or wavelength). It is a function only of the metal and viscoelastic material properties (loss factor, Young's modulus and densities) and geometric parameters, such as thickness ratio.

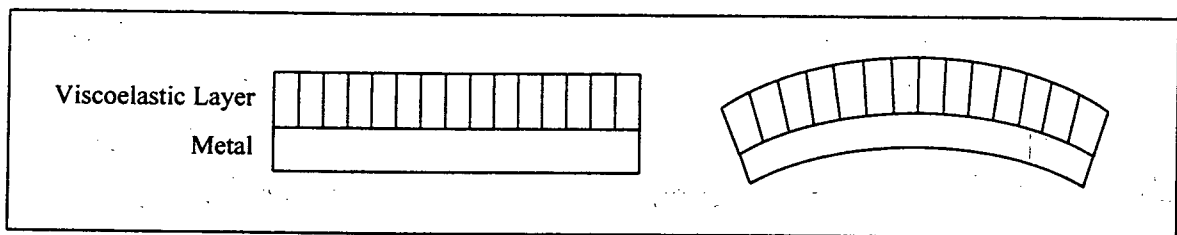


Figure 3.2 – Extensional or unconstrained layer damping

### 3.1.3 Damping Due to Thickness Deformation

Damping due to thickness deformation occurs when the thickness of the viscoelastic material is large enough so that strain occurs through the direction of thickness. According to Ungar and Kerwin [18], this mechanism may constitute an important damping source at the stationary wave resonances for thick viscoelastic materials with low stiffness.

The mathematical approach was developed by Ungar and Kerwin [13] and states that when the thickness of the viscoelastic material is equal to an odd multiple of  $\frac{1}{4}$  of the longitudinal wavelength, maximum strain occurs, leading to a maximum loss factor. If the configuration is composed of three layers, the stationary resonances will occur when the thickness of the viscoelastic material is equal to a half-wavelength multiple, as illustrated in Figure 3.3.

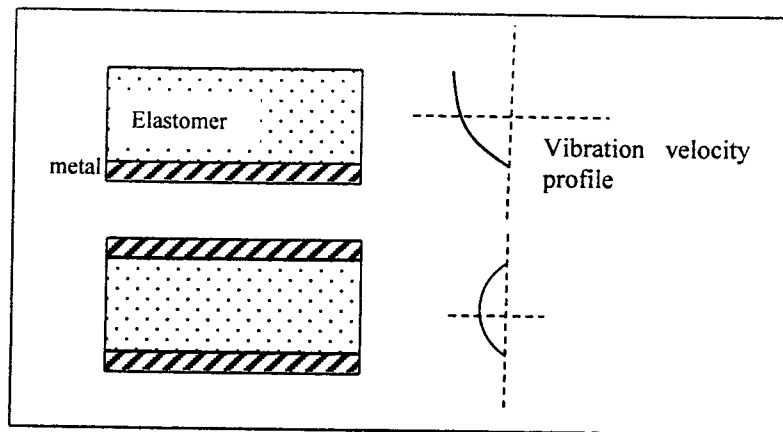


Figure 3.3 – Damping due to thickness deformation

### 3.2 BEHAVIOR CHARACTERIZATION OF VISCOELASTIC MATERIALS

The study of energy dissipation in materials is important for the development of products with better damping characteristics without compromising other properties (stiffness, density etc), such as high damping alloys and composite materials, or materials that will be applied to improve the energy dissipation characteristics of other structures. Viscoelastic materials are found in the latter group.

Viscoelastic materials are a class of materials that may show high internal damping due to the nature of their long molecule chains that provide a combination of elasticity and viscoelasticity [5]. As a result, the dynamic behavior is found between those of a solid and a liquid. The damping of a viscoelastic material results from the phenomena of relaxation and recovery of its chain of polymers, after deformation, having a strong dependency on frequency and temperature, as will be shown.

For the majority of the metals and structural materials, the loss factor and Young's modulus vary slightly with vibration amplitude, temperature (for temperatures far below fusion temperature) and frequency (within audible range) [5].

However, in contrast with metals, viscoelastic materials have a stiffness (Young's modulus and shear modulus) and loss factor strongly dependent on temperature and frequency, not mentioning other parameters. Understanding these two main variables, acting alone or together on the behavior of viscoelastic materials, is of utmost importance. First, however, a brief explanation of the concept of complex stiffness is required.

### 3.2.1 Dynamic Young's Modulus

The dynamic Young's modulus, along with the loss factor, is one of the major parameters in the characterization of viscoelastic materials. Under conditions of static load, Young's modulus is defined by the ration between stress ( $\sigma$ ) and strain ( $\epsilon$ ):  $E = \frac{\sigma}{\epsilon}$

When a dynamic load in the form of vibration is applied, the material internal friction provides resistance to the excitation. When this friction is of a viscous type, that is, proportional to velocity, a difference of phase occurs between stress and strain, as can be seen in Figure 3.4.

This phase difference is expressed as a complex Young's modulus

$$E^* = E' + iE'' \quad (3.2)$$

where

$E^*$  is the complex Young's modulus;

$E'$  is the Young's storage modulus;

$E''$  is the Young's loss modulus.

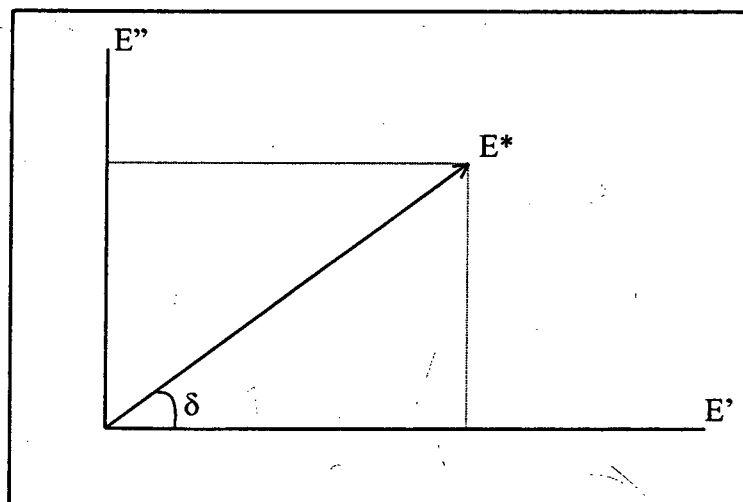


Figure 3.4 - Complex Young's modulus

The complex Young's modulus is generally expressed as:

$$E^* = E'(1+i\eta) \quad (3.3)$$

where

$$\eta = \frac{E''}{E'} = \text{tg} \delta \quad \text{is the loss factor.}$$

It is important to highlight that the aforementioned behavior also applies when using the shear modulus instead of Young's modulus.

### 3.2.2 Influence of Temperature

Temperature is seen to be the major influencing parameter for the damping properties of viscoelastic materials, and its effects, previously mentioned in Chapter 2, can be seen in Figure 3.5, where three distinct regions are observed.

In the glassy region, Young's storage modulus reaches its maximum value while the loss factor is at a minimum. In this region, the molecules of the material are rigidly coupled with little relative movement, which leads to high stiffness and low damping. In the transition region, Young's storage modulus rapidly decreases and the loss factor reaches its maximum value. The molecules in this region move more easily in relation to others, increasing the internal friction (as a consequence, the dissipated energy) and decreasing the material stiffness [7]. In the rubbery region, Young's storage modulus reaches its minimum value, being almost constant with temperature. In this condition, the molecules can move freely due to lower friction between the molecules, decreasing the damping and the stiffness. Some thermoplastic materials can also show a fourth region, beyond the rubbery, at which the loss factor tends to increase and the Young's storage modulus decreases even more [7].

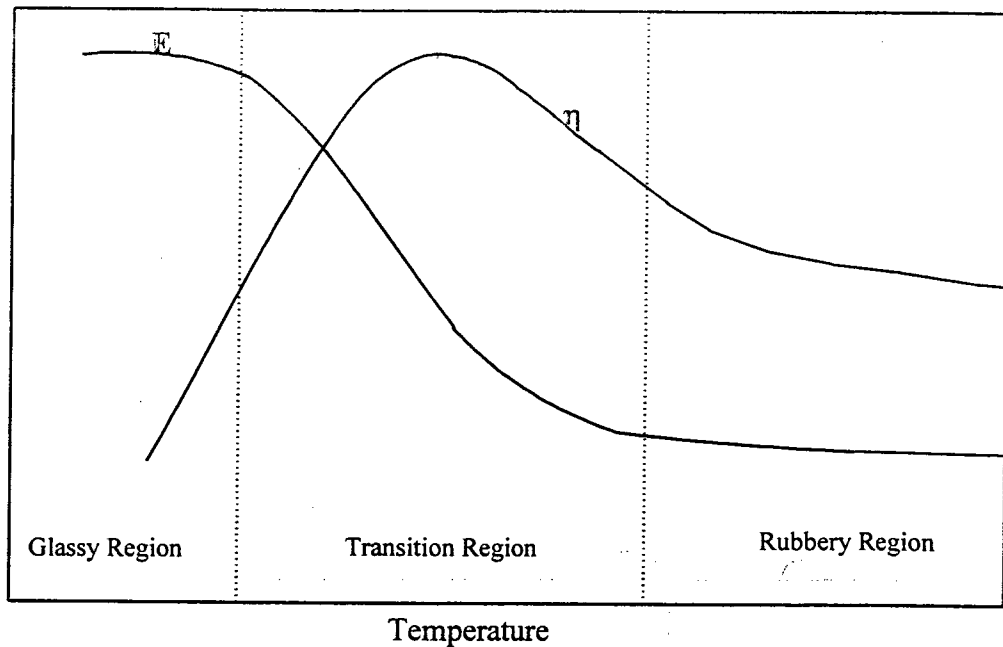


Figure 3.5 – Effect of temperature on Young's storage modulus and loss factor

As referred to in Chapter 2, the literature ([6], [7] and [8]) indicates that the Young's modulus of a viscoelastic material can reach values of up to  $10^9$  Pa in the glassy region and  $10^3$  Pa in the rubbery region. The transition region can have a bandwidth that may vary from a few degrees C, for some silicone rubbers, up to more than  $50^\circ$  C for acrylics. With regards to the loss factor, the values vary between  $10^{-3}$  and  $10^{-2}$  in the glassy region, and may reach values of magnitude of 1 or even 2 in the transition region.

### 3.2.3 Influence of Frequency

The effects of frequency on the properties of a viscoelastic material are depicted in Figures 3.6 and 3.7.

Young's storage modulus increases with frequency, however with different rates for each temperature range. The loss factor increases with frequency in the rubbery region, reaches its maximum value in the transition region and decreases with frequency in the glassy region.



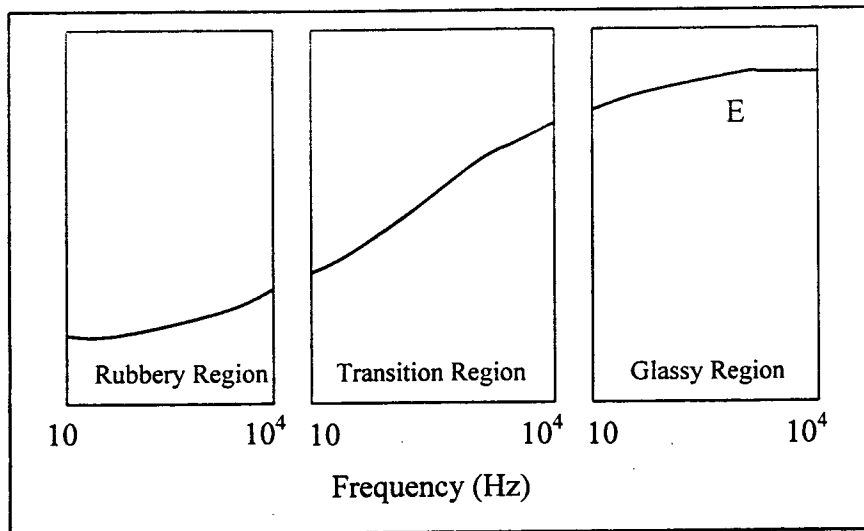


Figure 3.6 – Effect of frequency on the Young's storage modulus

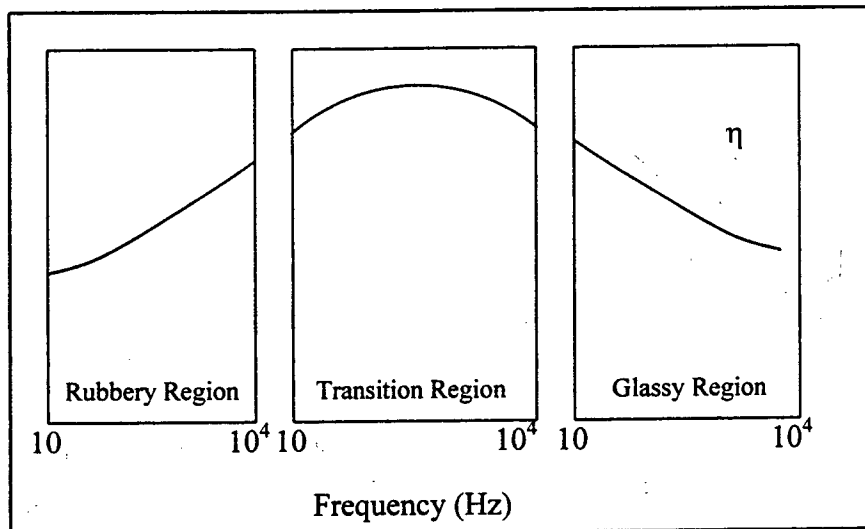


Figure 3.7 – Effect of frequency on the loss factor

### 3.2.4 Frequency-Temperature Superposition Principle

The effects of temperature and frequency on the properties of the viscoelastic materials were described separately in the former items. In practice, these two parameters work together and a more precise evaluation of their influences can be made through a 3-dimensional graph, as shown in Figures 3.8 (source: reference [5]).

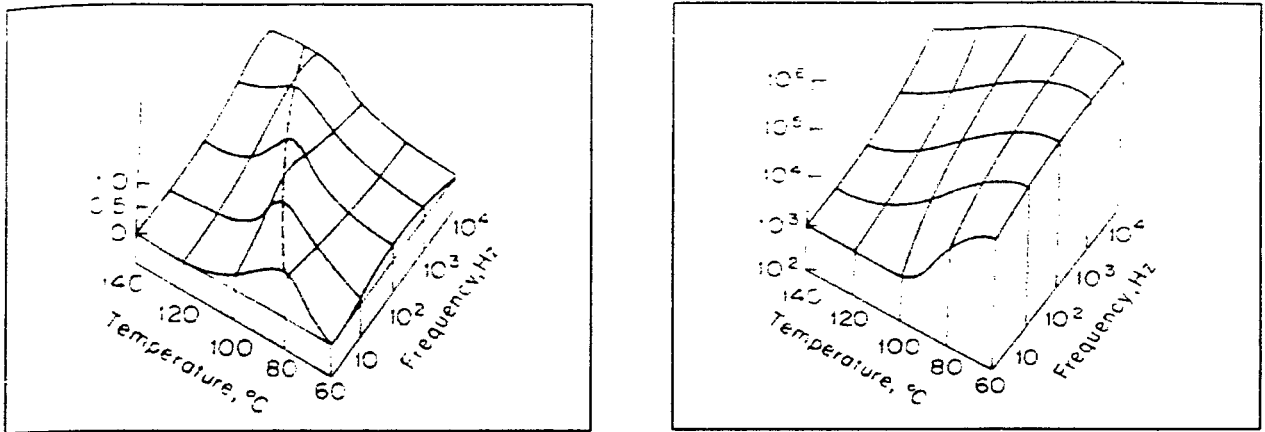


Figure 3.8 – Loss factor vs. temperature and frequency and Young's storage modulus vs. temperature and frequency (source: ref. [5])

Looking carefully to the above Figure, one can conclude that the effect of temperature on the properties of the material is qualitatively the inverse of the frequency effect. This means that, starting from a given initial temperature and frequency, if the temperature is increased, one can return to the former characteristics of the material by increasing also the frequency. In other words, an increment in temperature is equivalent to a decrement in frequency.

Nevertheless, it is important to note that the effect of changing the frequency is much less drastic than that resulting from a temperature change. A small increment in temperature can demand an increase in frequency of up to a few decades in order to return to the initial condition.

This important characteristic of viscoelastic materials is the basis for the frequency-temperature superposition principle, used to transform the properties of a material in the frequency domain into the temperature domain and vice-versa. According to this principle, measurements of properties of a viscoelastic material in terms of frequency, made at different temperatures, can be reduced in a single graph, usually called a *nomogram*, if a correct shift factor between temperature and frequency is defined for each temperature.

The complex Young's modulus of a thermo-rheologically simple viscoelastic material can be written as ([6],[7] and [15]):

$$E^* = \frac{E_0 + E_\infty [(\alpha_T)(i\omega)]^\beta}{1 + [(\alpha_T)(i\omega)]^\beta} \quad (3.4)$$

where

$E^*$  is complex Young's modulus;

$E_0$  is the minimum value measured for Young's modulus;

$E_\infty$  is the maximum value measured for Young's modulus;

$\alpha_T$  is the shift factor;

$\beta$  is an exponent that determines the inclination of the curve (rate of variation of the modulus with reduced frequency).

Separating the real and imaginary parts of Equation 3.4, graphs of  $E(\omega, T)$  and  $\eta(\omega, T)$  can be plotted in terms of  $\omega \cdot \alpha_T$ . Fitting of Equation 3.4 with the data measured implies that  $\alpha_T$  was chosen appropriately for each temperature and the variables  $\omega$  and  $T$  were reduced to a single variable  $\alpha_T$ . The essence of the procedure consists of the correct selection of  $\alpha_T$  for each temperature. The selection can be accomplished empirically, although most of the viscoelastic materials applied in NVH solutions obey defined equations for  $\alpha_T$ . The WLF equation and the Arrhenius equation are the most commonly applied.

The WLF equation is given by [7]:

$$\log \alpha_T = -C_1 \frac{T - T_0}{T - T_0 + C_2} \quad (3.5)$$

and the Arrhenius equation is given by:

$$\log \alpha_T = T_A \left[ \frac{1}{T} - \frac{1}{T_0} \right] \quad (3.6)$$

where

$C_1$  and  $C_2$  are constants to be determined;

$T_0$  is the reference temperature, generally chosen as the temperature where the loss factor is maximum for a given frequency;

$T_A$  is the activation temperature.

At first sight, the WFL equation has two degrees of freedom ( $C_1$  and  $C_2$ ) that can be adjusted until an appropriate curve fitting is obtained. Nevertheless, the constants  $C_1$  and  $C_2$  are related to the temperature at which the molecules of the material reach a state of almost zero relative movement. Thus,  $C_1$  and  $C_2$  are inherent properties of the viscoelastic material. Utilization of values other than the correct ones for  $C_1$  and  $C_2$  may lead to an erroneous curve fitting. In this way, Nashif [7] indicates that using the Arrhenius equation allows an analysis of the quality of the values obtained experimentally, since each material has a single activation temperature, and as a consequence, a single shift factor relation. The activation temperature  $T_A$  is given by:

$$T_A = C_3 \frac{T_0 T_g}{\Delta T} \quad (3.7)$$

where

$T_0$  is the temperature where the loss factor reaches its maximum value;

$T_g$  is the temperature where the loss modulus reaches its maximum value;

$\Delta T$  is the difference between  $T_0$  and  $T_g$ ;

The constant  $C_3$ , which is the logarithm of the shift factor  $\alpha_T$  at temperature  $T = T_g$ , can be assumed to be 2.55 for most viscoelastic materials [7].

It is important to observe that the relation  $(T_0 T_g)/\Delta T$  is independent of the frequency for which the values of  $T_0$  and  $T_g$  are chosen, this also being a property of the material.

### 3.2.5 Measurement of Young's Modulus and Loss Factor

The most common methods used to measure the dynamic properties of materials are the forced oscillation method and the resonance beam method, based on the equations of Ross, Ungar and Kerwin [13] and standardized by ASTM Standard E756-98 [12].

The resonance method, a special case of the forced oscillation, is described in references [9], [11] and [15] and may be applied to samples subjected to longitudinal dynamic forces or shearing, as shown in Figure 3.9.

In this method, samples are excited harmonically and the properties are determined in terms of the system resonance frequency. Varying mass  $M$  enables the dynamic properties to be calculated for different frequencies.

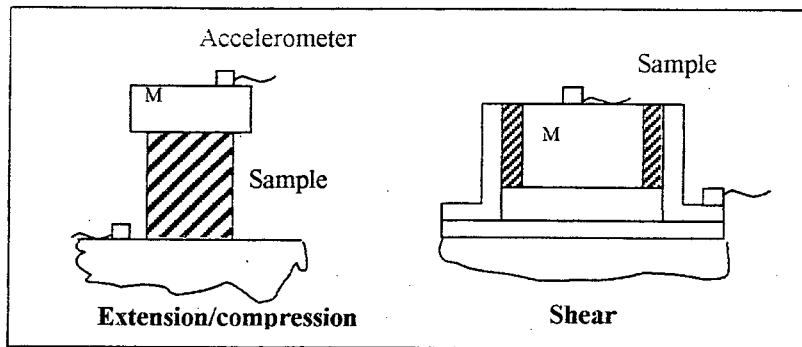


Figure 3.9 – Resonance method

The resonating beam method, described by the ASTM Standard E756-98 [12], consists of a metallic beam with one or more layers of the viscoelastic material, according to the beam configuration to be used. A non-contact transducer excites the beam and another non-contact transducer or a small weight accelerometer measures the response. The loss factor and Young's modulus for the viscoelastic material are obtained in terms of the natural frequencies of the configuration and of the basic beam.

The resonating beam method was the one used in order to measure the dynamic properties of the rubber coats RC1, RC2 and the pressure sensitive adhesive PSA (see Chapter 1). A diagram of the test-rig typically used in beam tests is shown in Figure 3.10.

The sample is excited by the non-contact transducer, which can be magnetic or capacitive. The beam is mounted in a rigid fixture that provides sufficient clamping force around the beam root. Good clamped boundary condition is essential, since the equations take into account the wavelength of sinusoidal waves in clamp-free beams. Either a sinusoidal or random signal can be applied to the excitation transducer. The response is measured by a second transducer.

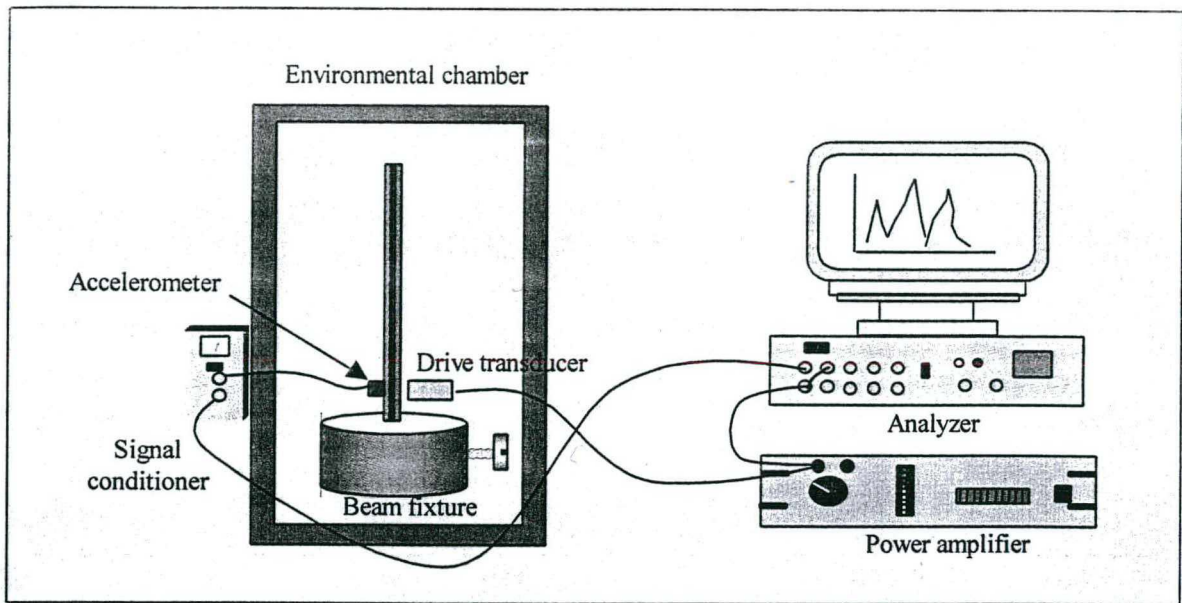


Figure 3.10 – Diagram of a typical laboratory test-rig for beam test

Here, it is important to be aware of the effect of magnetic forces, when two magnetic transducers are used. In this case, the magnetic field of one transducer can affect the response of the other, sometimes flattening the frequency response. Figure 3.11 shows this effect during the measurement of a beam of 180 mm length, using two magnetic transducers.

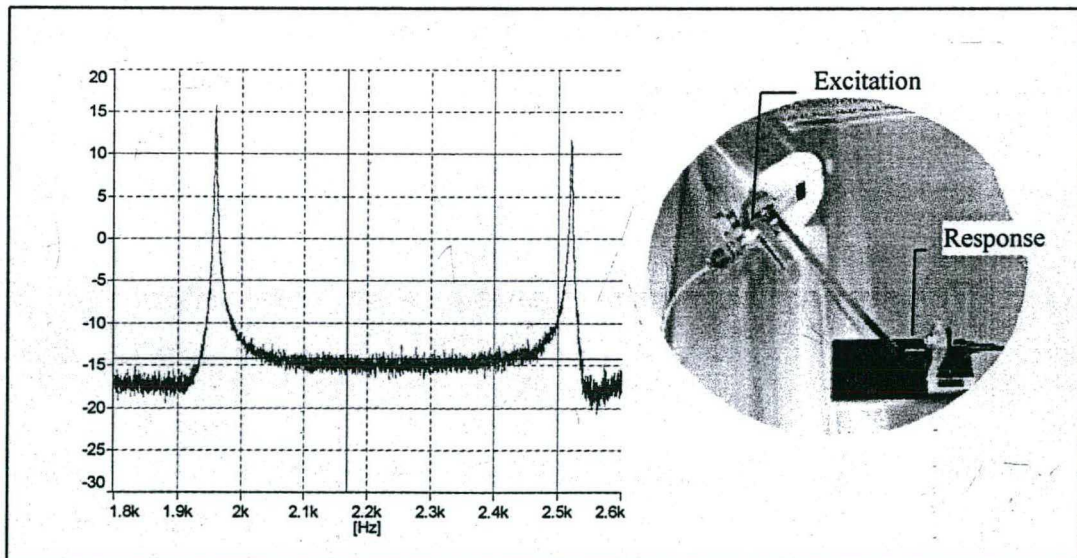


Figure 3.11 – Effect of magnetic pull on FRF. The photo shows the magnetic transducers

This problem can be avoided using one magnetic and one capacitive transducer, or, whenever possible, a small weight accelerometer. The setup is mounted inside an environmental chamber in order to evaluate the material properties as function of temperature. The response of the undamped beam is also needed. Therefore, the set of information necessary is as follow:

1. Frequency and loss factor of the damped beam for each mode;
2. Frequencies of the undamped beam for the same modes as for the damped beam;
3. Geometrical properties of the damped and undamped beam and their densities.

The Standard establishes four configurations for the beam: 1) Uniform beam (such as steel beam); 2) Oberst or externally coated beam (viscoelastic material coating one side of the uniform beam); 3) Symmetric or modified Oberst beam (viscoelastic material coating both sides of the uniform beam) and 4) Symmetric constrained layer (viscoelastic material sandwiched between two uniform beams).

Considering the geometric aspects in which the viscoelastic materials RC1, RC2 and PSA were available, the sandwich configuration (symmetric constrained layer) was used in this research.

For the uniform (undamped) beam, the Young's modulus and loss factor are given by:

$$(3.8) \quad E = \frac{12 \cdot \rho \cdot l^4 \cdot f_n^2}{H^2 \cdot C_n^2} \quad \text{and} \quad \eta = \frac{\Delta f}{f_n}$$

where

$\rho$  is the density of beam;

$l$  is the length;

$H$  is the thickness;

$f_n$  is the resonance frequency for mode  $n$ ;

$C_n$  is the coefficient for mode  $n$  (related to the wavelength - see ASTM E-756);

$\Delta f$  is the half-power bandwidth of mode  $n$ .

The shear modulus and loss factor of the damping material, for a sandwich specimen is calculated from the expressions:

$$G_1 = \left[ A - B - 2(A - B)^2 - 2(A \cdot \eta_s)^2 \right] \left[ \frac{\left( \frac{2\pi C_n E H H_1}{l^2} \right)}{\{(1 - 2A + 2B)^2 + 4(A \cdot \eta_s)^2\}} \right] \quad (3.9)$$

and

$$\eta_1 = \frac{(A \cdot \eta_s)}{[A - B - 2(A - B)^2 - 2(A \cdot \eta_s)^2]} \quad (3.10)$$

where

$$A = (f_s/f_n)^2 \cdot (2 + DT) \cdot (B/2);$$

$$B = 1/[6 \cdot (1 + T)^2];$$

$F_n$  is the resonance frequency for mode  $n$  of the uniform beam;

$f_s$  is the resonance frequency for mode  $s$  of the composite beam;

$\eta_s$  is the loss factor of the composite beam;

$D$  is the density ratio  $\rho_{\text{viscoelastic material}} / \rho_{\text{uniform beam}}$ ;

$H$  is the thickness of the uniform beam;

$H_1$  is the thickness of the viscoelastic material;

$T$  is the thickness ratio  $H_1 / H$ ;

$l$  is the beam length;

$E$  is the Young's modulus of the uniform beam.

The Standard and other references ([6] and [15]) report precautions that must be observed concerning some error sources, such as errors in specimen preparation (like poor adhesion, voids etc), temperature control, measuring resonant frequencies/modal damping and error magnification, because of unstable regions in the equations. Regarding the last item, the term  $(f_s/f_n)^2(1+2DT)$  acts to magnify errors in  $G_1$  and  $\eta_1$  and, for a sandwich configuration, ASTM E-756 recommends that this term should be equal or greater than 2.01.

As a matter of fact, RC1 properties were first measured using an Oberst specimen (viscoelastic material on just one side of the steel beam). However, the thickness ratio was too small, leading to errors. In this case, even negative values were obtained for the Young's modulus. For instance, the 6<sup>th</sup> mode of the uniform beam, at 65° C was found to be  $f_n = 1059$  Hz, while for the composite beam  $f_s = 1058$  Hz. Considering the properties included in Table 1.1, the Young's modulus and loss factor calculated for RC1 were  $E = 1.21 \cdot 10^{10}$  N/m<sup>2</sup> and  $\eta = 0.06$ , which are values that do not agree with literature. When  $f_s$  was changed to 1045 Hz, the values calculated were  $E = -5.5 \cdot 10^{10}$  N/m<sup>2</sup> and  $\eta = -10.36$ . The influence of the accelerometer on the beam resonances was found to be about 2 Hz,



while the magnetic pull was about 3 Hz. Therefore, it is of utmost importance to choose the right beam specimen as well as to use the correct geometric properties and densities.

### 3.2.5.1 Dynamic Properties of Rubber Coat RC1

As mentioned before, the sandwich configuration was used to measure the dynamic properties of the viscoelastic materials. A rubber coat RC1 layer 0.102mm thick was constrained between two layers of steel of thickness 0.762mm each. The free length of the beam was 218mm. A small weight charge accelerometer (~0.65 g) was used to measure the response (velocity). Figure 3.12 is a photograph of the test setup used for the measurements.

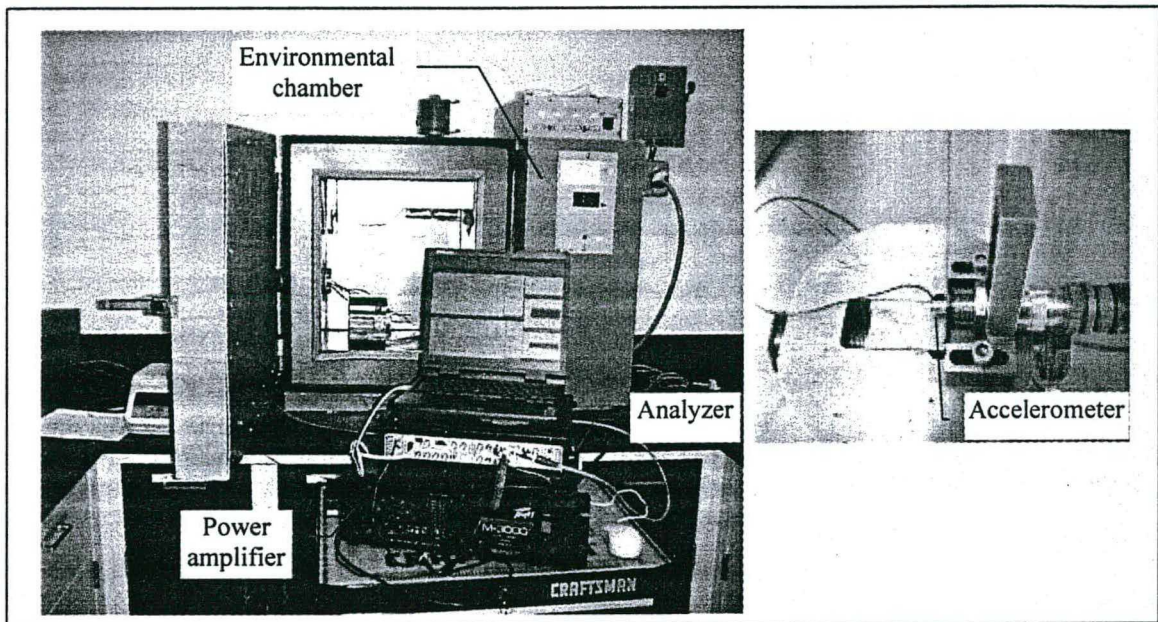


Figure 3.12 – Setup for beam test

The resonance frequencies and respective modal loss factor were measured from modes 2 to 8, for both uniform and composite beams. Modal loss factor was estimated using the half-power bandwidth (-3db) method:  $\eta = \Delta f / f_n$ . If it is necessary to use measurement setups with lower resolution or even to measure low values for damping, loss factor can be generally estimated from the bandwidth between any two points [6]. For instance, if one considers a bandwidth for a difference of -20 dB, the loss factor  $\eta$  calculated will be 10 times the real loss factor. Therefore, one can divide the loss factor calculated by 10 in order to estimate  $\eta$ .

According to the Standard, the equations 3.9 and 3.10 were developed and solved using sinusoidal expansion for the mode shapes of vibration. For sandwich beams, this approximation is acceptable only at higher modes, and it has been the practice to ignore the first mode. Data was obtained for temperatures between  $-18^{\circ}\text{C}$  ( $0^{\circ}\text{F}$ ) to  $121^{\circ}\text{C}$  ( $250^{\circ}\text{F}$ ), with steps of approximately  $14^{\circ}\text{C}$  ( $25^{\circ}\text{F}$ ). Figure 3.13 is the waterfall plot of the frequency responses measured between 10 and  $121^{\circ}\text{C}$ . It can be seen that the highest damping is reached in a temperature range between 25 and  $50^{\circ}\text{C}$ . Furthermore, as the temperature increases, the resonance frequencies decrease. Figure 3.14 shows the calculated loss factor and storage shear modulus, for modes 2 to 6.

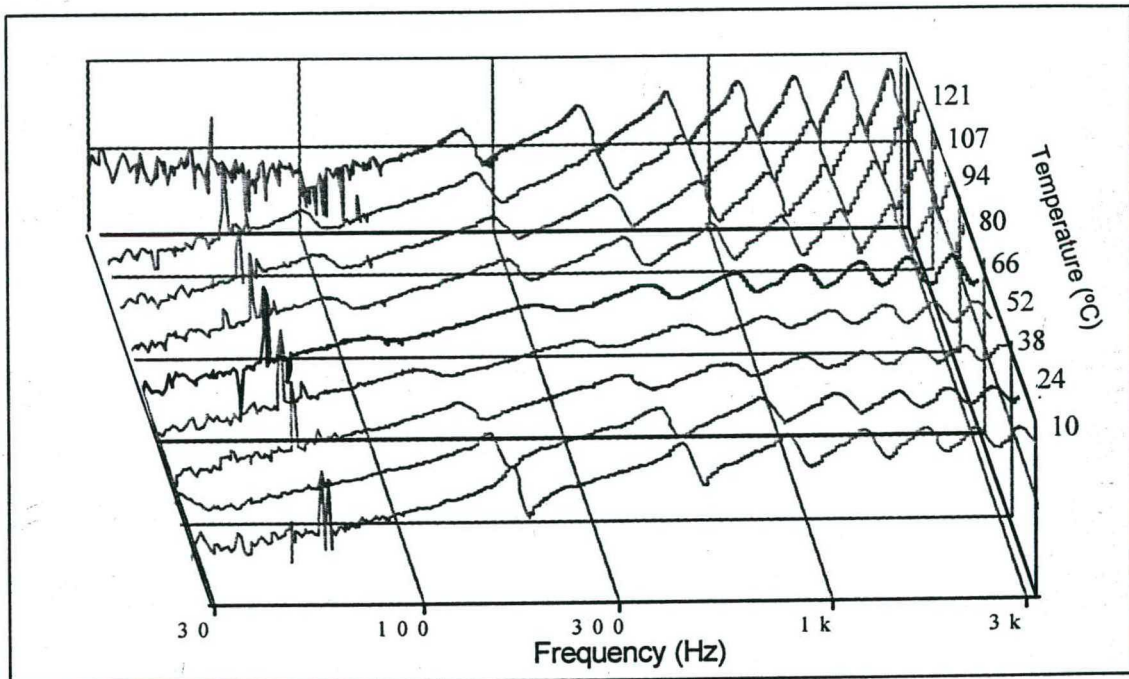


Figure 3.13 – Waterfall: FRF response/excitation as a function of temperature

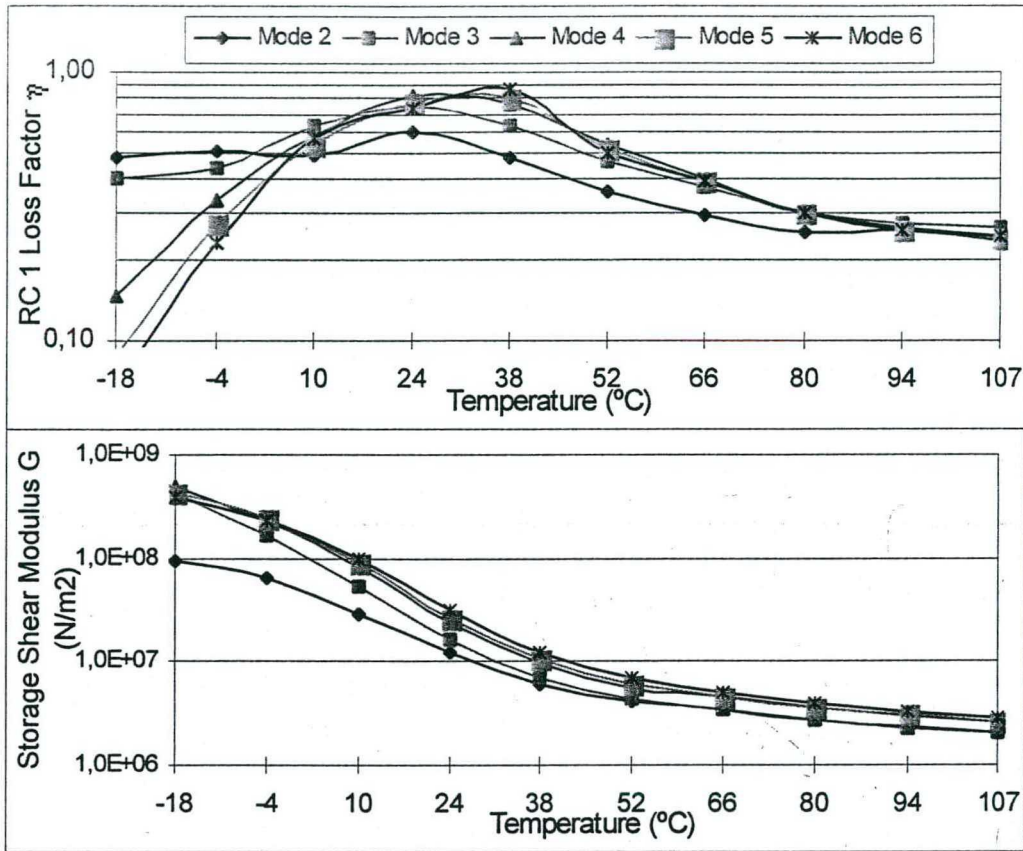


Figure 3.14 – Loss factor vs. temperature and storage shear modulus vs. temperature for RC1

These graphs only provide the properties at discrete points, specifically at the resonance frequencies of the beam. Furthermore, it is not possible to get any information about the resonance frequencies: a 3-dimensional graph would be necessary. In order to acquire the material's properties at any given combination of temperature and frequency, software based on the frequency-temperature superposition principle was used [44]. Shift factors were calculated using the Arrhenius equation and the nomogram is plotted in Figure 3.15. The current version of the software allows only data in Imperial units. Therefore, although the axes of the nomogram contains values primarily in the metric system, those for the Imperial system are given in a smaller size. The left-hand vertical axis is scaled in terms of both the loss factor and storage shear modulus. The lower horizontal axis is scaled in terms of the reduced-frequency (frequency times the shift factor).

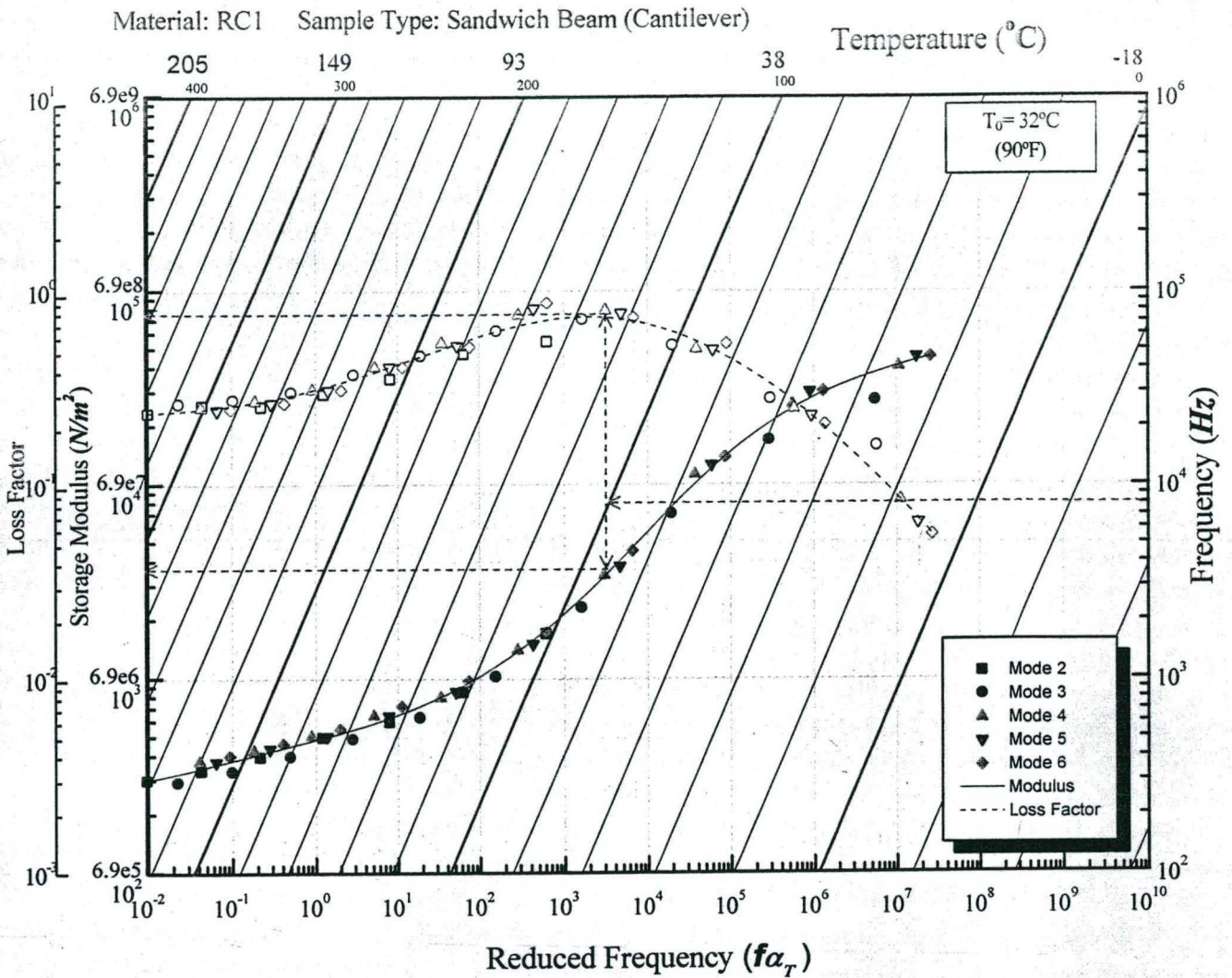


Figure 3.15 – Nomogram of rubber coat RC1

The measured data for the uniform and composite beams are firstly entered in the software, along with the geometric and physical parameters necessary. The reference temperature  $T_0$  and the glass transition temperature  $T_g$  (temperature where loss modulus is maximum) are chosen for a given frequency. For this nomogram, the frequency for reference was chosen to be 1000Hz. Once again, the selection of the frequency is not critical, since the ratio  $T_0.T_g/\Delta T$  is the same for any frequency.

With  $T_0$  and  $T_g$ , the activation temperature  $T_A$  is calculated from equation (3.7), considering  $C_3 = 2.55$ , and the shift factors, for each temperature, are calculated with the Arrhenius equation (3.6). Having reduced all the data using the shift factors, the analytical expression for the loss factor and storage modulus can be generated by curve fitting the data with equation (3.4).

Using the Arrhenius equation allows one to evaluate the reliability of the measured data, since only one combination of values of  $T_0$ ,  $T_g$  and  $\Delta T$  will give an adequate fitting of the data. If the measured data cannot be fitted with such a model, then the measurements should be repeated.

References [7] and [12] also suggest that, initially, two plots can be used to allow the evaluation of the consistency of the measured data: the graphs loss modulus vs. storage modulus and loss factor vs. storage modulus. If these plots are single curves, in the shape of an inverted “U”, without excessive scatter, then the data can be considered consistent. Caution must be taken that consistency of the data does not necessarily imply that the data are accurate. Figures 3.16 and 3.17 show these graphs for the rubber coat RC1.

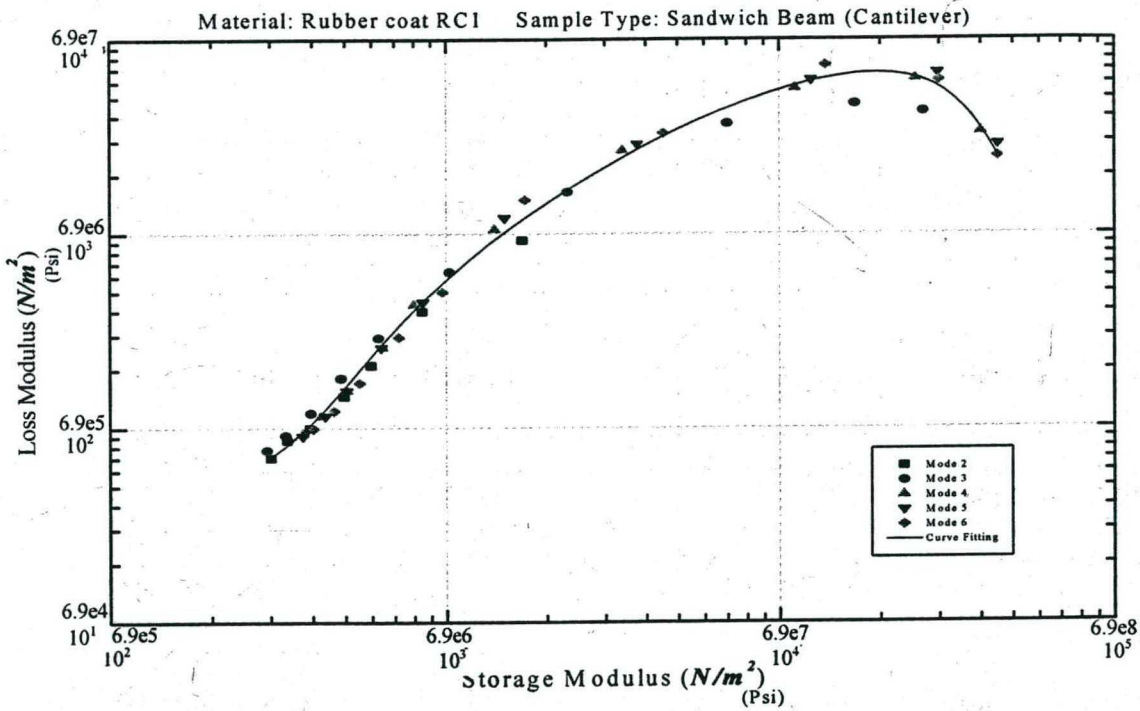


Figure 3.16 – Loss modulus vs. storage modulus for RC1

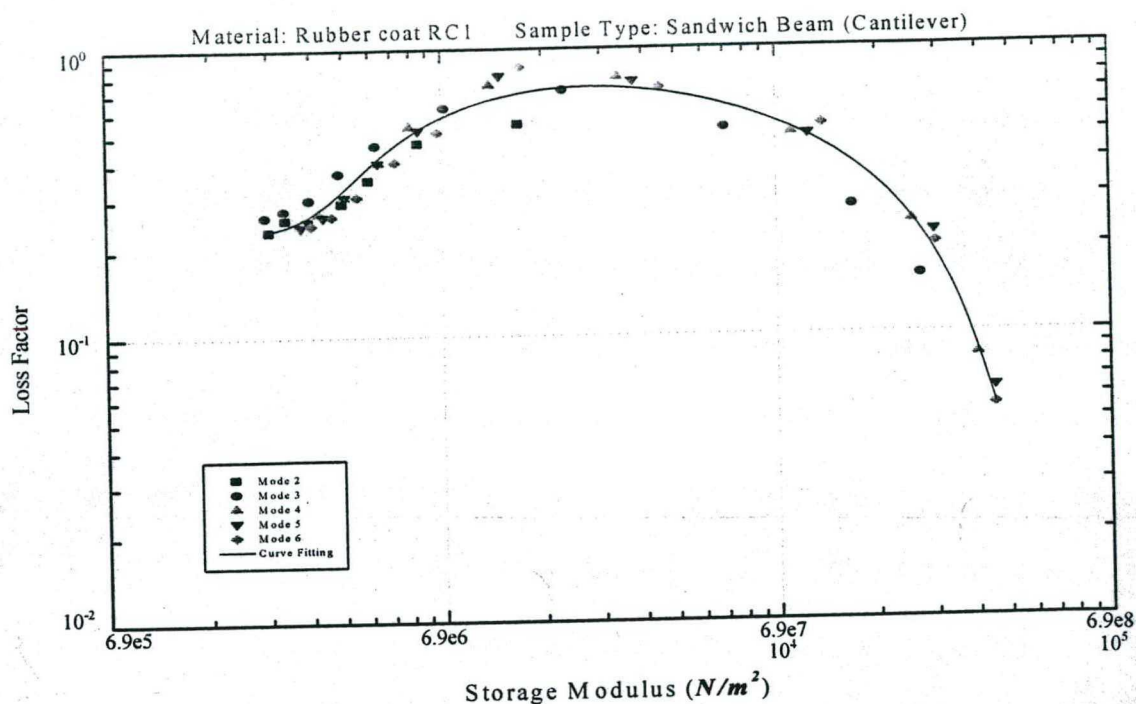


Figure 3.17 – Loss factor vs. storage modulus for RC1

The nomogram in Figure 3.15 can be read as follows:

- 1) A combination of temperature and frequency is selected. In Figure 3.15, an example is shown in dotted lines for  $f=8000\text{Hz}$  and  $T=38^\circ\text{C}$ . Find the point for the frequency on the right-hand axis. Follow the point horizontally to the line of temperature  $38^\circ\text{C}$ .
- 2) At this intersection, a vertical line is drawn. The storage modulus and loss factor values are read from the respective curves, at the intersection with the vertical line. For  $f = 8000\text{Hz}$  and  $T = 38^\circ\text{C}$ ,  $\eta \cong 0.75$  and  $G \cong 2.4e7 \text{ N/m}^2$  ( $3.5e3 \text{ Psi}$ ).

Referring to the nomogram in Figure 3.15, it becomes apparent that the major influence on the dynamic properties of the material is temperature, compared to frequency. For instance, if one starts from the former example of  $f=8000\text{Hz}$  and  $T_1=38^\circ\text{C}$  and increases the temperature to  $T_2 = 60^\circ\text{C}$ , the storage modulus drops from  $2.4e7 \text{ N/m}^2$  ( $3.5e3 \text{ Psi}$ ) to  $6.9e6 \text{ N/m}^2$  ( $3e3\text{Psi}$ ). If the temperature is kept the same  $T_1 = 38^\circ\text{C}$ , in order to drop the storage modulus from  $2.4e7 \text{ N/m}^2$  to  $6.9e6 \text{ N/m}^2$ , the frequency needs to drop from  $f_1=8000\text{Hz}$  to  $f_2\cong 350\text{Hz}$ . Therefore, it requires a large change of frequency in order to compensate a small variation in temperature.

Furthermore, it is interesting to note that, in Figures 3.15, 3.16 and 3.17, the lower modes present better data at higher temperatures. The difficulty in obtaining consistent data at lower temperatures is due to the fact that, at low temperatures, the stiffness of the viscoelastic material approaches the stiffness of the uniform beam. Since the mode wavelength is longer in lower modes, little shearing will occur in the viscoelastic layer. Furthermore, the stiffness of the composite beam starts approaching the stiffness of the fixture, changing the beam length and, as consequence, the mode wavelength.

Once the data reduction and the curve fitting are done, curves of the loss factor and storage modulus as functions of frequency can be analytically plotted for different temperatures. In the same way, graphs of loss factor and storage modulus as a function of temperature are also analytically plotted for different frequencies. Figures 3.18, 3.19 and 3.20 show such graphs for the rubber coat RC1.

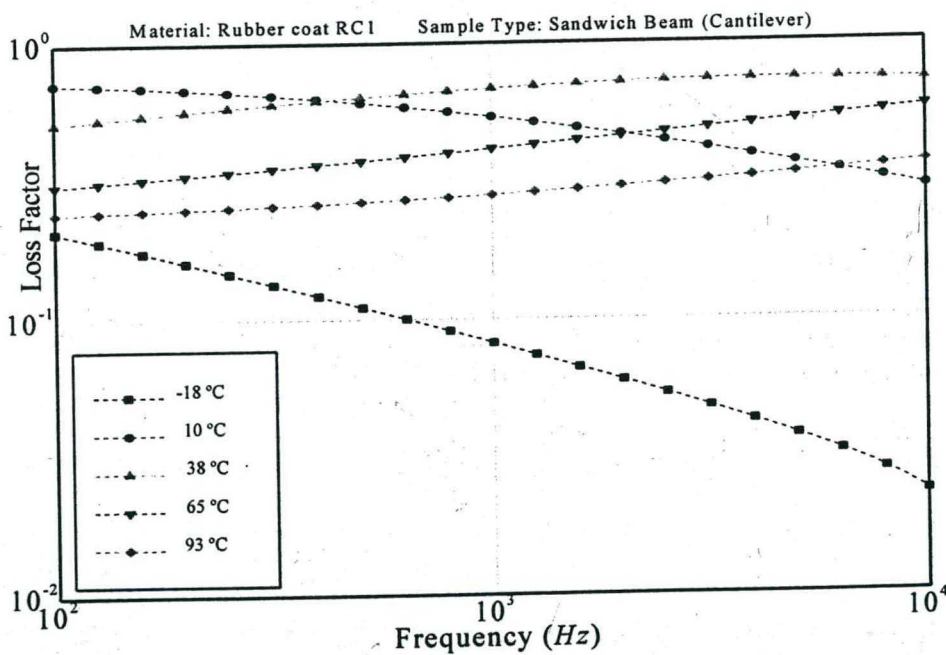


Figure 3.18 - Analytical curves for loss factor vs. frequency

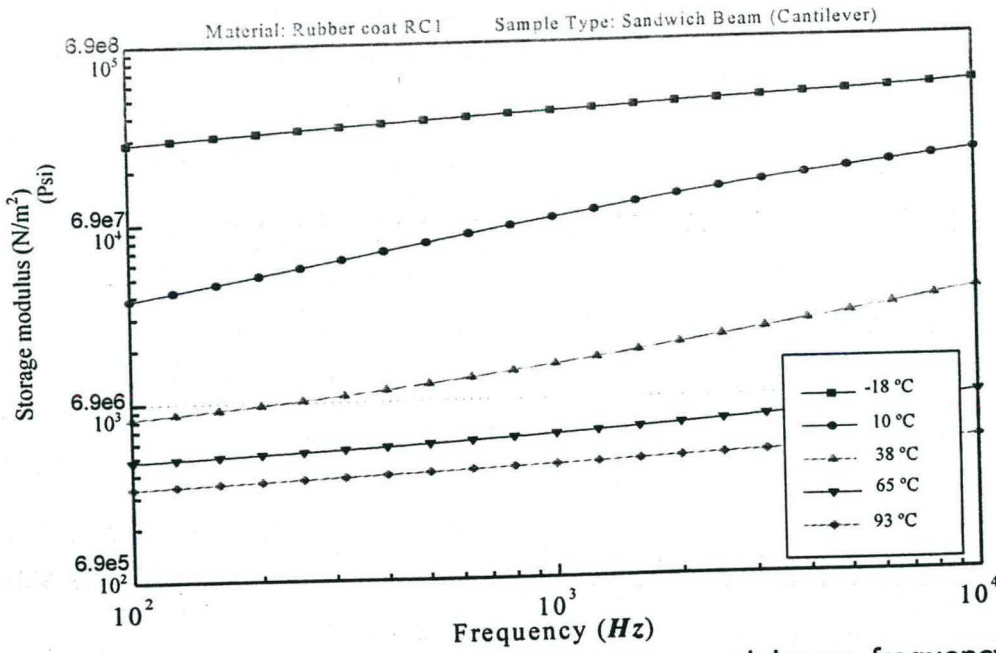


Figure 3.19 – Analytical curves for storage modulus vs. frequency

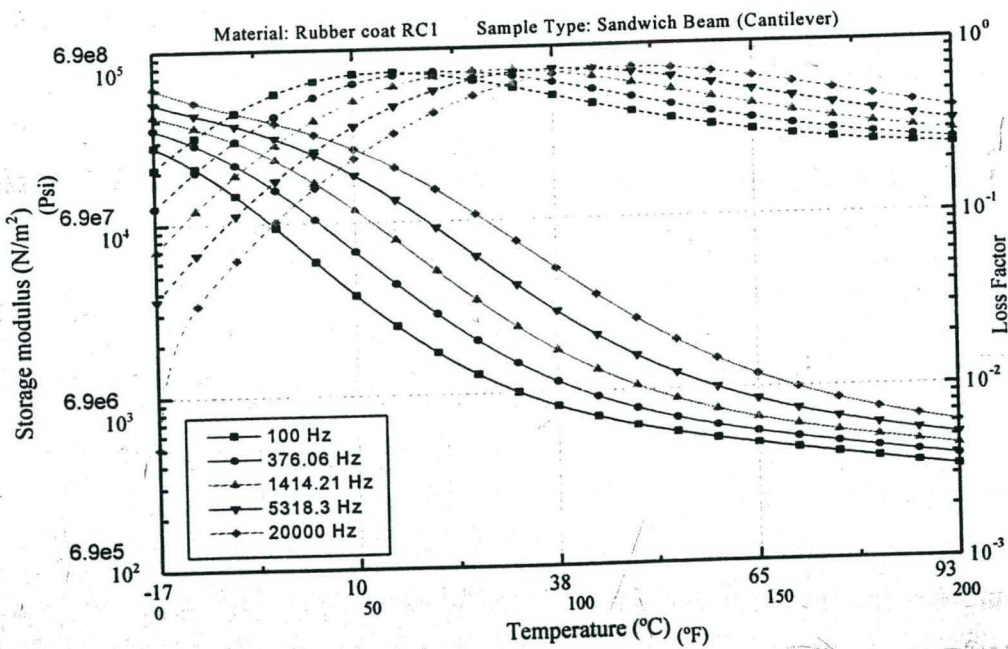


Figure 3.20 – Analytical curves for loss factor and storage modulus vs. temperature

Figure 20 allows one to verify that, in the range between 100 and 20000Hz, the storage modulus of the material can vary up to a factor of ten, keeping the temperature constant.



### 2.5.2 Dynamic Properties of Pressure Sensitive Adhesive PSA

The former procedures were also used in order to measure the dynamic properties of the pressure sensitive adhesive PSA (Chapter 1).

A PSA layer of 0.106mm thickness was constrained between two steel layers of 762mm each. The thickness of the PSA layer was almost twice the thickness given in Chapter 1 (0.055mm). This is because, unlike the RC1 beam, one beam of PSA+steel configuration number 3 in Chapter 1) was bonded to another PSA+steel beam. The density of the PSA was measured to be about  $939\text{Kg/m}^3$ .

The resonances and respective loss factors were measured from the 2<sup>nd</sup> to the 8<sup>th</sup> ending modes of vibration of the cantilever sandwich beam. Unlike in the RC1 measurements, the loss factors were estimated by the half-power bandwidth method.

The temperature range of the measurements was between  $-63^\circ\text{C}$  ( $-82^\circ\text{F}$ ) and  $176^\circ\text{C}$  ( $350^\circ\text{F}$ ). Figure 3.21 shows the nomogram for the PSA.

The PSA nomogram shows a higher transition temperature for this material, when compared to RC1. Practical experience indicates that this is a silicon based viscoelastic material, and it, therefore, reaches its best damping performance at higher temperatures compared to rubbers, considering the range of frequency typical for squeal noise problems (2000 to 16000 Hz).

Once again, the graphs loss factor vs. storage modulus and loss modulus vs. storage modulus can provide a qualitative evaluation of the data obtained, as shown in Figures 3.22 and 3.23.

It was not possible to fit the curves for the PSA nomogram, although it shows that the measurement provided reasonable data. This is explained by the fact that neither the maximum nor the minimum storage modulus was found, i.e., the temperature range used was not wide enough to measure the temperatures where the storage modulus reaches its minimum and maximum values, with a tendency for stabilization. From Figure 3.21, one can see that the transition region extends beyond the highest temperature measured ( $176^\circ\text{C}$ ). In order for reduced data to be fitted, Equation (3.4) indicates that the values of  $E_0$  and  $E_\infty$ , or the minimum and maximum storage modulus, respectively, are required.

Material: PSA      Sample Type: (Cantilever)      Temperature (°C)

315   260   205   149   93   38   -18  
600   500   400   300   200   100   0

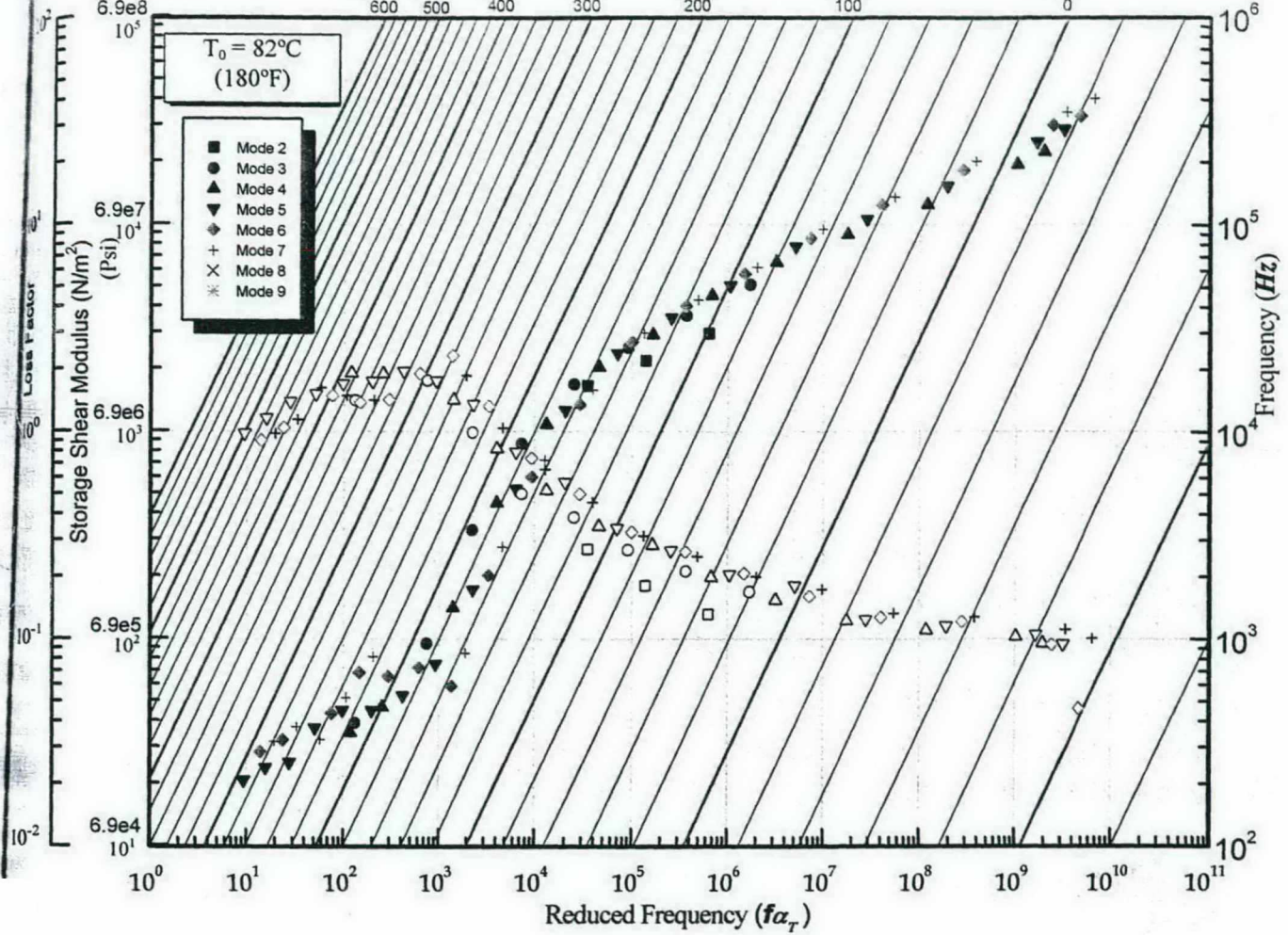


Figure 3.21 – Nomogram of pressure sensitive adhesive PSA

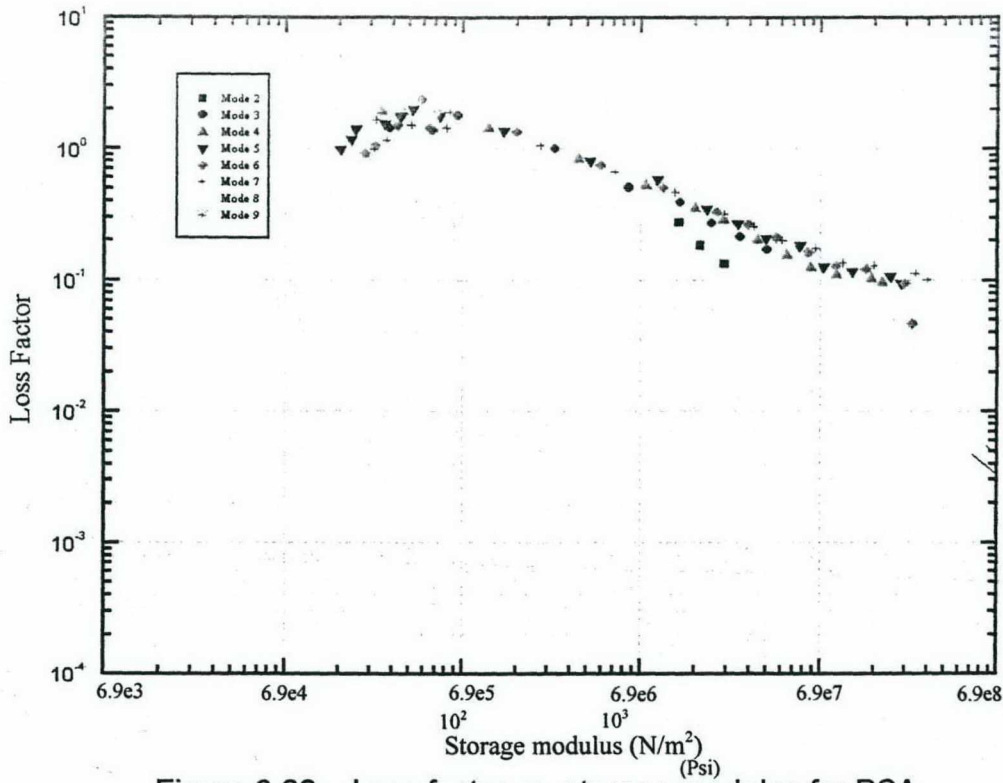


Figure 3.22 – Loss factor vs. storage modulus for PSA

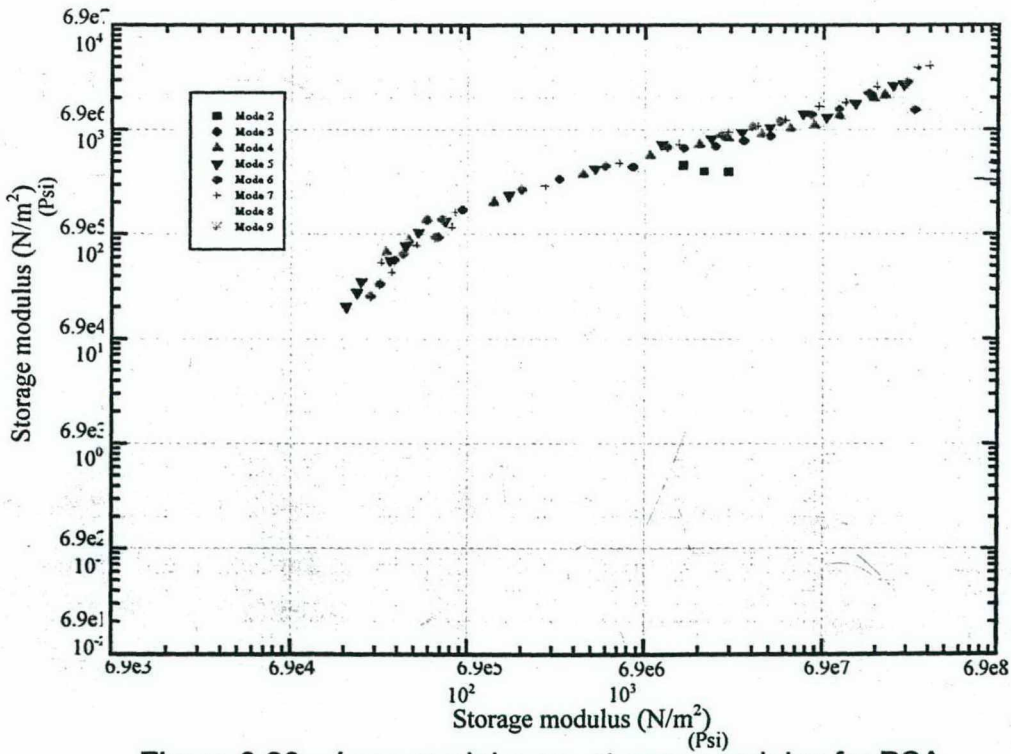


Figure 3.23 – Loss modulus vs. storage modulus for PSA

### 3.2.5.3 Dynamic Properties of Rubber Coat RC2

The RC2 material was only available in the form of shims. Therefore, there was a limitation in the length of the prepared beam for the tests. Figure 3.24 shows the original configuration of the RC2 shim along with the main dimensions.

A beam 120.6mm long was used for the measurements. The cold pressure adhesive and the respective rubber layer were removed from one side. To complete the configuration, in another beam, the adhesive and both layers of rubber were removed and the steel beam was bonded to the former RC2+steel beam, by a structural adhesive, with a higher modulus and lower damping than RC2.

The thickness of the RC2 layer was 0.15mm, with a measured density of  $996\text{Kg/m}^3$ . Resonance and loss factor were estimated for bending modes 2 to 5, for a temperature range from  $-28^\circ\text{C}$  ( $-18^\circ\text{F}$ ) to  $149^\circ\text{C}$  ( $300^\circ\text{F}$ ).

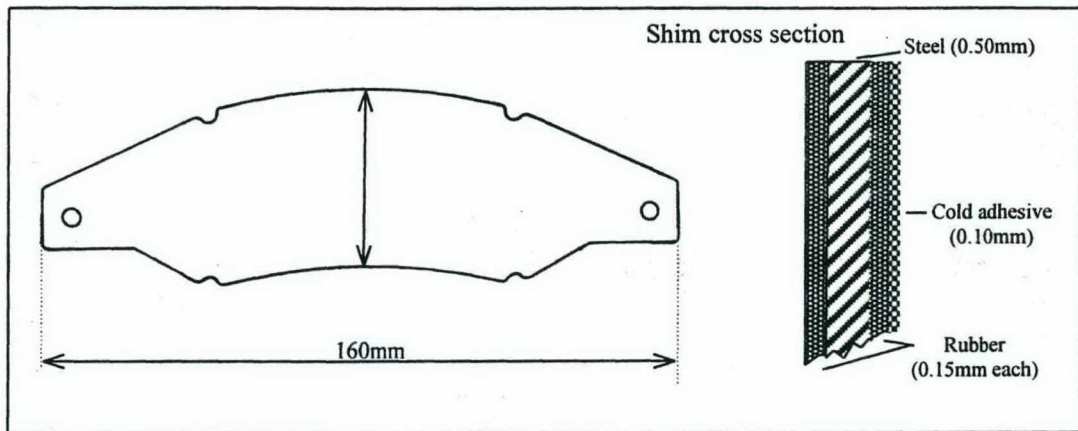


Figure 3.24 – RC2 shim configuration and cross section

Figure 3.25 shows the nomogram for RC2. As was expected, there is a scattering of the reduced data, since the dimensions of the beam tested were not the recommended ones. Nevertheless, it is possible to note that the transition region temperature for RC2 is slightly lower than that measured for RC1. Moreover, maximum damping for RC1 and RC2 are quite the same. These numbers are in agreement with typical properties of nitrile rubbers, as is the case of the rubbers investigated.

Material: Rubber coat RC2

Sample Type: (Cantilever)

Temperature (°C)  
(°F)

205  
400

149  
300

93  
200

38  
100

-18  
0

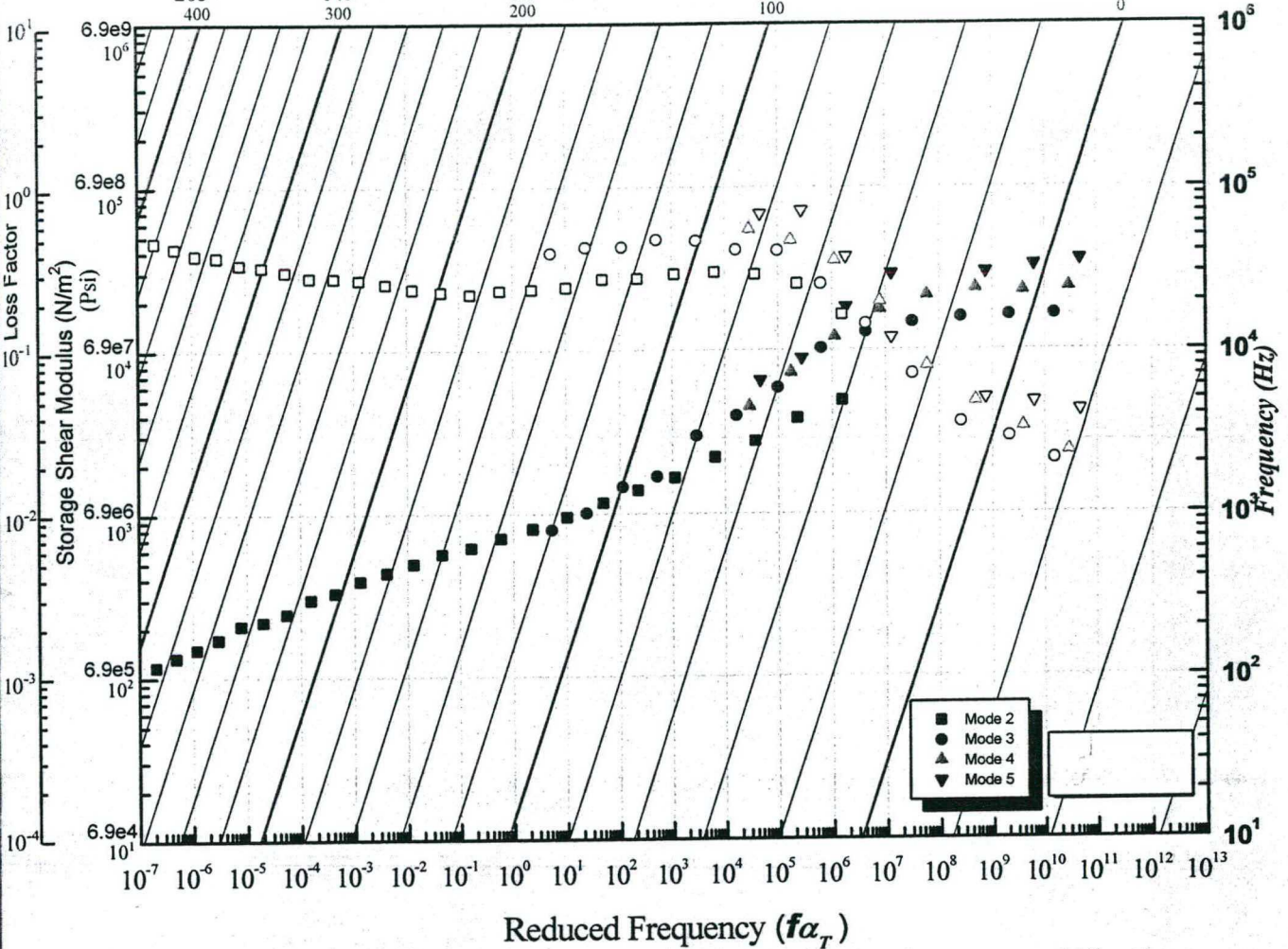


Figure 3.25 – Nomogram of rubber coat RC2

With the estimation of the material properties, the dynamic behavior of the brake system can be studied as different shim configurations are applied. Results of measurements for different pressures and temperatures can be correlated to the dynamic behavior of each viscoelastic material.

## CHAPTER 4

### DYNAMICS OF THE BRAKE SYSTEM

As stated by Fieldhouse [4], “a high coefficient of friction provides for an effective brake: it is better to have too much braking force than too little”. The saying “*a noisy brake is a good brake*” is well founded on the fact that the brake will have a high coefficient of friction, but, as will be seen in this chapter thru an analytical 2 degree-of-freedom system, high kinetic friction coefficients may lead to noise radiation. Although the assertive may be considered valid with respect to braking performance, it becomes questionable when the warranty claims are taken into account. A noisy brake makes it an expensive brake for the vehicle manufacturer, both in terms of cost and credibility.

Once reviewing the literature, one is able to realize the enormous efforts undertaken specially to understand squeal noise in brake systems. For years, researchers have developed several theories to explain squeal phenomena, which may be categorized [39] as: 1) stick-slip; 2) sprag-slip; 3) negative friction-velocity slope or negative damping; 4) modal coupling; 5) hammering theory etc. It seems that no single theory is able to explain every brake squeal phenomenon.

As mentioned in Chapter 1, the most accepted mechanism nowadays presumes a combination of the stick-slip theory with modal coupling, by which the squeal can be explained.

#### 4.1 SQUEAL MECHANISM

At first, brake squeal has its energy source in the friction between the lining material and the rotor. This friction behavior, called stick-slip, is believed to be the excitation that triggers brake squeal. Stick-slip motion is generated by the variation of friction coefficient during braking. It can be introduced by the difference between coefficients of kinetic and static friction, the change of friction coefficient due to contact area variation, or the alternation of kinetic friction coefficient as sliding speed changes [39]. Unlike in a viscous case, the relationship between sliding friction force  $f_f$  and relative sliding velocity  $V_r$  is  $\delta f_f / \delta V_r < 0$ , as shown in Figure 4.1.

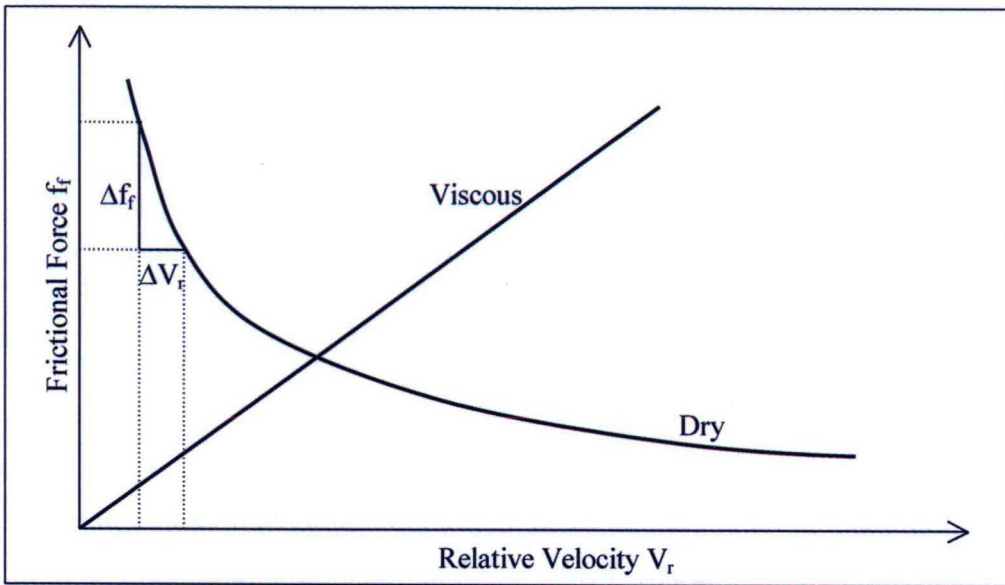


Figure 4.1 – Graphic illustration of dry and viscous friction force as function of sliding velocity

A simple example is a person moving a violin bow across a string. If one is moving the bow forward, at first moment, static friction exists between bow and string and the relative velocity between the parts is zero. When the kinetic frictional forces overcome, the string will spring back towards its equilibrium position, while the bow is still being pushed forward. Therefore, a relative velocity arises while the friction force is reduced. This is the same situation as if one tries to push a table over a tile floor. It is generally necessary to apply more effort to push the table in a lower velocity than in a higher velocity. The higher the relative velocity between table and floor, the lower is the friction force.

However, friction cannot be taken as the only cause of squeal. Dihua et al. [28] mentioned that the tendency of squeal is different when the same friction couple pair is used in different brake systems.

Squeal noise in brake systems occurs in well-determined frequencies (actually, in well determined narrow frequency ranges, since temperature changes the modal behavior of the rotor). These frequencies are generally kept constant for a given rotor, which brings the evidence that the modal parameters of the brake components play a very important role on the propensity of squeal noise occurrence as well as determining at which frequencies.

According to Kung [1], the stick-slip mechanism acts as a negative damper in tangential direction that causes a self-excited vibration. In the later case, two system

modes of vibration geometrically matched eventually couple at the same frequency and become unstable.

Therefore, squeal occurrence strongly relies on the geometric parameters of the system components, in terms of mode coupling.

By this reason, one of the ways of controlling squeal noise occurrence is to keep the brake components from vibrating together, i.e., keeping the resonances away from each other. However, this approach becomes difficult if one considers that the modal parameters of the brake components are strongly affected by other system variables, such as temperature and braking pressure. This problem becomes more evident when the research made by Ouyang et al. [32] is considered. Ouyang et al., after performing a numerical analysis of a brake system, concluded that varying the stiffness of the rotor does not give a unique tendency of decrease or increase of the unstable condition. Reducing the stiffness of the rotor will reduce its resonances, but squeal may happen for higher braking pressures or friction coefficient. Furthermore, squeal noise may arise due to other modes that were stable before and now are closer in frequency and with the same mode shape/wavelength.

Since the input force during a braking excites a wide frequency band, it is a difficult task to mismatch the components modal parameters over the entire range. According to Nashif [7], efforts in this area continue to concentrate on mismatching the most critical conditions from vibrating together.

From the analytical point of view, the excitation phenomenon is difficult to pinpoint, because it involves the modeling of the friction coefficient as a velocity dependent variable. In this case, transient dynamic codes are necessary to model the non-linear friction behavior [46]. On the other hand, analysis of the modal coupling effect can be feasibly handled. Moreover, parametric analyses can be accomplished in order to evaluate the influence of dynamic properties, such as damping, stiffness etc, of some of the brake components or even the whole system.

In order to understand the modal coupling phenomenon, a 2 degrees-of-freedom system is modeled and analyzed as function of different parameters such as friction coefficient and damping.



## 4.2 MODAL COUPLING IN A 2 DEGREES-OF-FREEDOM MODEL

The 2 degrees-of-freedom model here analyzed was first addressed by Hamabe et al. [30] to explain the modal coupling mechanism. This previous work did not consider the effect of damping on the system stability, neither the phenomenon later observed by Tuchinda et al. [34], who concluded that an unstable mode could split back into two stable modes, if the coefficient of friction exceeded a certain critical value.

The 2 degrees-of-freedom system is illustrated in Figure 4.2. The mass  $M$ , connected to a rigid structure by two springs of stiffness  $K_1$  and  $K_2$ , rests over a surface that slides with a velocity  $V$ . The friction coefficient between the mass  $M$  and the surface is  $\mu$ . As a simplification, the friction coefficient is considered constant with the velocity, i.e., the stick-slip phenomenon (negative slope of the friction force in relation to the relative velocity) is not taken into account.

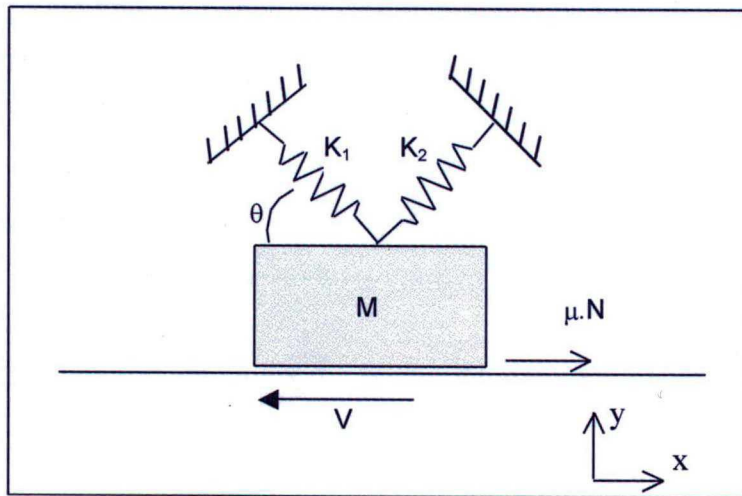


Figure 4.2 – 2 degrees-of-freedom model

The equation of motion for the model can be written as:

$$\begin{bmatrix} K_{11} & K_{12} \\ K_{21} & K_{22} \end{bmatrix} \begin{Bmatrix} x \\ y \end{Bmatrix} - \omega^2 \begin{bmatrix} M & 0 \\ 0 & M \end{bmatrix} \begin{Bmatrix} x \\ y \end{Bmatrix} = \begin{Bmatrix} 0 \\ 0 \end{Bmatrix} \quad (4.1)$$

where

$$K_{11} = K_1 \cdot \cos^2\theta + K_2 \cdot \sin^2\theta + \mu \cdot \sin\theta \cdot \cos\theta \cdot (K_2 - K_1)$$

$$K_{22} = K_1 \cdot \sin^2\theta + K_2 \cdot \cos^2\theta$$

$$K_{12} = (K_1 - K_2) \cdot \sin\theta \cdot \cos\theta - \mu \cdot (K_1 \cdot \sin^2\theta + K_2 \cdot \cos^2\theta)$$

$$K_{21} = \sin\theta \cdot \cos\theta \cdot (K_2 - K_1)$$

A routine was implemented in the software Mathcad<sup>®</sup> for the analysis of the model stability. The development of the equations of motion, as well as an example of the routine implemented on Mathcad<sup>®</sup>, is depicted in Appendix 1.

The initial input values for the model were:  $K_1 = 600\text{N/m}$ ;  $K_2 = 1000\text{N/m}$ ;  $M = 1\text{Kg}$ ;  $\theta = \pi/3$  ( $60^\circ$ ). The system stability can be evaluated by two ways: 1) Imaginary part of the eigenvalues (a negative imaginary part means an unstable mode); 2) Real part of the roots of the characteristic equation (a positive real part means an unstable mode).

The characteristic equation of the 2 degrees-of-freedom model is:

$$\omega^4 \cdot M^2 - \omega^2 \cdot (K_{11} + K_{22}) + K_{11} \cdot K_{22} - K_{12} \cdot K_{21} = 0 \quad (4.2)$$

Therefore, for each value of  $\mu$ , 2 eigenvalues were calculated along with the 4 roots of the characteristic equation, which are the square roots of the eigenvalues, i.e.:

$$s_1^{1,2} = -\sqrt{-\lambda_1} \quad s_2^{1,2} = -\sqrt{-\lambda_2} \quad (4.3)$$

For  $\mu = 0.1$ , the calculated eigenvalues and roots of the characteristic equation were:

Eigenvalues:  $\lambda_1 = 980.9$  and  $\lambda_2 = 636.4$

Roots:  $s_1 = -31.3i$   $s_2 = 31.3i$   $s_3 = -25.2i$   $s_4 = 25.2i$

Undamped stable systems always present, for the characteristic equation, pure imaginary complex conjugate roots. The solution is a harmonic motion, so that the system does not tend to the static equilibrium point neither increase its amplitude of movement [48]. The imaginary part of the roots are the natural frequencies of the system, in radians. Only the roots with positive imaginary are considered for the analysis of stability, since it can be assumed that a negative imaginary part means a negative frequency, which is not feasible in practice. Figure 4.3 shows the system displacement on time for the former results.

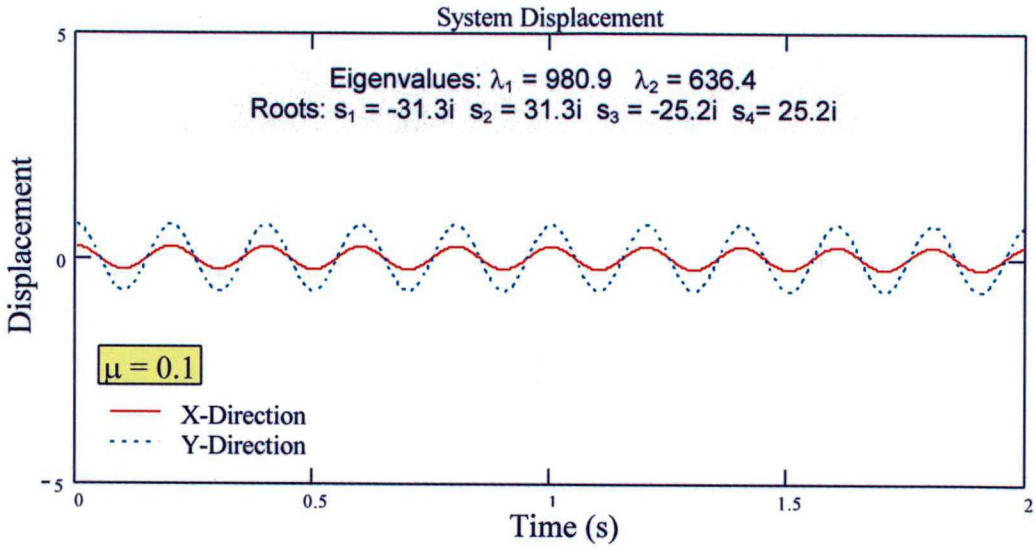


Figure 4.3 – System displacement vs. time for  $\mu=0.1$

The same analysis was made for different values of friction coefficient and the results are shown in the Figures 4.4 to 4.6.

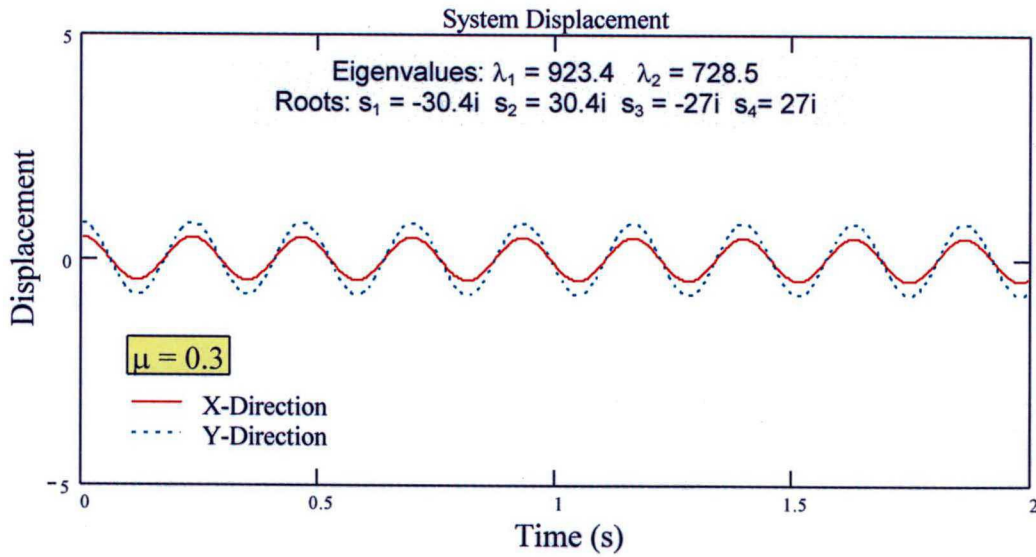


Figure 4.4 – System displacement vs. time for  $\mu=0.3$

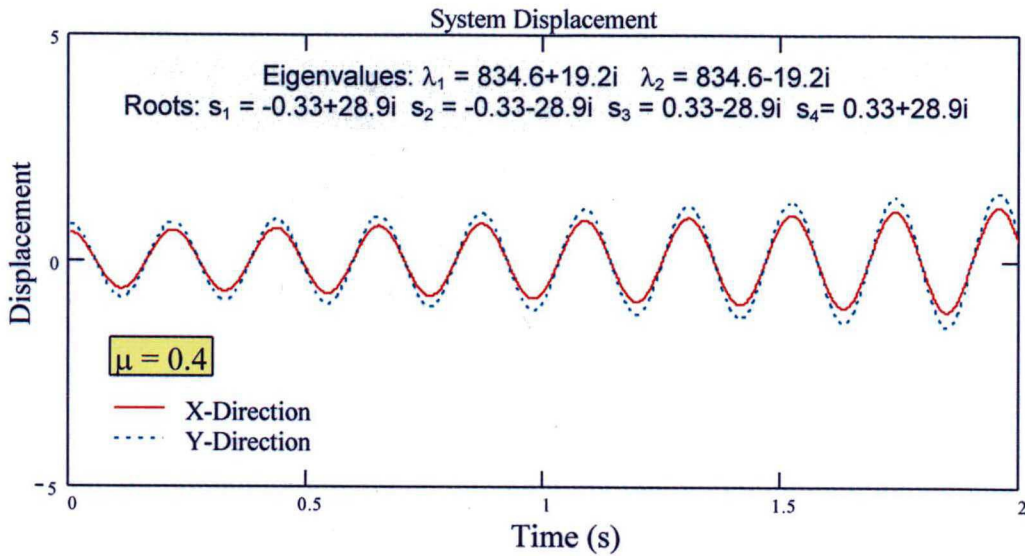


Figure 4.5 – System displacement vs. time for  $\mu=0.4$

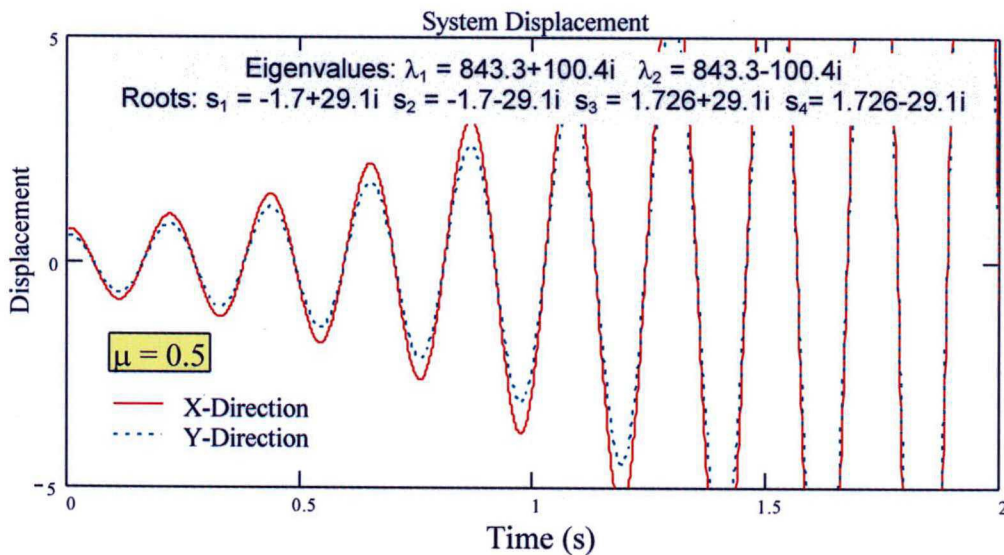


Figure 4.6 – System displacement vs. time for  $\mu=0.5$

The stability model relates the stable condition of a system to a specific value of  $\mu$ . There is a range of values for the friction coefficient which can lead to the instability of the system, i.e., more energy is being introduced into the system than its capacity of dissipation. For some value of  $\mu$  between 0.3 and 0.4 the roots  $s_i$  of the characteristic equation are no longer pure imaginary complex conjugates, but complex conjugates. The factor corresponding to the real part plays the role of a time-dependent amplitude. It establishes how fast, along through the time, the system response decays. Therefore, a positive real part indicates that the movement will increase with time rather than to

decrease. The factor corresponding to the imaginary part varies harmonically with time, i.e., is related to the angular frequency of vibration.

For values of  $\mu$  below 0.3, the system presents two distinct eigenvalues. As the friction coefficient increases, these eigenvalues approach to each other along the imaginary axis until the point at which the two eigenvalues coincide. At this point the two eigenvalues turn into a pair of complex conjugates eigenvalues, one of which is stable, with a positive imaginary part, and other unstable, with a negative imaginary part.

A similar idea can be applied if the roots of the characteristic equation are considered. As stated before, the analysis is made considering the two roots with positive imaginary parts. For low values of  $\mu$ , the roots are two pairs of pure imaginary conjugates. The real parts, related to the exponential decay of the vibration, are null. In this case, the amplitude of vibration will remain constant with time. After the modal coupling, the roots turn into two pairs of complex conjugate. The root with a positive real part (it is considered only the roots with positive imaginary part) is the unstable mode, since a positive real part means an exponential growth of the vibration amplitude.

Figure 4.7 is a graph showing the coupling of the two system modes of vibration, as function of the friction coefficient. It can be seen that, for the input values used in the model, the modes will couple when the friction coefficient reaches a values around 0.4. Actually, this condition is function of the input parameters, like stiffness, mass and the angle of the springs.

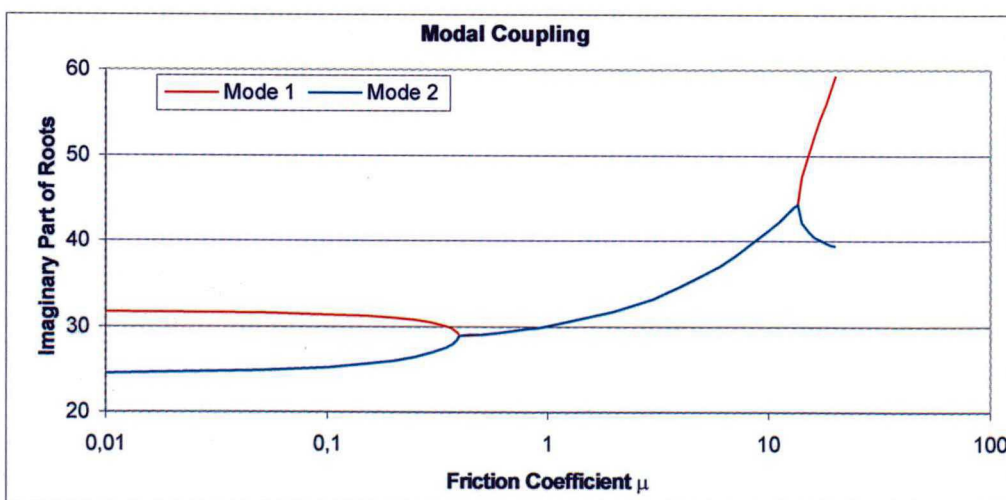


Figure 4.7 – Modal coupling: Imaginary part of system modes vs. friction coefficient

Figure 4.8 is a *root locus* plot with the real part of the system modes vs. imaginary part, as function of the friction coefficient  $\mu$ . When  $\mu \cong 0.39$ , the mode represented by the red line become unstable and its real part, initially equal to 0, assumes positive values.

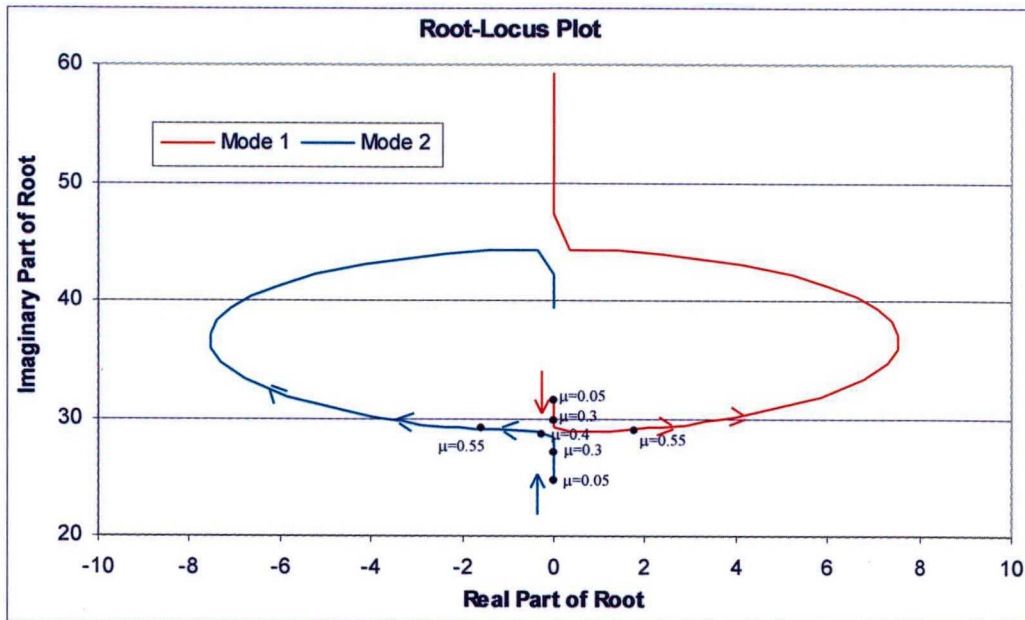


Figure 4.8 – Root locus plot of the complex roots of the characteristic equation

One important characteristic of this model can be seen in Figures 4.7 and 4.8. At higher values of coefficient of friction, the coupled modes separate into two stable modes and instability ceases to exist. The roots of the characteristic equation turn back to two pairs of pure imaginary complex conjugates. This phenomenon had been also observed by Tuchinda et al. [34], in a pin-on-disc system.

As seen before, in order for the system to become unstable, the roots of the characteristic equation (Equation 4.2) should be complex and the real part positive. Complex roots situation occurs when, in the characteristic equation,  $b^2 - 4ac < 0$ , where  $a = \omega^4 \cdot M^2$ ,  $b = M \cdot (K_{11} + K_{22})$  and  $c = K_{11} \cdot K_{22} - K_{12} \cdot K_{21}$ . In this model, increasing the friction coefficient will make  $b^2 < 4ac$ .

For each combination of values of  $K_1$ ,  $K_2$ ,  $M$  and  $\theta$  there is a value of the friction coefficient that makes the system to return to the stability. In this example, the friction coefficient that brings the system back to stability is  $\mu \cong 14$ . Obviously, there is no practical meaning for a friction coefficient of fourteen, but this number can be switched to feasible ranges by changing the model input parameters. Figure 4.9 shows the friction coefficient range for which  $b^2 < 4ac$ , where the system becomes unstable.

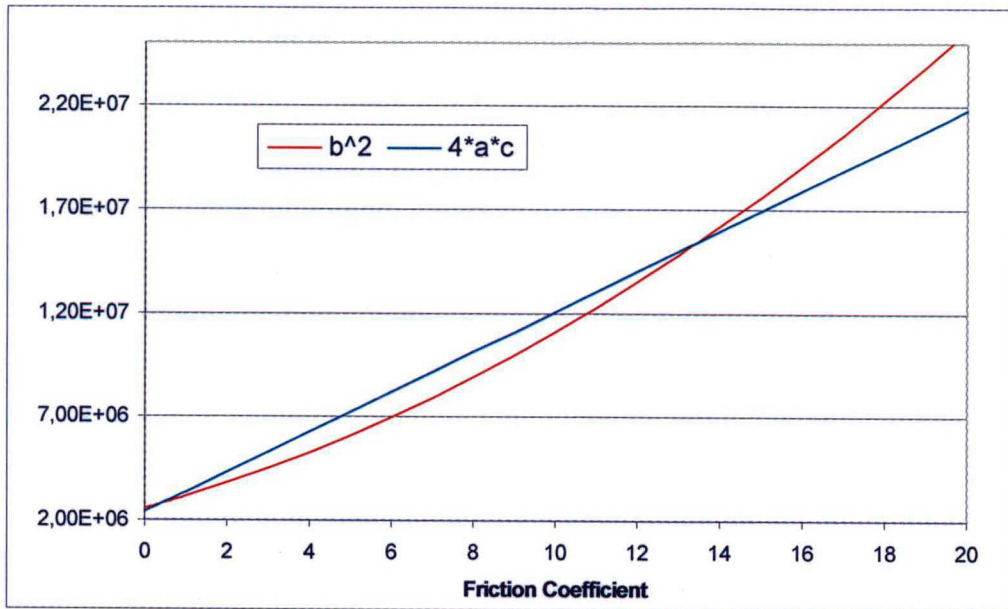


Figure 4.9 – Values of  $b^2$  and  $4ac$  for the 2 DOF model, indicating the instability range

Until now, the effects of the friction coefficient on the dynamic stability were analyzed considering the system as undamped. As mentioned previously, adding damping is one of the techniques for solving brake squeal noise and it becomes useful to examine, analytically, its influence on the 2 degrees-of-freedom system stability.

Damping can be added to the model by making use of a hysteric damping approach, in the form of a complex stiffness for the springs. Figures 4.10 to 4.13 show the system response when complex values are used for  $K_1$  and  $K_2$ .

When damping is applied in terms of complex stiffness to the system, the eigenvalues do not share the same imaginary part anymore. This can be explained by the fact that now the damped natural frequencies are being taken into account instead the undamped ones.

By definition, in a self-excited system, the amplitude of vibration controls the input force and vice-versa. When the amplitude of the response is reduced, the excitation is also reduced. Moreover, reducing the excitation will reduce the response and so on. Therefore, the system response will collapse to a situation of low vibration amplitude, as shown in Figures 4.11 and 4.12, or it will increase indefinitely until the energy introduced is compensated by noise radiation, as already shown in Figures 4.5 and 4.6.

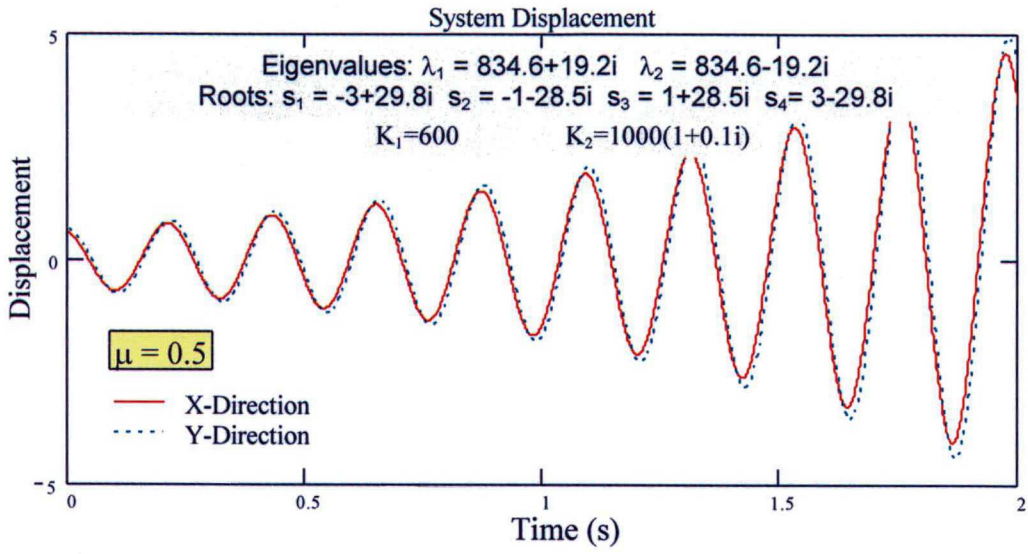


Figure 4.10 – System displacement vs. time for  $K_1=600\text{N/m}$  and  $K_2=1000(1+0.1i)\text{N/m}$

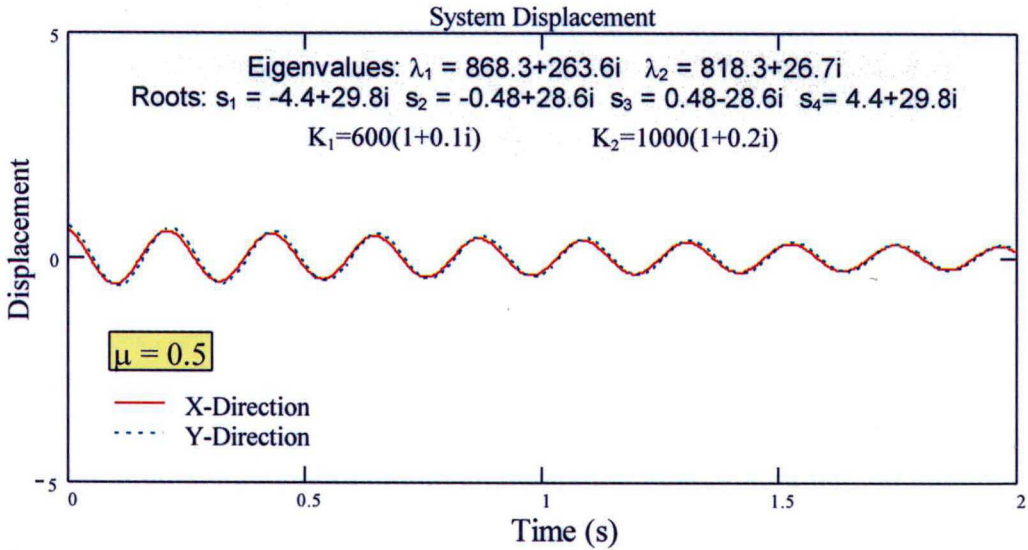


Figure 4.11 – System displacement vs. time for  $K_1=600(1+0.1i)\text{N/m}$  and  $K_2=1000(1+0.2i)\text{N/m}$



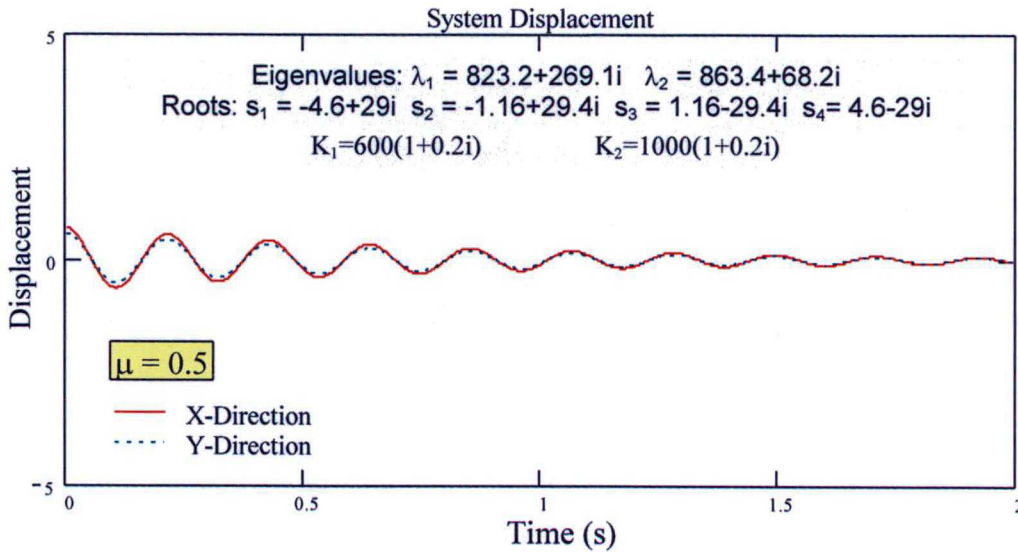


Figure 4.12 – System displacement vs. time for  $K_1=600(1+0.2i)$ N/m and  $K_2=1000(1+0.2i)$ N/m

### 4.3 SQUEAL MECHANISM IN THE BRAKE SYSTEM

Based on the prior discussion, squeal noise in brake systems can be defined as the result of vibration due to the coupling of two vibration modes of brake components. Squeal noise occurs whenever two or more system components start vibrating together due to modal coupling.

The forcing function exciting the system is the friction force between the pads and the rotor. The amplitude of vibration is controlled by the dynamics of the individual components, the input forcing function and the damping.

If the forcing function keeps introducing more energy into the system and its damping is at such a low level that it cannot dissipate as much energy as is being applied to it by the friction force, the vibration level of the system will increase until this energy is balanced by noise radiation.

One class of brake squeal noise mechanism is due to the coupling between the bending modes of vibration of the rotor and the pad. When the two components, rotor and pad, start vibrating together and in phase, the system damping for that specific system resonance is reduced, since the joint damping between rotor and pads decreases. As a consequence, the friction forces may introduce more energy into the system than it can dissipate.

In some cases, the dynamics of the caliper and suspension components can also play a role in the system mode responsible for the noise. Reference [39] deals with cases where squeal noise is generated by energy exchange between in-plane and out-of-plane modes of the rotor. Nevertheless, based on experience and data from literature, it can be assumed that the modes of vibration of the rotor usually play the most important role in establishing the squeal noise frequencies. Hence, it can be considered, in general, as the component whose surface radiates most part of the energy.

Figure 4.13 shows the situation of the brake system analyzed in this thesis, where the 3<sup>rd</sup> bending mode of the pad can couple with the 7<sup>th</sup> bending mode of the rotor. Coupling between rotor and pad modes occurs when they have the same wavelength and close frequencies.

Geometrically, the pad mode of vibration will ride on top of the rotor mode, as shown in Figure 4.13. Effectively, the frictional damping is lost at this moment, since rotor and pad are now vibrating in phase.

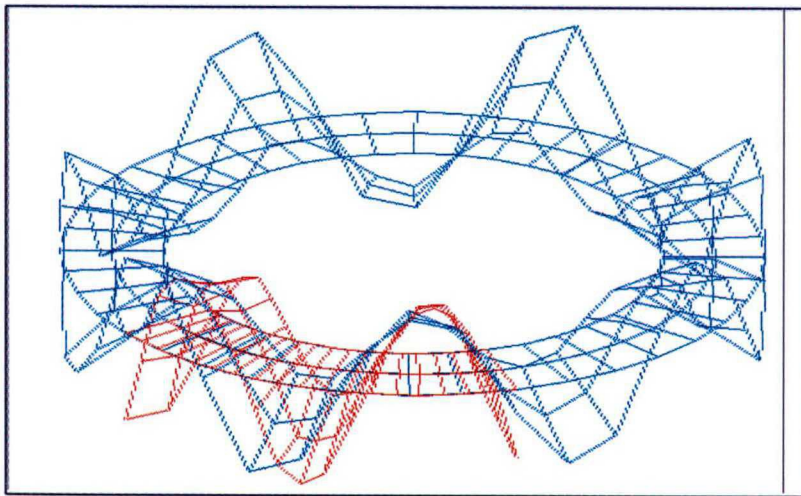


Figure 4.13 – Coupling between modes of vibration of rotor and pad. The modes have close wavelength

As aforementioned, at first sight, squeal noise can be avoided with an adequate design of the components, keeping the resonances apart, changes in the geometry of the pads, like chamfers and/or slots, or changes in the mechanical properties of the components (stiffness, mass), in order to avoid possible modal couplings.

However, the modal coupling mechanism is also influenced by the boundary conditions of the system, specially braking pressure and temperature. Figure 4.14 is an example of how these two parameters affect the resonances of rotor and pad.

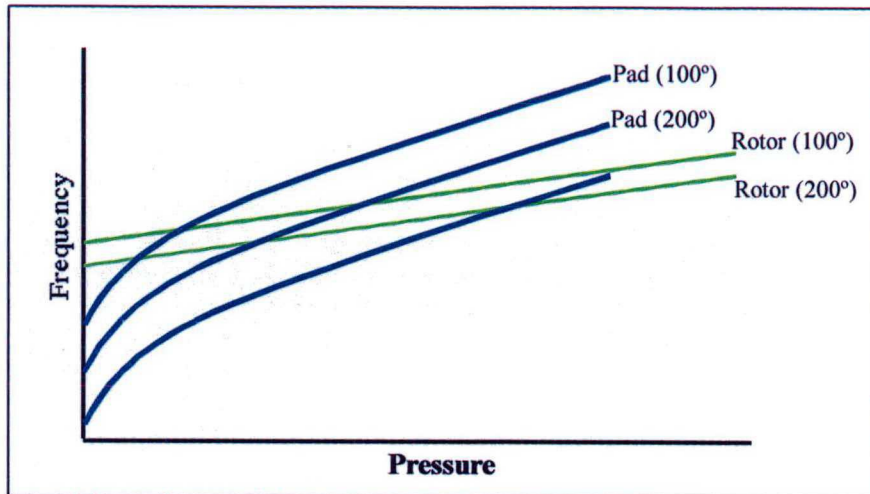


Figure 4.14 – Influence of temperature and pressure on modes of rotor and pad

One can conclude that even with changes in the geometry of the pad, pressure and temperature may contribute to the coupling of the same modes in a different boundary condition. Even more likely, modes formerly uncoupled may have their frequencies closer and wavelength matched, generating squeal noise at a different frequency.

In order to understand and evaluate how brake shims, specially the rubber coated ones, can affect the dynamic behavior of the system, it is of utmost importance to characterize the brake noise. The approach used for this purpose involved brake dynamometer measurements, modal analysis of individual components, frequency response of the assembled brake system, sound intensity, as described here and in the following Chapters.

#### 4.4 DYNAMOMETER RESULTS OF BASELINE

The first step was to identify the noise condition of the brake system. The most common method for that is to utilize brake dynamometers to simulate brake events at a corner of the vehicle suspension. This tool is effective in identifying squeal noise frequencies and temperature ranges at which it occurs. The shortcoming is that no insight is gained as to the mechanism for squeal noise generation and the root causes are not identified. For this research, an inertia dynamometer was used for the brake squeal screening. Figure 4.15 shows the main components of an inertia dynamometer for brake systems. The dynamometer can control temperature, pressure and rotational speed, while recording the sound pressure level and frequency of noise occurrences.

Maximum sound pressure level was recorded for approximately 800 brake events. A microphone was connected to an analyzer that recorded, during each brake event, the autospectrum containing the maximum sound pressure level.

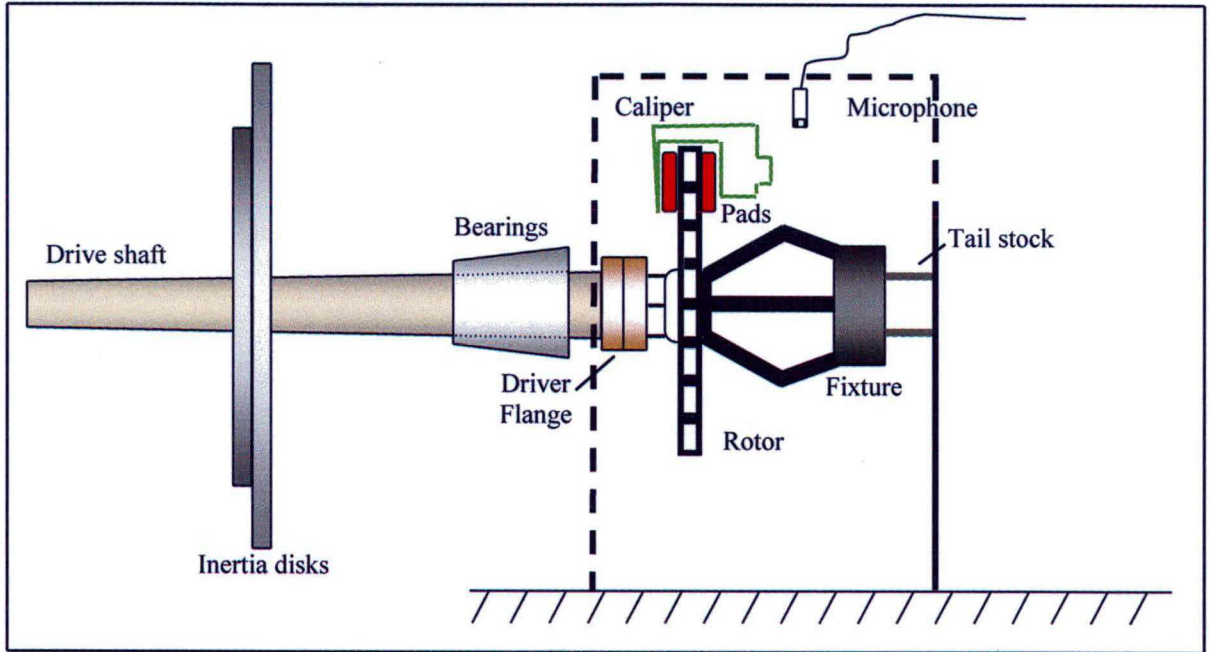


Figure 4.15 – Sketch of a typical inertia dynamometer for brake systems

Table 4.1 is a resume of the results obtained for the baseline, i.e, no shims attached to the pads, and Figures 4.16 and 4.17 present the noisy occurrence distribution as function of pressure, temperature and frequency.

Table 4.1 – Resume of dynamometer test for baseline

Shim Configuration	BASELINE	Top 10 Noise Frequencies	
Minimum Frequency (Hz)	1600	Hz	% Occ.
Maximum Frequency (Hz)	16000	8000	4.7%
SPL Minimum Threshold (dB)	70	8400	4.5%
Max. dB	110.1	8200	3.5%
		7800	3.3%
Total Stops	806	7400	3.1%
>70 dB	197 stops	7200	2.2%
>80 dB	163 stops	7600	1.4%
>90 dB	101 stops	6800	0.6%
>100 dB	39 stops	7000	0.5%
		8600	0.5%
%>70 dB	24.4%	8600	0.5%
%>80 dB	20.2%		
%>90 dB	12.5%		
%>100dB	4.8%		

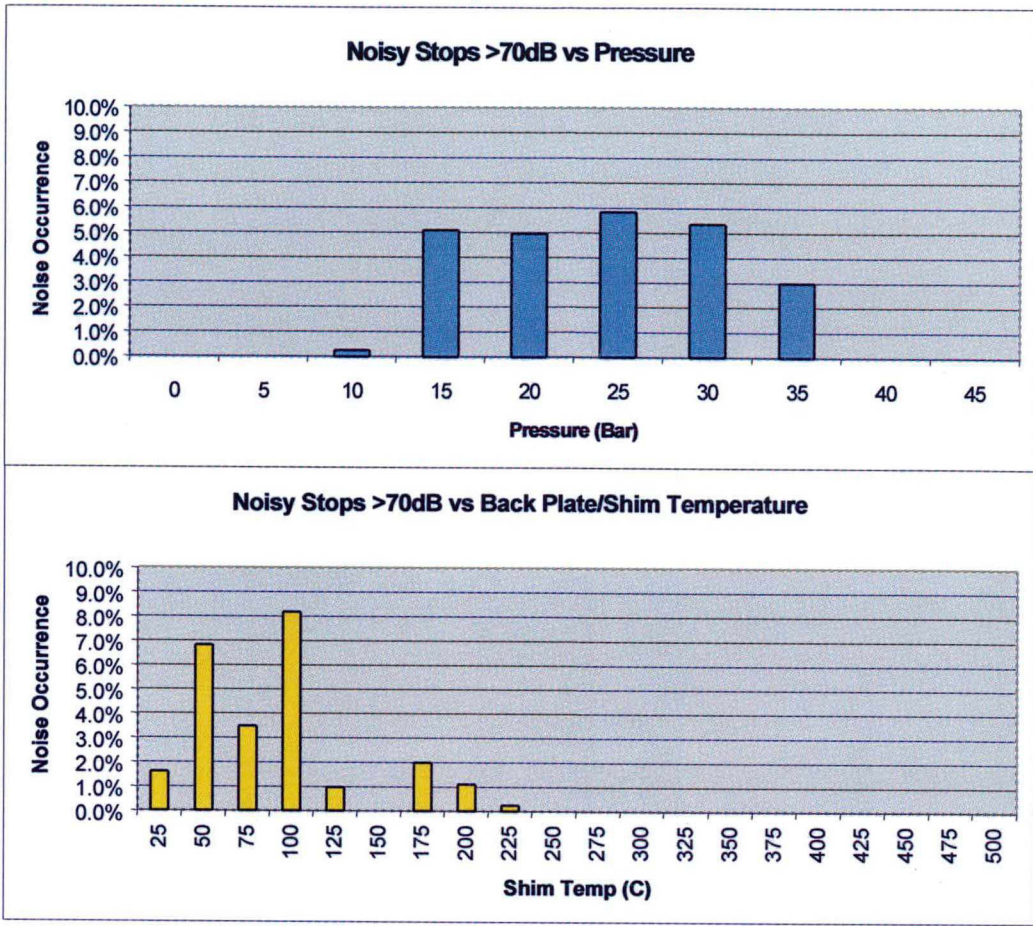


Figure 4.16 – Percentage of noisy occurrence (>70dB) vs. pressure and temperature

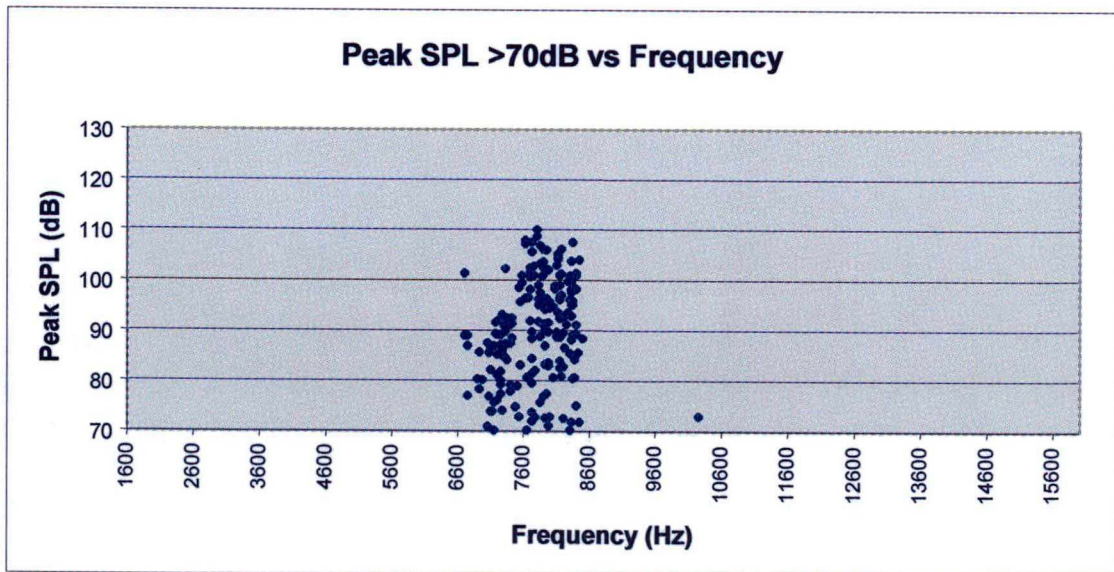


Figure 4.17 - Noisy occurrence distribution as function of frequency

The majority of the noise occurrences are spread over a range of frequency between 7.8KHz and 8.4KHz, as can be seen on Table 4.1 and Figure 4.17. They occurred at medium and high braking pressures and most part concentrated on temperatures below 100°C. As will be seen later, these results can be correlated to informations obtained thru frequency responses of the whole brake system as function of the lining pressure and temperature.

Despite identifying the boundary conditions and frequencies at which squeal occurs, no information was obtained with regards to the potential coupling modes. For this purpose, modal analysis of rotor, pad and caliper was performed, as following.

## **4.5 COMPONENT MODAL ANALYSIS**

Modal analysis of individual components allows gaining insight into potential coupling modes, which is, as stated before, the cause of squeal noise generation. Individual components are modeled with a mathematical mesh of the geometry.

Pad, rotor and caliper frequency responses were performed by exciting each component with a piezoelectric hammer and recording the response with an accelerometer. The frequency responses functions (FRF) were processed in the software STAR System [49] in order to identify the resonances of the components and their associated modal stiffness, mass and damping values.

A variety of curve fitting methods, both single mode (SDOF) and multiple modes (MDOF), can be used selectively on a set of measurements to obtain the best possible modal parameter estimation.

### **4.5.1 Pad Modal Analysis**

The pad was the simplest geometry submitted to a modal analysis. The structure was supported by two pieces of foam in order to simulate a free-free boundary condition. The purpose of the free-free condition is to allow the structure to vibrate without interference of other elements. In a practical viewpoint, this is impossible. However, a good approximation for the free-free condition can be obtained using flexible elements for the fixation. Thus, the natural frequencies of the assembly are put in a lower range than that of the natural frequencies of the structure.

Excitation was applied thru a hard tip impulse force hammer and the response was measured by a small weight charge accelerometer (0.65g). As in the beam tests discussed in Chapter 3, a small weight accelerometer is necessary in order to assure that the measured dynamic properties of the structure are not affected by the presence of the transducers. In light structures, like the beams and the pads, even the cable of the transducer can affect the modal parameters measured, specially damping.

The frequency range measured was from 0 to 12800Hz, which include the squeal noise frequency. The accelerometer was kept fixed in one point, while the excitation was applied at all points of the mesh. Figure 4.18 show the mesh defined in the software STAR system.

The major steps of the parameter identification was as follow:

- 1) Determination of the number of modes, by visual inspection and modal peak functions.
- 2) Set up of curve fitting bands. Since the modes of the pad were relatively away from each other, a SDOF curve fitting method was selected, the Polynomial Method. Each frequency band comprised one mode.
- 3) Auto fit of all measurements, specifying the measurement DOF (in this case, the z-direction)
- 4) Display of the mode shapes and comparison of synthesized FRFs with measured FRFs.

Table 4.2 presents the modal parameters estimated for the brake pad and Figure 4.19 shows the respective mode shapes. Figure 4.20 is the comparison between the synthesized curve and the sum of the 40 FRFs.

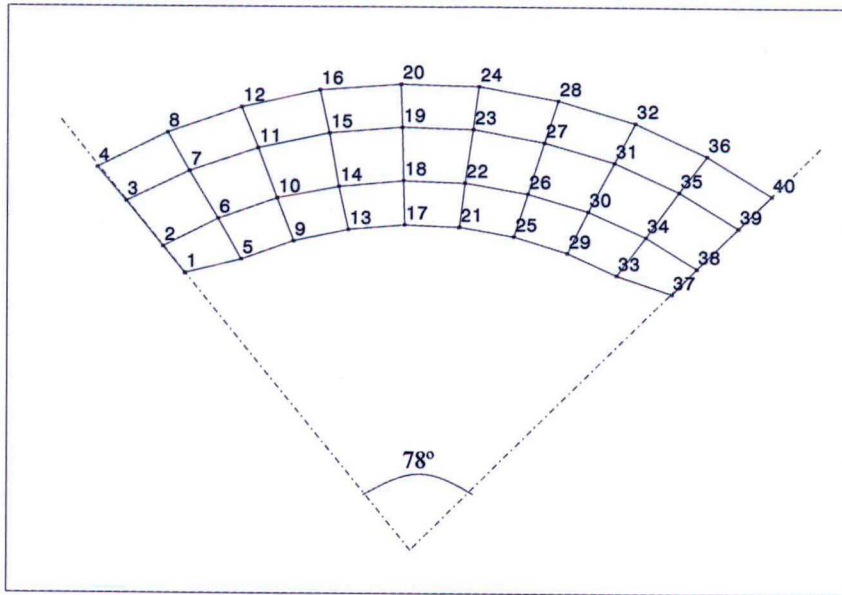


Figure 4.18 – Mesh of the pad

Table 4.2 – Modal parameters for the pad

Mode	Frequency (Hz)	Damping (%)	Loss Factor	
1	1245	0.464%	0.0093	1 <sup>st</sup> bending
2	2597	0.671%	0.0134	1 <sup>st</sup> twisting
3	3991	0.654%	0.0131	2 <sup>nd</sup> bending
4	5317	0.413%	0.0082	2 <sup>nd</sup> twisting
5	6558	0.775%	0.0155	3 <sup>rd</sup> bending
6	6950	0.334%	0.0067	----
7	8812	0.385%	0.0077	3 <sup>rd</sup> bending+1 <sup>st</sup> transversal bending
8	9961	0.810%	0.0162	4 <sup>th</sup> bending
9	10278	0.525%	0.0105	4 <sup>th</sup> bending+1 <sup>st</sup> transversal bending



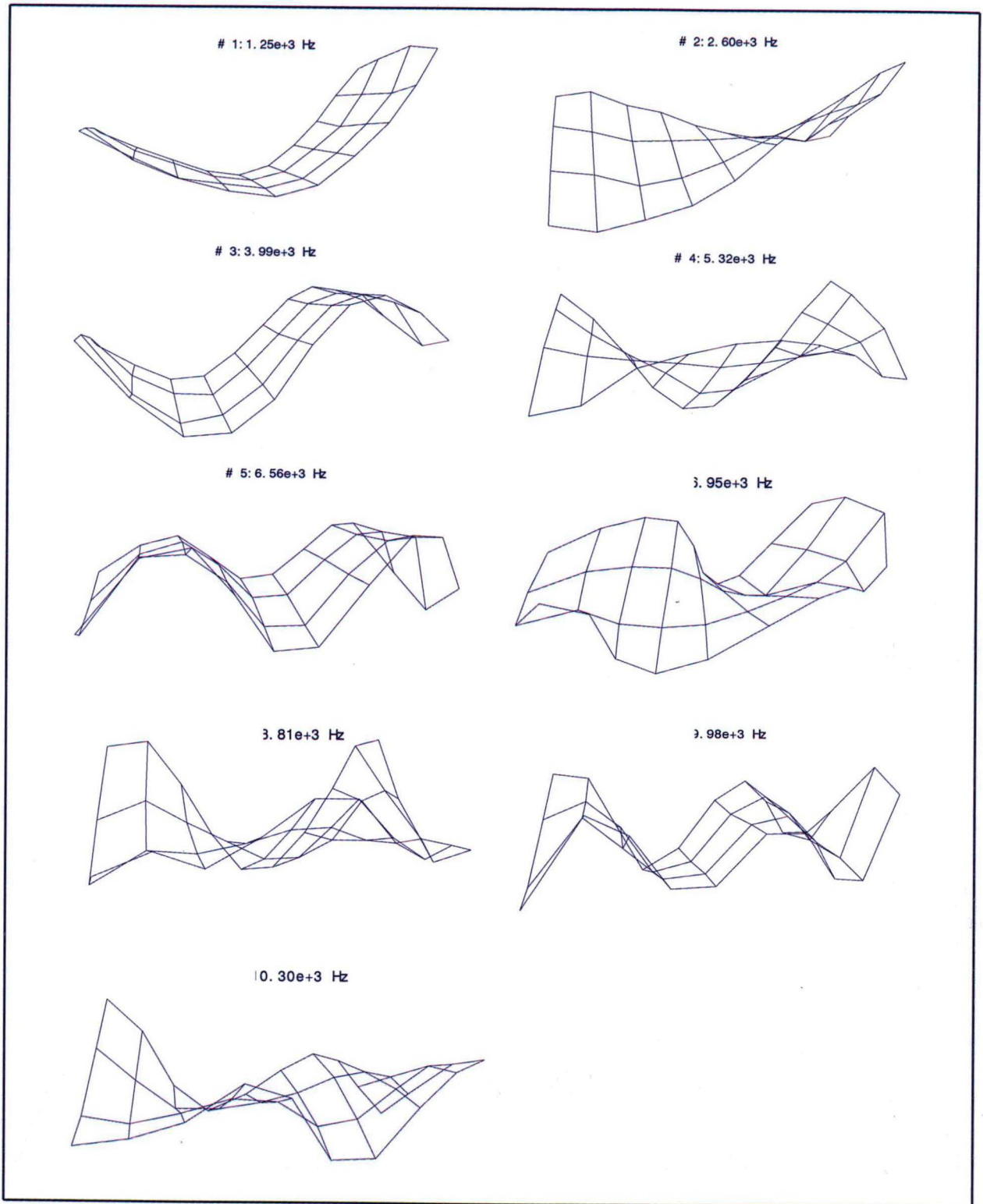


Figure 4.19 – Modes of vibration of the pad

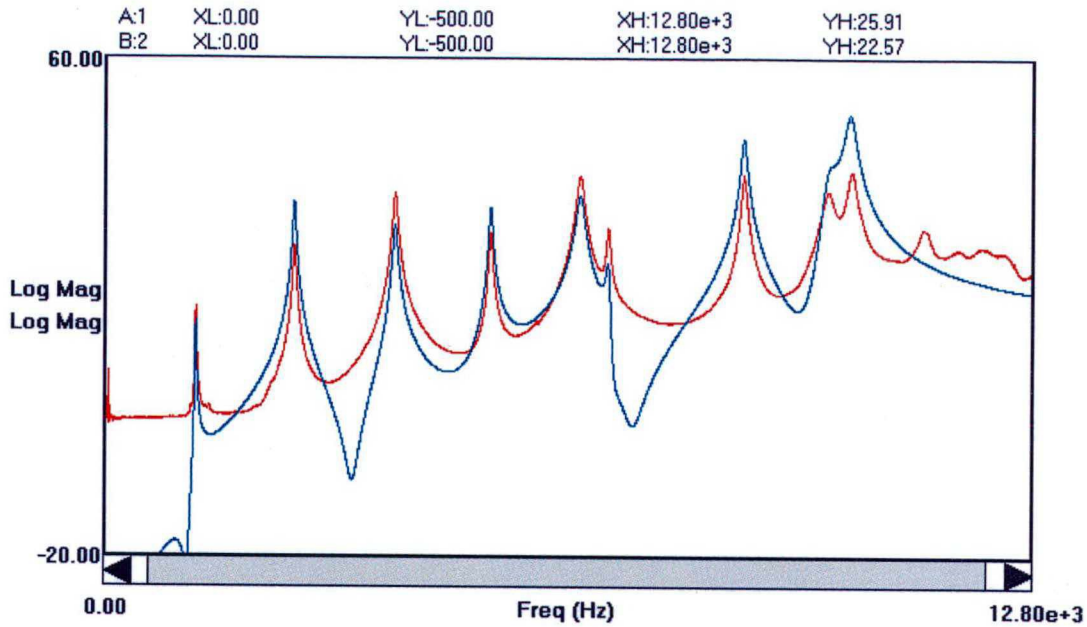


Figure 4.20 – Synthesized curve (blue) and sum of the 40 FRFs (red)

The modes of the pad are very similar to bending and twisting modes of beams. If the pad is rather long compared to its width, lower modes are dominated by bending along the longer edge. If pad's length is in the same order of magnitude as its width, then twisting modes are more prevalent at lower frequencies followed by bending modes at higher frequencies. It is also possible to have a combination of bending or twisting in one direction with bending or twisting modes in the adjacent edge.

#### 4.5.2 Rotor Modal Analysis

A mesh with 384 points was generated for the rotor model. During the measurements, the rotor was fixed to the knuckle in order to obtain a boundary condition as closer as possible to practice. As a matter of fact, modal analysis with this boundary condition proved to generate clearer mode shapes compared with measurements made with the rotor in a free-free boundary condition.

With regards to the rotor modes, one is usually interested mostly in the bending modes. The rotor mesh also considered the radial modes. This step was taken due to the fact that literature mentions also the possibility of modal coupling between radial and bending modes of the rotor [39]. Hence, the investigation about the presence of radial modes in the squeal frequency range was also performed.

Furthermore, the area containing the bolts was also meshed in order to investigate possible bending modes on that surface. Nevertheless, modal analysis showed that this part of rotor was too rigid and there was no need for this to be considered in the analysis of potential coupling modes. Figure 4.21 shows the picture of the rotor during modal analysis and the mesh generated.

A total of 1152 FRFs were measured with three accelerometers, located in points such that the bending and radial modes of the rotor could be achieved. Accelerometers were positioned in the following points: 1) point 1 (radial direction); 2) point 60 (z-direction), located at the rotor's lap area; 3) point 240 (z-direction), located at the surface containing the fixture bolts.

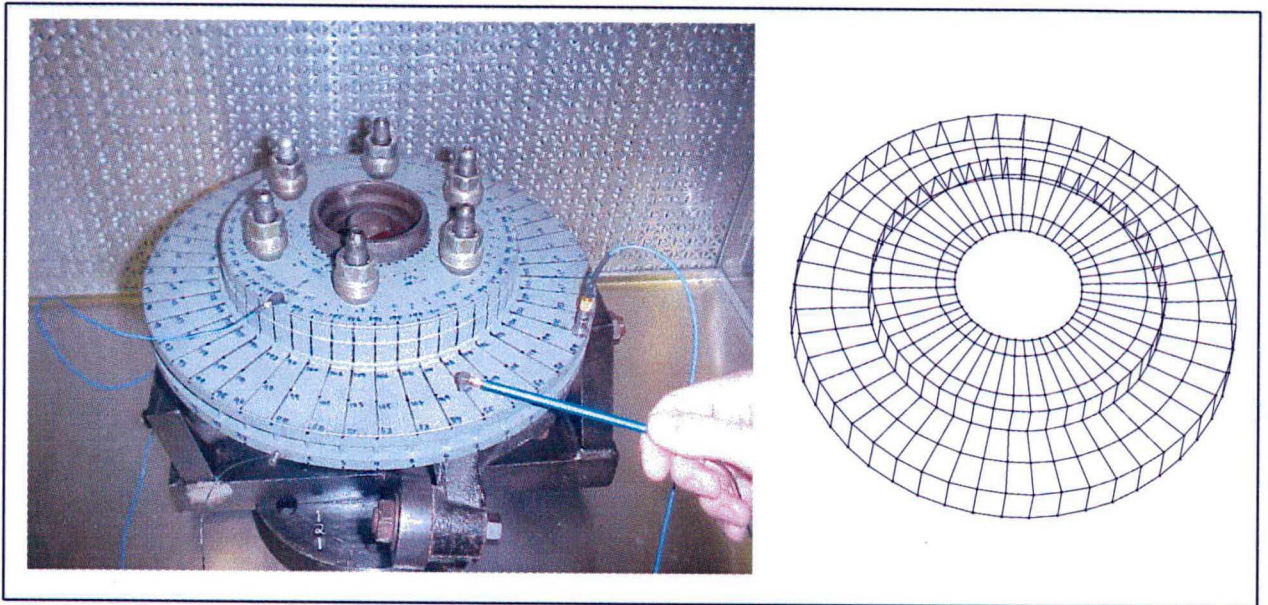


Figure 4.21 – Modal analysis of rotor and its mesh

An advanced curve fitting procedure was used for modal parameters estimation. In this case, all the measured FRFs (or a group of FRFs selected) are taken into account in the estimation of the modal parameters, unlike the former method used for the pad, where the modal parameters were selected from one chosen FRF. Thus, all the measurements with reference in the points 60z and 1r were considered in the estimation of the modal parameters. Measurements with reference in point 240z were used to estimate parameters of modes involving the deformation of the surface where the bolts were located.

The estimation of the mode shapes had to be made with reference to just one point. In this case, computing a modal participation factor was useful to evaluate which reference point would better fit the mode shapes. In the rotor case, reference 60z was chosen for the bending modes and reference 1r was used for some radial and twisting modes. Modal participation factor allows one to evaluate which reference point provides the best fitting in order to obtain the mode shapes.

Figure 4.22 shows the frequency response function measured at point 60z, with the excitation applied at the same point. Note that there is always an anti-resonance after each resonance; this is a typical characteristic of point frequency responses.

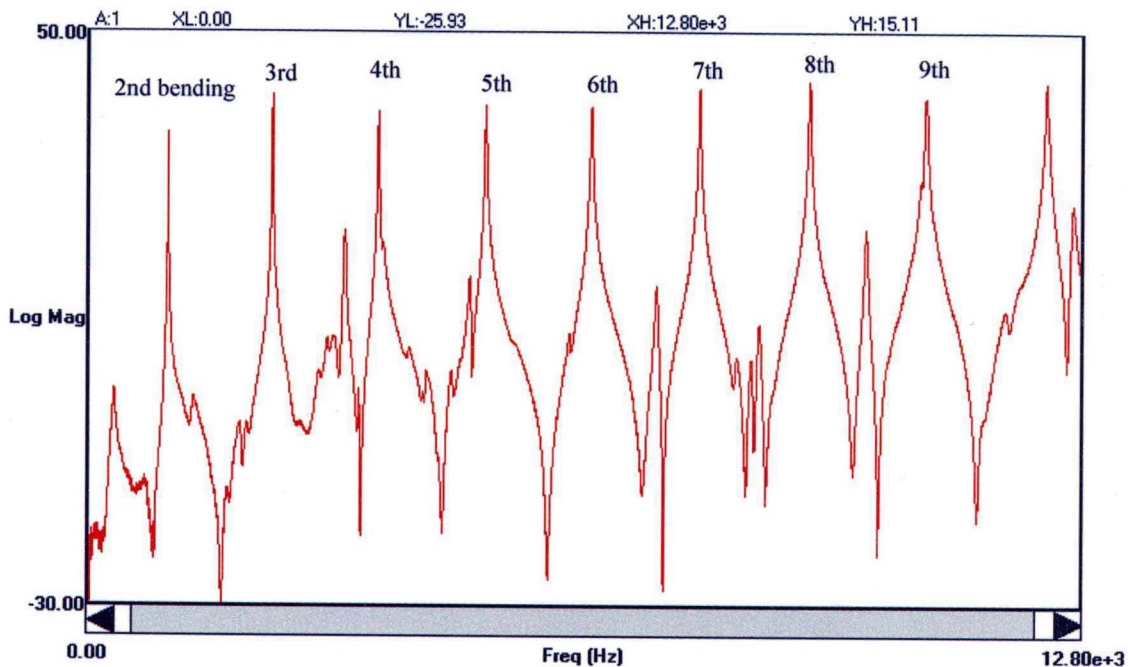


Figure 4.22 – FRF for point 60z/60z (point frequency response function)

Table 4.3 shows the estimated parameters for the bending modes of the rotor. Some of these mode shapes are illustrated in Figure 4.23.

Table 4.3 – Modal parameters for the bending modes of the rotor

Mode	Frequency (Hz)	Damping (%)	Loss Factor	
1	1011	0.132%	0.0026	2 <sup>nd</sup> bending mode
2	2355	0.077%	0.0015	3 <sup>rd</sup> bending mode
3	3725	0.123%	0.0024	4 <sup>th</sup> bending mode
4	5120	0.133%	0.0026	5 <sup>th</sup> bending mode
5	6480	0.138%	0.0027	6 <sup>th</sup> bending mode
6	7870	0.105%	0.0021	7 <sup>th</sup> bending mode
7	9293	0.106%	0.0021	8 <sup>th</sup> bending mode
8	10788	0.085%	0.0017	9 <sup>th</sup> bending mode
9	12340	0.109%	0.0021	10 <sup>th</sup> bending mode

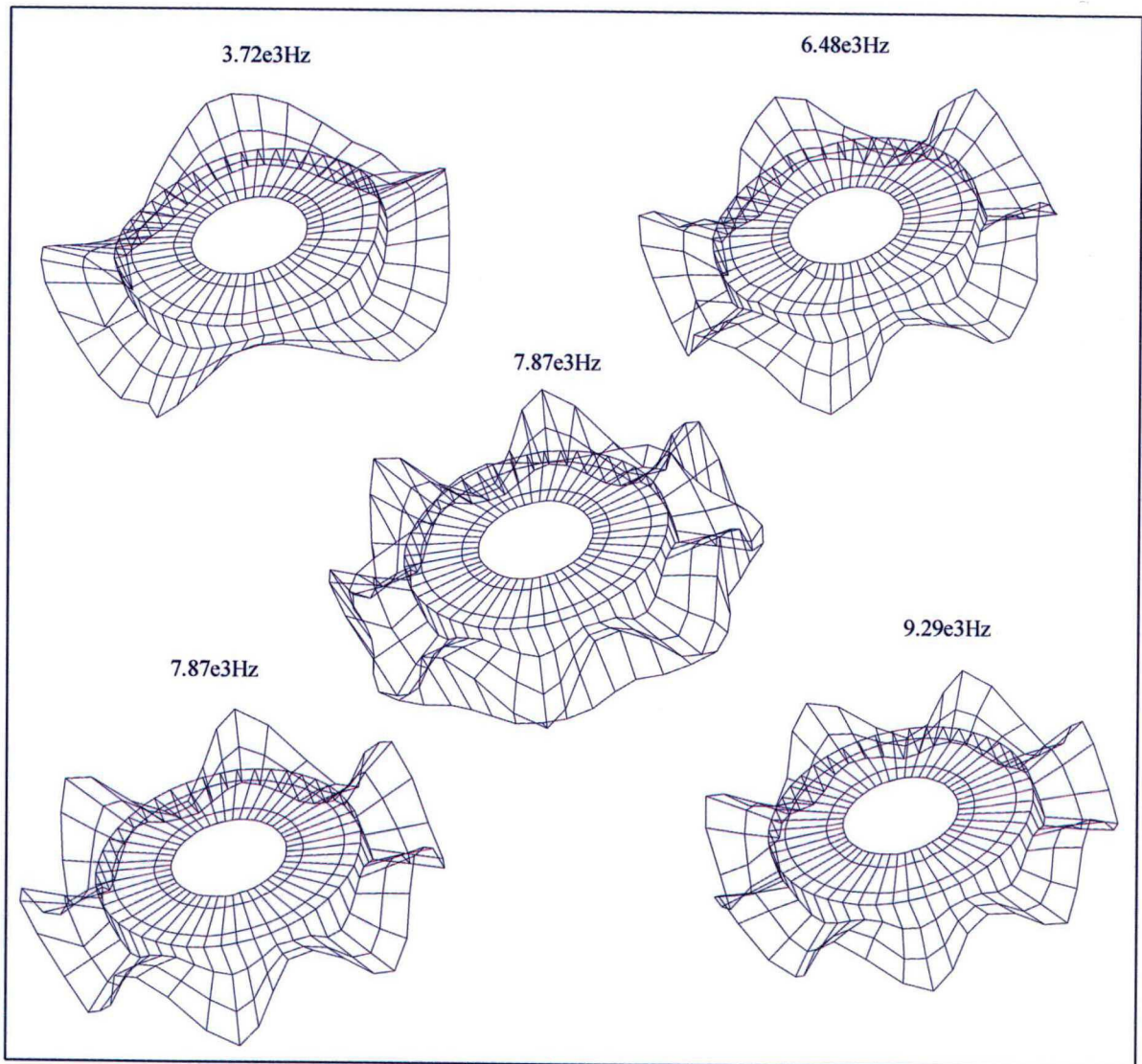


Figure 4.23 – Examples of bending modes of the rotor

Between the resonances of the bending modes, the rotor had also radial and twisting modes, which peaks can be seen in Figure 4.22. Figure 4.24 shows the estimated modes other than the bending modes, in the frequency range from 6500 to 9000Hz. Figure 4.25 is the stability diagram of the modes from 6300 to 8340Hz.

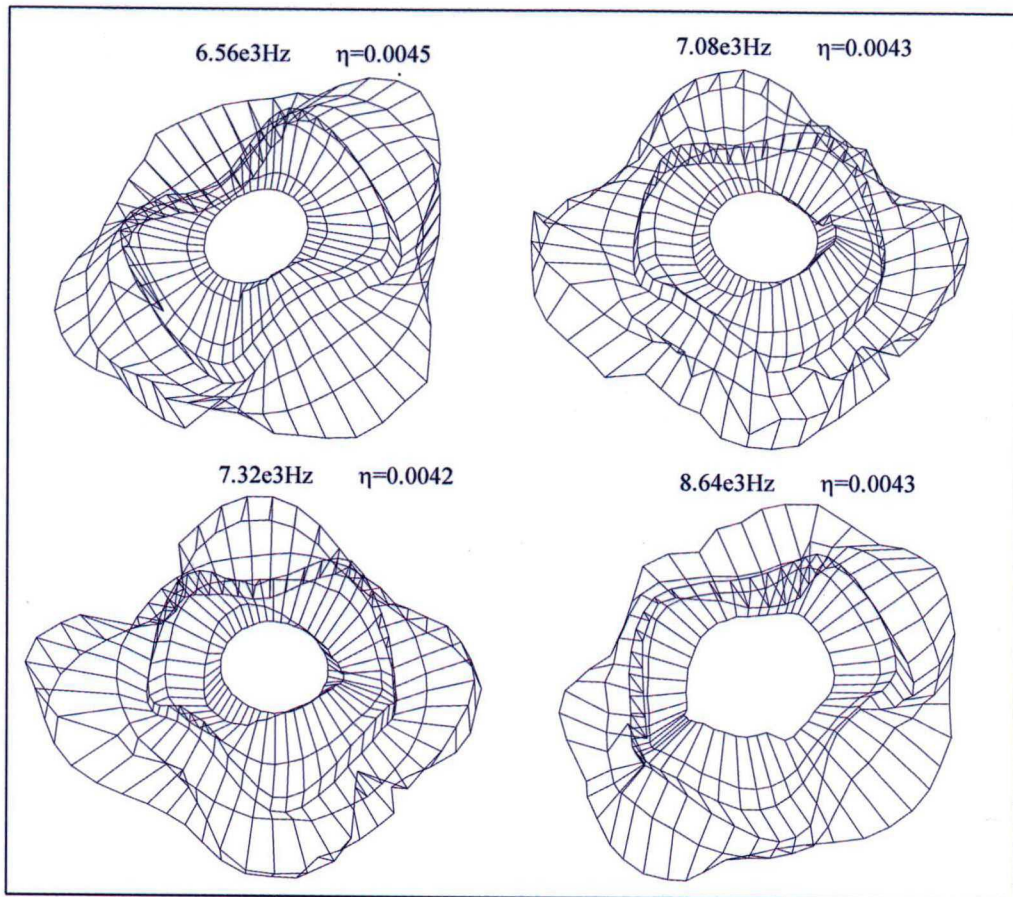


Figure 4.24 – Radial and twisting modes of rotor in the frequency range from 6500 to 9000Hz

Stability diagrams are one of the tools used to select the right number of eigenvalues (and the right eigenvalues) in a frequency range or, in a mathematical point of view, the correct model order (highest power in the polynomial equation). The key of the process is the fact that not all resulting eigenvalues have physical meaning. Some of them are due to noise or mathematical effects.

As the model order is increased, more modal frequencies are estimated, but the estimation of the physical modal parameters tends to stabilize as the correct model order is found. For modes that are poorly excited in the FRFs, the modal parameters may stabilize only at higher model orders. Nonphysical modes will not stabilize at all during the

process and can be sorted out. A deeper discussion about model order determination can be found in references [43] and [50].

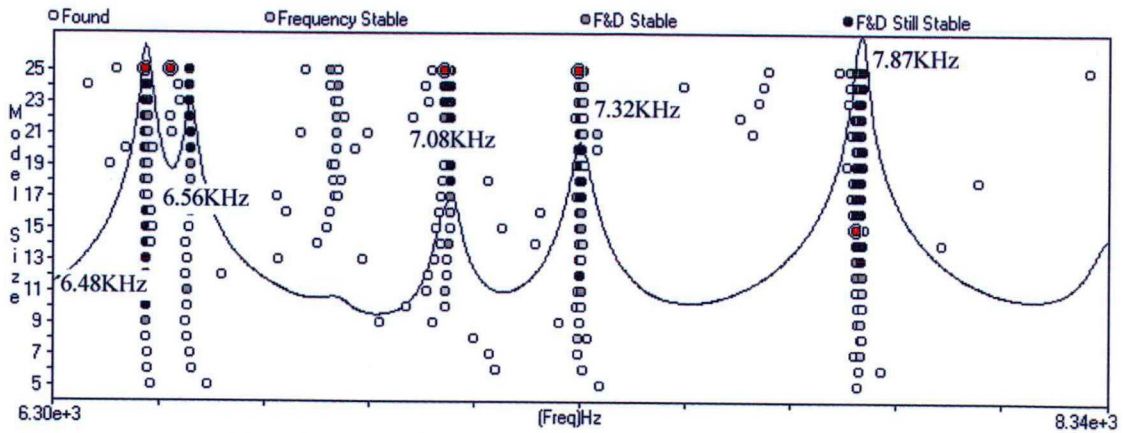


Figure 4.25 – Stability diagram from 6300 to 8340 Hz (1024 lines)

Examining the results of the modal analysis for the pad and rotor, some observations can be made:

- 1) The rotor surface containing the bolts behaves rigidly in the bending modes.
- 2) The number of vibration modes in the pad is less than in the rotor, over the same frequency range.
- 3) The damping values associated with the modes of vibration of the pad are higher than those of the rotor. This is because the friction material (which is a significant part of the pad) has considerably more damping than the cast steel used in the rotor. This reinforces the aforementioned tendency of rotor modes to be the major determinant of the squeal frequency.
- 4) As can be seen in the stability diagram in Figure 4.25, no twisting or radial mode was estimated around the squeal noise frequency range.

As stated before, squeal noise usually occurs whenever a number of the brake components, such as pad and rotor, vibrate together to create a system mode. In the case of rotor and pad bending modes, when their modes have the same wavelength and frequencies, they will be geometrically matched and will vibrate in phase. The consequence is that the system damping (Coulumb damping) decreases and noise may be radiated.

The analysis of potential coupling modes was made based on geometric parameters of pad and rotor, as shown in Figure 4.26. The wavelength of the modes of the pad, in a free-free boundary condition, was compared with modes of the rotor and the potential coupling modes were determined.

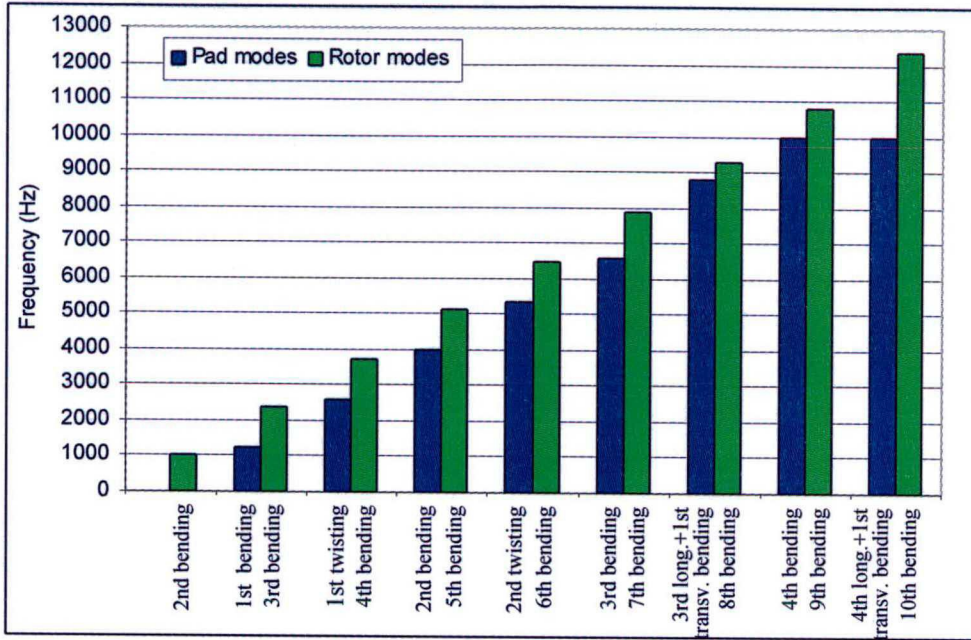


Figure 4.26 – Resonant modes for rotor and pad

The 7<sup>th</sup> bending mode of the rotor was found to be the responsible for the squeal noise around 8100Hz. Although the estimate resonance was around 7870Hz, lining pressure increases this frequency, as will be seen later. This mode can geometrically match with the 3<sup>rd</sup> bending mode of the pad, as formerly shown in Figure 4.13.

The pad covers an angular area of the rotor of approximately 78 degrees. Considering that the 3<sup>rd</sup> bending mode of the pad contains 3 semi-wavelength along 78 degrees, it potentially couples with the 7<sup>th</sup> bending mode of the rotor. The 7<sup>th</sup> bending mode of the rotor contains 14 semi-wavelength along 360 degrees. Thus, each wavelength occupies an angular surface of 25.7 degrees, compared with 26 degrees from the pad mode.

Fieldhouse [4] recommends that 80 to 100% of the total angular surface of the pad must be used when analyzing potential coupling modes of rotor and pad.

At first sight, rotor and pad resonances are distant to each other. However, during braking, the frequency of the 3<sup>rd</sup> bending mode of the pad can increase dramatically with increasing pressure until it matches with the frequency of the rotor to create the system resonance.



For instance, Figure 4.27 is the frequency response of a pad model, different than the one analyzed in this thesis, for two boundary conditions: simply rested on a table and under pressure, manually applied by a C-clamp. Note the increment in frequency of the 2<sup>nd</sup> bending mode. Under operation conditions, brake system is subjected to higher pressures and resonances reach even higher values.

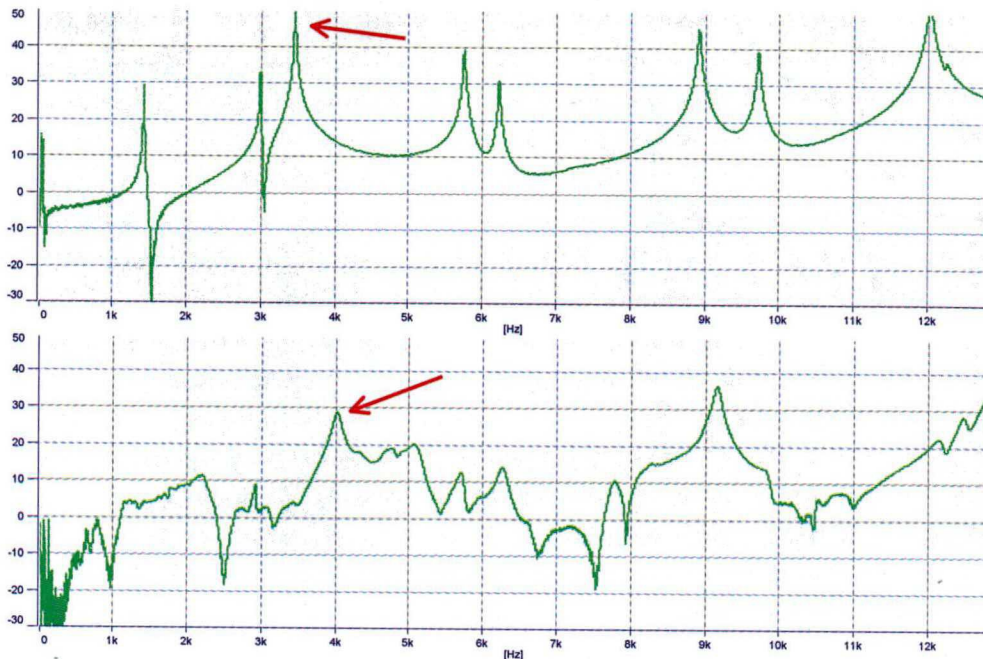


Figure 4.27 – FRF of a pad simply rested on a table and under pressure

In order to verify the former conclusions, modal analysis of the caliper was performed to establish if there was any influence of the caliper dynamics in the squeal noise generation.

### 4.5.3 Caliper Modal Analysis

Table 4.4 presents the resonances resulted from the modal analysis of the caliper. The frequency range in sight was divided in three blocks and stability diagrams were obtained for each block, in order to estimate the modal parameters.

Table 4.4 – Estimated resonances and loss factor of caliper modes

Mode	Frequency (Hz)	Damping (%)	Loss Factor
1	1954	0.602%	0.0120
2	5145	1.24%	0.0248
3	5890	1.46%	0.0292
4	6720	1.48%	0.0296
5	7044	0.811%	0.0162
6	9175	0.098%	0.0020
7	9940	0.577%	0.0115
8	10255	1.16%	0.0232
9	11030	1.36%	0.0272
10	11637	0.451%	0.0090

The caliper does not have modes of vibration at the squeal frequency range. Furthermore, the estimated loss factors for the caliper modes are higher than the loss factors of rotor and pad modes, reducing the potential of a caliper mode to be the major cause of the noise radiation.

This is an important information, since it permits the analysis of the system response to be focused on the coupling between the rotor 7<sup>th</sup> bending mode and the pad 3<sup>rd</sup> bending mode. Figure 4.28 shows some of the related mode shapes of the caliper, as well as a frequency response measured.

Once the response of the components was understood, frequency response functions of the assembled brake were performed, pinpointing the dynamic properties of the system resonance, around the frequency of the rotor 7<sup>th</sup> bending mode. Frequency and specially damping of this mode were measured as function of lining pressure and temperature. This approach allowed the analysis of the performance of the shim configuration at different boundary conditions of the break system.

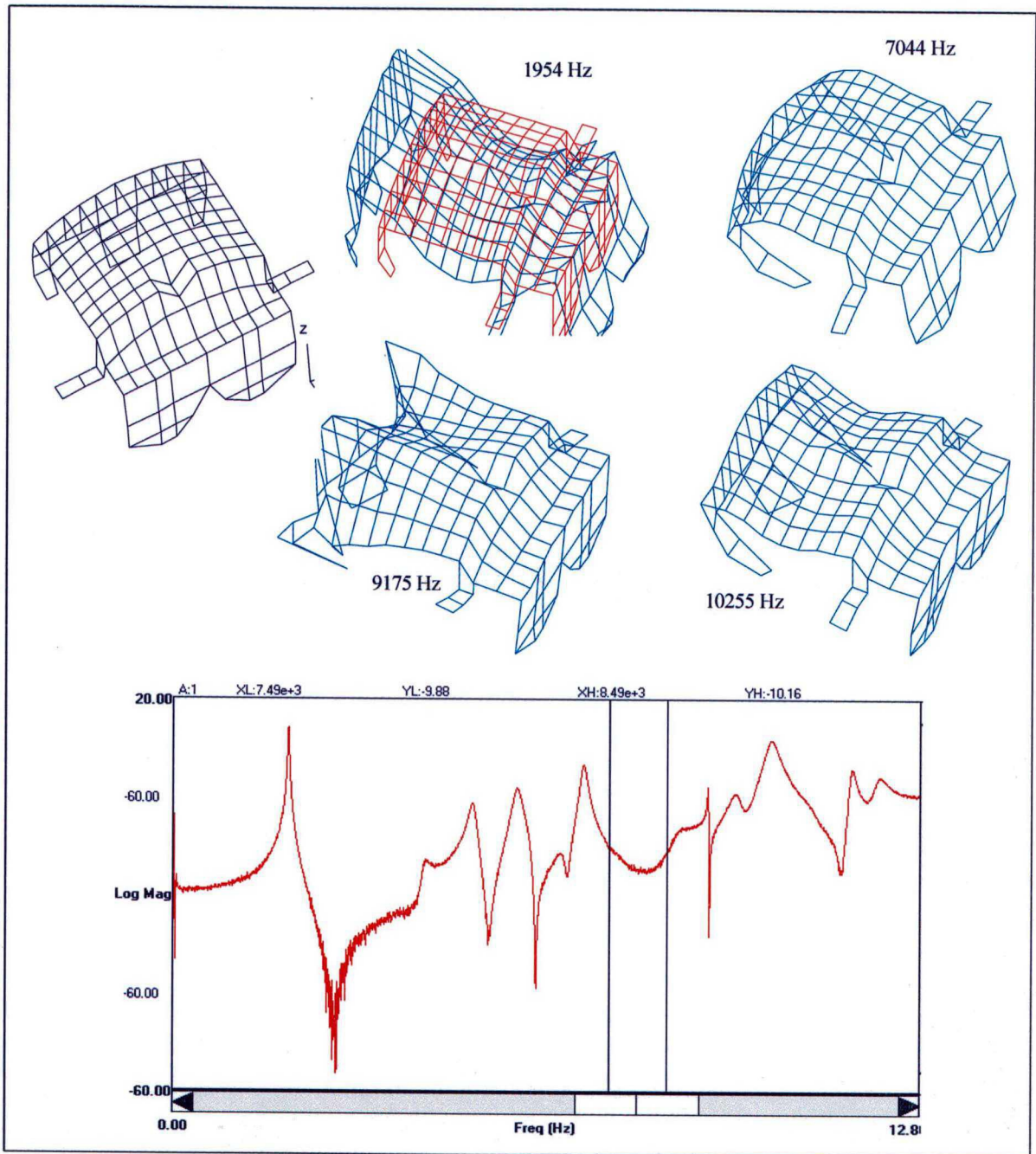


Figure 4.28 – Mode shapes of the caliper and FRF example

## 4.6 ANALYSIS OF ASSEMBLY BRAKE SYSTEM

The frequency response analysis of the knuckle assembly was performed, at first, for a determined range of pressures. This technique allowed the point where the system became unstable to be identified and, most importantly, to quantify the damping of the system at the critical mode for each shim configuration. This testing provided the level of damping in the system and the interaction to the noise problem.

The technique consisted of measuring the system frequency response at points of rotor and pads, exciting the rotor by an impact hammer. With this procedure, the system mode of vibration was tracked and the mode coupling situation broken down. Figure 4.29 presents a sketch and a picture of the setup used for these tests.

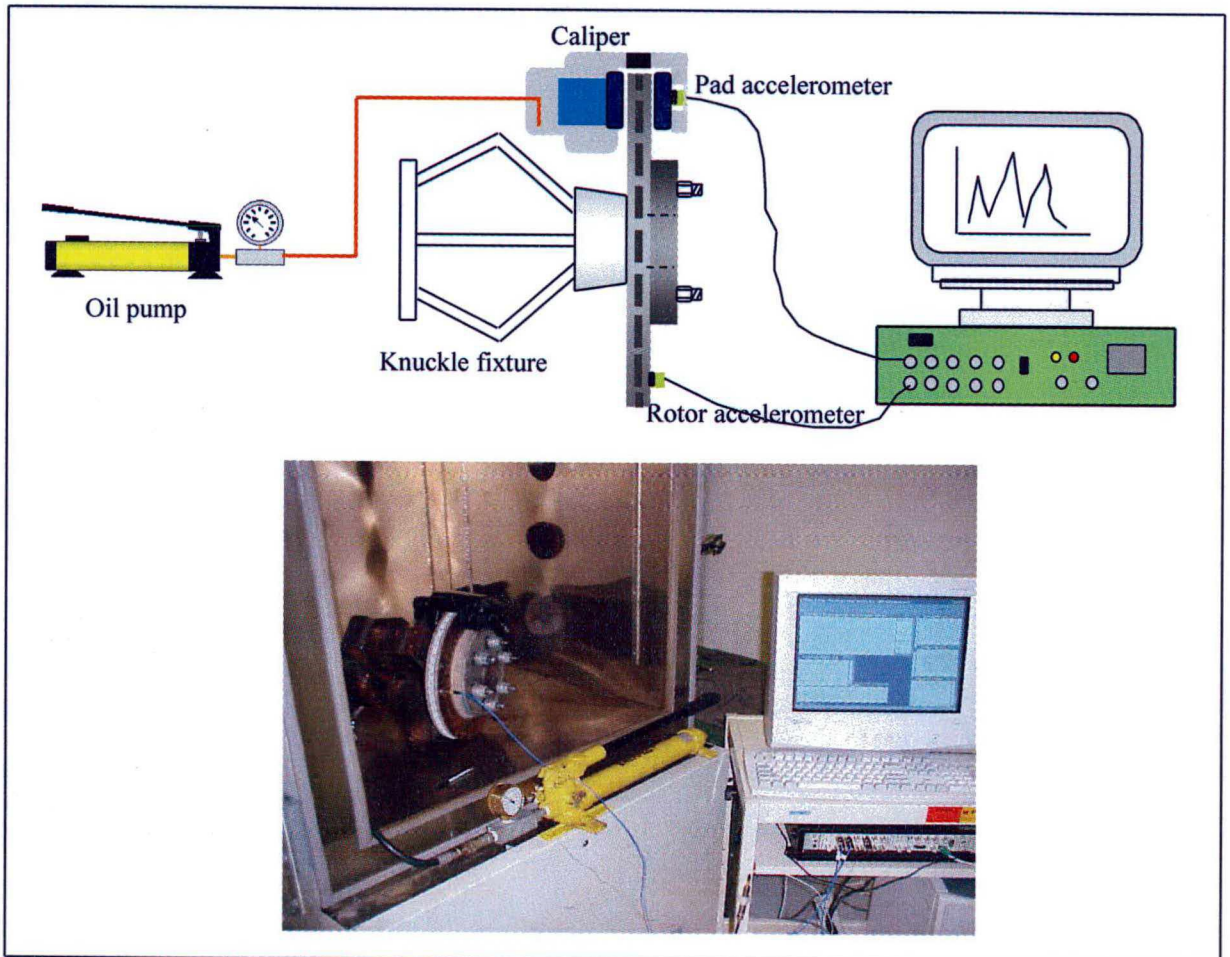


Figure 4.29 – Sketch and picture of test setup for measurement of system FRF as function of pressure

In this experimental method, the rotor remained static. In this case, the friction mechanism was not taken into account. Thus, the input energy introduced by the friction between rotor and pad was substituted by the excitation from the impact hammer and patch actuators (patch actuators were used in other experiments discussed in Chapter 5). Furthermore, this input energy was kept constant, regardless of the changes in the system's dynamic properties as function of lining pressure and temperature. In practice, the excitation energy varies as a function of braking pressure and temperature, and this may play an important role in the squeal noise level.

However, the advantage of this technique is that it allows the analysis exclusively of the mode coupling phenomena and the measurement of the system damping.

In this way, once determined the main modes responsible for the squeal noise had been determined, the system loss factor could be evaluated for different shim configurations. Quantifying the system loss factor makes it possible to predict the potential of squeal occurrence and which shim fits better for a specific problem. As shown in the 2DOF model, the higher the system damping is, the less is the chance of squeal noise generation.

At first, frequency responses were measured, at room temperature, for different lining pressures, in steps of about  $1.7 \times 10^5 \text{ N/m}^2$  (25 Psi). The measurements were taken with a Bruel & Kjaer Pulse Analyzer, using a zoom option with a center frequency of 8200Hz and frequency span of 3200Hz, in a spectrum of 3200 lines.

The point frequency responses (response measured at the same position as the hammer impact) for the rotor were taken at the same location for all the measurements, with different shim configurations. Color marks were drawn on the rotor such that it remained at the same angular position when the pads with different shims were changed.

Figure 4.30 is a waterfall plot of the frequency responses measured for the baseline, i.e., no shims attached to the pads. Responses of the accelerometers located at the rotor and pad are shown. The two smaller graphs are zooms of the waterfall plots, in a frequency range including the squeal noise mode.

Loss factor and frequency of the critical mode, as function of the lining pressure, are shown in Figure 4. 31.

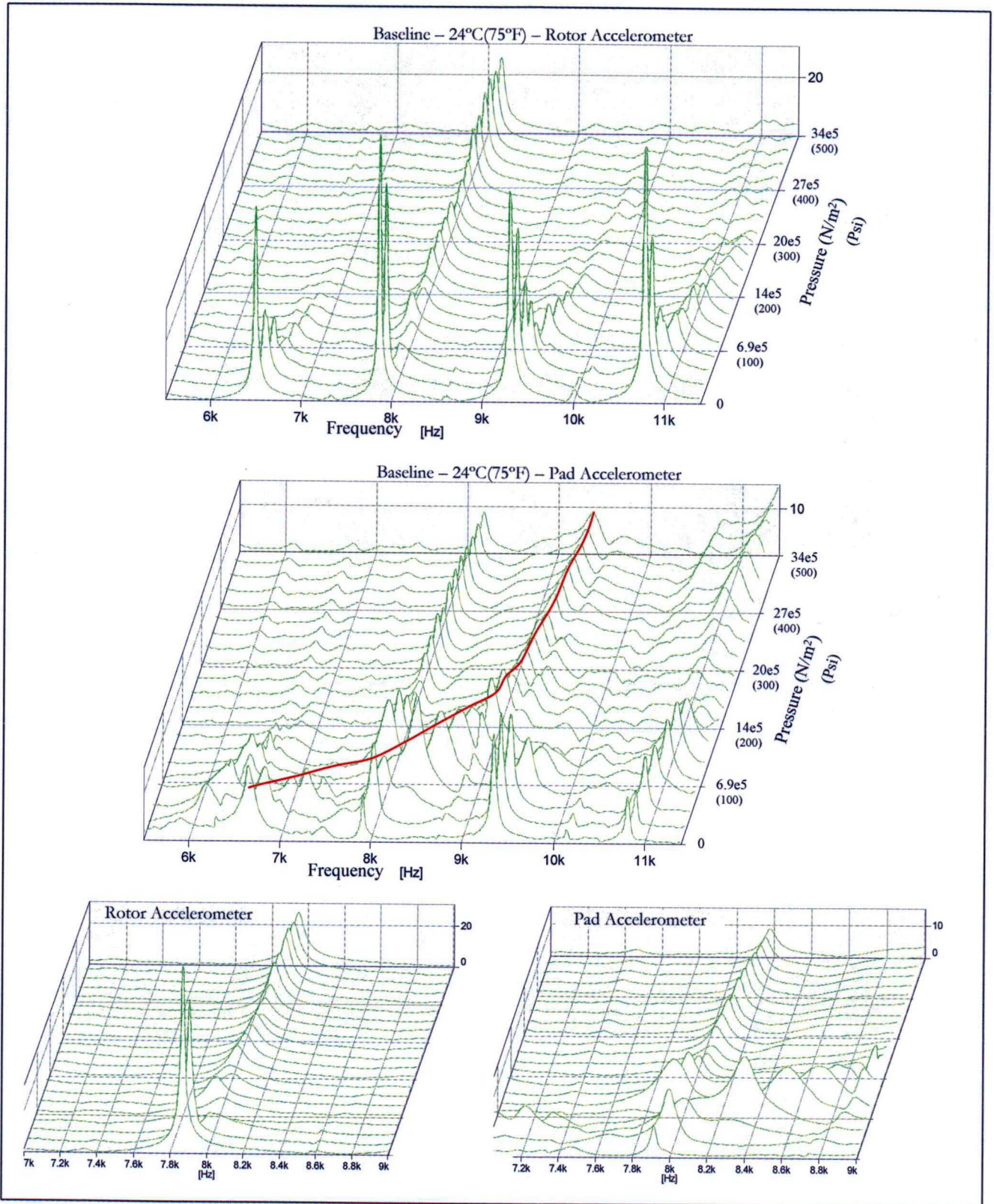


Figure 4.30 – FRFs for Baseline: Accelerometers located at rotor and pad

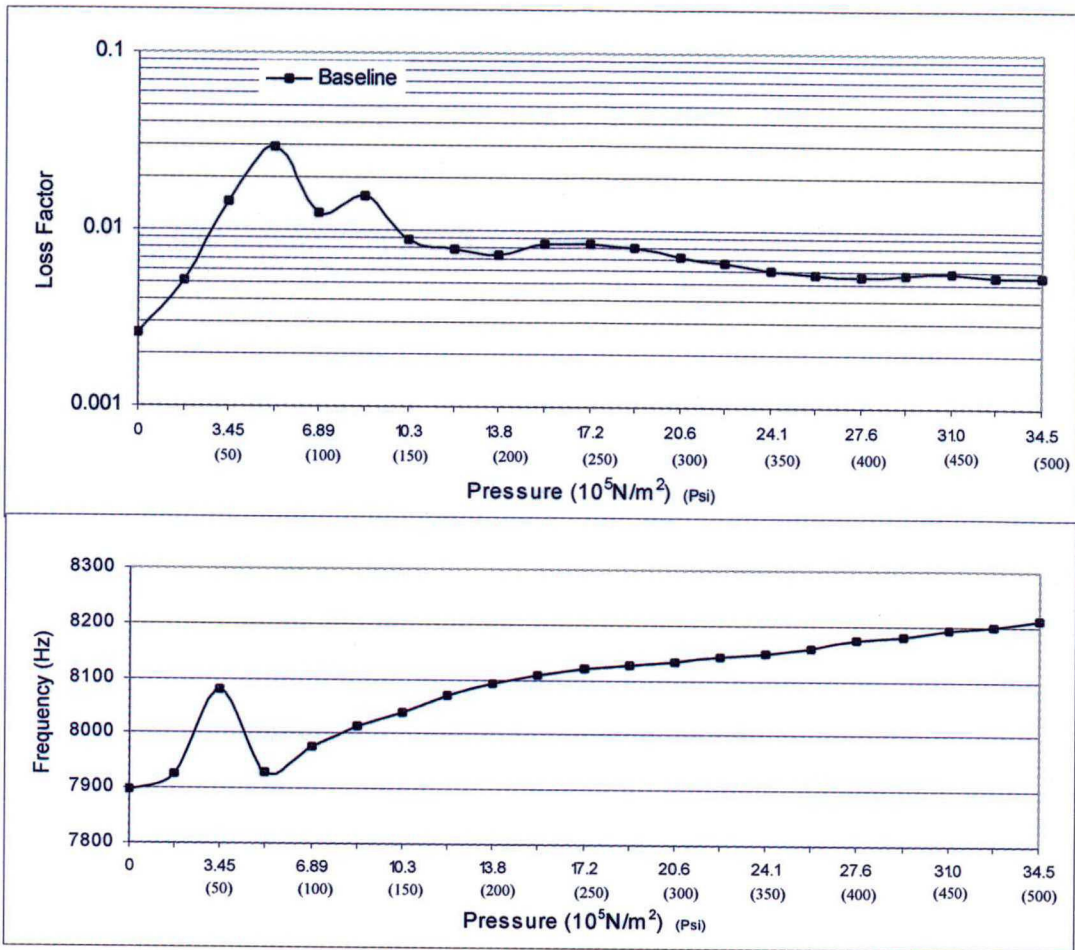


Figure 4.31 – System loss factor and resonance vs. lining pressure for Baseline

Analysis of Figures 4.30 and 4.31 allows obtaining important information about the system dynamics.

At very low pressure, close to zero  $\text{N/m}^2$ , rotor and pads are barely touching and the measured damping of the system mode is similar to that of the 7<sup>th</sup> bending mode of the rotor, measured in a free-free boundary condition (see Table 4.3), which is around  $\eta = 0.0021$ . As the pressure starts to increase and the rotor comes in contact with the pads, the system damping also starts to increase. This is because, at very low pressure, the frequency of the third bending mode of the pads is around 6600Hz, much lower than the 7<sup>th</sup> bending mode of the rotor, around 7900Hz. Under this condition, when measuring the response of the system, the pads are vibrating as rigid body modes, while the rotor is deforming in its bending mode, which causes the increase in the joint damping between the pads and the rotor. However as the pressure continues to increase, the frequency of

the pad increases in a higher rate than the rotor mode, until both modes couple and the components start vibrating together in the same deformation pattern. For this brake system, this condition occurred between  $6.9 \times 10^5$  and  $10.3 \times 10^5$  N/m<sup>2</sup> (100 and 150 Psi), and the damping in the system went down.

When looking to the frequency responses measured with the accelerometer at the outer pad, the system mode becomes clearer as the lining pressure increases, because pads are now vibrating in the same mode shape (wavelength) than rotor.

Note also the mode tracked by the red line in Figure 4.30. At low pressure, the resonance is located at a frequency around 6600Hz and may be likely related to the 3<sup>rd</sup> bending mode of the pad. This assumption is based on the superposition principle, i.e., the system response is a modal superposition of individual brake components modes of vibration. Around the pressure at which modal coupling occurs, this mode is superimposed by the system mode related to the 7<sup>th</sup> bending mode of the rotor. As pressure increases more, it becomes visible again. This phenomenon can be observed in most of the waterfall plots measured, as seen in further Figures in this Chapter. Here it is important to mention the research of Fieldhouse [4], whom based on results of holography interferometer measurements, suggested that different modes of the system may have the same rotor diametrical mode order. In order to verify that, modal analysis of the exposed part of the rotor lap was performed. This allowed visualizing the mode shape of such peaks. The frequency responses were measured at room temperature for a lining pressure of  $8.6 \times 10^5$  N/m<sup>2</sup> (125Psi). Figure 4.32 shows a zoomed frequency response obtained during the measurements.

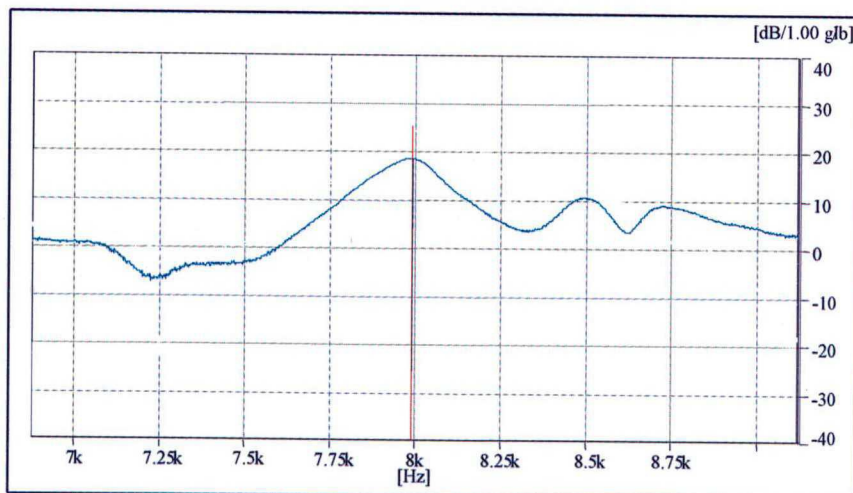


Figure 4.32 – Frequency response of brake system: Baseline at  $8.6 \times 10^5$  N/m<sup>2</sup>



Figure 4.32 and also Figure 4.30 (waterfall plot of the FRF measurements with the accelerometer on pad) indicate that the system has three resonances in the frequency range between 8000 and 8800Hz. The mode shapes of these resonances, obtained by modal analysis, are shown in Figure 4.33. The non-deformed part of the rotor lap was the portion under the pads and caliper and no measurement was taken in this region.

The resonance at 8000Hz is related to the rotor lap 7<sup>th</sup> bending mode. This result was expected. The mode at 8700Hz is related to a twisting mode of the rotor lap and was also predicted by the former modal analysis of the rotor, as shown in Figure 4.24. The resonance around 8500Hz can be better described as a combination of other mode shapes, however it is apparent that this mode has an important participation of the rotor lap 7<sup>th</sup> bending mode. Besides, this mode presented a difference of phase, when compared to the 7<sup>th</sup> bending mode at 8000Hz.

These results indicate that different resonances may have similar diametrical mode shapes for the rotor lap. In this case, one of the reasons here believed for the squeal be related to just the mode at 8000Hz is the fact that, in this mode, rotor and pad vibrate in-phase, what may not happen for the other resonance, which mode shape is nearly the same as the resonance at 8000Hz.

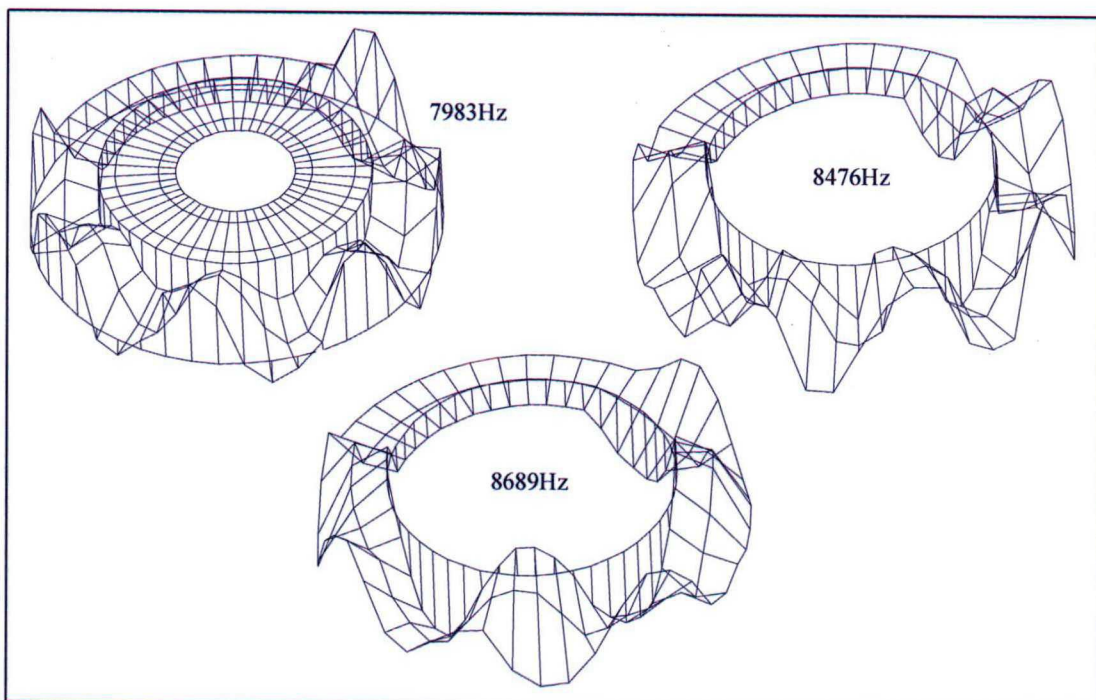


Figure 4.33 – Mode shapes of the rotor lap under pressure ( $8.6e5\text{N/m}^2$ )

At the pressure range that rotor and pad start vibrating in phase, the system mode drops in frequency. This can be explained by the fact that, when the modal coupling occurs, the system rigidity is reduced, since pads are now vibrating in phase with the rotor and the most dominant effect is the pads adding mass to the system mode.

Another phenomenon affecting the brake noise mechanism is related to the fact that the rotor is moving in space while the pads are stationary. Under typical braking conditions, the friction forces between pads and rotor have enough energy to excite all modes of the pads and rotor in the audible frequency range. However, when the squeal noise occurs, the system mode becomes stationary in space, because the nodelines of the rotor lock in together with those of the pads. Once the system mode becomes stationary in space, then it can radiate noise. This is an important assumption defined for the squeal mechanism and had been discussed in papers ([3] and [4]). In this thesis, the sound intensity technique was used in order to verify this condition and the results are presented in Chapter 5.

Under the conditions described, when pads and rotor vibrate together and the system damping is reduced, there is a need to increase the damping into the brake system in order to avoid the squeal noise generation.

It is interesting to compare the results obtained for the Baseline with those measured for the different shim configurations used in this research. Figure 4.34 is the graph of the loss factor and frequency for the critical mode of the brake system, when Shim number 6 (configuration 6, as described in Chapter 1) is bonded to the pads. This is a commercial shim which highest damping values are reached at temperatures around 25°C, as shown in Figure 4.34. This shim was used as a reference for the measurements at room temperature.

As can be seen, bonding the Shim 6 to the pads improved the system damping. Figure 4.35 is the waterfall of the frequency responses measured for the brake system with the Shim 6. Comparisons can be made between the peaks of frequency in Figures 4.30 and 4.35. The sharpness of the peak of the frequency response is an indicator of damping in the system.

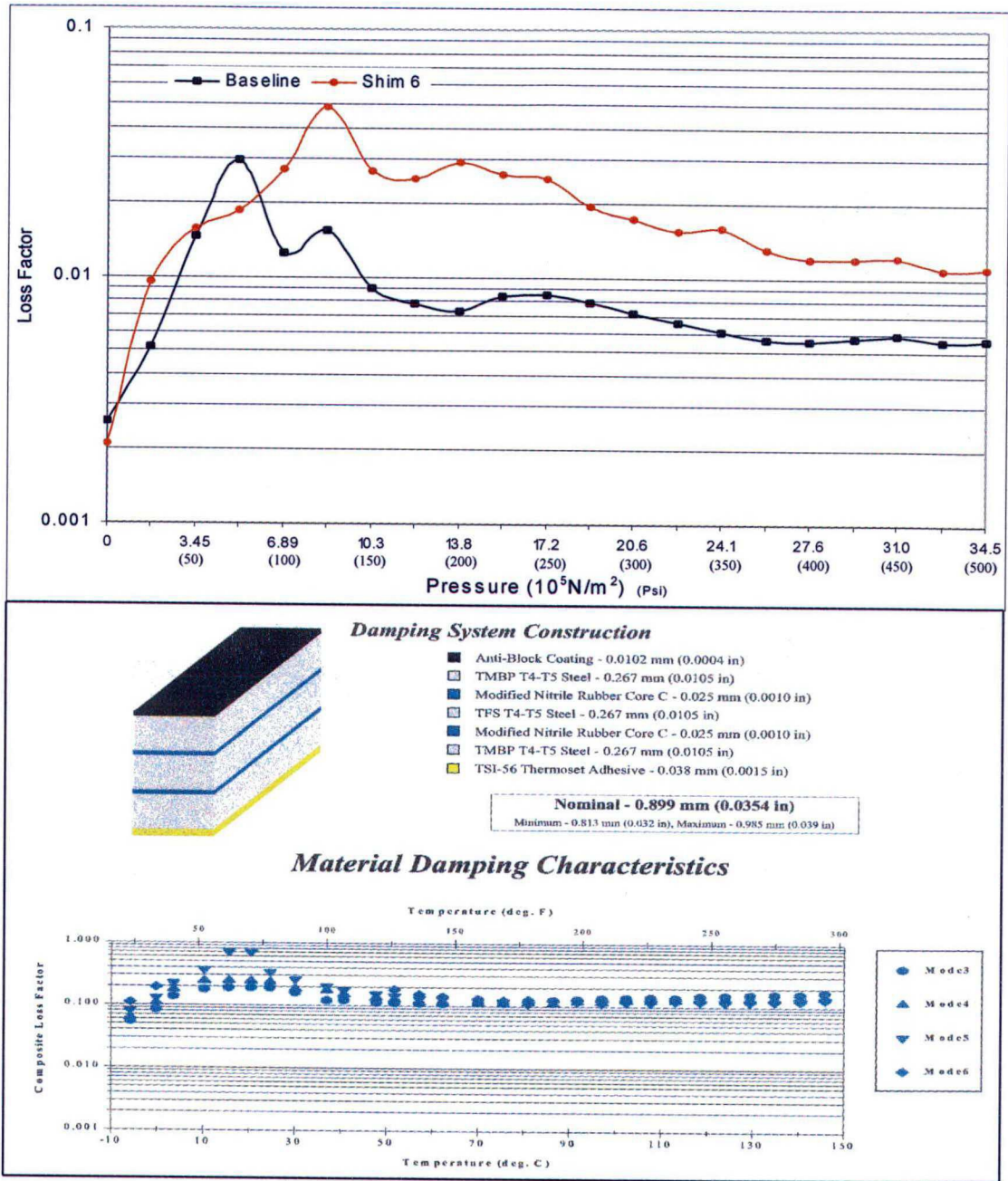


Figure 4.34 – System loss factor for Baseline and Shim 6 and description of Shim configuration 6

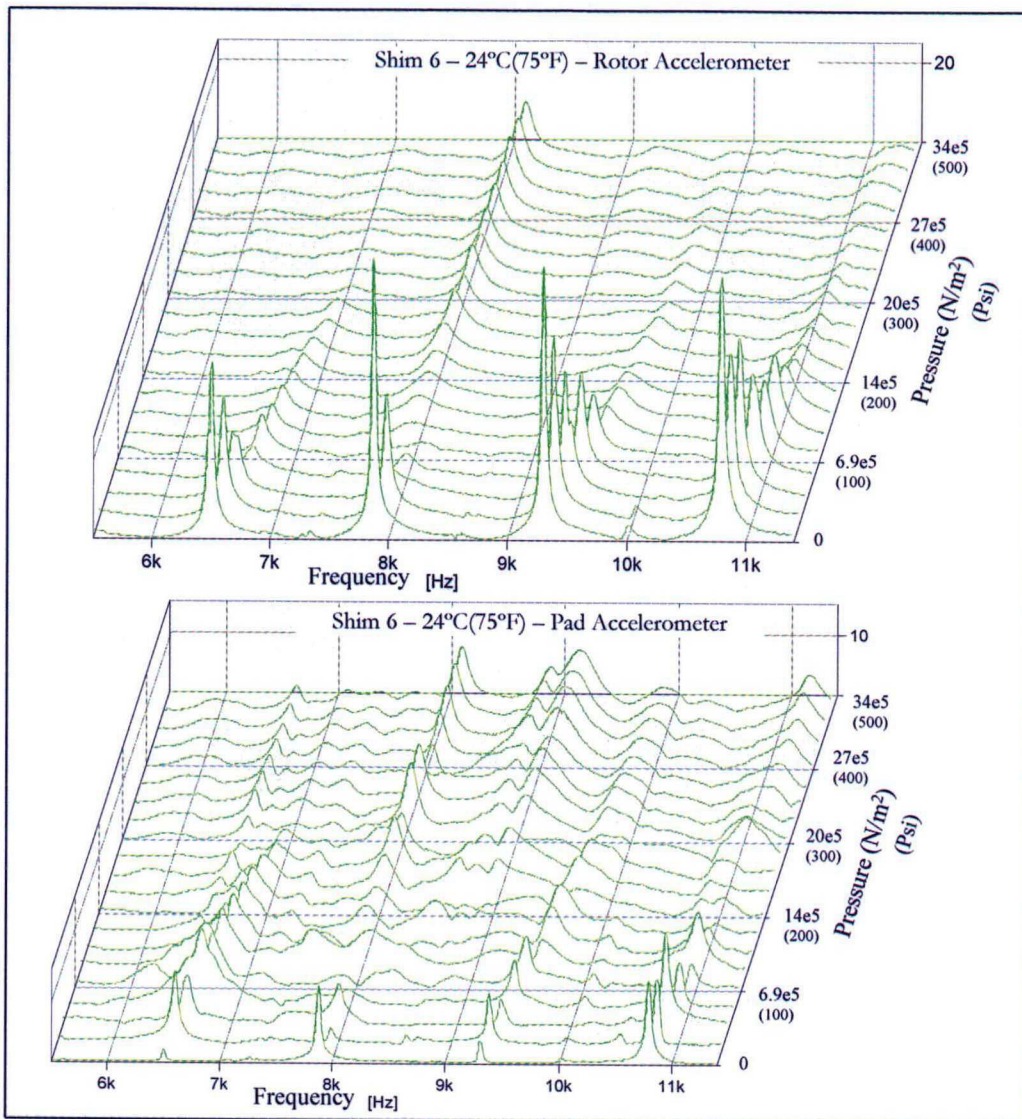


Figure 4.35 – FRFs for Shim 6: Accelerometers located at rotor and pad

Once the squeal noise phenomenon was broken down, it was possible to analyze the performance of the different shims and, specially, the shims made of rubber coats RC1 and RC2. Quantifying the damping added by the rubber coats was achieved in order to evaluate if these configurations could improve the system damping and by which mechanism.

The results formerly presented for the Baseline and Shim 6, as well as the results for the other shim configurations can be better evaluated if information about the dynamic properties of the pads with the different shims, as a function of temperature, are available.

Hence, the different shim configurations were applied to pads and measurement of resonance and loss factor for the 3<sup>rd</sup> bending mode was carried out as function of

temperature. The pads were supported by foam blades, in order to approach a free-free boundary condition. Figure 4.36 shows the loss factor measured for each shim configuration and a picture of the setup and pads inside the oven. The shim numbering is depicted in Chapter 1. Once again, size of the transducers was an important issue, since the component dynamics could be affected by any mass or damping added by the transducer and the cables.

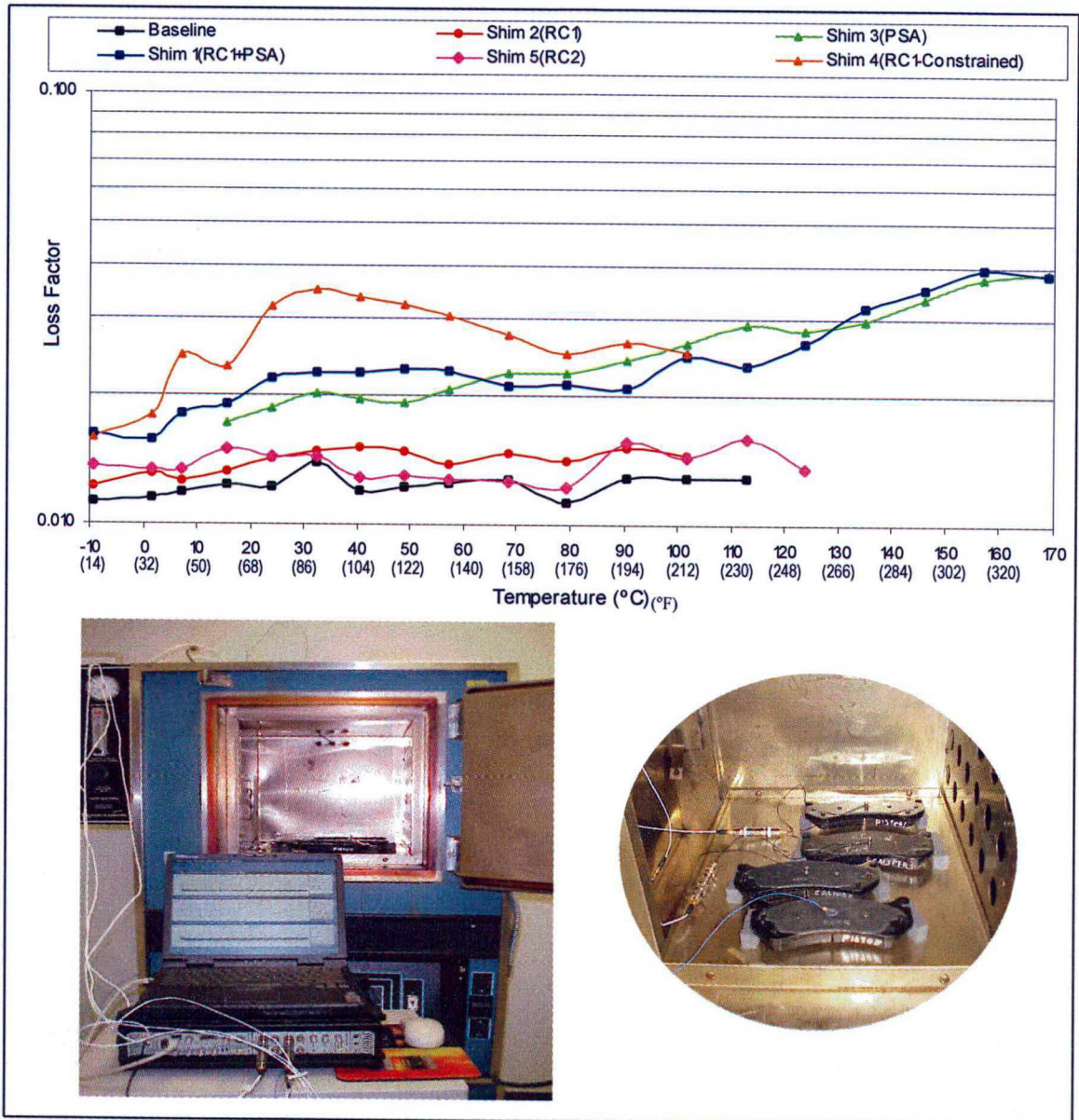


Figure 4.36 – Loss factor for the pad using different shim configurations under various temperature conditions for the 3<sup>rd</sup> bending mode

Generally, the frequency response of the pads in a free-free boundary condition is a preliminary information about the performance of the shim configuration in the brake system. As can be seen in Figure 4.36, constrained layer treatments Shim 1 (RC1+PSA), Shim 3 (PSA) and specially Shim 4 (RC1 as a constrained layer) presented higher damping, even although, in the case of the shim configurations 1 and 3, the constrained material was the PSA, whose transition temperature is above room temperature. This corroborates the well-known characteristic that viscoelastic materials can improve significantly the damping of structures when applied as constrained layers.

As expected, the Baseline presented low damping for the whole range of temperature. The loss factor may slightly increase for higher temperatures, when the transition region of the components of the friction material is reached.

Shim 2 and Shim 5 barely increased the pad loss factor. This is because, in these configurations, damping mechanism is the cyclical deformation due to flexural vibration (see extensional damping mechanism, in Chapter 3). This mechanism usually is not so effective as the shear damping introduced when the viscoelastic layer is constrained. However, it is still possible to note the little increase in the loss factor at the temperature around 35°C (95°F) for Shim2 (RC1) and 20°C (68°F) for Shim 5 (RC2). These temperatures are approximately the respective transition temperatures for each viscoelastic material, where the material loss factor reaches its maximum value.

Comparing the performance of Shim2 and Shim 4, one can note that the material RC1 works better when applied as a constrained layer. Even with the Shims 1 and 3, whose constrained viscoelastic material had a transition temperature well above room temperature, the pads have a higher loss factor when compared with the rubber coats RC1 and RC2.

However, as will be seen in the next paragraphs, the behavior of the assembly system, when the rubber coats were bonded to the pad, was different from the one that would be expected if only the results of the pads in a free-free boundary condition were considered.

With the aforementioned conclusions in mind, analysis of the dynamics of the assembled system was performed in the same way as formerly depicted for the Baseline and for Shim configuration 6. The system critical mode was tracked as function of lining pressure and resonance and loss factor were measured for pads with Shims 1 (PSA+RC1), 2 (RC1), 3 (PSA), 4 (RC1 as a constrained layer) and 5 (RC2).

Figure 4.37 presents the loss factor of the system mode, including the data measured for the aforementioned shim configurations and also for the Baseline and Shim 6, formerly discussed. For better visualization, the same data is shown in Figure 4.38, but only for some of the shim configurations.

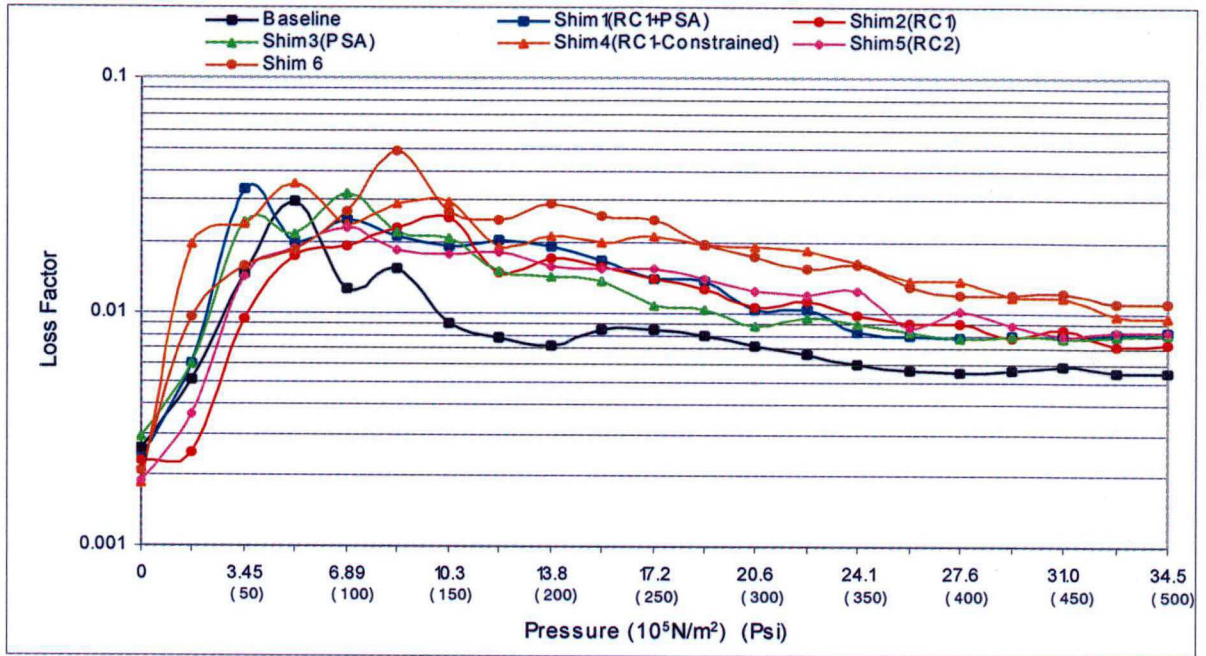


Figure 4.37 – System loss factor for the shim configurations

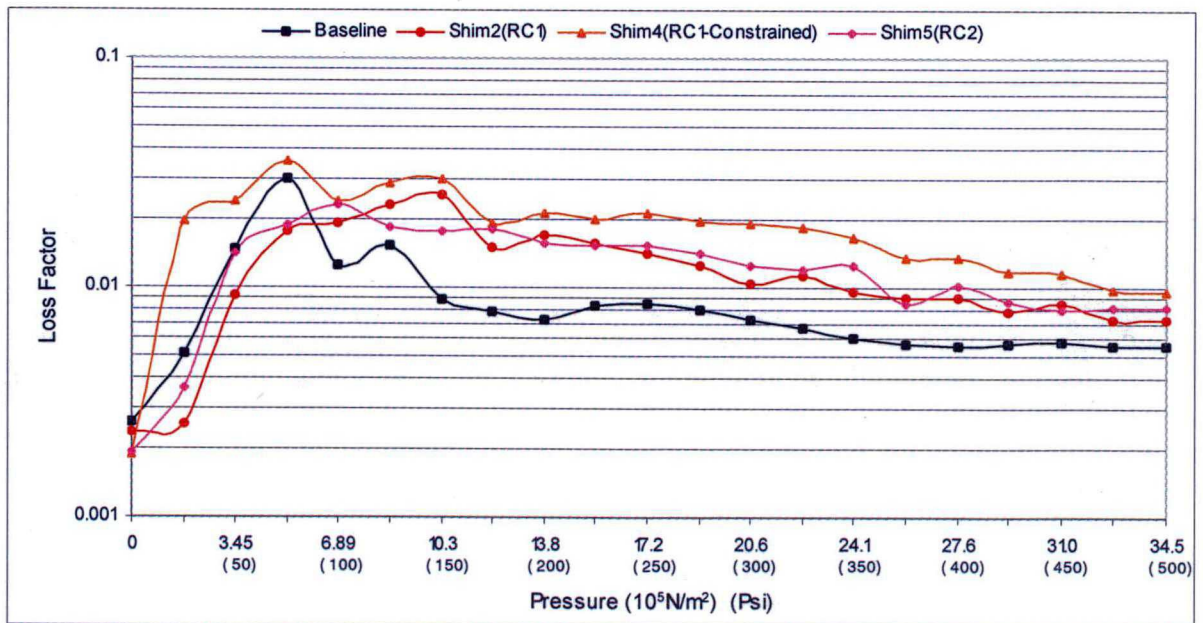


Figure 4.38 – System loss factor some of the shim configurations

The frequency values of the system mode for Shims 2, 4 and 5 are shown in Figure 4.39. The same behavior was also seen and discussed in Figure 4.31.

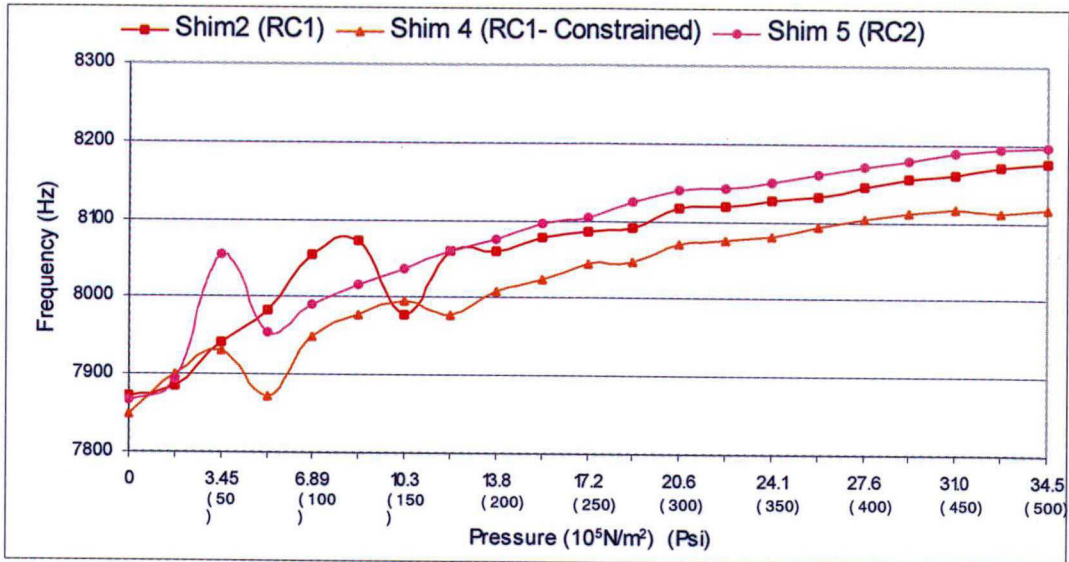


Figure 4.39 – System resonance as function of lining pressure

The first observation regards to the comparison between the results obtained from the frequency responses of the pads, in a free-free boundary condition, and the frequency responses of the assembly brake system, for the Shims 2 and 5 (rubber coat RC1 and RC2, respectively). The shims with rubber coat treatments (Shims 2 and 5) increased the system modal damping, although the free-free analysis of the pads did not indicate this behavior. As mentioned before, when measuring the modal loss factor of the pad under a free-free boundary condition, the damping mechanism of Shims 2 and 5 (RC1 and RC2, respectively) is the elastomer deformation through its length, due to flexural vibration.

However, in the assembled brake system, this is no longer the major mechanism. The difference in the damping performance of the Shims 2 and 5 in the pad frequency response analysis and in the brake system strongly suggests that another mechanism takes place.

When pressure is applied during braking, the rubber coat is statically compressed between the components rotor+pad and caliper. As a simplification of the analysis, at this moment, the caliper is considered rigid when compared to the stiffness of the damping treatment. When rotor and pad start vibrating together, the rubber coat will undergo the same displacement pattern as rotor and pad. Therefore, it will dynamically be compressed and relaxed through its thickness, increasing the energy dissipation capacity of the system.



This compression/relaxation along the thickness was concluded to be the major damping mechanism of the elastomers, when applied as coatings.

It was mentioned above that, at first, the caliper was considered rigid when compared to the stiffness of the damping treatment, i.e., the rubber coats. However, this assumption is not completely feasible and a boundary condition for the caliper must, in practice, take into account its stiffness. Since the rubber coat dissipates energy by the compression/relaxation along its thickness, it is desirable to obtain the maximum dynamic deformation of the elastomer layer during each vibration cycle in order to increase the energy dissipated. In the case of that a finite stiffness being considered for the caliper, this maximum deformation is achieved under a set of parameter combinations of the dynamic properties of the rubber coat and the brake components (rotor, pads and caliper). When the subsystem rotor+pad+shim and the caliper vibrate out-of-phase, the rubber coat will undergo the maximum deformation along its thickness. This subject is further detailed in Chapter 6.

At first sight, the damping added by the shims may seem low, but its efficiency in reducing the squeal noise occurrence was proven by dynamometer tests, as will be shown in Chapter 7.

It is important to point out the similar performance of the Shim 1 (RC1+PSA) and Shim 2 (RC1). One can conclude that, at room temperature, the damping introduced by the shims is mostly due to the rubber coat. At room temperature, the constrained layer of PSA does not play an important role on the system damping.

However, it must be remembered that the measurements were made at room temperature and PSA has its transition region in a higher temperature. Therefore, the effects of temperature on the system loss factor are also important for a complete analysis of the performance of the shims. The dynamics of the brake system as function of temperature is discussed in Chapter 6.

It is also important to note that the drop in the resonant frequency, observed in the Baseline and Shim6 analysis, occurred for all measurements.

Figure 4.40 are the waterfalls of the frequency responses measured with the accelerometers in the rotor and pad, for the different shim configurations.

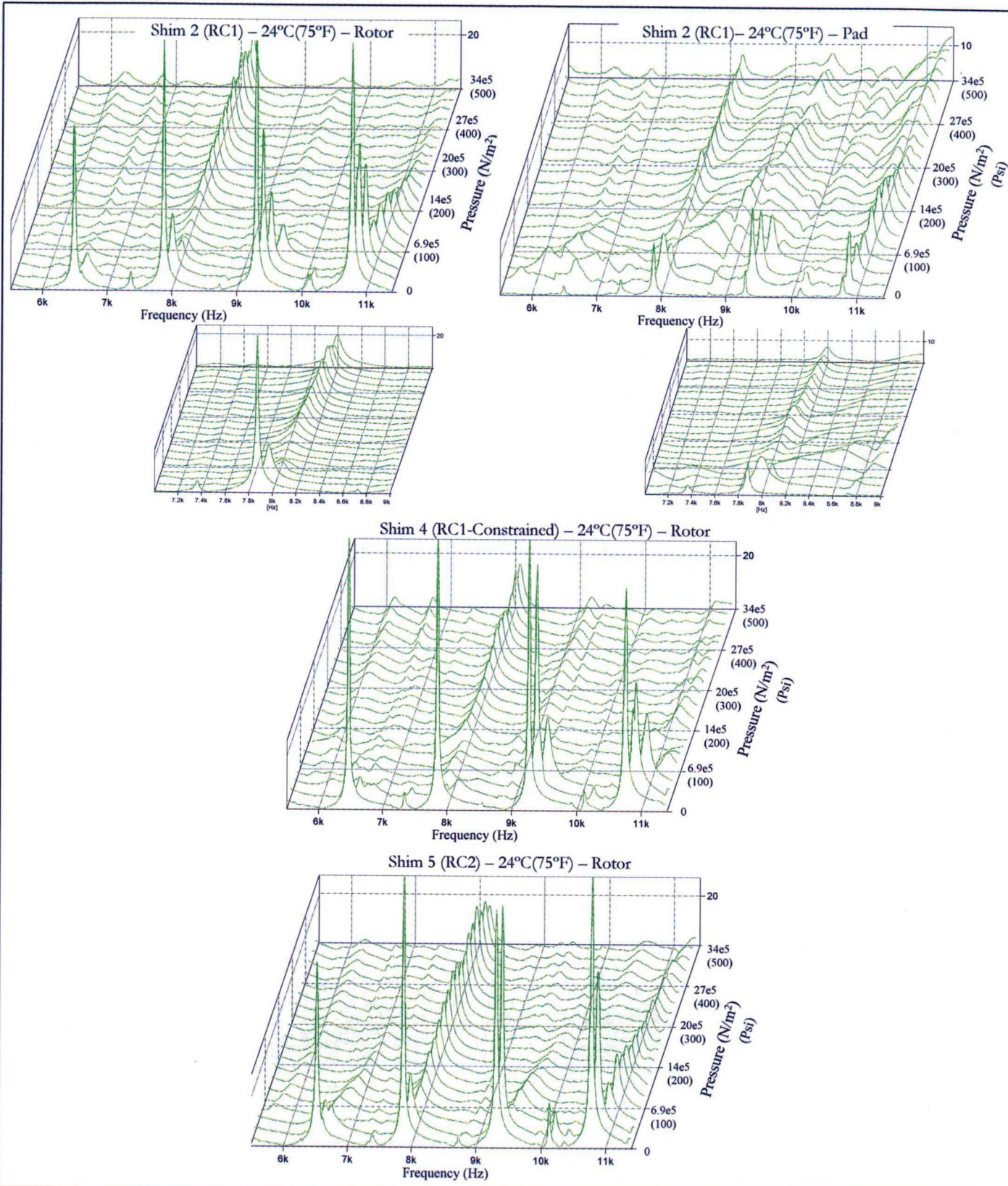


Figure 4.40 – Waterfalls of FRFs for the shim configurations

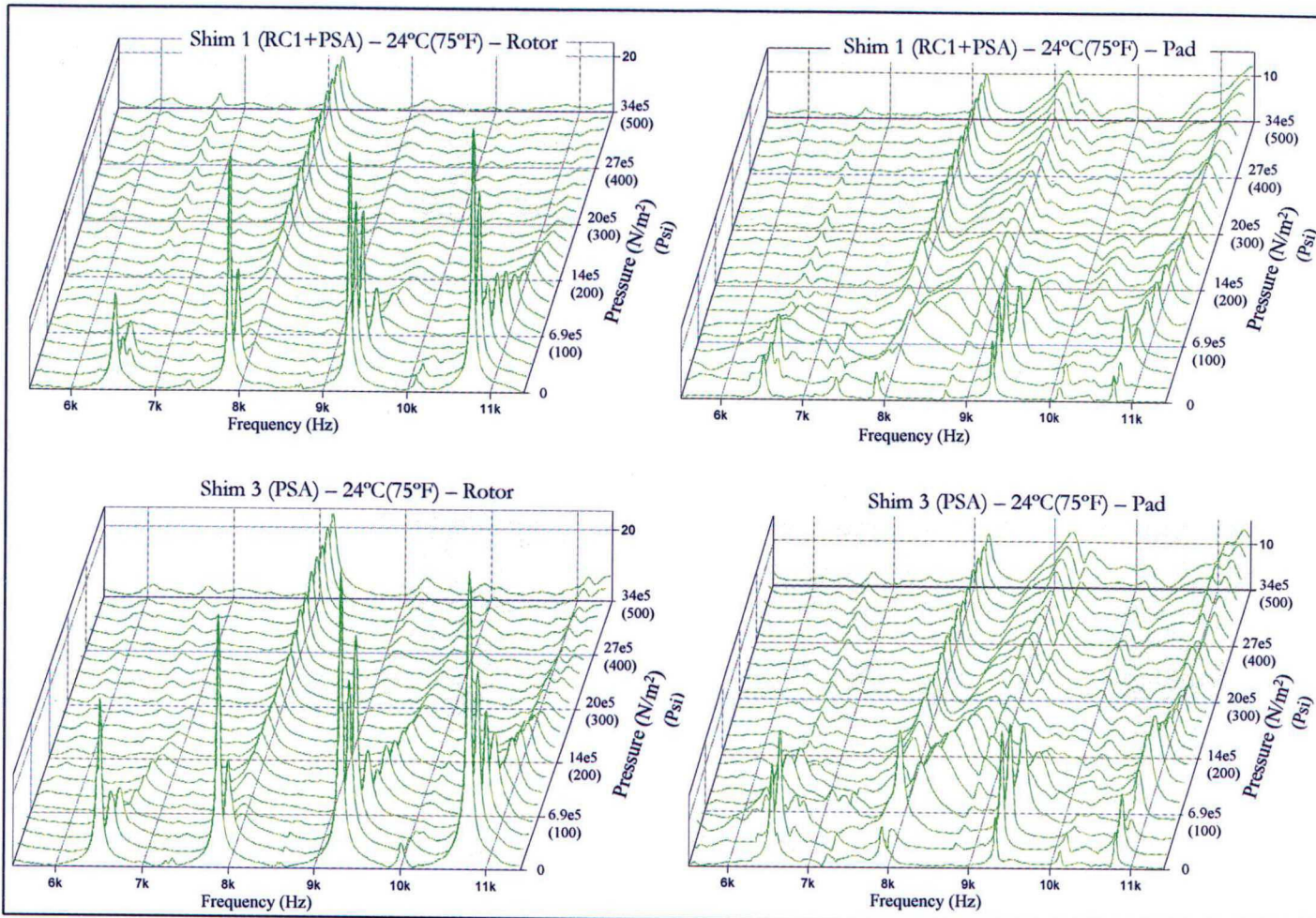


Figure 4.40 - Continued

In this Chapter, the analysis of the brake system was performed as function of lining pressure. In Chapter 6, the system dynamic is evaluated as function of temperature, for specific lining pressures, complementing the data depicted in this Chapter.

In the next Chapter, the locking mechanism of the nodelines of rotor and pad modes, mentioned in item 4.6, is studied using the sound intensity technique.

## CHAPTER 5

### SOUND INTENSITY AND ACOUSTICAL MEASUREMENTS

As discussed in Chapter 4, when squeal noise occurs, the system mode becomes stationary in space, due to the nodelines locking of rotor and pad modes. Once the system mode becomes stationary in space, it can radiate noise, whenever the vibration amplitude of the system reaches certain level and becomes audible.

In this Chapter, the coupling mechanism and the nodelines locking are investigated by constructing Sound Intensity maps of the rotor under different braking pressures. Measurements of sound pressure levels for the system with and without shim treatment are also discussed.

The phenomenon of nodelines locking between rotor and pad modes had been addressed in the literature, such as in references [3] and [4], although it had not been directly measured. On other hand, techniques using acoustical measurements like sound intensity technique and holography had been used to provide insight to components modes of vibration, especially rotor, during squeal event.

One of the main problems in using sound intensity scanning in brake systems under operation is that it is time-consuming and, as a complicating factor, brake squeal usually last for few seconds. Furthermore, during its occurrence, the Sound Pressure Level (SPL) does not remain constant. In order to avoid this shortcoming, a method using a swept sine input force was developed. The focus remains in the coupling mechanism and its consequences, since, like in Chapter 4, the input energy mechanism of this method is independent of the amplitude of vibration (unlike in a self-excited system).

#### 5.1 SOUND INTENSITY

Crocker and Jacobsen [51] define sound intensity as a vector quantity to measure the magnitude and direction of the flow of sound energy. It is not within the scope of this research to discuss the theory of the sound intensity technique, although some insights are useful for a general understanding.

It can be shown that in a medium without mean flow, the intensity vector equals the time-averaged product of the instantaneous pressure and the corresponding instantaneous particle velocity at the same position [52]:

$$\vec{I} = \overline{p(t) \cdot \vec{u}(t)} \quad (5.1)$$

This equation has the electrical analogy, Power = Voltage \* Current.

In a simple harmonic sound field, the above multiplication may be divided into two components [51]: 1) The *instantaneous active intensity*, or simply *sound intensity*, that is the product of the sound pressure and the in-phase component of the particle velocity; 2) The *instantaneous reactive intensity*, that is the product of the sound pressure and the out-of-phase component of the particle velocity.

Very near a sound source, the reactive field is usually stronger than the active field. At a moderate distance from sources, the sound field is dominated by the active field. Ginn [53] states that, basically, an active intensity map yields information about the sound energy flow and thus can be used to determine sound power and to locate sources whereas a reactive intensity map reveals the structure of the sound field, i.e., regions of maximum and minimum pressure.

The sound intensity in a given direction can be determined from measurements of the sound pressure at two points separated by a small distance along that direction. Sound pressures are measured with a two-microphone probe. In this case, two methods are available in order to calculate the sound intensity vector: the direct method, or time domain formulation, and the indirect method, or frequency domain formulation.

In the direct method, the particle velocity is obtained through Euler's equation and the sound intensity vector is calculated from:

$$\vec{I} = \overline{p(t) \cdot \vec{u}(t)} = -\frac{1}{2\rho\Delta r} \overline{(p_A + p_B) \cdot \int (p_B - p_A) dt} \quad (5.2)$$

where

$p_A$  and  $p_B$  are the sound pressures measured by the microphones A and B, respectively;

$\rho$  is the air density;

$\Delta r$  is the distance between the microphones.

In the direct method, sound intensity is calculated from the imaginary part of the cross-spectrum  $G_{AB}$  between the two microphone signals:

$$\vec{I}(\omega) = -\frac{1}{\omega \cdot \rho \cdot \Delta r} \text{Im}\{G_{AB}(\omega)\} \quad (5.3)$$

where

$G_{12}$  is the cross-spectrum between the two microphones A and B.

The time domain formulation and the frequency domain formulation are equivalent. The Fast Fourier Transform (FFT) analyzer used in this research utilized the frequency domain method. Deeper discussions about these formulations, as well as the sound intensity technique, are found in references [5],[51],[52],[53] and [54].

In the probe design, there are several requirements that must be fulfilled: The presence of the probe should not disturb the sound field and the shadowing of one microphone on the other must be minimized. Others limitations, like the distance between microphones, which directly determines the measurement frequency range, and the distance between probe and vibrating surface also must be considered. Some of the microphone configurations usually applied are shown in Figure 5.1. Each configuration has advantages and disadvantages with regards to the shadowing of microphones, distance between the probe and the vibrating surface etc. For the measurements in this research, the configuration *side-by-side* was used, since it allowed a closer approximation of the probe to the vibrating surface. This was an important issue, considering that the frequency range of interest was around 8000Hz.

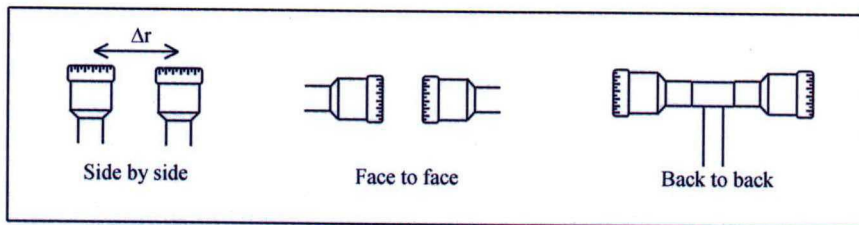


Figure 5.1 – Different probe configurations

### 5.1.1 Sources of Error and Probe Calibration

There are many sources of errors in the measurement of sound intensity, and literature is available concerning with identifying and studying such errors ([51], [52] and [55]). The main sources of errors during sound intensity measurements can be resumed as follow [51]:

- Finite difference error;
- Microphones phase mismatch.

Other possible errors that are usually less serious are random errors associated with a given finite averaging time and bias error caused by turbulent airflow.

#### 5.1.1.1 Errors due to the Finite Difference Approximation

One of the limitations of the measurement principle based on two microphones is the frequency range. This is a systematic error inherent in the approximation of the pressure gradient between the two microphones by a finite pressure difference. This error is most severe at high frequencies. As the distance between microphones approach as a half-wavelength of the sound wave, the ratio  $(p_A - p_B)/\Delta r$  tends to increasingly more different than  $\delta p/\delta r$ . This is exemplified in Figure 5.2.

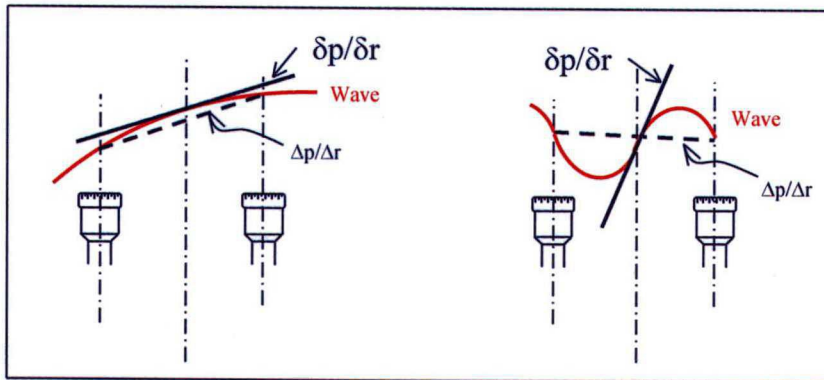


Figure 5.2 – Example of error due to the finite difference approximation

For a given space between microphones, there will be a high frequency limit for the measurements. In principle, the finite difference error depends on the sound field and wave type and curves quantifying this error with frequency, as a function of the spacing between microphones, are found in literature ([51], and [55]). For instance, for a separation distance of 12mm between the microphones, the finite difference error of a

plane wave at 8000 Hz is approximately -2.5 dB, while for a distance of 8.5mm the error reduces to -1.25 dB.

In the measurements of this research, the distance between the centers of the microphones was approximately 9.5mm. Note that this is a systematic error and must be accounted for especially when one is interested in absolute values, like in the determination of Sound Power Level (SWL).

#### 5.1.1.2 Microphones Phase Mismatch

When measuring sound intensity, it is not sufficient to calibrate for sound pressure. It is necessary to know if the phase matching of the instrumentation is in accordance. If a phase error exists, the intensity and velocity levels will be measured incorrectly. Crocker and Jacobsen [51] confirm that this is the most serious source of error in the measurement of sound intensity, even with the best equipment available today. This error is magnified at low frequencies, where the difference between the pressures  $p_A$  and  $p_B$  measured by the microphones is so small it can be masked by the phase error of the probe and analyzer [56].

The phase matching verification is usually made measuring the so-called Pressure-Residual Intensity Index (P-I Index) in a diffuse field. The P-I Index gives a good indication of the accuracy of the phase matching of the two channels where the microphones are connected.

The P-I Index is the ratio of the sound pressure and the residual intensity. It is the intensity indicated by the instrument when the two microphones are exposed to the same sound pressure, for instance, in a small cavity or a coupler volume. If the ratio is too small, the quality of the intensity measurement is poor.

#### 5.1.1.3 Phase Mismatch Evaluation

A pair of ¼" intensity microphones with sensitivities of about 4mV/Pa was used for the measurements. To determine the phase-match of the intensity probe the P-I index of the instrumentation was measured using a closed coupler volume for phase and level calibration of sound intensity, as shown in Figure 5.3. Closed coupler volumes have the characteristic of submitting both microphones to a signal with the same amplitude and phase. In theory, the amplitude of the intensity signal should therefore be zero for the whole frequency range. In practice, the phase mismatch leads to a residual intensity.



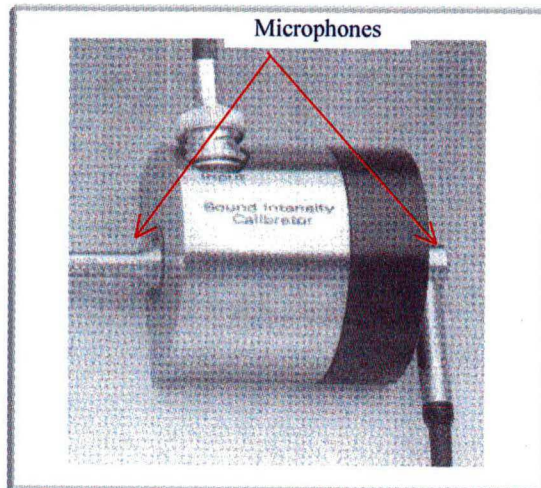


Figure 5.3 – Sound intensity calibrator (closed coupler volume)

A Brüel & Kjaer Pulse analyzer was used for the measurements of the P-I Index, sound intensity and cross-spectrum. The analyzer was also used as the noise generator. A white noise source was generated into the coupler with the microphones placed in chambers opposite to each other.

Before measuring the P-I index of the sound intensity probe, it should be checked if the phase match of the two channels of the analyzer was sufficient. This was done by electrically measuring the P-I Index of the analyzer alone. The white noise signal was connected to the two inputs of the analyzer and the respective P-I index was measured, with the analyzer set to a microphone spacing corresponding to 25mm. According to the closed coupler manufacturer, the P-I index of the analyzer itself should be at least 29 dB for frequencies above 300Hz. For the analyzer used in the measurements, the P-I index measured was around 34dB.

After assuring that the P-I Index of the analyzer was large enough, the intensity probe consisting of the microphone pair and preamplifiers was checked. Once again, white noise was generated inside the calibrator and the P-I Index was measured for an equivalent distance between microphones of 25mm. According to the calibrator manufacturer, in order to determine the P-I Index accurately, long averaging times are necessary. As recommended, during the measurements, the averaging time was approximately 5 minutes.

Figure 5.4 presents the P-I indexes measured for the analyzer itself and for the intensity instrumentation.

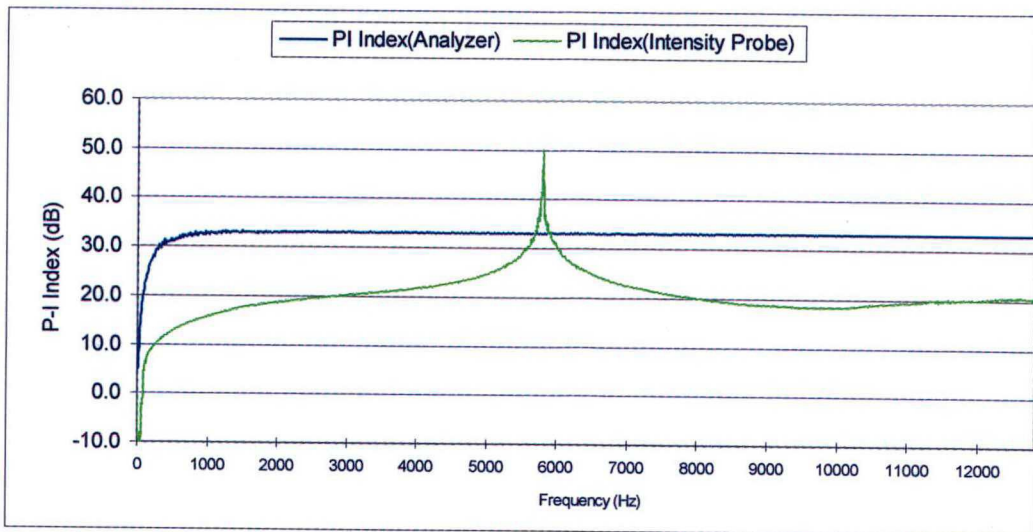


Figure 5.4 – P-I Index for analyzer and intensity instrumentation

The IEC Standard 1043 “Electroacoustics – Instruments for the measurements of sound intensity – Measurement with pairs of pressure sensing microphones” states the P-I index for nominal separations of 8.5, 12, 25 and 50mm, in 1/3 octave frequency bands. For instance, for a Class 1 instrument, the P-I index measured should be at least 19.0dB, for the center frequency of 6300Hz. For a Class 2 instrument, it should be at least 16dB.

Standard ISO 9614 [57] defines the *Dynamic Capability Index*,  $L_D$ , given by  $L_D = \delta_{p10} - K$ , where  $\delta_{p10}$  is the residual P-I Index and  $K$  is the Bias Error Factor, a value selected according to the grade of accuracy required. Gade [55] mentions that the Dynamic Capability Index should be at least 7dB lower than the residual P-I Index to ensure an error due to phase mismatch of less than  $\pm 1$ dB. The aforementioned Standard ISO 9614 establishes the values for  $K$ : for a precision or engineering grade of accuracy (grades 1 and 2, respectively),  $K$  must be equal to 10dB and for a survey grade of accuracy (grade 3),  $K$  must be equal to 7dB.

Therefore, when measuring sound intensity, for each location, the measurements are valid for the frequency range at which the Dynamic Capability Index  $L_D$  is higher than the P-I Index measured for that location.

#### 5.1.1.4 Intensity Calibration

The calculation procedures for sound intensity were also checked with the sound intensity calibrator. For this, an acoustic resistor was introduced into the calibration chamber. A sinusoidal signal was generated inside the coupler. The sound pressure level measured by microphone channel A must be adjusted to 94dB re.  $2 \cdot 10^{-5}$  Pa, by adjusting

the output level of the analyzer. For a sound pressure level of 94 dB in the microphone at channel A, the intensity level measured should be 91.1dB re.  $10e-12W/m^2$ , for a sinusoidal frequency of 250Hz (2.9dB difference value), and 92.2dB re.  $10e-12W/m^2$ , for a sinusoidal frequency of 1000Hz (1.8dB difference value). The sound intensity level measured for  $f=250Hz$  was  $I = 90.7dB$  and for  $f=1000Hz$  the intensity level was  $I = 91.5dB$ . Therefore, there was a systematic error of 0.4dB and 0.7dB in the intensity measurements for the frequencies of 250Hz and 1000Hz, respectively.

## 5.2 SOUND INTENSITY RESULTS

In order to avoid the influence of external noise sources, the measurements were performed in a small hemi-anechoic room. Figure 5.5 shows the background noise measured inside the room, for 1/3-octave bands and also for discrete frequency bands, since the results for sound intensity were measured for constant bandwidths around the critical mode peak.

Sound intensity was measured for the assembly brake system, at room temperature, for different lining pressures. The main purpose was to evaluate the behavior of the critical mode in terms of the nodes and antinodes position as well as to gain insight the modal coupling mechanism in a different way than the one introduced in Chapter 4. Sound intensity maps were obtained for the exposed portion of the rotor lap.

In order to simulate the friction excitation between rotor and pads, patch actuators were inserted into the pads, as shown in Figure 5.6. This allowed an approach of the excitation mechanism, while keeping the input force constant during the measurements. As aforementioned, keeping the input force constant allowed the analysis only of the modal coupling mechanism. The patch actuators were piezoceramic crystal devices that vibrate when submitted to an electrical voltage. The patch actuators used weighted 14 grams each, with dimensions of 109x21.3x1.27 mm.

The patch actuators were inserted into slots cut in each pad, which were later filled with aluminum epoxy mass, with the aim of keeping the pads dynamic properties. Table 5.1 shows the resonances and respective loss factors for the first three bending modes of the pads, before and after inserted the patch actuators.

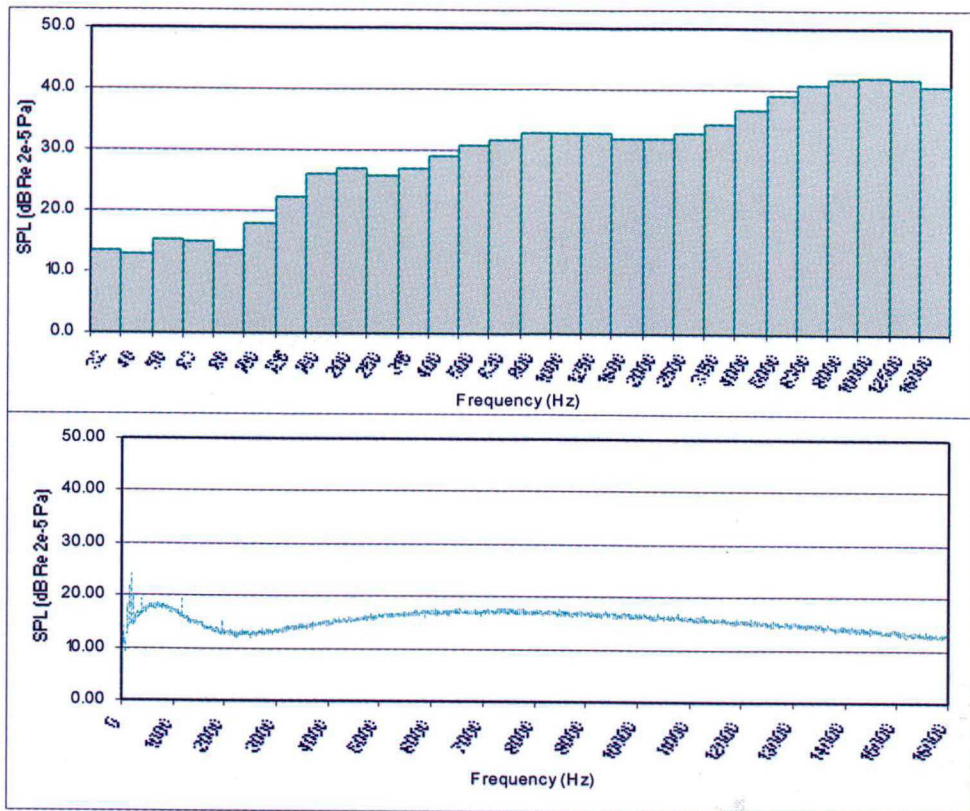


Figure 5.5 – Background noise. 1/3 octave band and constant band

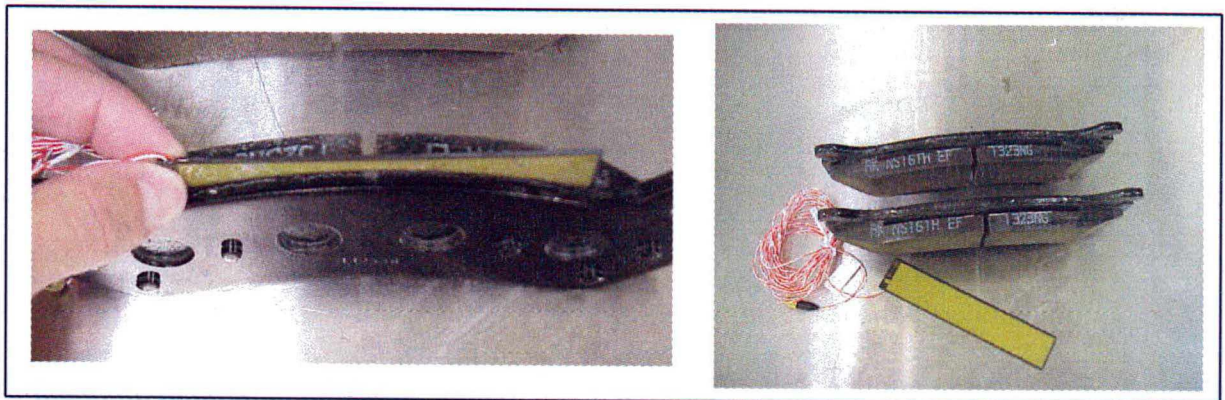


Figure 5.6 – Pads with patch actuators

Table 5.1 – Modal parameters of pads with and without patch actuators

PAD 1				PAD 2			
Without Patch Actuator		With Patch Actuator		Without Patch Actuator		With Patch Actuator	
Bending mode (Hz)	Loss Factor $\eta$	Bending mode (Hz)	Loss Factor $\eta$	Bending mode (Hz)	Loss Factor $\eta$	Bending mode (Hz)	Loss Factor $\eta$
1 – 1212Hz	0.0139	1 – 1298Hz	0.0113	1 – 1214Hz	0.0092	1 – 1268Hz	0.0129
2 – 3992Hz	0.0152	2 – 4050Hz	0.0138	2 – 3962Hz	0.0157	2 – 4066Hz	0.0184
3 – 6638Hz	0.0103	3 – 6694Hz	0.0122	3 – 6656Hz	0.009	3 – 6704Hz	0.0120

Figure 5.7 shows pictures of the test setup used for the sound intensity measurements.

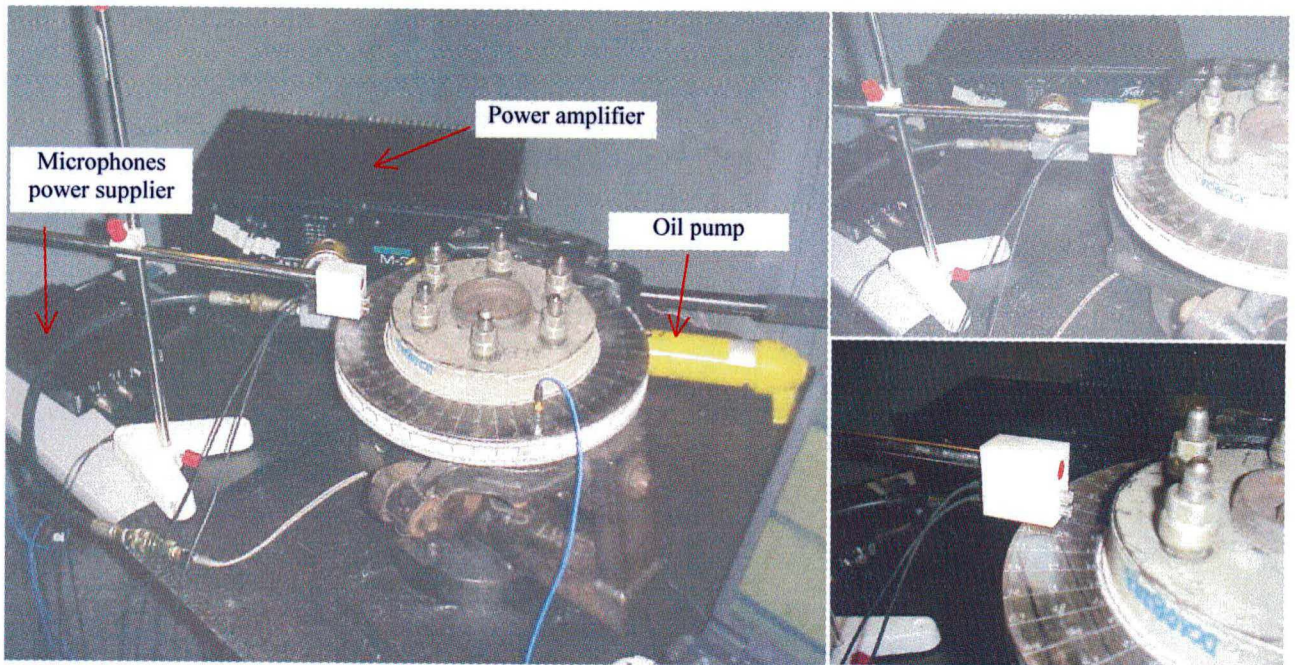


Figure 5.7 – Test setup used for the sound intensity measurements

The pads were excited by a swept sine signal applied thru the patch actuators. The rotor was excited by the contact to the pads. The amount of energy exciting the rotor was dependent of the boundary conditions in the surface of contact between pads and rotor.

The analyzer configuration was as follow:

Lines of the Spectrum: 3200  
Frequency Span: 12800Hz

Average Mode: linear  
Number of Averages: 500  
 $df = 4\text{Hz}$   
 $T = 250\text{ms}$   
 $dt = 30.52\mu\text{s}$

Signal: Swept Sine  
Start Frequency: 6000Hz  
Stop Frequency: 9000Hz  
Sweep Direction: Bi-directional  
Sweep Type: Logarithmic  
Sweep Rate: 0.1 decades/second

Measurements of cross-spectrum between the microphones signals were taken in 105 points (3 point in the radial direction time 35 points along the angular direction), for each lining pressure. The sound intensity maps were calculated with the software Star Acoustics, using Equation 5.3. For each lining pressure, sound intensity was calculated at a frequency range of 80Hz around the critical mode. The center frequencies at which the intensity maps were calculated are listed below.

Pressure ( $1e5N/m^2$ )	0.68	1.72	2.41	3.44	5.17	6.89	10.3	13.8	17.2	20.7	24.1	27.6	31.0
Pressure (Psi)	10	25	35	50	75	100	150	200	250	300	350	400	450
Center Frequency (Hz)	7.94e3	7.96E4	8.14e3	8.18e3	7.94e3	7.94e3	8.06e3	8.10e3	8.14e3	8.14e3	8e19	822e3	8.23e3

Figure 5.8 presents the sound intensity maps calculated as a function of the lining pressure. Figure 5.9 shows the residual P-I Index calculated for the analyzer, for the intensity probe, the Dynamic Capability Index for grades 1 (10dB) and 3 (7dB), and the P-I Index measured at point 53 for a lining pressure of  $20.7e5N/m^2$  (300Psi). The lower graph is a zoom of the excitation frequency range and also includes the P-I Index measured at point 53 for a lining pressure of  $13.8e5N/m^2$  (200Psi).

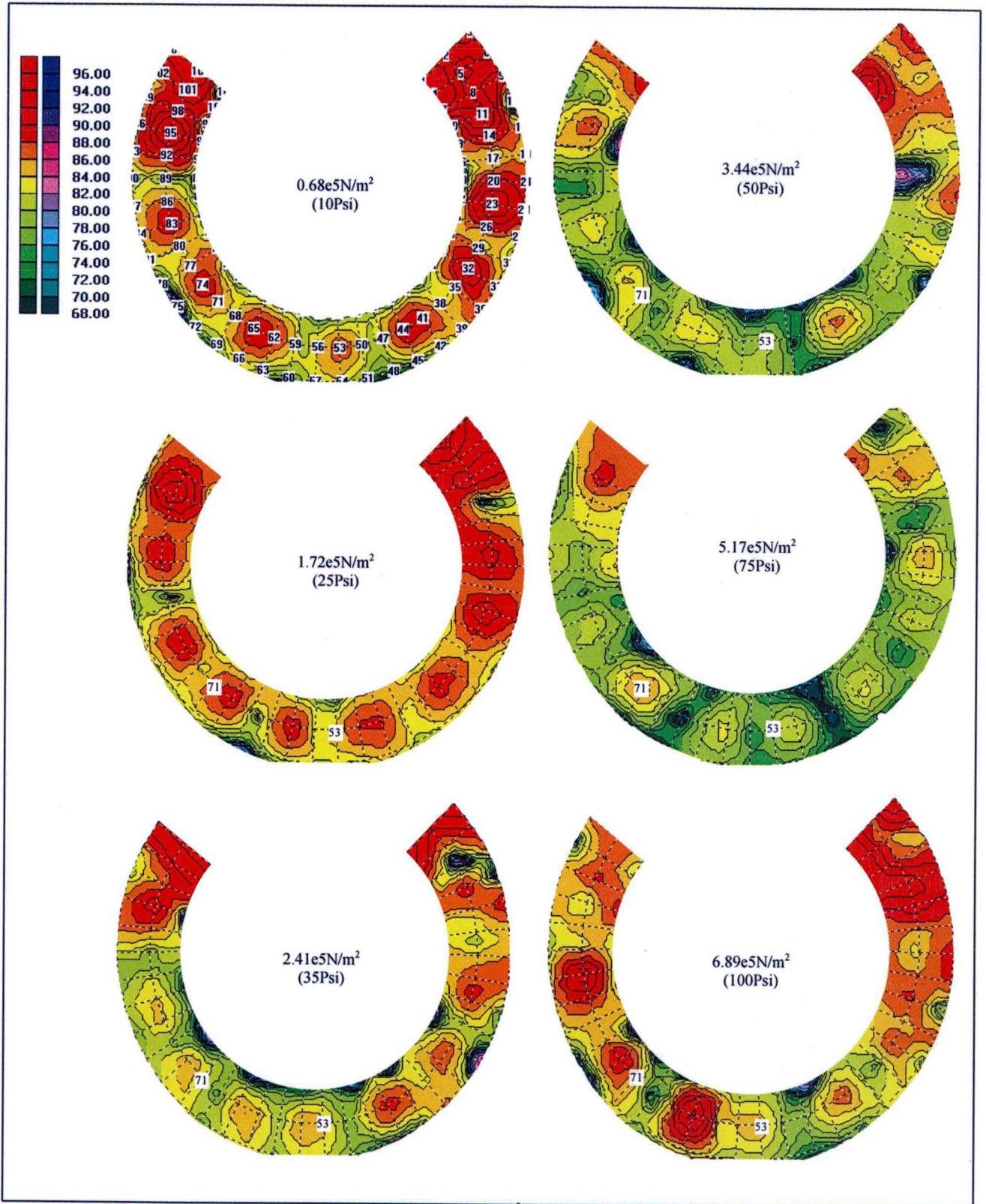


Figure 5.8 – Sound intensity maps of the exposed rotor lap as function of lining pressure

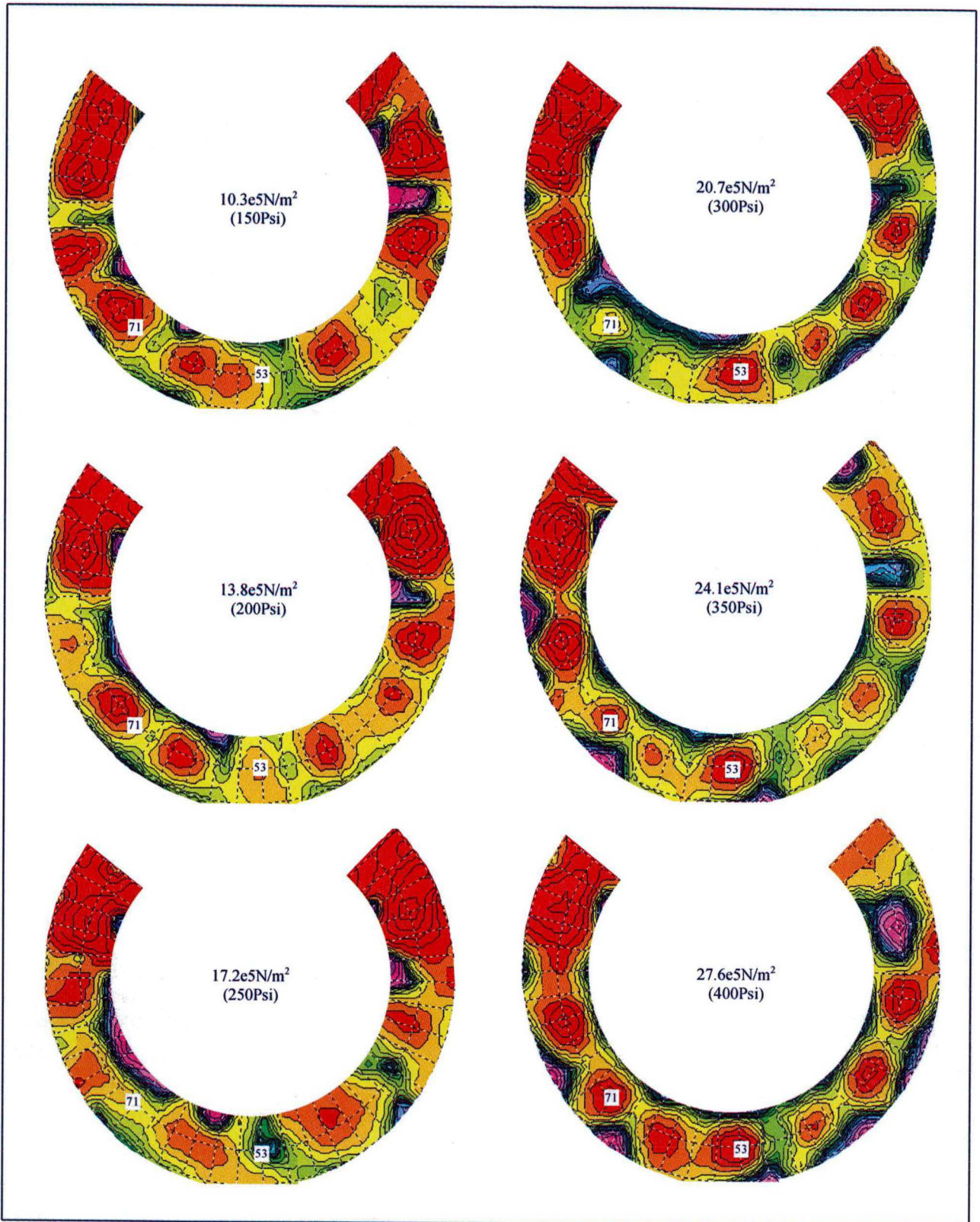


Figure 5.8 - Continued



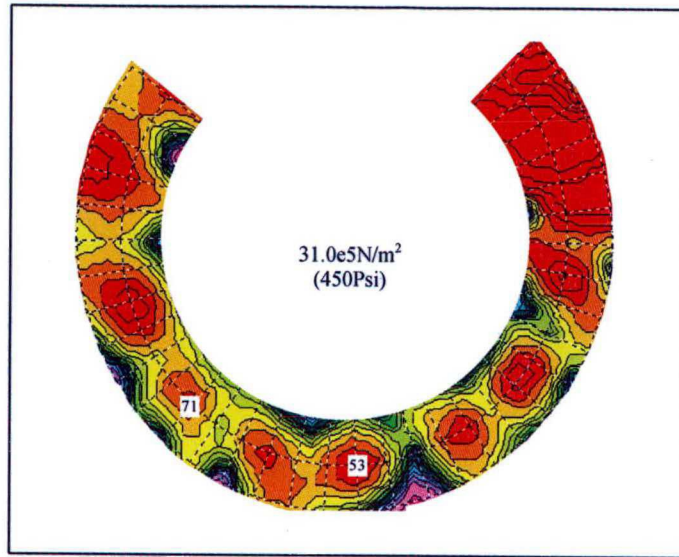


Figure 5.8 – Continued

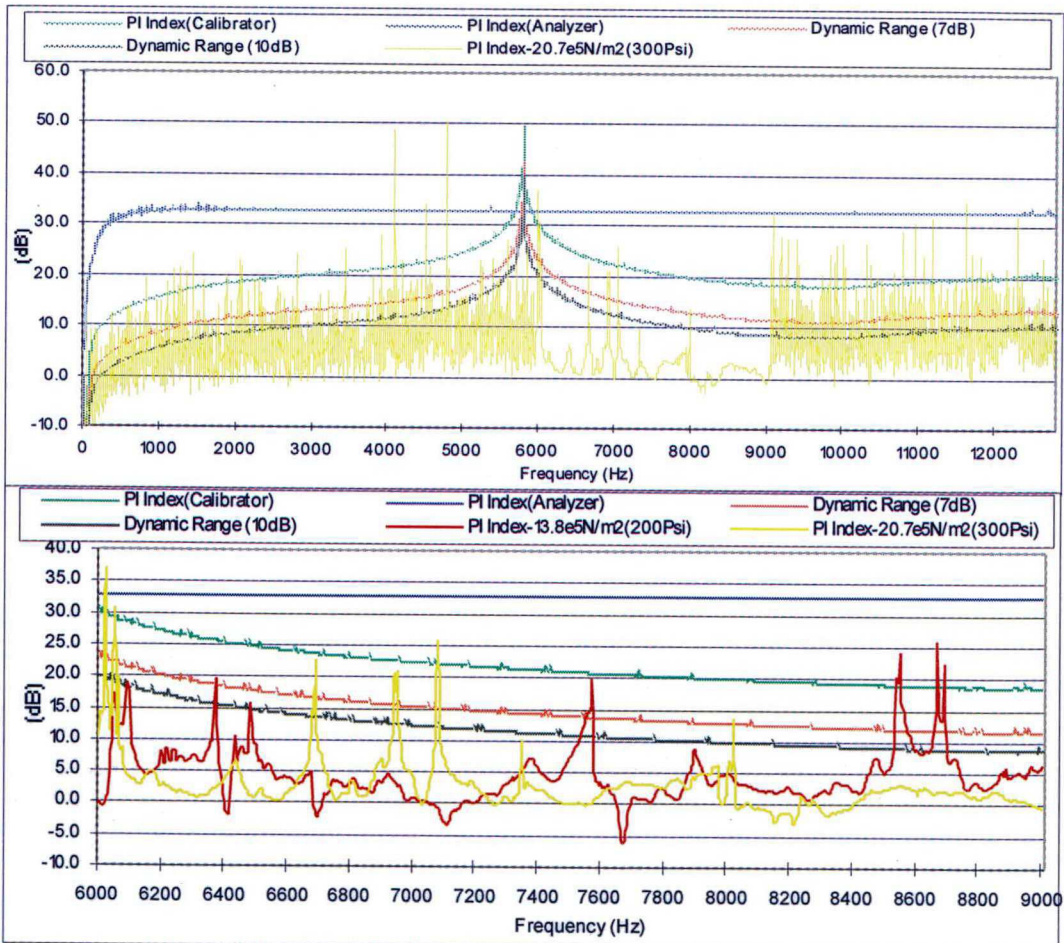


Figure 5.9 – Pi-Index for the analyzer, for the intensity probe and at point 53 (lining pressures of 13.8e5 and 20.7 N/m<sup>2</sup>)

A total of 14 antinodes are formed around the rotor (although the sound intensity maps does not show the whole circumference of the rotor lap), resembling the rotor's 7<sup>th</sup> bending mode. The presence of fourteen antinodes may be explained by the fact that, in theory, the intensity of a dipole source is only positive, although it comprises a combination of positive and negative volume velocity. If the intensity pattern were anti-symmetric, no sound energy would be radiated. The active intensity is a time-averaged quantity and does not oscillate in time, unlike the reactive intensity: Negative volume velocity generates negative surface pressure, and so the product is positive.

At low pressures, rotor and pads are barely in contact. As lining pressure increases, the intensity peaks rotate, i.e., the mode related to the squeal frequency starts to move with respect to the pads. In this situation, rotor and pads are not vibrating in phase and no squeal noise is radiated. At a pressure between  $3.44 \times 10^5 \text{N/m}^2$  and  $6.89 \text{N/m}^2$  (50 to 100Psi) rotor and pad modes start vibrating in phase. It can be noted that the anti-nodes no longer rotate, remaining in the same position along the rotor diameter. This is an essential condition, since it is been considered that rotor and pads vibrate in phase during squeal occurrence.

Another observation is related to the variation of the sound intensity radiated. Around the pressure at which modal coupling occurs, the sound intensity radiated by the rotor lap was lower than at lower pressures and the anti-nodes positions are not so clearly visualized. As the pressure increase above  $13.8 \text{N/m}^2$  (200Psi), the radiated sound intensity also starts to increase: If one assumes that at higher pressures the input energy is kept constant (this assumptions becomes more feasible as lining pressure increases and the system rigidity becomes less dependable of the pressure variation), as long as pad and rotor starts vibrating together, the friction damping is gradually lost and the radiated energy tends to increase.

### **5.3 MEASUREMENTS OF SOUND PRESSURE LEVEL**

With the same test-rig of the sound intensity test, the dynamic behavior of the brake system was evaluated based on measurements of sound pressure and frequency responses involving a microphone autospectrum. Using the same patch actuators inside the pads, sound pressure level was measured considering three configurations for the pads: Baseline, Shim 2 (RC1) and Shim 6.

A random noise was applied through the patch actuators and a microphone, at a distance of approximately 30cm, measured the sound pressure level. This distance was taken in order to avoid the near field at the frequency range of the squeal noise. Figure 5.10 shows two pictures of the test setup.

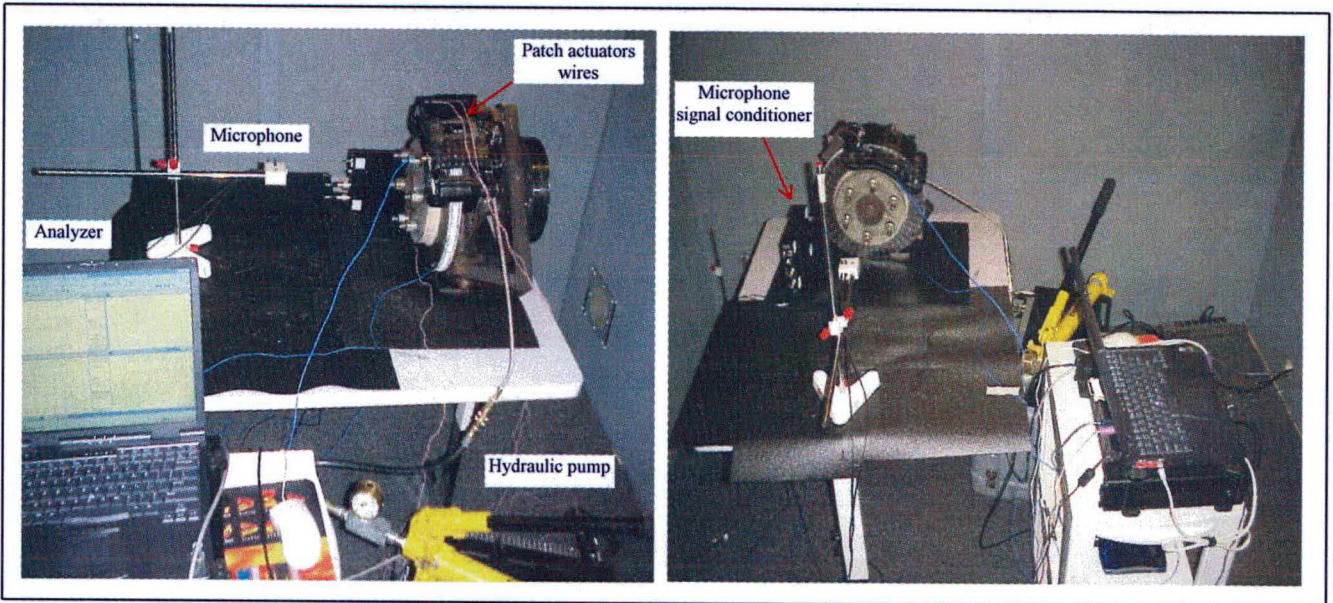


Figure 5.10 – Test setup for measurements of sound pressure level

The analyzer configuration for these acoustical measurements was set as follow:

Signal: Random	Freq. Span Type: Band-Pass
Lines of the Spectrum: 3200	Center Frequency: 7800Hz
Frequency Span: 12800Hz	Frequency Span: 6400Hz
df = 4Hz	
T = 250ms	Average Mode: Exponential
dt = 30.52 $\mu$ s	Number of Averages: 150
Exciter Channel Sensitivity: 2 KVV	

The results were obtained in terms of Frequency Response Functions (FRF) between the microphone autospectrum and the excitation signal. This procedure was employed in order to clean up the autospectrum signal: the FRF results presented lower noise signal levels.

Figure 5.11 shows the FRF values measured at the peak of the critical mode for the three pad configurations, as a function of lining pressure. These are average values, since for each pad configuration, two measurements were taken in order to qualitatively estimate the variability of the values. Figure 5.12 shows the individual measurements made for the Baseline and Shim 2. It can be seen that, although showing some variance, there is a distinct tendency that Shim 6 shows lower sound pressure levels.

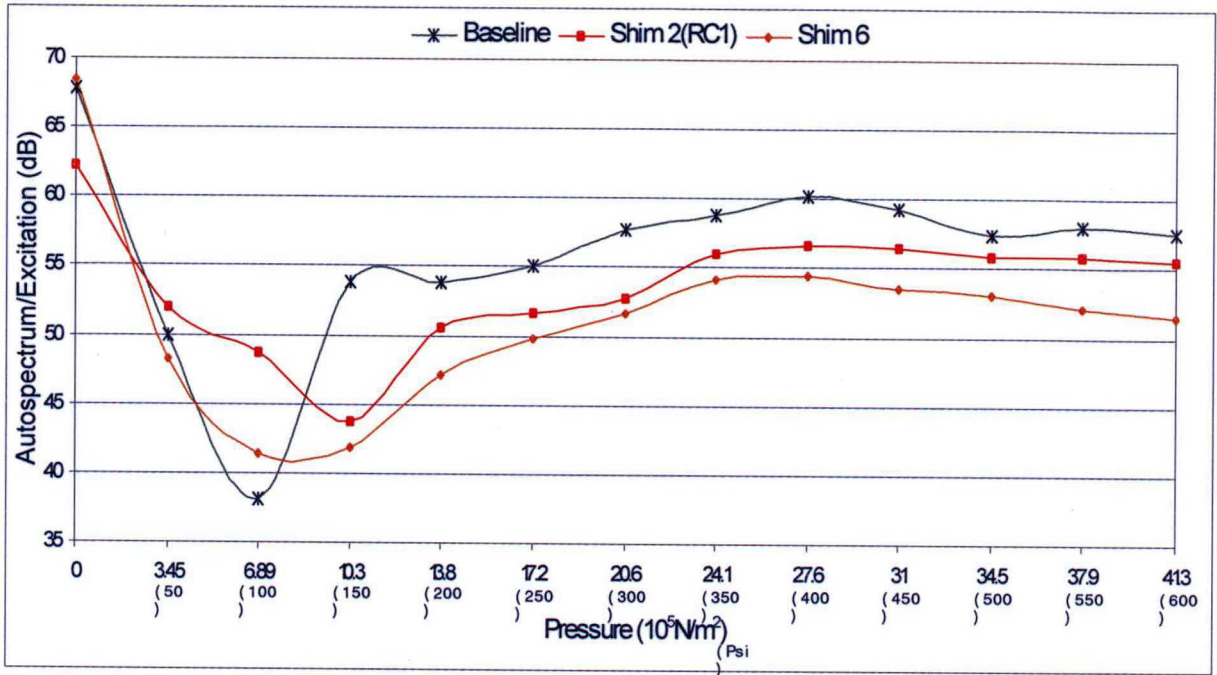


Figure 5.11 – FRF of microphone autospectrum and excitation signal. Values measured at peak

The curves plotted in Figure 5.11 indicate the same tendency as the curves of loss factor discussed in Chapter 4, but in an inverse way. Here, as the brake pressure increases, damping due to friction between rotor and pad also increases, since these two components are vibrating out-of-phase, and the sound pressure level decreases. After the modal coupling, the system components starts vibrating in phase and the sound pressure level increases, with a tendency of stabilization in pressures beyond  $34\text{N/m}^2$  (500Psi).

The drop of the resonance frequency around the pressure at which the components modes couple was also observed, as in the system frequency response analysis in Chapter 4. Once again, when modal coupling occurs, system stiffness is reduced due to in-phase components vibration and the pads act as virtual modal masses added to the rotor mode. This reduction in the modal frequency is shown in Figure 5.13.

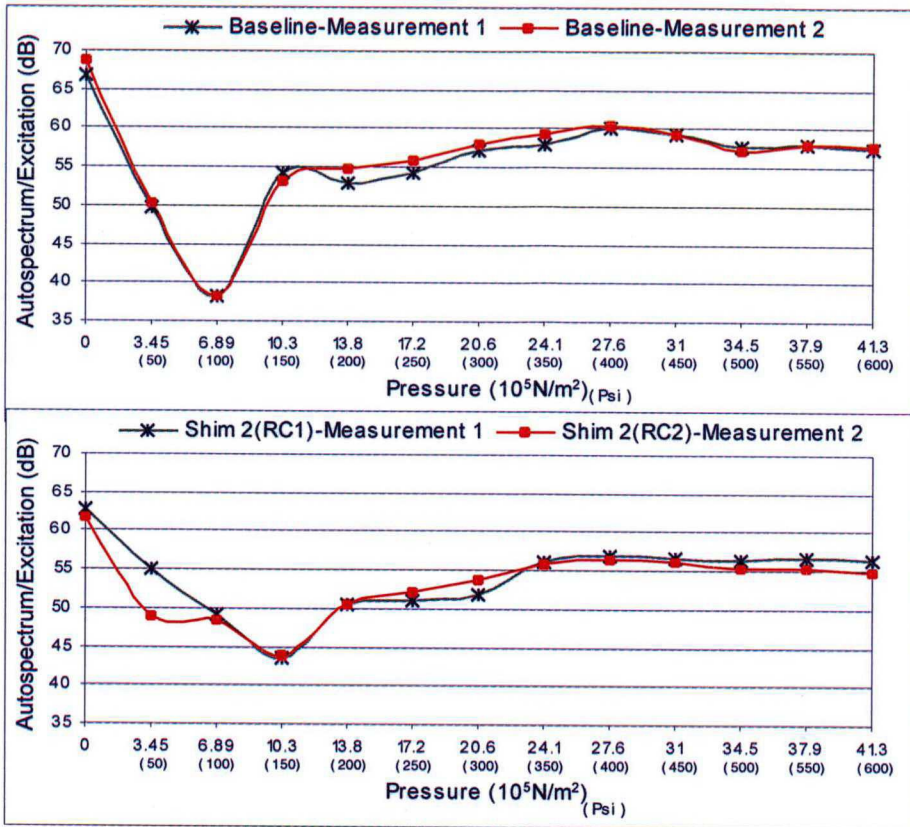


Figure 5.12 – Measurements of FRF microphone autospectrum/excitation signal, for Baseline and Shim 2

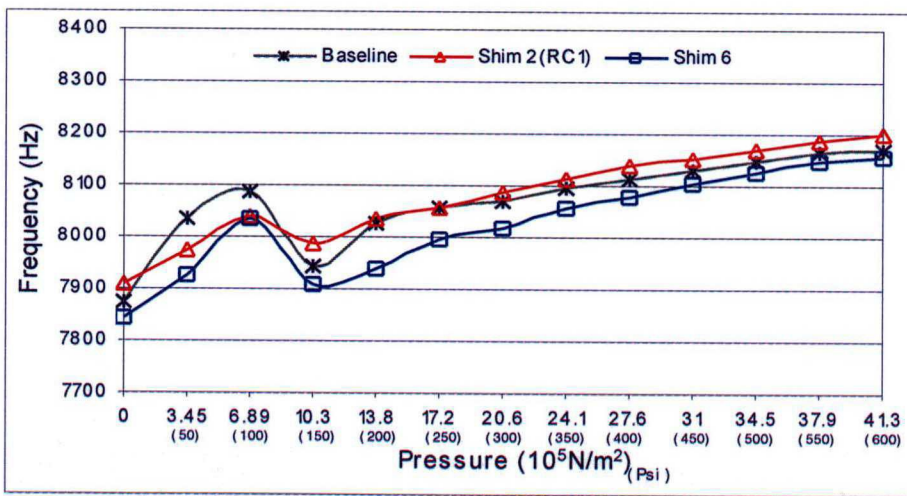


Figure 5.13 – Resonance frequency as function of pressure for the pad configurations

Figure 5.14 shows the contour plots of the FRF microphone autospectrum/excitation signal.

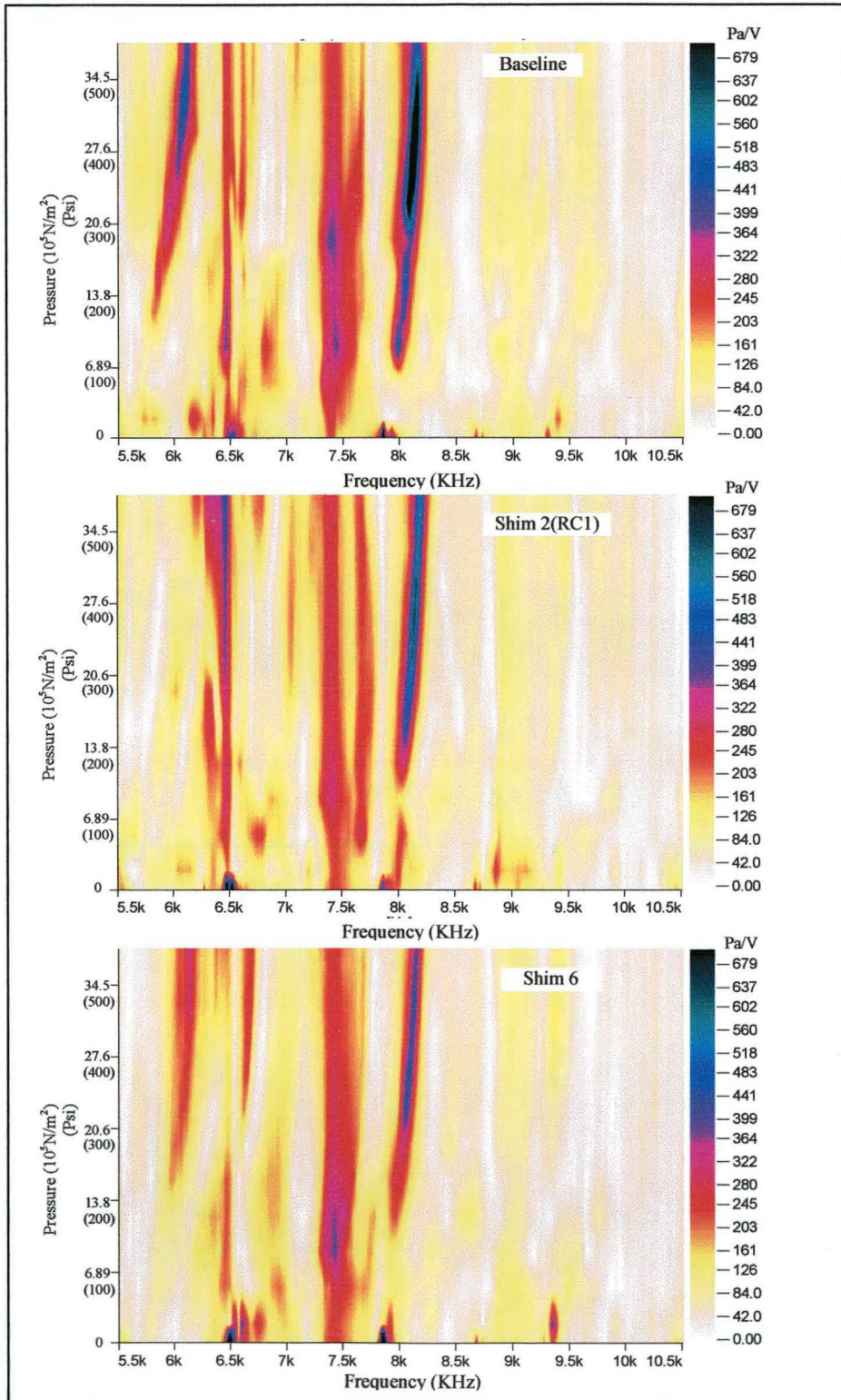


Figure 5.14 – Contour plots of Baseline, Shim 2 and Shim 6

It can be seen that after the modal coupling, the system response at the mode responsible for the squeal noise started to increase.

It must be kept in mind that the values showed in Figures 5.11, 5.12 and 5.13 are the system response at a discrete frequency, i.e., the autospectrum of the microphone at the frequency of the mode peak. However, it is also important to analyze this type of data in a frequency band around the squeal noise peak. In these acoustics measurements, the sharpness of the mode peak cannot be evaluated without information about its bandwidth: A higher peak with a narrower bandwidth may radiate less energy than a lower peak with a wider bandwidth. The analysis of the contour plots in Figure 5.14 provides a qualitative estimation of the peak level and its bandwidth for each lining pressure and Figure 5.15 are values of the FRF microphone autospectrum/Excitation signal for a frequency range between 7700 Hz and 8500Hz.

Figures 5.11 and 5.15 exhibit the same tendencies although, when considering the noise radiated by a wider frequency range around the mode peak, the differences between Shim 2 and Shim 6 tends to be reduced. This can especially be due to the fact that, once again, the input energy mechanism was kept constant, regardless of the variation of the system dynamics (damping, stiffness etc) with the lining pressure. Therefore, the self-excitation mechanism was not considered, which may affect the noise level radiated, as discussed in Chapter 4.

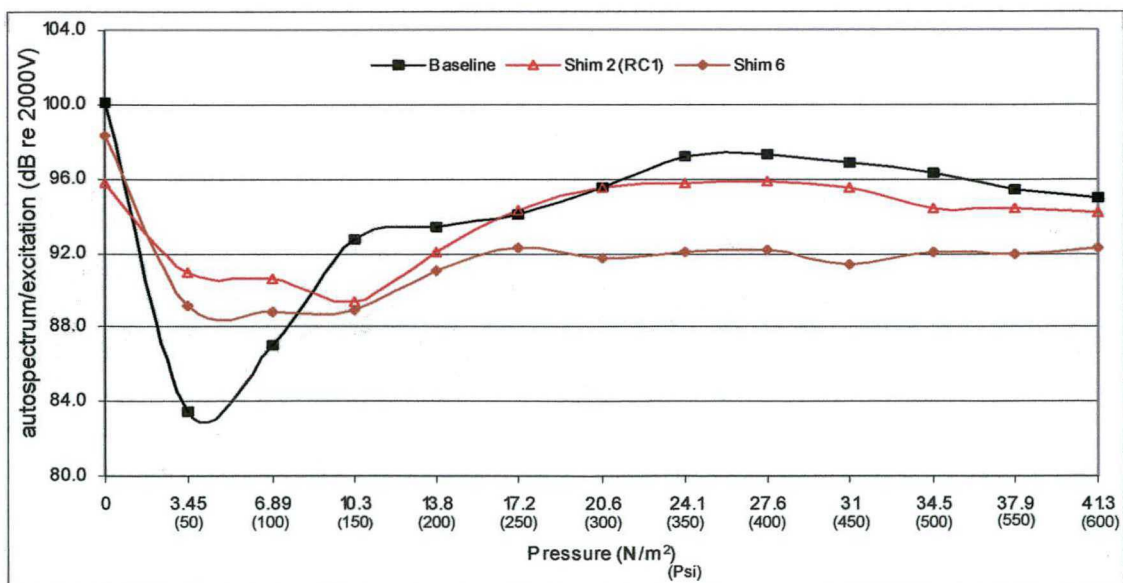


Figure 5.15 – FRF Microphone autospectrum/excitation signal: Frequency range of 7700 to 8500Hz

# EFFECT OF TEMPERATURE ON THE DYNAMICS OF THE BRAKE SYSTEM RUBBER COAT DAMPING MECHANISM

In Chapter 4, the dynamic behavior of the assembly brake system for the shim configurations was evaluated as a function of the braking pressure. The modal coupling mechanism was depicted and the system damping, the dynamic parameter taken as that responsible for the noise squeal control, was measured and discussed. The modal loss factor of the pad in a free-free boundary condition, using different shim configurations, was compared to those measured for the assembled brake system. This led to information about the dynamic behavior of the system when squeal noise occurs and, most importantly, some primary conclusions about the damping mechanism of rubber coats.

In this Chapter, measurements of the system loss factor as a function of temperature are presented in order to complement these former conclusions. A more detailed discussion is made about the damping mechanism of rubber coats.

Finally, a simple 2 degrees-of-freedom system is modeled to explain the importance of the modal parameters of the brake components in the damping of rubber coats.

### 6.1 EFFECTS OF TEMPERATURE ON THE SYSTEM DYNAMICS

Frequency response analysis of the assembled brake system was performed as function of temperature, for pre-determined lining pressures. In this case, the values chosen for the pressure measurements were over the range at which the modal coupling occurred. Therefore, the responses were measured under the conditions of squeal noise occurrence and the estimation of the system loss factor allowed the evaluation of the performance of the different shim configurations.

The system setup was basically the same as that used for the measurements discussed in Chapter 4. The brake system was put inside an oven, as shown in Figure 6.1.



The temperature range was between  $-10^{\circ}\text{C}$  ( $15^{\circ}\text{F}$ ) and  $170^{\circ}\text{C}$  ( $335^{\circ}\text{F}$ ). The brake pressures at which the loss factor was measured were  $17.2\text{e}5\text{N/m}^2$ ,  $20.6\text{e}5\text{N/m}^2$ ,  $24.1\text{e}5\text{N/m}^2$  and  $27.6\text{e}5\text{N/m}^2$  ( $250,300, 350$  and  $400$  Psi, respectively). As mentioned previously, these pressure values were chosen in order to simulate the squeal noise occurrence condition. Also, the measurements of loss factor as a function of the lining pressure proved to be more consistent in this pressure range.

Measurements for each pressure were taken in steps of approximately  $6.67^{\circ}\text{C}$  ( $20^{\circ}\text{F}$ ). For each temperature, the system loss factor was measured for the lining pressures aforementioned. This procedure was performed for the brake system using each shim configuration bonded to the pads. This procedure proved to be time-consuming, since each temperature step took approximately 1 hour. As the temperature went higher, it took more time to warm up the brake system to the target temperature.



Figure 6.1 – Pictures of the setup for measurements of the brake system under temperature

The system was excited by an impact hammer and the response was taken using a magnetic accelerometer. It was possible to remove the magnetic accelerometer from the oven during the heating period, thus avoiding any potential damage, due to the high temperatures. As in Chapter 4, the rotor was kept at the same angular position during the measurements for the different shim configurations and point frequency responses were obtained.

Figure 6.2 shows the loss factor measured, as a function of temperature, for the system mode at which squeal noise occurs. The four graphs correspond to the lining pressures at which measurements were taken.

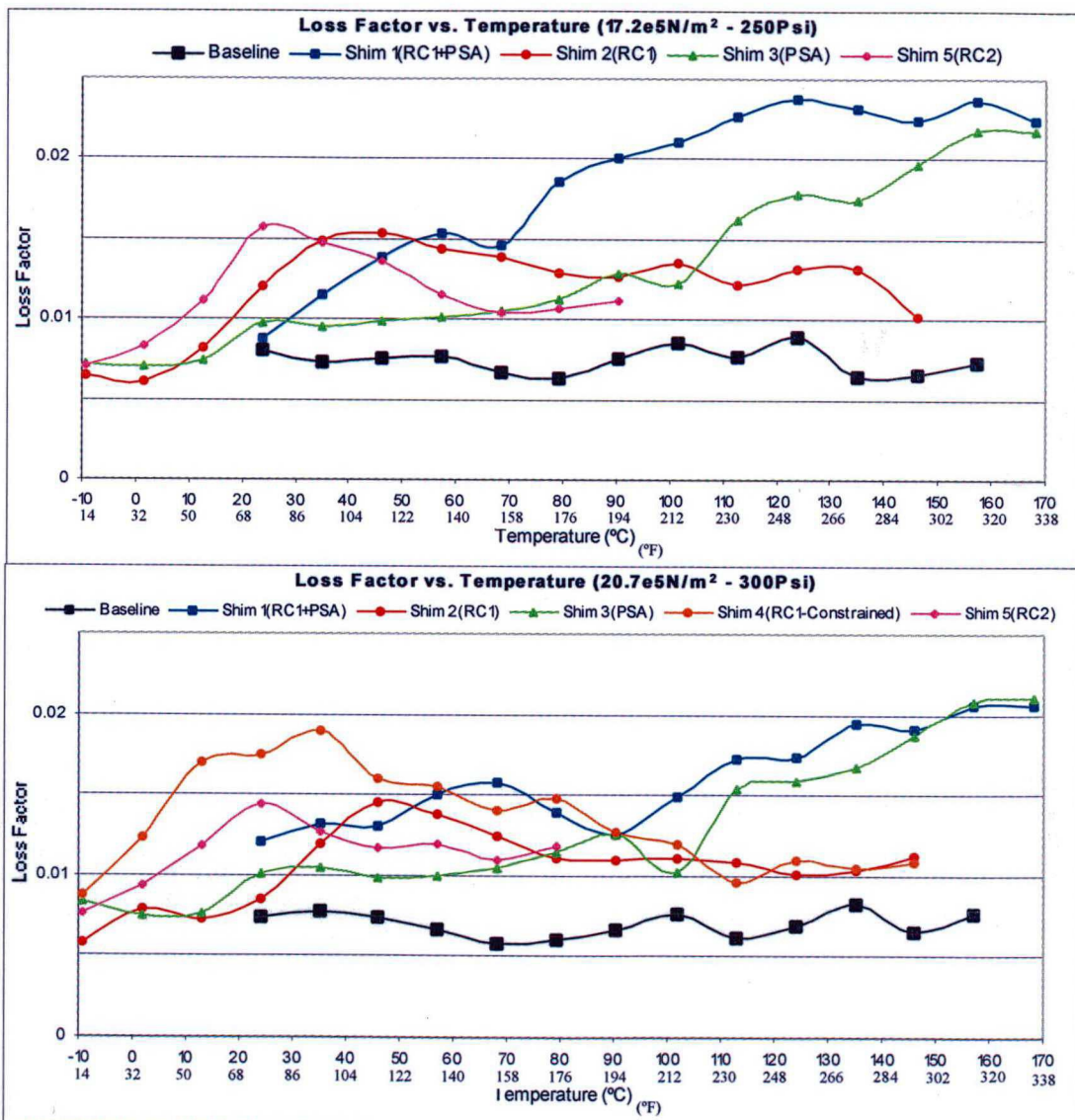


Figure 6.2 – Modal loss factor vs. temperature for the brake system for different braking pressures

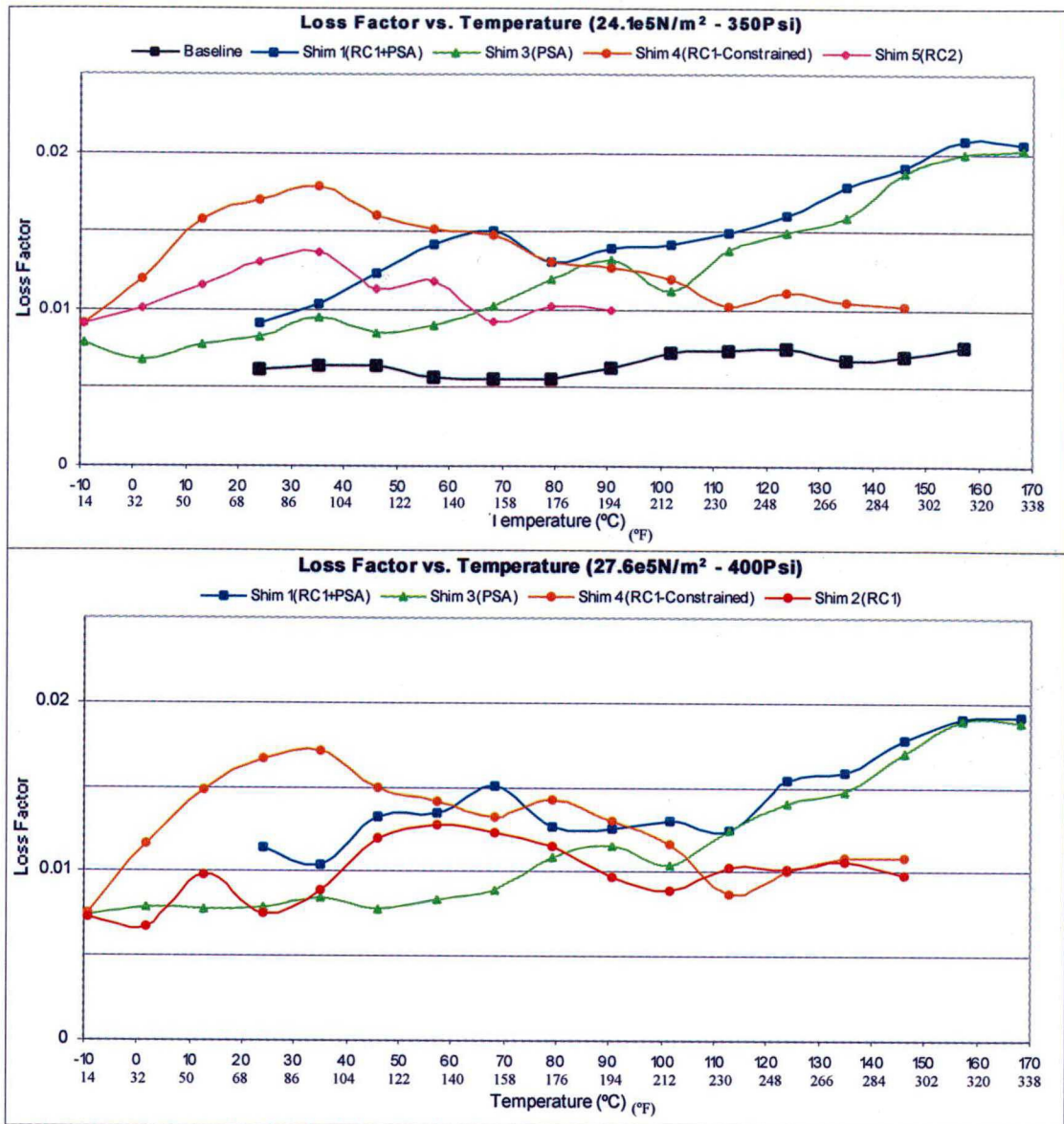


Figure 6.2 - Continued

Some observations can be made when these graphs are compared with the curves of loss factor vs. lining pressure at room temperature, determined in Chapter 4.

Damping of the brake system as a function of temperature, at the critical mode, remained roughly the same for the pads without shims (Baseline). The values were also much lower when compared to those with shim treatments, even though the friction material presented some damping properties. For instance, its loss factor was measured using cantilever beams made of the friction material and the known beam equations (Euler equations), as shown in Figure 6.3. The loss factor of the pad friction material was

estimated to be around 0.035 for a range of temperature between 24°C (75°F) and 120°C (200°F).

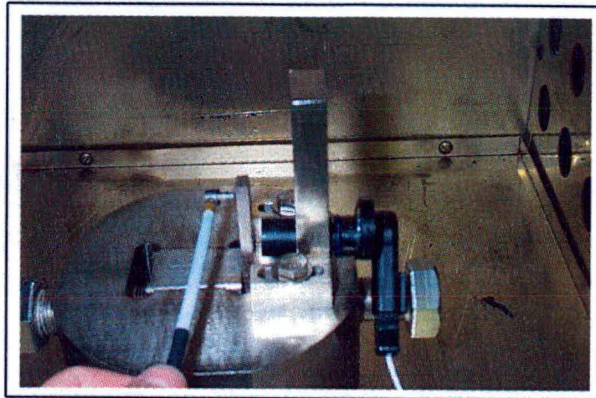


Figure 6.3 – Measurement of the pad friction material dynamic properties

As expected, the brake system with the Shims 1 and 3 (RC1+PSA and PSA, respectively), exhibited higher damping at temperatures around 160°C (320°F). According to the nomogram of the viscoelastic material PSA, shown in Chapter 3, this is around the temperature where its loss factor is maximum, for a frequency of about 8000Hz. At room temperature, Shim 3(PSA) has a lower damping when compared to Shim 2(RC1). It is interesting to note that Shim 1(RC1+PSA) also has a higher damping than Shim 3(PSA) at room temperature. This is an indication of the contribution of the rubber coat RC1 in the system damping, around 25°C. As the temperature increases, the modal loss factors of the brake system with Shim 1 and Shim 3 tend to the same values. This means that the rubber coat no longer contributes to the system damping, compared to the PSA constrained layer. The values of loss factor measured for Shim 1 at 17.2N/m<sup>2</sup> (250Psi) did not follow the tendency of the other measurements, indicating that the coupling phenomenon, in some situations, was extended up to higher pressures.

### 6.1.1 Damping mechanism of rubber coats

As in Chapter 4, Shim 2 and Shim 5 (RC1 and RC2, respectively) increased the system modal damping, although the FRFs measured only for the pads in a free-free boundary condition, as a function of temperature (Figure 4.36), did not indicate this trend. Note also that RC1 increased the system modal damping in a more effective way when used in a constrained layer configuration rather than as a rubber coat. As already

discussed in Chapter 4, this is due to the different damping mechanism of the elastomer when it is applied as a coating. In this case, when the braking pressure is applied, the rubber coat is statically compressed between rotor+pad and the caliper fingers. When pad and rotor vibrate, the rubber coat will be compressed and relaxed along its thickness, increasing the energy dissipation capacity of the system.

Therefore, shearing of the constrained viscoelastic layer is no longer the major damping mechanism in such configurations and some considerations are made here in order to assert this assumption:

- 1) As discussed in Chapter 3, one of the most important assumptions in the shear damping mechanism is the coupling between layers, i.e., all the three layers (metal/viscoelastic material/metal) share the same mode shape (movement). This assumption is strongly related to the performance of such damping treatment as a function of the *shear parameter* (see Chapter 3). In the case of a rubber coating, the rubber layer could be constrained between pad and caliper. However, the caliper is not subjected to the same mode shape as the pad and rubber coat. Since the rubber coat is being compressed and relaxed along its thickness, pad and caliper will not necessarily vibrate in-phase and do not share the same deformation.
- 2) In order for caliper and rubber coat+pad to share the same mode shape deformation, each finger of the caliper should deform along its longitudinal direction, as shown in Figure 6.4. In practice, this does not happen, since the fingers are too rigid in this direction.

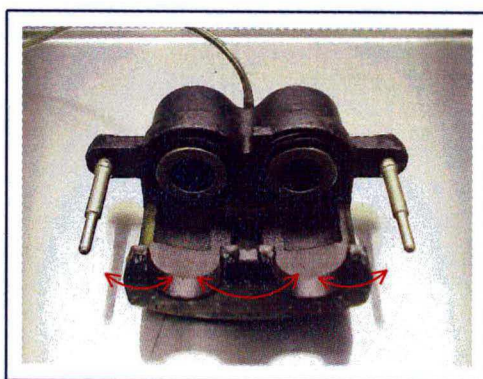


Figure 6.4 – Deformation of the caliper fingers necessary for shear damping to occur in the rubber coat layer

3) Shearing of constrained layers happens mostly at the nodes of a vibration mode, as shown in Figure 6.5. If the constraining layer (in this case, the caliper) is considered too rigid in the longitudinal direction such that it will not share the same deformation as the constrained layer (rubber coat), the nodes of the vibration mode that the rubber coat is subjected to will not shear. Furthermore, even if the caliper fingers were submitted to the same deformation as the rubber coat and pad, their positions and wavelength should be such that shear deformation would take place at the rubber coat layer. Figure 6.6 illustrates how the wavelength dependency can affect the shear deformation in damping treatments with different lengths of constraining layer. As discussed in Chapter 3, for a given viscoelastic material, constraining layer, frequency range and temperature, there is an optimum length for the constraining layer (in this case, the caliper), mathematically determined by the *shear parameter*.

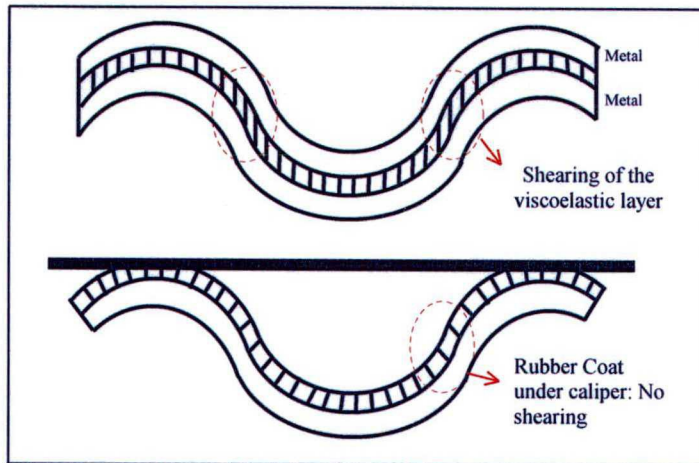


Figure 6.5 – Constrained layer damping treatment and rubber coat under caliper: No shearing occurs at the rubber coat under the caliper

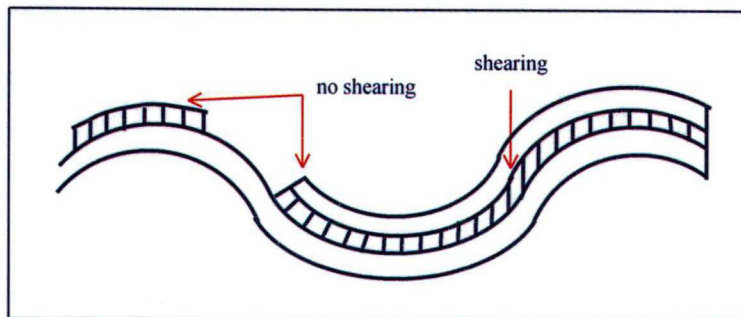


Figure 6.6 – Wavelength dependency on shear deformation

4) Finally, the hypothesis of extensional damping (deformation along the length) is opposed by the results of the measurements of loss factor  $\eta$  for the pads, in a free-free boundary condition, and for the assembled brake system (Chapter 4). Results strongly suggested that lining pressure also plays a role on the damping performance of rubber coats.

There is a difference between the temperatures at which the loss factor is maximum for RC1 when applied as a rubber coat and as a viscoelastic constrained layer. For the rubber coats, the temperature at which damping is maximum differs from that expected from the nomogram. This can be explained by the fact that, in the characterization of the damping performance of coating materials, the dynamic properties of the brake system components also play an important role. As formerly discussed, if the rubber coat stiffness is kept constant, the higher the deformation of the rubber along its thickness the higher the energy dissipated.

If one considers the caliper rigid, the deformation at the rubber coat layer will be a function of the dynamic properties of the elastomer and the subsystem rotor+pad. However, since the caliper has a finite stiffness, the maximum deformation in the rubber coat thickness will be achieved under a set of parameter combinations of the dynamic properties of the rubber coat and the brake components, also taking into account the modal parameters of the caliper. In this case, the rubber coat layer is modeled as an elastomer dynamically compressed between two system components, these being here, caliper and the subsystem rotor+pad. When rotor and pad modes have the same frequency and wavelength, these two components start vibrating in-phase, and the rubber coat is compressed and relaxed between rotor+pad and caliper. The rubber coat layer works as a spring connecting these two parts (rotor+pad and caliper), transmitting the vibration energy to the caliper. Maximum deformation will then be achieved whenever these two parts starts vibrating out-of-phase, increasing the energy dissipated.

The energy dissipated per radian by a spring with a complex Young's modulus can be shown to be ([5],[6],[7],[15]):

$$D = \eta \cdot K \cdot x^2 / 2 \quad (6.1)$$

where

K is the spring stiffness;

x is the deformation (strain) of the spring.

Considering the rubber coat layer as a complex spring connecting rotor+pad and caliper, one could conclude that by increasing its deformation, the energy dissipated by damping also increase. Furthermore, increasing the deformation can be achieved by decreasing the rubber coat stiffness  $K_{RC}$ . However, the energy dissipated by the rubber coat is proportional not only to the deformation, but also to its stiffness. Therefore, one must be careful when reducing  $K_{RC}$  in order to increase the deformation  $x$ . Furthermore, in viscoelastic materials, reducing  $K_{RC}$  means a reduction in the Young's modulus  $E$ , which can be achieved by increasing the temperature. However, over the transition region, not only  $K_{RC}$  will be reduced, but also  $\eta$  and the consequence may be a reduction in the energy dissipated.

The loss factors measured for Shims 2 and 4 and 5, as functions of temperature, for each lining pressure, are individually presented in Figure 6.7.

There is a tendency that, when the rubber coat shims are considered, lining pressure has a more noteworthy influence on the determination of the temperature at which the system loss factor is maximum, when compared to constrained layer treatments. The temperature of maximum loss factor showed a tendency to increase with the increasing of lining pressure.

By increasing the system pressure, the rubber coat will be more compressed and its stiffness, represented by the Young's modulus, will also increase. As a consequence, it is necessary to have a higher temperature to dissipate the same energy. Looking at the nomograms in Chapter 3, increase the Young's modulus is equivalent to increase the frequency and, in order to return to the former properties, it is necessary to increase the temperature.



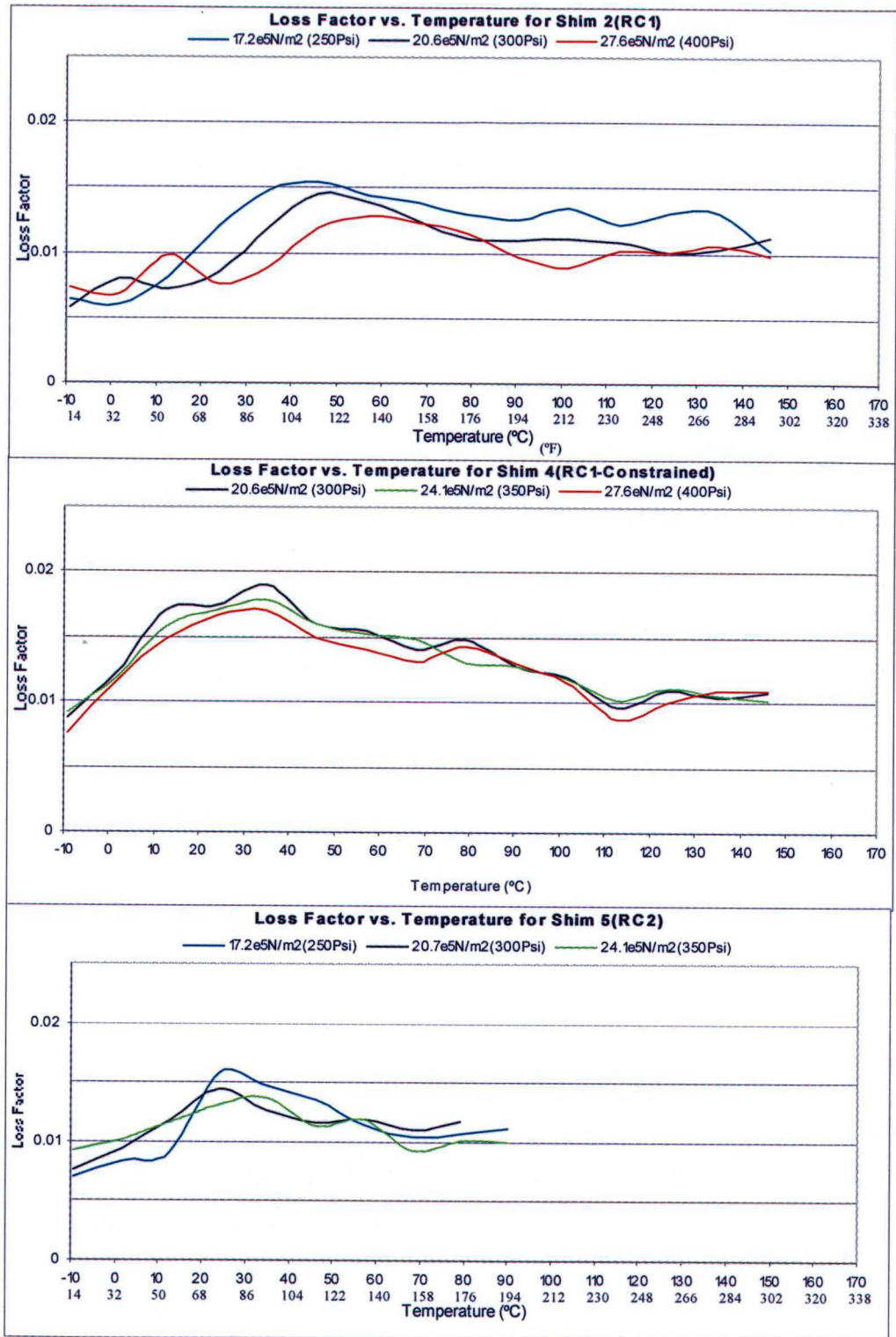


Figure 6.7 – Modal loss factor vs. temperature for the brake system with Shims 2, 4 and 5

Also, the lining pressure is equivalent to a static pre-load on the rubber coat. The effect of static pre-loads on Young's modulus of viscoelastic materials is described in reference [7] and qualitatively shown in Figure 6.8. When a static pre-load is applied, the Storage modulus increases and the loss factor tends to decrease, since the energy dissipation capacity of the material should remain the same. The energy dissipated is proportional to the product of the storage modulus and the loss factor of the material.

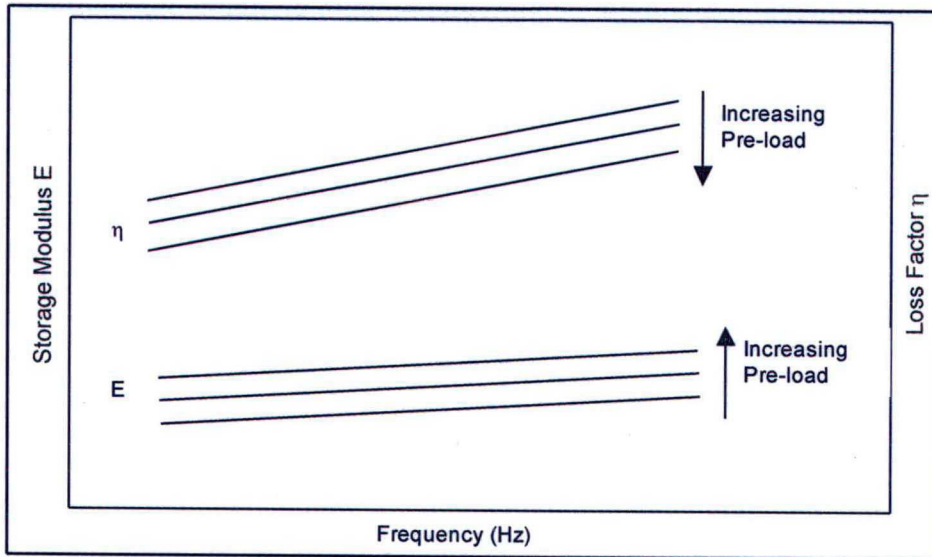


Figure 6.8 – Effects of static pre-load on the loss factor and storage modulus

This tendency may be less noticeable in constrained layer treatments due to the fact that in these configurations, the most part of the shearing occurs at the nodelines of the vibration mode, where the shim is not supposed to be under pressure and the stiffness of the viscoelastic material is not so strongly affected.

Figure 6.9 shows the variation of the brake system resonance frequency as a function of temperature, for the lining pressure of  $20.7\text{N/m}^2$  (300Psi). As expected, the resonance frequency decreases with the increasing of the system temperature. In practice, the variation in the temperature of the rotor during braking can be even higher, which may explain the variability in the squeal noise frequency usually measured in dynamometer tests.

Figure 6.10 presents some waterfalls and contour plots of the measurements made for the shim configurations, as a function of temperature.

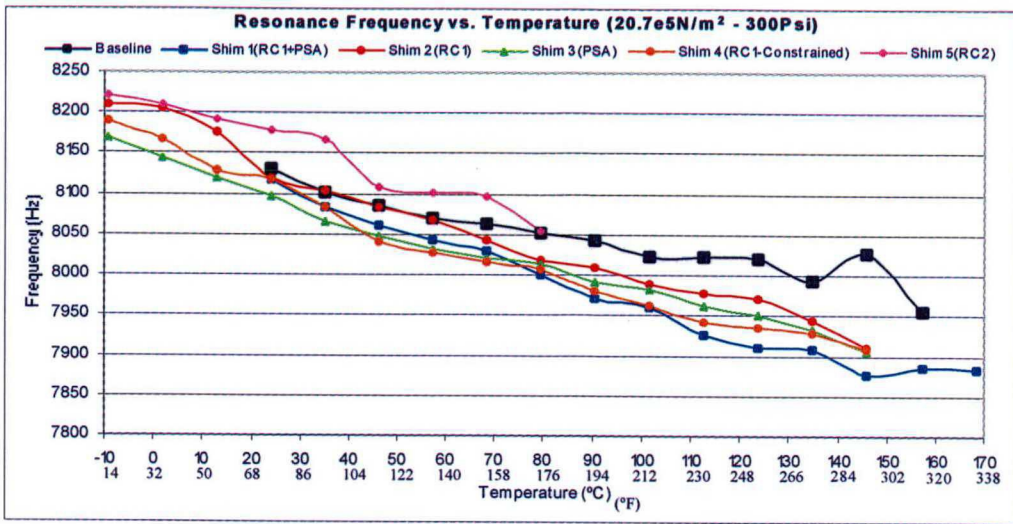


Figure 6.9 - Brake system resonance frequency vs. temperature

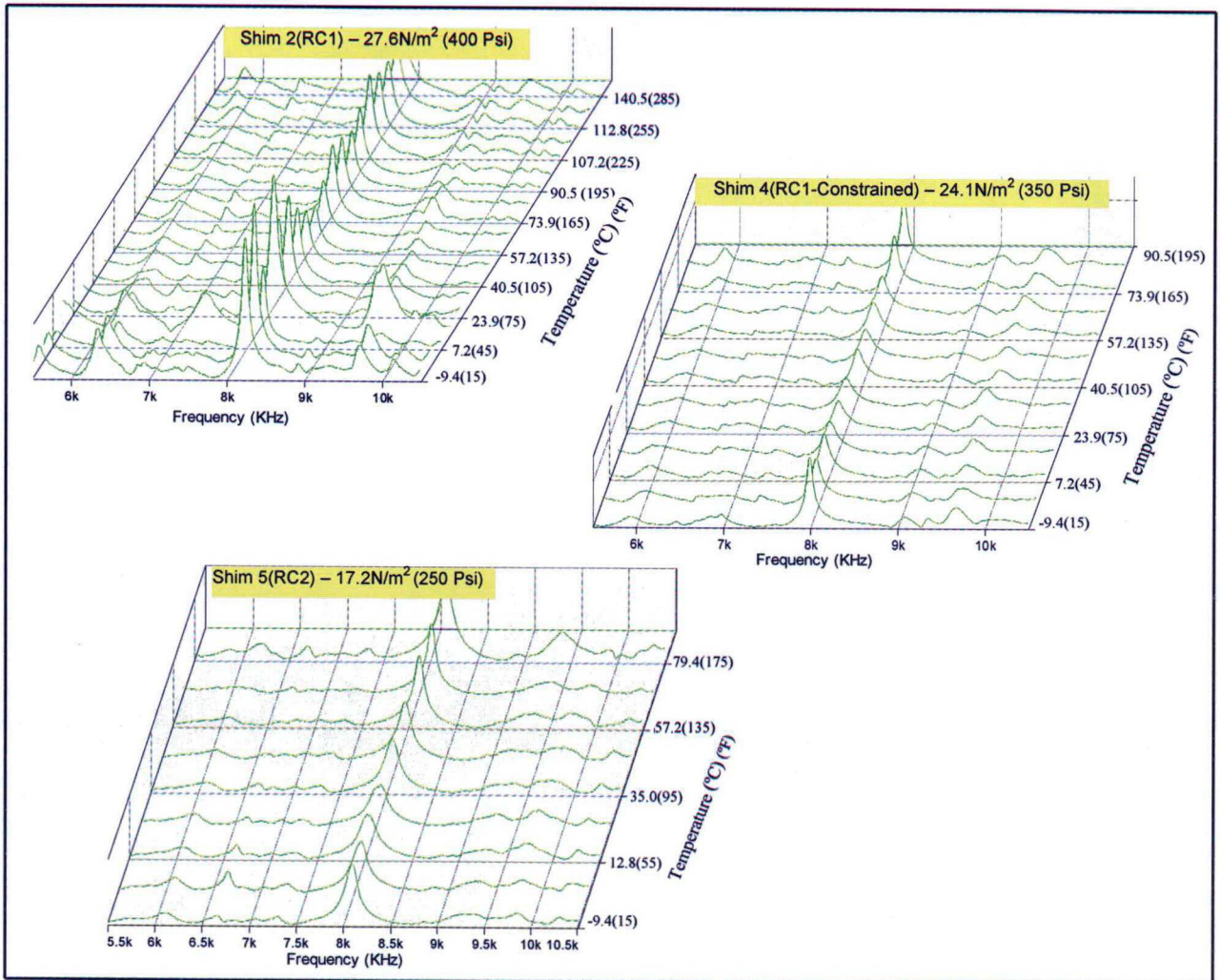


Figure 6.10 – Waterfall and contour plot of FRFs for the shim configurations

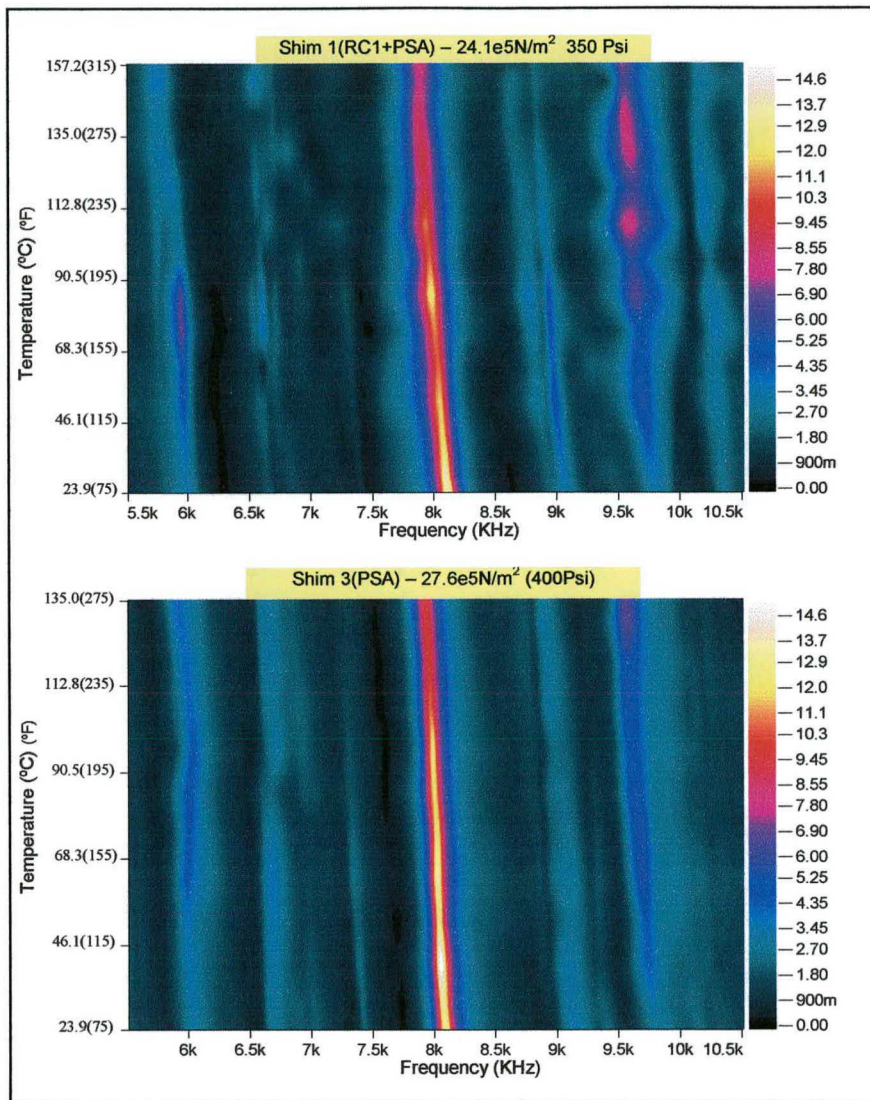


Figure 6.10 - Continued

## 6.2 ANALYTICAL MODEL

As formerly discussed, for the rubber coat treatments, the temperature at which the system loss factor reaches its maximum value is not only related to the material behavior, as a function of temperature and frequency, as depicted in the material nomograms. It also depends on the dynamic parameters of pad, rotor, caliper and the rubber coat layer. The highest system loss factor is reached for a specific combination of the dynamic properties of the brake components and the loss factor and stiffness of the rubber coat layer.

This dependency is demonstrated here through a 2 degrees-of-freedom model, relating the dynamic properties of rotor, pad, caliper and rubber coat. The dynamics of a brake system is very complex to be described by a 2DOF model and it is not the purpose of this model to predict the loss factor of the system. Nevertheless, this model allows another way to visualize the damping mechanism of rubber coats, as well as the influence of the dynamic properties of the elastomers and the modal parameters of the brake components. Hence, the model was used in some parametric analysis, where the influence of model parameters, such as stiffness and thickness of the rubber coat and stiffness of the caliper, were evaluated. The 2DOF model is depicted in Figure 6.11.

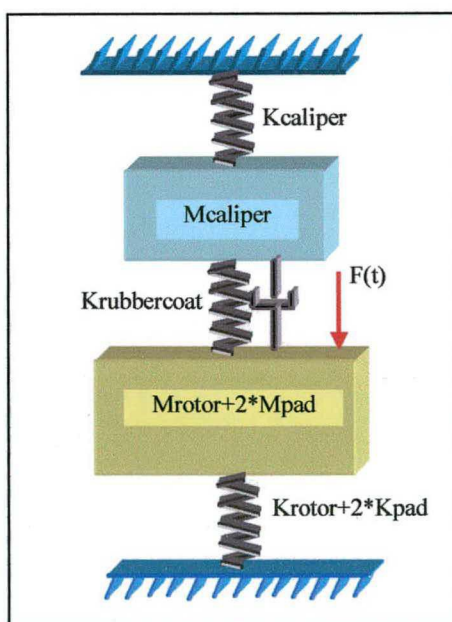


Figure 6.11 – 2 degrees-of-freedom model

Rotor and pads were modeled as one spring/mass system, since the modal coupling condition was considered (stiffness of rotor and pad in parallel). Hence, rotor and pads vibrate in-phase in the same deformation pattern. The rubber coat layer was modeled as a massless spring with a complex Young's modulus, being compressed and relaxed along its length (rubber coat thickness).

The stiffnesses of pads, rotor and rubber coat were modeled by the complex modulus approach, where the relation between the Young's modulus and damping was carried over the frequency domain by replacing the real Young's modulus with the corresponding complex modulus.

Since the rubber coat layer was modeled as a spring being compressed and extended, its stiffness was given by:

$$K_{RC} = \frac{E \cdot A}{t} \quad (6.2)$$

where

$K_{RC}$  is the rubber coat stiffness;

$E$  is the Young's modulus of the rubber coat material;

$A$  is the area of the rubber coat under the caliper;

$t$  is the thickness of the rubber coat layer;

The Young's modulus was set in the model calculations as three times the shear modulus, equivalent to a Poisson coefficient equal to 0.5. The area of rubber coat compressed under the caliper was measured to be about  $25.1\text{cm}^2$  ( $3.9\text{in}^2$ ), as shown in Figure 6.12. The RC1 thickness, given in Table 1.1, was  $0.102\text{mm}$  ( $0.004\text{in}$ ).



Figure 6.12 – Area of rubber coat in contact with caliper fingers

It was also necessary to define the boundary conditions for the brake components. At first, one could consider the rubber coat spring as fixed to ground. In this case, the caliper would be considered rigid compared to the rubber coat and other brake components stiffnesses. The rubber coat would be compressed and relaxed between a vibrating system (rotor + pads) and a static surface (caliper). However, as formerly discussed, the dynamics of the caliper also play a role in the deformation of the rubber coat and, as a consequence, in the system modal damping. When pressure is applied to the system, in a static condition, the caliper body will stretch longitudinally and the caliper fingers will be submitted to some deformation, as cantilever beams. This is due to the fact that, in practice, the caliper is not entirely rigid when compared to the rubber coat and the other brake components. Therefore, the longitudinal stretching of the caliper body and the fingers deformation as cantilevers give the spring stiffness to be considered for the caliper.

The corner was considered rigid compared to the brake components, i.e., no vibration energy was transferred to the fixture. Therefore, the springs representing the rotor/pads and caliper were connected to ground.

The dynamic equations of the model are developed in Appendix 2. The shortcoming of this model was the determination of the modal parameters of rotor, pad and caliper. In such complex systems, it is not feasible to apply a static force in order to measure the static deformation (in this case, the deformation equivalent to the mode shape under study for each component), and, as consequence, the stiffness. This can be overcome by employing data from the point frequency response of the system components. The system compliance (ratio between displacement and force) was first determined from existing data of the modal analyses. The second step was the determination of the amplification factor  $Q$  (inverse of the loss factor), i.e., the ratio of the dynamic to static displacement, as shown in Figure 6.13. From these values, the component modal spring constant and subsequently modal mass could be determined.

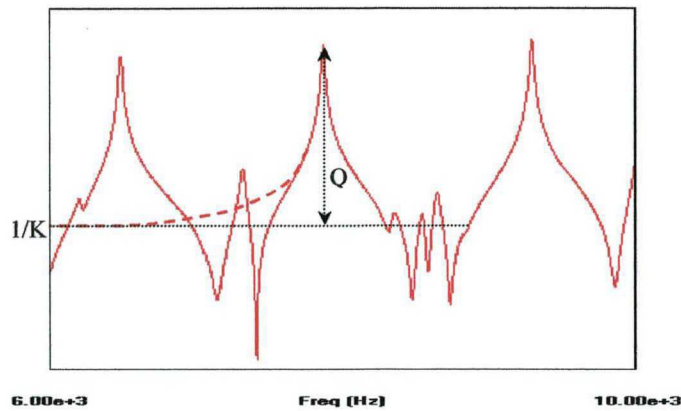


Figure 6.13 – Determination of component modal parameters

For instance, for the rotor, the modal parameters were determined as follows:

$f = 7856\text{Hz}$	FRF Compliance (Displacement/Force) = $4.274\text{e-}8\text{m/N}$	
Loss factor $\eta_{\text{rotor}} = \mathbf{0.00344}$	$Q = 1/\eta = 290.7$	
Modal Stiffness $K_{\text{rotor}} = Q/\text{FRF Compliance} = 290.7 / 4.274\text{e-}8$		<b><math>K_{\text{rotor}} = 6.8\text{e}9 \text{ N/m}</math></b>
Modal Mass $M_{\text{rotor}} = K_{\text{rotor}} / (2.\pi.f)^2$		<b><math>M_{\text{rotor}} = 2.786\text{Kg}</math></b>

The modal parameters for the pads were:

Modal stiffness	<b><math>K_{\text{pad}} = 6.39\text{e}8 \text{ N/m}</math></b>
Modal mass	<b><math>M_{\text{pad}} = 0.369\text{Kg}</math></b>
Loss factor	<b><math>\eta_{\text{pad}} = 0.0143</math></b>

As aforementioned, the stiffness to be considered for the caliper is that related to the stretching of the caliper body and deformation of the fingers as in-phase cantilever beams. The mode shape of the caliper at 10.26KHz was found to be the best approach to this condition. This leads us to consider that, under a static condition, the caliper will deform in the pattern referred to this mode shape, i.e., this will be the caliper spring acting to compress/relax the rubber coat layer. In this way, the averaged values (for three measurements) of the modal parameters for the caliper were found to be:

Modal stiffness	<b><math>K_{\text{caliper}} = 4.725\text{e}9 \text{ N/m}</math></b>
Modal mass	<b><math>M_{\text{caliper}} = 1.225\text{Kg}</math></b>
Loss factor	<b><math>\eta_{\text{caliper}} = 0.0206</math></b>



A routine was written in the software MATLAB in order to plot the frequency response Rotor+Pad Acceleration / Force and calculate the respective loss factor. This is presented in Appendix 2.

The stiffness of rotor and pad were adjusted such that both components had the same resonance of 8100Hz. This procedure aimed to put rotor and pad into the condition of modal coupling, since one is interested in the system behavior after the modal coupling. The rotor stiffness had an increment of about 6%, from 6.9e9 to 7.21e9N/m, while the pad stiffness was increased from 6.39e8 to 9.58e8N/m. This is in agreement with the experimental tests, which had shown an increment ratio in the pad stiffness higher than that for the rotor, as a function of the lining pressure. Table 6.1 presents the loss factor and shear modulus used to simulate the material RC1. The values were extracted from the nomogram of RC1, presented in Chapter 3. The loss factor vs. system temperature was calculated, for the 2DOF model, as a function of the Young's modulus and loss factor of the rubber coat. These dynamic properties varied with temperature and the results are shown in Figure 6.14.

Table 6.1 - Loss Factor & Shear Modulus x Temperature for RC1

Loss Factor & Shear Modulus x Temperature for RC1		
Temp. (°C)(°F)	G (N/m <sup>2</sup> ) (Psi)	Loss Factor
4.4 (40)	1.79e8 (2.60E+04)	0.2
15.5 (60)	1.03e8 (1.50E+04)	0.4
26.7 (80)	4.82e7 (7.00E+03)	0.63
32.2 (90)	3.45e7 (5.00E+03)	0.67
37.8 (100)	2.41e7 (3.50E+03)	0.73
43.3 (110)	1.52e7 (2.20E+03)	0.74
48.9 (120)	1.24e7 (1.80E+03)	0.71
54.4 (130)	8.96e6 (1.30E+03)	0.69
60.0 (140)	7.58e6 (1.10E+03)	0.63
65.5 (150)	6.20e6 (9.00E+02)	0.58
71.1 (160)	5.51e6 (8.00E+02)	0.54
82.2 (180)	4.27e6 (6.20E+02)	0.45
93.3 (200)	2.96e6 (4.30E+02)	0.35
104.4 (220)	1.72e6 (2.50E+02)	0.3
115.5 (240)	1.52e6 (2.20E+02)	0.27
126.7 (260)	1.24e6 (1.80E+02)	0.26
137.8 (280)	1.10e6 (1.60E+02)	0.26
148.9 (300)	1.03e6 (1.50E+02)	0.25

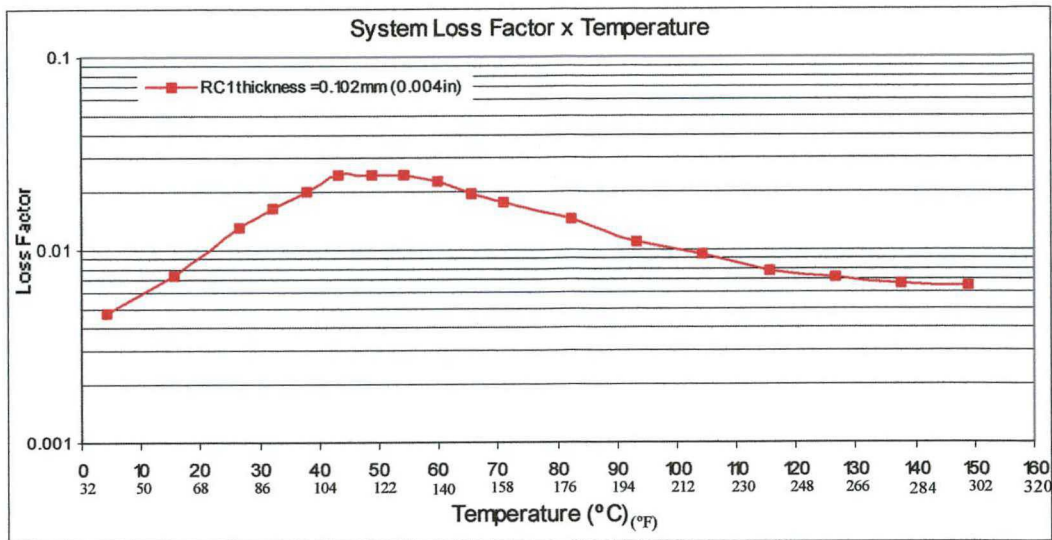


Figure 6.14 – 2DOF model: Loss factor vs. temperature

As previously discussed, the modal parameters of the brake system components also influence on the damping performance of the rubber coat layer. For instance, in a physical sense, if the stiffness of the rubber coat layer is too high, rotor and caliper will vibrate in-phase and no deformation will occur in the rubber coat layer.

On the other hand, decreasing  $K_{rc}$  (which can be achieved by increasing the temperature) may increase the rubber layer deformation, until the stiffness and loss factor become small enough (for temperatures over the transition region) such that the increment in the rubber coat deformation is compensated by the decrease in the loss factor and stiffness.

Therefore, good damping performance of rubber coat layers is not only dependent on the dynamic properties of the elastomer, but also relies on the dynamic properties of the brake components. Nevertheless, the material loss factor still remains as a major determinant of the system damping behavior. Changes in the modal parameters of the brake components, such as the stiffness and mass of caliper, pad or rotor, will change the relative values of the system damping calculated by the 2DOF model. For small variations, the peak will remain around the temperature at which the elastomer loss factor is maximum, according to the nomogram, for the frequency range of interest. For instance, Figure 6.15 compares the results calculated when the modal parameters of the caliper and rotor/pad are varied.

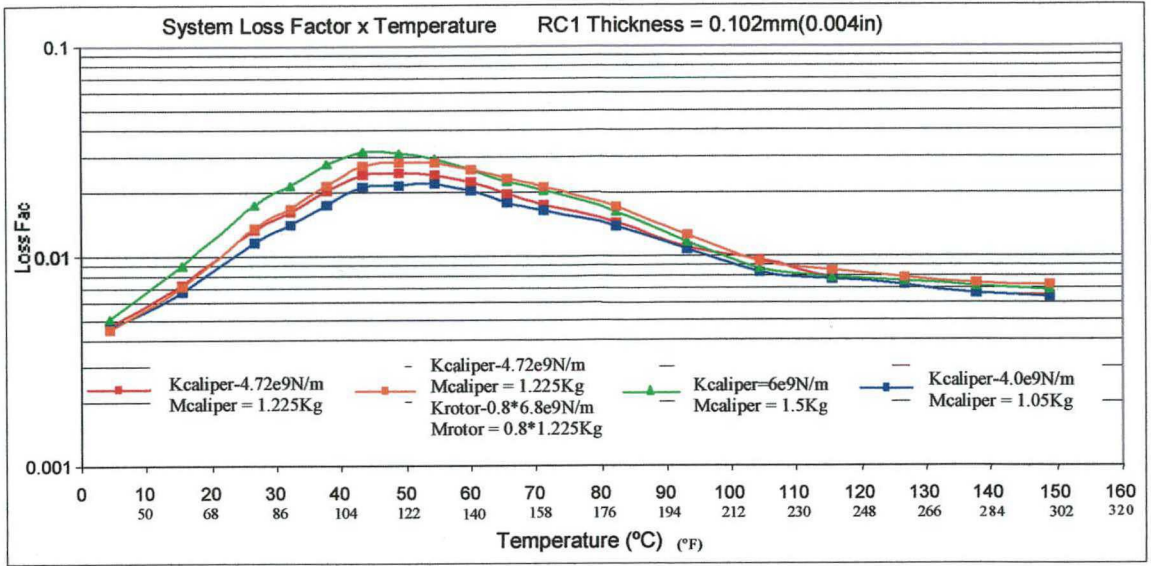


Figure 6.15 – 2DOF model: Loss factor for different values for the modal parameters of the brake components

Figure 6.16 presents an example of the frequency response function calculated by the 2DOF model routine.

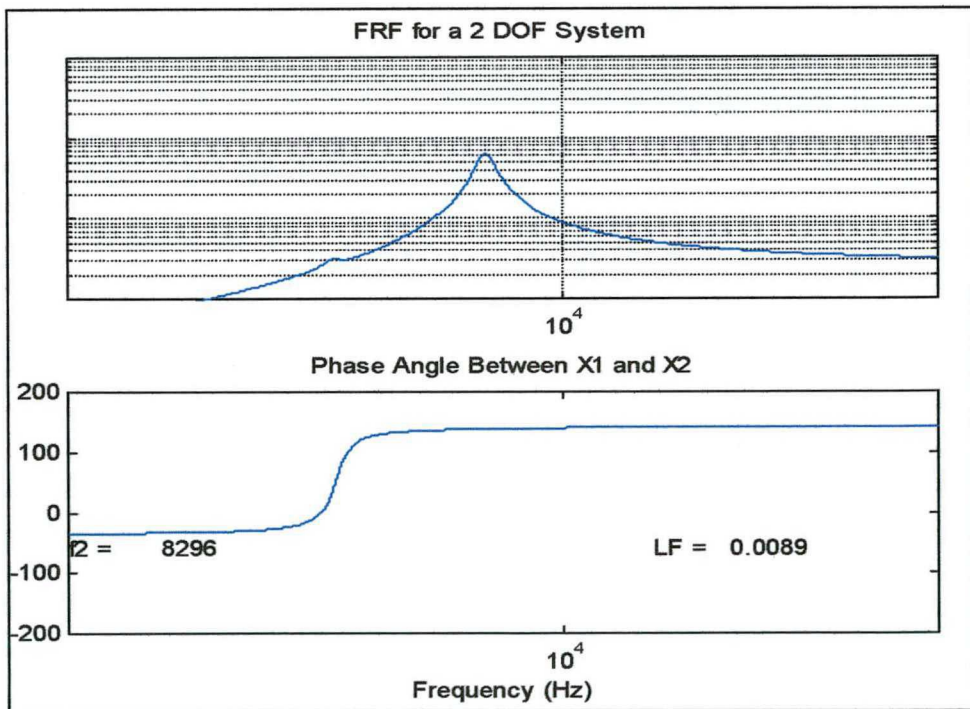


Figure 6.16 – Example of FRF calculated by the 2DOF model

Figure 6.17 presents the loss factors calculated for various thicknesses of the rubber coat layer RC1.

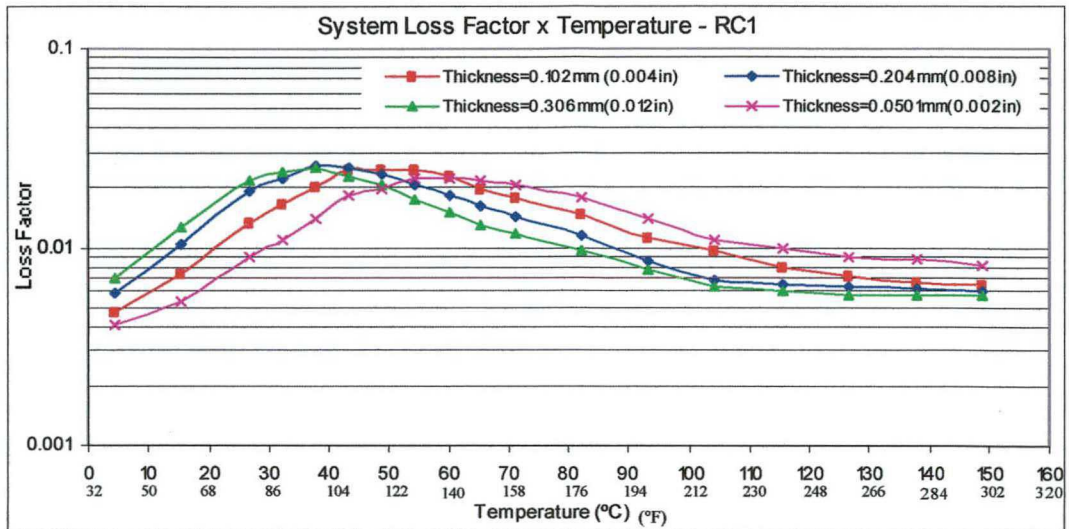


Figure 6.17 – Loss factor vs. temperature for different rubber coat RC1 thicknesses

It is interesting to observe the change in temperature for the respective peak loss factor. The change in the thickness influences the stiffness of the rubber coat layer. If the thickness is increased, the stiffness decreases and maximum damping will be reached at a lower temperature. Once again, it is important to point out the frequency-temperature superposition principle. In this case, the tendency of reduction in the temperature of the peak could also be predicted considering the values of the Young's modulus vs. temperature. Doubling the thickness of the rubber coat layer is equivalent to dividing its stiffness by two. Therefore, the peak tends to be displaced to the temperature at which the Young's modulus is half of its former value.

For instance, consider in Figure 6.17 the temperature at which the loss factor is maximum for an RC1 layer of 0.102mm(0.004in) thickness, i.e., approximately 46°C (115°F). The equivalent value for the shear modulus (or the Young's modulus) is then found in the material nomogram, in Chapter 3, for the temperature above calculated and for a frequency around 8000Hz. Looking at the nomogram, one finds the shear modulus of approximately  $1.86e7\text{N/m}^2$  ( $2.7e3\text{Psi}$ ).

A thickness twice the initial value is equivalent to dividing this shear modulus by two. Therefore, for a thickness of 0.204mm(0.008in), the shear modulus should be about  $9.3e6\text{N/m}^2$  ( $1.35e3\text{Psi}$ ).

In the nomogram, the temperature at which the loss factor is maximum, for a shear modulus equal to  $9.3e6N/m^2(1.35e3Psi)$ , is found. This is achieved by drawing a vertical line from the maximum loss factor and a horizontal line from the referred shear modulus. A line parallel to the temperature line is then drawn from where vertical and the horizontal line cross.

Validation of the model can be made by comparing the temperature obtained in the nomogram with that calculated by the model. In this example, according to the nomogram, the temperature was found to be about  $32^{\circ}C(90^{\circ}F)$ , while the temperature calculated by the model was about  $38^{\circ}C(100^{\circ}F)$ . For the RC1 thickness of three times the initial value ( $0.306mm$ ), the temperature at which the loss factor was maximum for a shear modulus equal to  $6.2e6N/m^2(9e2Psi)$  was about  $29^{\circ}C(85^{\circ}F)$ , compared to a temperature of about  $35^{\circ}C(95^{\circ}F)$  for the model.

It is also of interest to consider the hypothetical situation of when the caliper is totally rigid. In this case, according to the 2DOF model (a value for the caliper stiffness dramatically higher than the other components is assumed), the temperature at which the loss factor reaches its maximum is about  $27^{\circ}C(80^{\circ}F)$ . If the caliper is considered rigid, the rubber coat spring can be modeled as a spring in parallel with the rotor+pad spring. In this case, in order for the elastomer to be compressed, its stiffness must be within the same order of magnitude as the system stiffness, i.e., the rubber coat spring must have a value close to that of the rotor+pad spring. If the rubber coat stiffness is too high, the rubber coat layer will not be compressed and all the deformation will be concentrated in the brake components.

In this Chapter, the damping behavior of the assembly brake system was evaluated as a function of temperature and compared with that obtained as a function of pressure, in Chapter 4. Results allowed conclusions about the influence of boundary conditions, like pressure and temperature, on the dynamic behavior of the brake system, with regards to the potential for squeal noise occurrence. The next Chapter discusses the dynamometer results obtained for some of the shim configurations, verifying the data and tendencies obtained with the measurements up to this point.

## CHAPTER 7

### DYNAMOMETER TESTS

Perhaps one of the most important findings of this study is the verification of the performance of the shim configurations via a brake dynamometer. These measurements are significant for the qualitative corroboration of the results and conclusions presented in the preceding chapters. Dynamometer tests allow an approximation to the real behavior of a brake system in practice.

As already described in Chapter 4, an inertia dynamometer was used for the screening of this brake system. The inertia dynamometer allowed the control of parameters such as rotation, braking pressure and temperature, while recording the sound pressure level and frequency of noise occurrences. The disc rotation is achieved by electric motors connected to a shaft with inertial wheels, simulating the inertia effects of the vehicle. Figure 7.1 presents some pictures of the brake system assembled in the dynamometer.

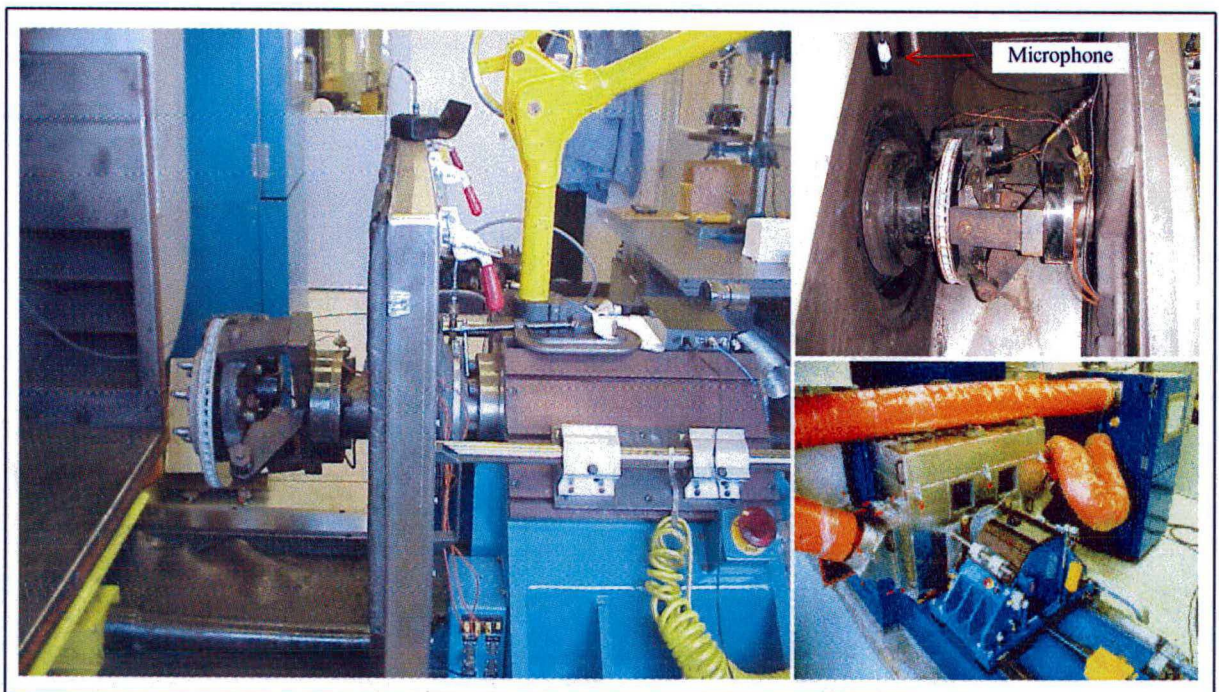


Figure 7.1 – Inertia dynamometer

Measurements were taken for shim temperatures in the range between 25 and 225°C. The temperature of the shims is lower compared to the temperature of the friction material: during the measurements, the difference in temperature was as much as 120°C (for instance, temperature of the friction material around 310°C and temperature of the shim around 200°C). The braking pressure varied from  $5 \times 10^5$  to  $40 \times 10^5 \text{ N/m}^2$  (5 to 40 bar). The acquisition system stored the data of the brake events in blocks with the same temperature and pressure conditions.

Each brake event lasted approximately 10 seconds. During this period, data was collected for a certain number of autospectra of the microphone signal. The number of autospectrum curves collected is a function of the sampling frequency established for the measurements. The Sound Pressure Level (SPL) indicated in each brake event is the maximum value measured among all autospectra. For instance, if 50 autospectra were measured during the brake event, the system selected the autospectrum containing the highest peak (SPL), also indicating the corresponding frequency of the maximum SPL on the selected autospectrum.

The shortcoming is that no information is obtained regarding to the duration of the squeal noise event. Therefore, for instance, a 5 second squeal event is weighted as the same as a 0.1 seconds squeal event. Obviously, the driver/passenger perception of such squeal events will be quite different.

Figure 7.2 gives the results obtained for the Baseline, i.e., pads without any damping treatment. The dynamometer results present some scattering of the squeal frequency. This may be explained by the strong influence of the boundary conditions, especially temperature and braking pressure, on the dynamics of the brake components. It must also be kept in mind that during braking, the temperature of the rotor surface is much higher than the temperature of the pad back plate and shim. Therefore, the system damping behavior should be analyzed considering the pad back plate and shim temperature, but rotor temperature strongly influences the squeal noise frequency. In Chapter 6, measurements were taken for the whole brake system at constant temperatures. The system damping must be analyzed considering these temperatures, although, in practice, the system mode frequency may be lower, since the rotor temperature is usually much higher than the shim temperature.

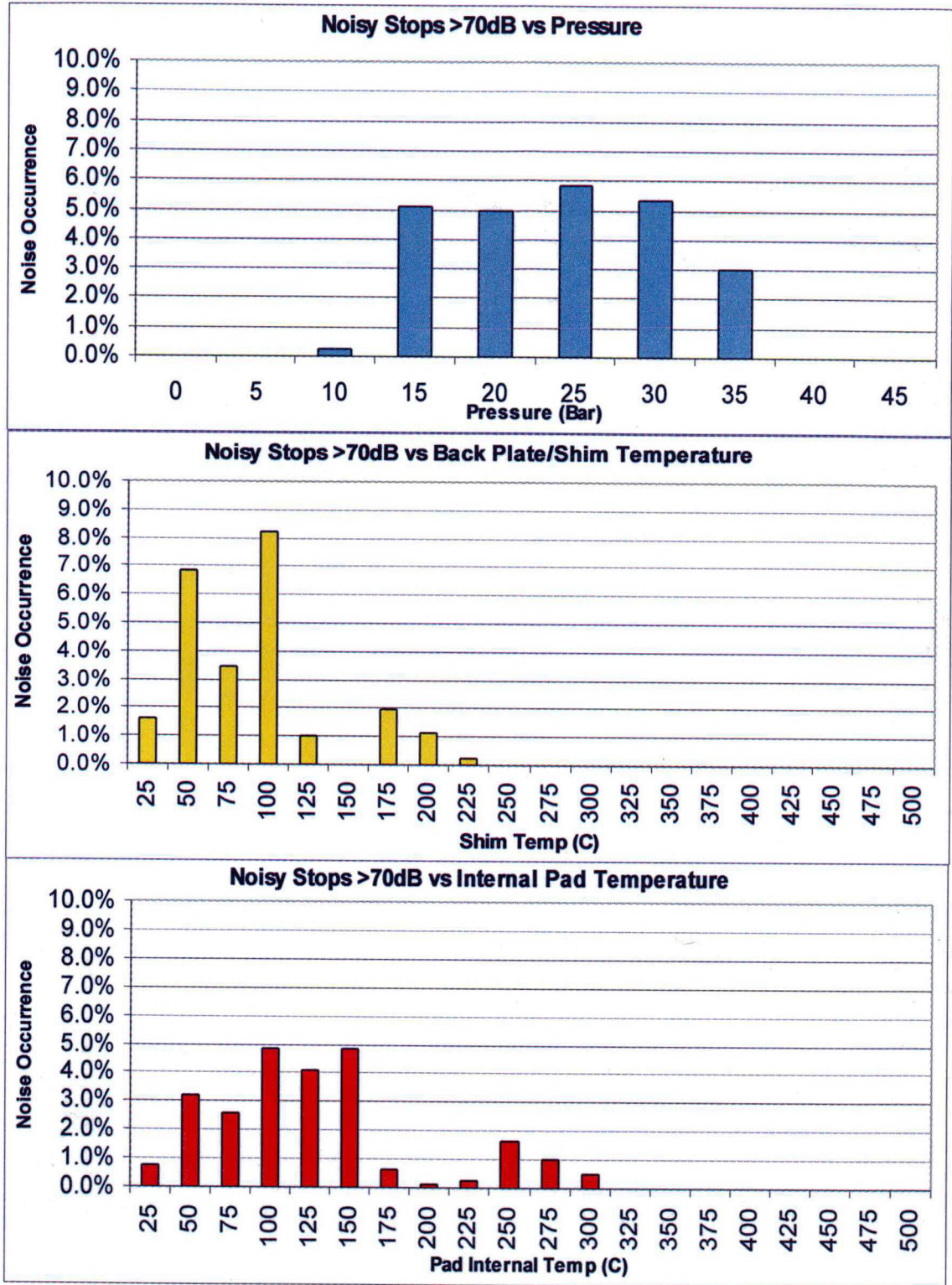


Figure 7.2 – Dynamometer results for Baseline



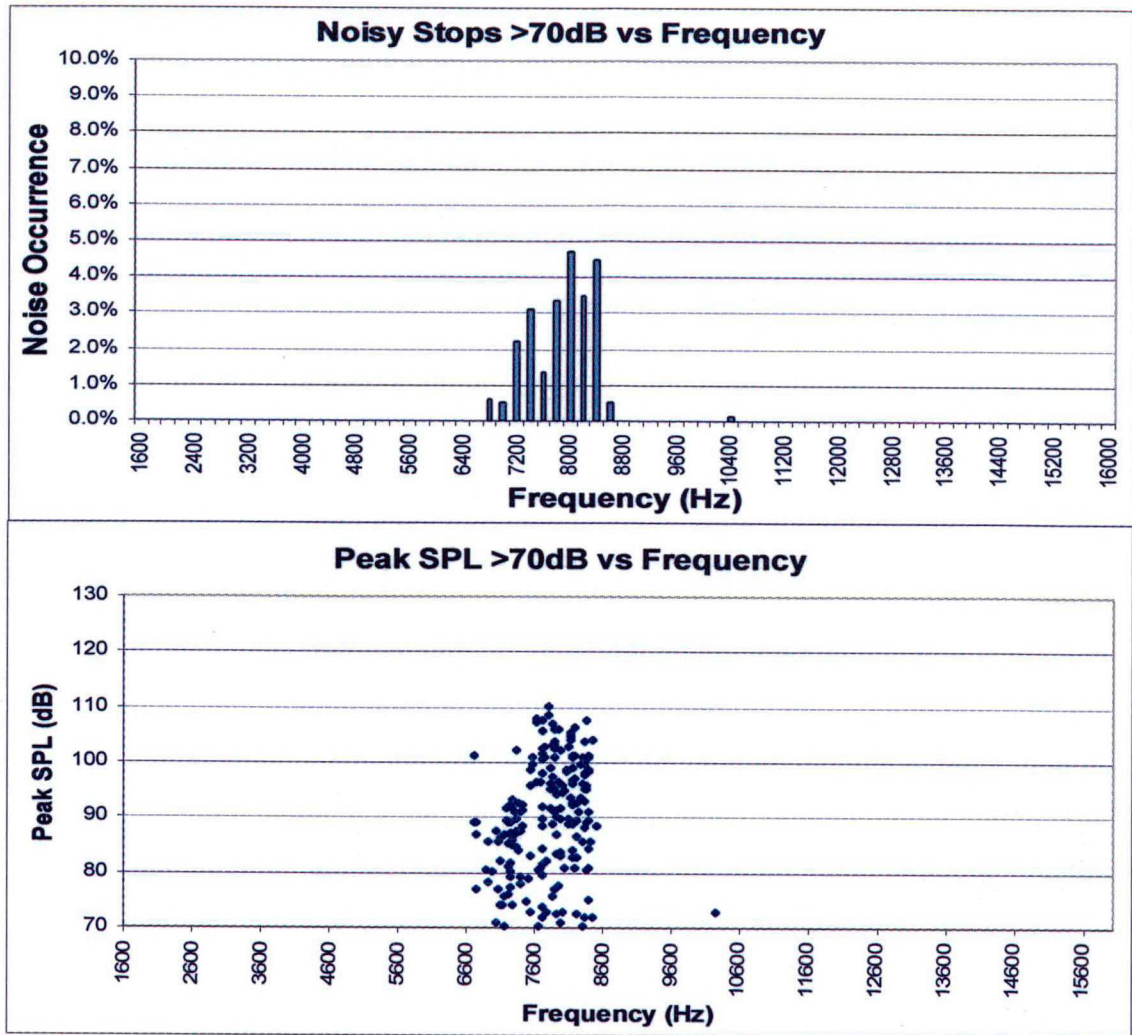
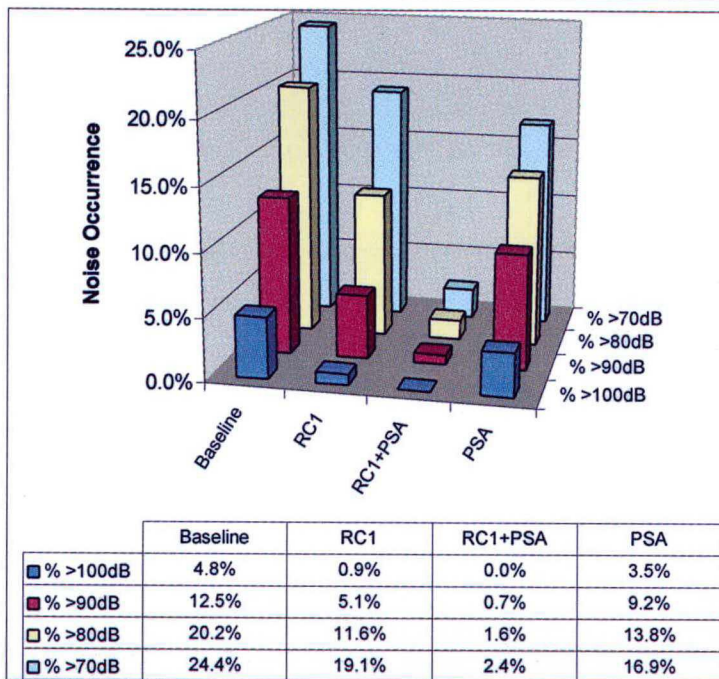


Figure 7.2 - Continued

Dynamometer tests were also made for pads with the shim configurations 1, 2 and 3 (RC1+PSA, RC1 and PSA, respectively). The results are summarized in Table 7.1.

Table 7.1 – Summary of the dynamometer results for the shim configurations

Shim Configuration	Baseline	Shim 1 (RC1+PSA)	Shim 2 (RC1)	Shim 3 (PSA)
Minimum Frequency (Hz)	1600	1600	1600	1600
Maximum Frequency (Hz)	16000	16000	16000	16000
SPL Minimum Threshold (dB)	70	70	70	70
Max. dB	110.1	98.5	105.0	118.4
Total Stops	806	807	807	807
>70 dB	197	19	154	136
>80 dB	163	13	94	111
>90 dB	101	6	41	74
>100 dB	39	0	7	28
%>70 dB	24.4%	2.4%	19.1%	16.9%
%>80 dB	20.2%	1.6%	11.6%	13.8%
%>90 dB	12.5%	0.7%	5.1%	9.2%
%>100dB	4.8%	0.0%	0.9%	3.5%
Top Noise Frequency - KHz (% Noisy stops)				
1	8 (4.7%)	7.4 (0.6%)	7.4 (4.2%)	7.4 (4.2%)
2	8.4 (4.4%)	7.6 (0.4%)	7.2 (3.9%)	8.4 (3.3%)
3	8.2 (3.4%)	7.8 (0.3%)	7.8 (3.3%)	7.8 (2.3%)
4	7.8 (3.3%)	8.0 (0.2%)	8 (1.7%)	8.6 (1.6%)



Results of the dynamometer tests indicate that, when the shims were applied to the pads, the percentage of noise occurrences was reduced, as a consequence of the increase in the modal damping of the unstable mode responsible for the squeal noise. Obviously, this rate varied with the different shim configurations. Figures 7.3, 7.4 and 7.5 present the graphs of noisy stops, for each shim configuration under analysis, as a

function of temperature, pressure and frequency. These graphs give a rough indication regarding the temperature range at which each shim configuration works best.

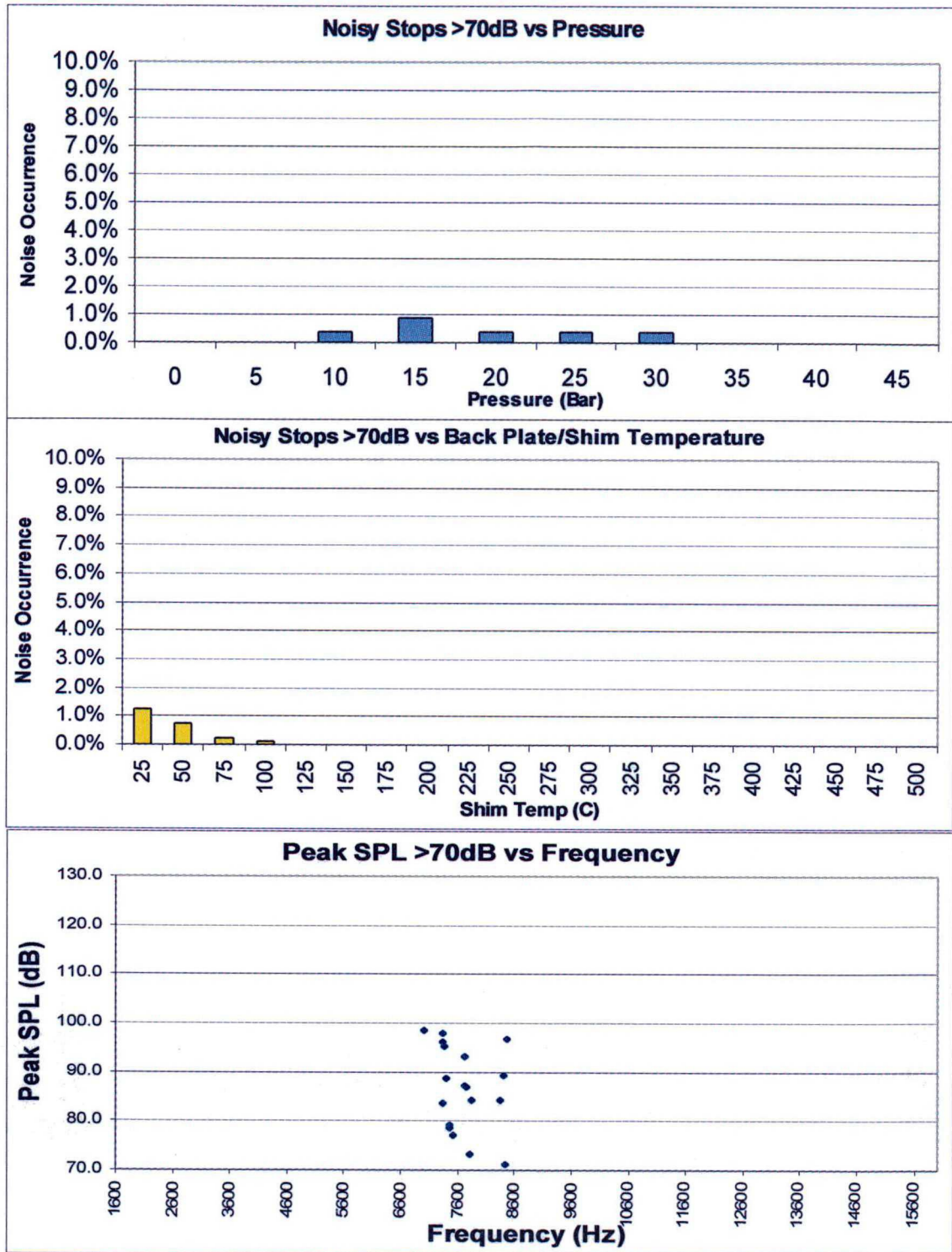


Figure 7.3 – Dynamometer results for Shim 1 (RC1+PSA)

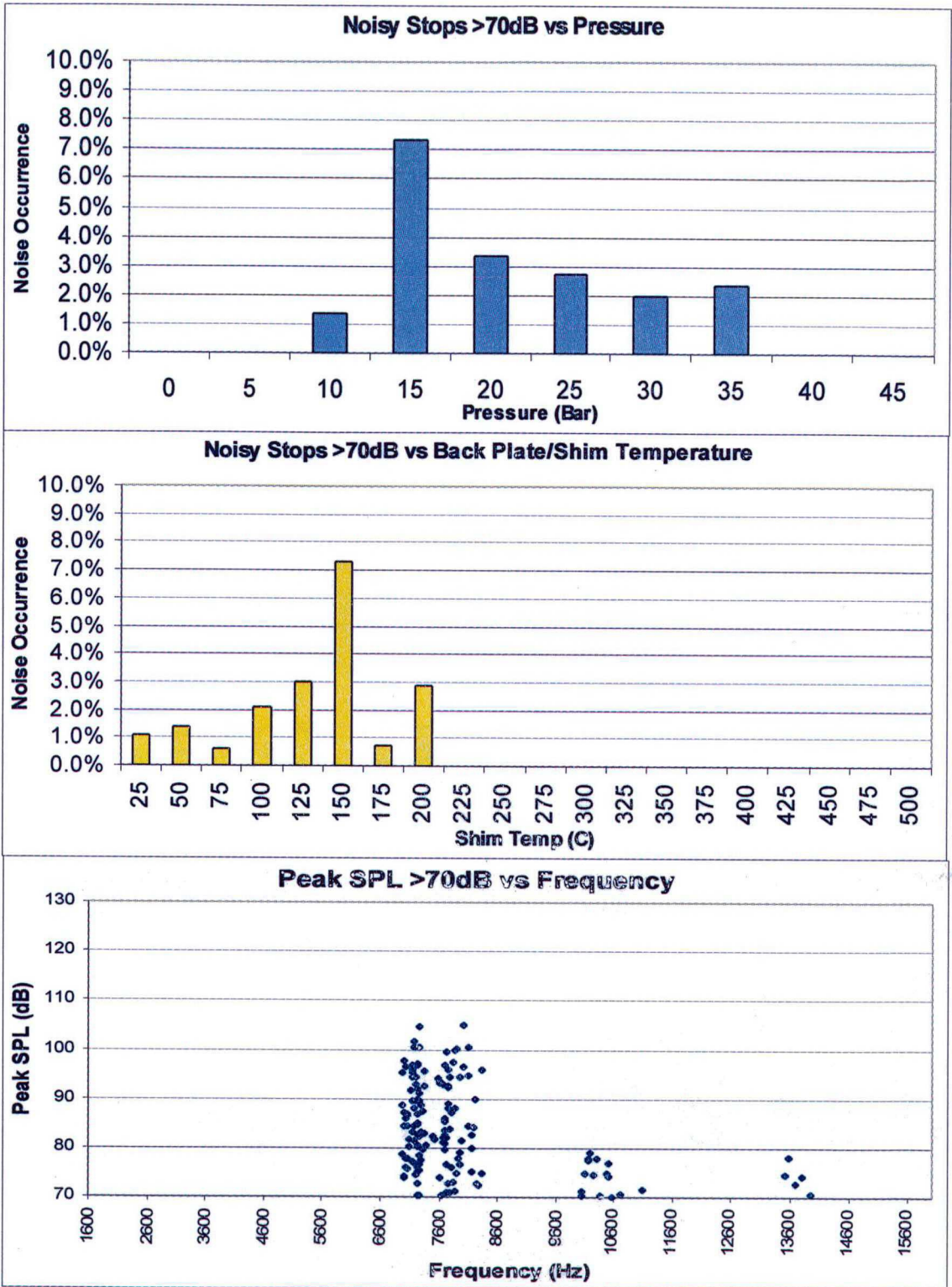


Figure 7.4 – Dynamometer results for Shim 2 (RC1)

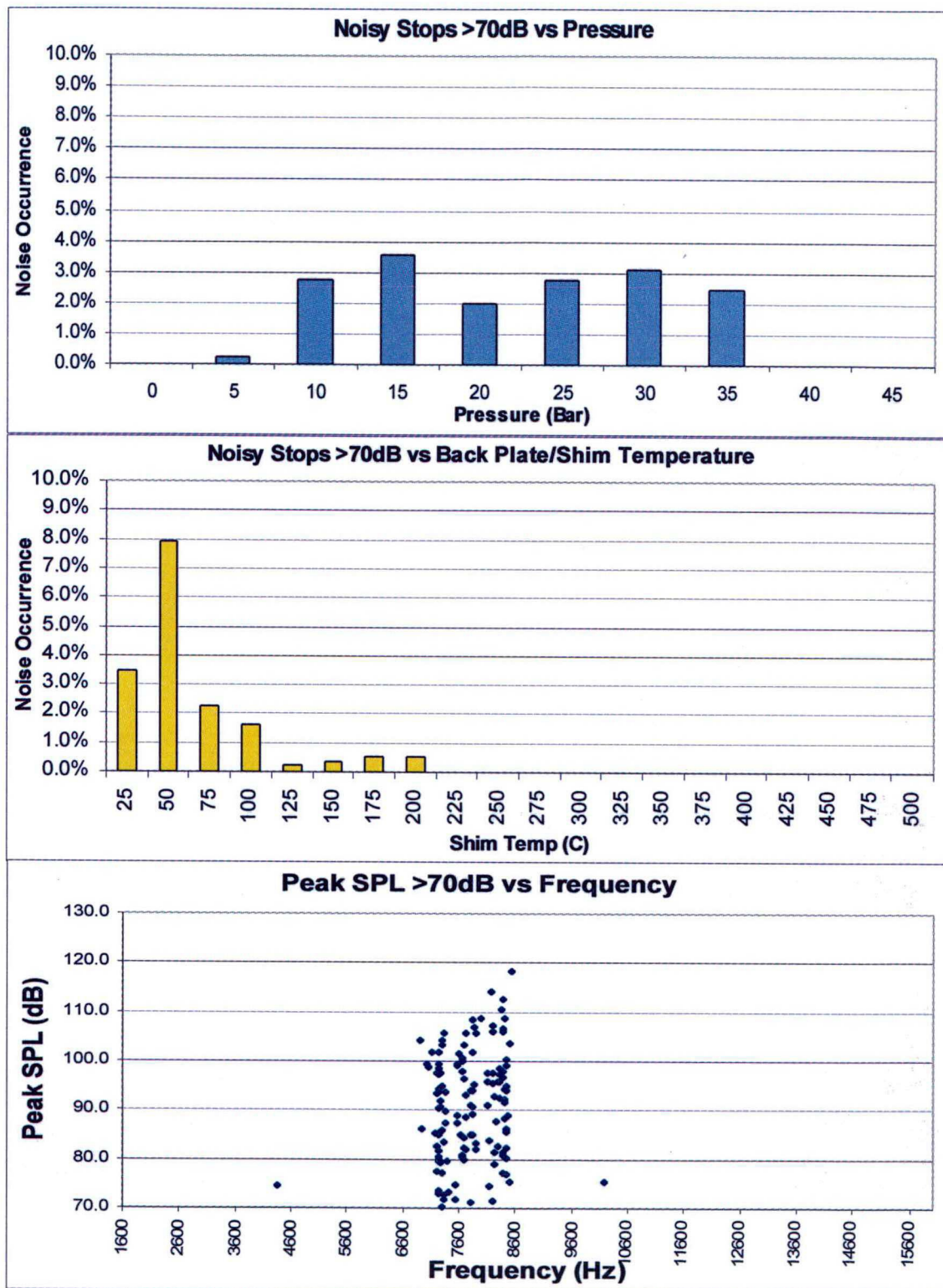


Figure 7.5 – Dynamometer results for Shim 3 (PSA)

Note the difference in best performance temperature between the Shims 2 and 3 (RC1 and PSA, respectively). Based on data from Table 1 and Figures 7.3 and 7.5, one can verify that there was a tendency of the noise occurrences for the RC1 shim to occur at lower frequencies compared to the PSA. One of the reasons here assumed is that, as already discussed, for Shim 2 (RC1 as a coating layer) the best performance was at lower temperatures when compared to Shim 3 (PSA as a constrained layer). Therefore, the noise occurrences for the RC1 shim tended to be at higher temperatures, where the damping performance of the viscoelastic material was not so effective, and, as a consequence of these higher temperatures, the resonance frequencies of the brake system decreased.

When comparing performances between Shims 2 and 3, one must observe that, for this brake system, squeal noise is mostly a low temperature issue. As Figure 7.2 shows, the majority of squeal occurrences for the baseline was for shim temperatures (or backplate temperature, since the Baseline is being considered) below 100°C. This is the temperature range at which Shim 2 has its maximum loss factor, while Shim 3 is more effective in higher temperatures. Nevertheless, Shim 3 still presented a lower percentage of noise occurrences when compared to Shim 2, indicating the effectiveness of the constrained layer configuration compared to the damping mechanism due to compression/relaxation along the elastomer thickness.

The results for Shim 2 also indicated some noise occurrences in other frequency ranges, especially between 10100 and 10500Hz. The analysis of the entire brake data for Shim 2 had shown that the noisy stop events for this frequency range occurred mostly at temperatures above 100°C, with maximum Sound Pressure Levels among the lowest ones measured. For instance, the highest SPL for a noisy stop in this frequency range was 77.9dB. The occurrence of squeal noise in such frequency ranges indicates that other system modes may also become unstable under specific boundary conditions. The 4<sup>th</sup> bending mode of the pad (9961Hz) may couple with the 8<sup>th</sup> or 9<sup>th</sup> bending mode of the rotor. Some inferences could also be made about the coupling involving a caliper mode, since this component presented some resonances at the frequency range under study.

It was formerly mentioned that the dynamometer results took into account as a noise occurrence all the stop events for which the Sound Pressure Level was more than 70dB at some instant, regardless of how long the squeal noise lasted. In order to gain some insight into this issue, another microphone was installed into the dynamometer chamber and the autospectra were measured, for several brake events. The frequency range measured

was from 0 to 12800Hz, with a frequency resolution of 4Hz (3200 lines). Therefore, the total sample time of each autospectrum was 0.25 seconds (resolution of  $3.05e-5$  seconds). Considering that the braking events last for approximately 10 seconds, 40 autospectrums were measured for each event. Figure 7.6 presents a sample collection of graphs and waterfalls of the measurements, including the sound pressure in the time and frequency domain, during squeal noise occurrence and also for braking events without squeal noise.

It becomes apparent that the squeal noise always occurs in discrete tones, indicating the influence of the modal coupling phenomenon on the squeal generation mechanism. From the first two waterfalls (autospectra measured before and during the braking event), it is interesting to note how the braking event cleared the signal for frequencies above 4000Hz. Note also that the signal increased at the frequency range around 8000Hz, although the SPL remained below 70dB. This phenomenon can also be observed in one of the waterfalls for the Shim 1 (RC1+PSA), where there is a clear peak of 63.1dB at 8116Hz.

The frequency at which squeal noise occurs can also vary, either increasing or decreasing, as can be seen in some of the waterfalls for the Shim 3 and Shim 1.

The analysis of the microphone signal during the braking event showed how the squeal noise phenomenon in a brake system can change in terms of time duration, amplitude and frequency range, although the discrete tone characteristic of the squeal noise reinforces the hypothesis of the interaction between the excitation mechanism and the modal parameters of the brake system. The variability in the time duration, sometimes lasting for the whole brake event and sometimes just for few tenths of a second, suggests the possibility, in the future, of improvement in the criteria to compare the performance of different shim configurations.

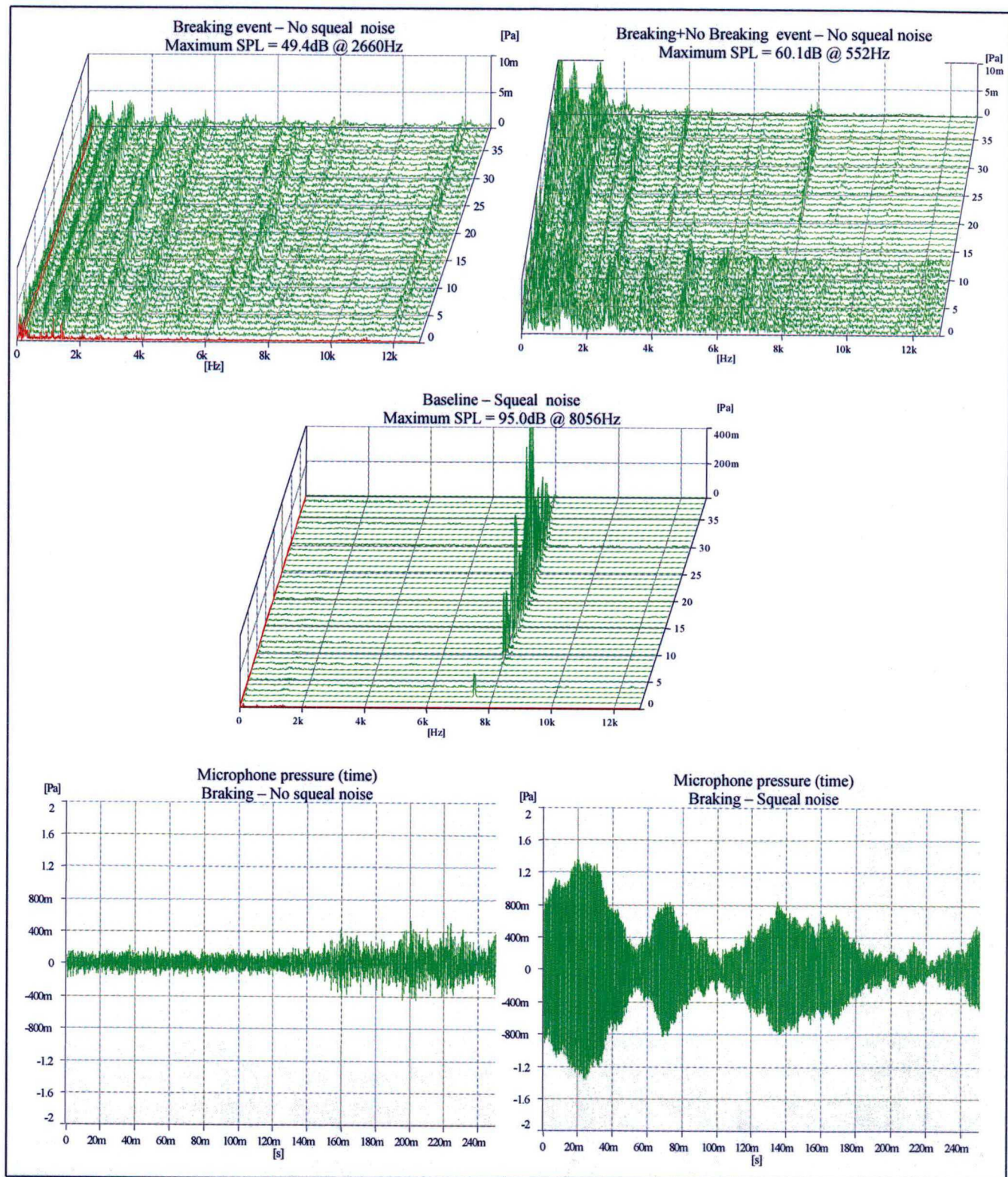


Figure 7.6 – Graphs and waterfalls of the dynamometer tests measured under the conditions of squeal noise and quiet system



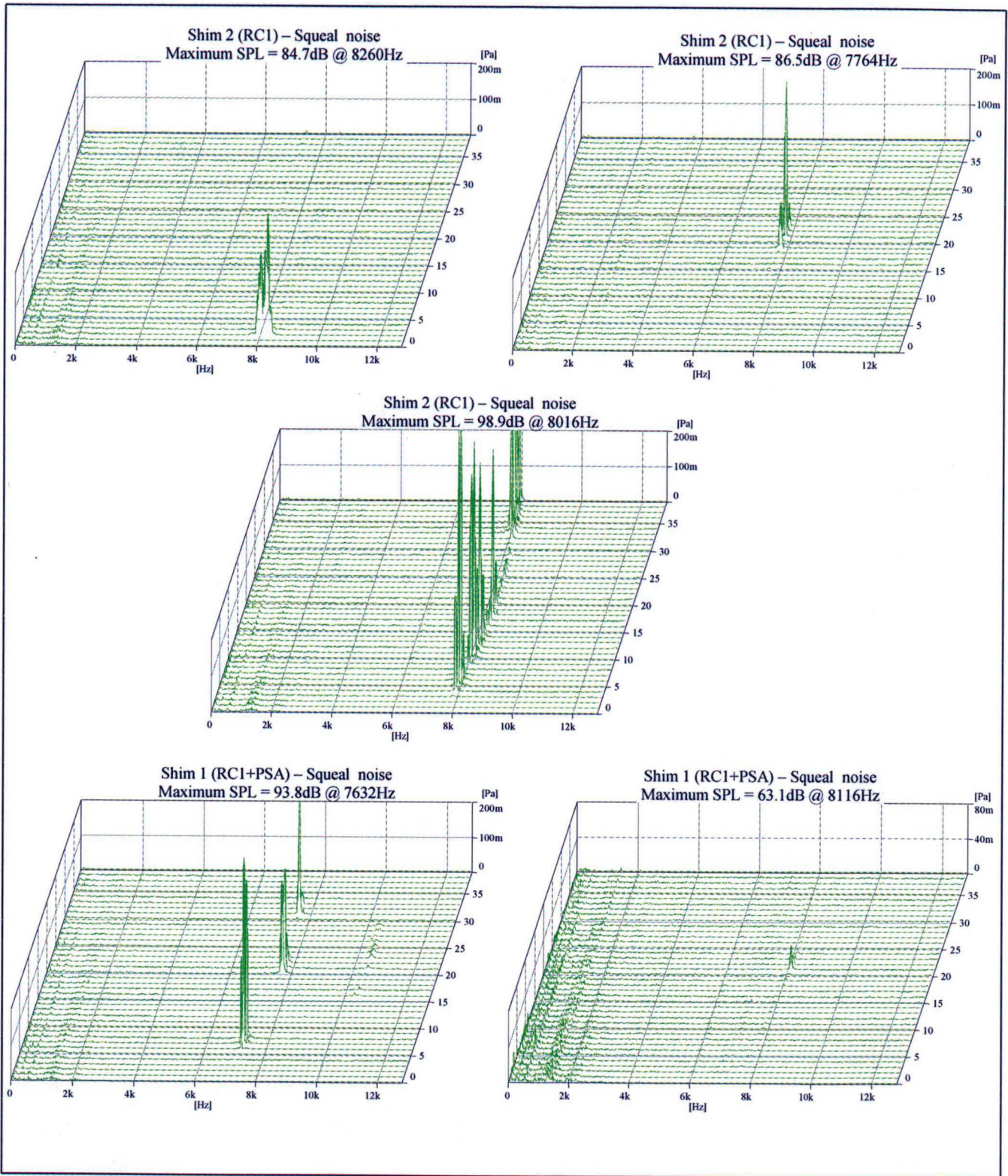


Figure 7.6 - Continued

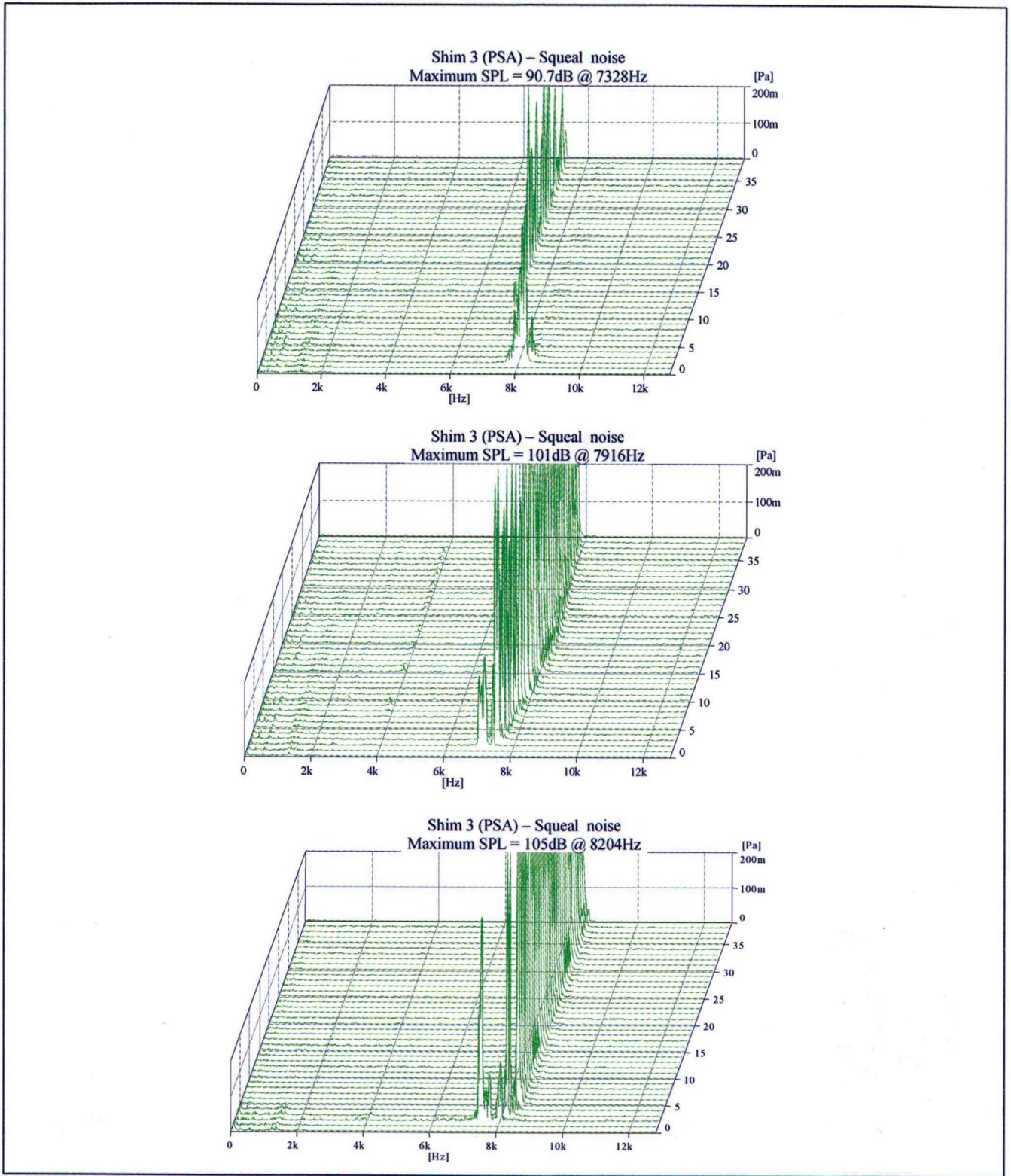


Figure 7.6 - Continued

### CONCLUSIONS AND RECOMMENDATIONS

The main purpose of this research was the analysis of the influence of elastomer coatings on the performance of brake shims. In order to achieve this, a series of techniques were applied, improved and developed to gain insight into the squeal noise mechanism and to quantify the influence of each viscoelastic material, according to the shim configurations.

First, the dynamic properties of the viscoelastic materials used in this thesis were measured and represented in nomograms. This first step was of essential importance, since all the analyses of shim performances relied on the viscoelastic material properties, especially the Young's modulus (and shear modulus) and loss factor.

In Chapter 4, it was seen that the condition of squeal noise occurrence in the brake system under analysis relies on modal coupling between a bending mode of the rotor and a bending mode of the pad. In this case, rotor and pad vibrate in-phase, with the same frequency and close wavelengths for the mode shapes, and the frictional damping is lost. The modal coupling phenomenon and the effects of adding damping to the system were explained in terms of a 2 degrees-of-freedom model. According to this 2-DOF model, adding damping to the system can bring it back to a stable condition, i.e., physically, damping helps to dissipate the energy introduced into the system by the friction between rotor and pads.

In order to pinpoint the potential coupling modes, modal analysis of the individual components was performed. Having determined the potential coupling modes, the performance of the different shims was evaluated in the assembly brake system, under different conditions of pressure and temperature. The system remained in a static condition (no rotation). In this case, although the input energy mechanism was not taken into account, it allowed measurement of the modal loss factor of the system critical mode as function of pressure and temperature. The results indicate that adding shim treatments to the pads could improve the system damping, reducing the propensity for squeal noise occurrence. It is important to point out that the analysis of the system modal loss factor does not allow one to predict whether the squeal noise will or will not occur: A damping treatment may be just partially efficient as the friction characteristics and the dynamic

properties of the system change during the brake event. However, it was shown through frequency response measurements and dynamometer results that there is a direct relation between the system modal damping and the squeal noise occurrence. This relation can be used as an effective means to compare the squeal occurrence potential in a brake system as function of different shims.

Through dynamometer tests, it was verified that squeal noise occurs in discrete tones, indicating the dependence of the coupling modes of the brake components on the determination of the squeal frequency. The dynamometer results also showed some variation in the squeal noise frequency. This was attributed to the strong dependence of the system parameters on the operating boundary conditions of the brake system, especially braking pressure and temperature. This phenomenon was also seen during the system frequency response measurements, where the system resonance varied by about 400 Hz as a function of pressure.

Sound intensity measurements revealed interesting results concerning the characteristics of the system critical mode as a function of lining pressure. During squeal conditions, the anti-nodes of the system mode responsible for the squeal noise (in this case, related to the 7<sup>th</sup> bending mode of the rotor) remained fixed in space, i.e., they no longer rotated, remaining in the same position along the rotor diameter.

The damping mechanism of the rubber coating was found to be the dynamic compression/relaxation of the elastomer through its thickness direction. As expected, the performance of such shim configurations is strongly dependent on the elastomer loss factor as a function of temperature and frequency. However, it was also concluded that the modal parameters of the brake components could influence the damping performance of the rubber coatings. This influence was depicted by a 2 degrees-of-freedom model, where the rubber coat layer was modeled as a spring with a complex stiffness, connecting to subsystems, related to the modal parameters of caliper and rotor+pad. In a physical meaning, if the stiffness of the rubber coat layer is too high, rotor and caliper will vibrate in-phase and no deformation will occur in the rubber coat layer. On the other hand, decreasing its stiffness may increase the rubber layer deformation, to the point where stiffness and loss factor become small enough (for temperatures over the transition region) such that the increase in the rubber coat deformation is compensated by the decrease in the loss factor and stiffness.

Results have shown that the damping of constrained layers is more effective than the other damping mechanisms, such as extensional deformation or the compression/relaxation mechanism of the rubber coatings. However, it is not uncommon for the engineers to be confronted with squeal noise issues over a wide range of temperatures and, sometimes, for different frequencies. In this case, an adequate shim design with viscoelastic materials in constrained layers along with a rubber coating, optimized for different temperature and frequency ranges, could be presented as one of the solutions, not to mention the necessity, sometimes, for additional structural modifications to the brake components.

Many issues concerning squeal noise in brake systems still challenge the engineers. Over the years, much research studies have been carried out attempting to gain insight into the squeal mechanism and solutions have been proposed. The field is still open and many questions are not yet answered. During the period of this research, some issues came to light that could turn into new research areas of the utmost importance for the understanding and solution of squeal noise.

- The techniques applied in this thesis for the measurement of the system loss factor did not take into account the excitation mechanism. In order to improve such a technique, one suggestion would be the development of a setup involving a feedback between the amplitude of vibration and the excitation force. In such a setup, the self-excitation phenomenon could be studied in a more realistic situation;
- Analysis of the mode-locking phenomenon in-loco. Some tools that could be used for this are sound intensity and the laser vibrometer. One shortcoming is that such measurements rely basically on stationary excitations. Squeal noise lasts for a few seconds and one must guarantee the repeatability of the squeal occurrence, especially in terms of frequency. This is a difficult task, since temperature plays an important role in the squeal frequency variation. The literature [40] suggests some techniques to suppress this problem, like utilizing the ratio of the response signal to some reference signal, for instance, surface velocity. In this case, the squeal noise level is considered proportional to the velocity of vibration of the component. Furthermore, it is reasonable to suppose that this reference signal should be captured on the surface of a component directly responsible for the squeal. An

alternative could be the application of an array of non-contact transducers, measuring the operational deflection shape of the rotor during the squeal event;

- Results show that squeal noise occurs in discrete frequencies. The identification of the sound waveform could be helpful to the study of squeal radiation patterns and, consequently, its mechanism;
- A lot of effort has been dispensed with in modeling the squeal noise problem by the finite element method. The most part of this effort is directed toward developing adequate models of coupling and friction among the brake components. The results are usually described in terms of stability / instability of system modes. Few studies have been done concerning the system damping. Analysis of modal stability and system harmonic analysis involving models with shims are still wide fields of study.

## LIST OF REFERENCES

- [1] KUNG S. W., SALIGRAMA V. C. and RIEHLE M. A., "Modal participation analysis for identifying brake squeal mechanism", SAE Paper 2000-01-2764, 2000.
- [2] BLASCHKE P., TAN M. and WANG A., "On the analysis of brake squeal propensity using finite element method", SAE Paper n. 2000-01-2765, 2000.
- [3] NASHIF A. and PARDUS G., "Controlling disc brake noise with constrained layer damping", 4<sup>th</sup> International Brake colloquium, Gramado – Brazil, April/1998.
- [4] FIELDHOUSE J. D., "A proposal to predict the noise frequency of a disk brake based on the friction pair interface geometry", SAE paper n. 1999-01-3403, 1999.
- [5] BERANEK L. L., "Noise and Vibration Control", ed. L. L. Beranek - INCE, Revised edition, 1988.
- [6] NASHIF A., JONES D. I. G. and HENDERSON, J. P., "Vibration Damping", John Wiley & Sons Inc., 1985.
- [7] NASHIF A., "Properties, behavior and applications of damping materials", non-published, 2000.
- [8] NIELSEN L. E., "Mechanical properties of polymers and composites", Vol. 1, Marcel Dekker Inc, 1974.
- [9] JONES D. I. G. and PARIN M. L., "Technique for measuring damping properties of thin viscoelastic layers", J. Sound Vib., 24(2), pp. 201 - 210, 1972.
- [10] JONES D. I. G., "Temperature-frequency dependence of dynamic properties of damping materials", J. Sound Vib., 33(4), pp. 451 - 470, 1974.
- [11] GADE S., ZAVERI K., HERLUFSEN H. et al., "Stress / Strain measurements of viscoelastic materials", Sound and Vibration, Mar, 1995.
- [12] ASTM Standard E 756-98, "Standard test method for measuring vibration - damping properties of materials", 1998.
- [13] KERWIN Jr. E. M., UNGAR E. E. and ROSS D. "Damping of plate flexural vibrations by means of viscoelastic laminate", Sec. 3 - Structural Damping, ASME, New York, 1959.
- [14] FERRY J. D., "Viscoelastic properties of polymers", 2<sup>nd</sup> ed., Wiley, 1970.
- [15] "Vibration damping short course notes", University of Dayton – Research Institute, 1993.

- [16] MEAD D. J., "The damping properties of elastically supported sandwich plates", *J. Sound Vib.*, 24(3), pp. 275 - 295, 1972.
- [17] UNGAR E. E. and KERWIN Jr. E. M., "Loss factor of viscoelastic systems in terms of energy concepts", *J. Acoust. Soc. Am.*, vol. 34, pp. 954 - 957, July, 1962.
- [18] UNGAR E. E. and KERWIN Jr. E. M., "Plate damping due to thickness deformations in attached viscoelastic layers" *J. Acoust. Soc. Am.*, vol. 36, pp. 386 - 392, 1964.
- [19] DANILOV O., FESSINA M. and STAROBINSKI R., " Experimental research on the damping behavior of automotive structural adhesives", *Int. J. of Acoust. Vib.*, vol. 4, n. 4, pp. 189 - 197, 1999.
- [20] LENZI A., "SEA - Análise estatístico-energética", *Notas de aula - Apostila*, 2000.
- [21] BROWN K. T. and NORTON M. P., "Some comments on the experimental determination of modal densities and loss factors for statistical energy analysis applications", *J. Sound Vib.*, 102(4), pp. 588 - 594, 1985.
- [22] HECKL M., CREMER L. and UNGAR E. E., "Structure-Borne Sound – Chapter III", 2<sup>nd</sup> edition, ed. Springer-Verlag, 1998.
- [23] LU Y. P., KILLIAN J. W. and EVERSTINE G. C., "Vibrations of three layered damped sandwich plate composites", *J. Sound Vib.*, 64(1), pp. 63 - 71, 1979.
- [24] LU Y. P. and EVERSTINE G. C., "More on finite element modeling of damped composite systems", *J. Sound Vib.*, 69(2), pp. 199 - 205, 1980.
- [25] LU Y. P. and KILLIAN J. W., "A finite element modeling approximation for damping material used in constrained damped structures", *J. Sound Vib.*, 97(2), pp. 352 - 354, 1984.
- [26] MIGNERY L. A., "Vibration analysis of metal/polymer/metal components", *Proceedings of the Design Engineering Technical Conferences, DE-vol. 84-3, Volume 3 - Part C, ASME*, 1995.
- [27] MIGNERY L. A. and VYDRA E. J., "Vibration analysis of metal/polymer metal laminates - Approximate versus viscoelastic methods", *SAE Noise and Vibration Conference*, paper n. 971943, May, 1997.
- [28] DIHUA, G., DONGYING, J., "A study on disc brake squeal using finite element methods", *SAE technical paper series*, paper n. 980597, 1998.
- [29] NASHIF A. and MIGNERY L., "Prediction of damping treatment dynamics as bonded to a brake shoe and lining", *SAE, 17<sup>th</sup> Annual Brake Colloquium*, paper n. 1999-01-3407, Oct., 1999.

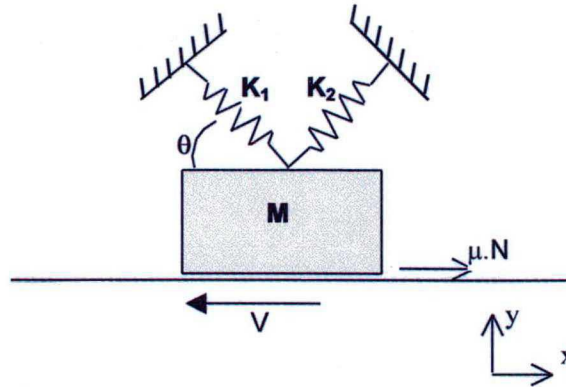


- [30] HAMABE, T., YAMAZAKI, K., YAMADA, H. et al., "Study of a method for reducing drum brake squeal", SAE technical paper series, paper n. 1999-01-0144, 1999.
- [31] LIU W. and PFEIFER J., "Reducing high frequency disc brake squeal by pad shape optimization", SAE World Congress, paper n. 2000-01-0447, March, 2000.
- [32] KUNG S. W., DUNLAP B. and BALLINGER R. S., "Complex eigenvalue analysis for reducing low frequency brake squeal", SAE World Congress, paper n. 2000-01-0444, March, 2000.
- [33] OUYANG H., MOTTERHEAD J. E. and BROOKFIELD D. J., "A methodology for the determination of dynamic instabilities in a car disc brake", Int. J. of Vehicle Design, vol. 23, n. 3/4, pp. 241 - 262, 2000.
- [34] TUCHINDA A., HOFFMAN N. P., EWINS D. J. et al., "Mode lock-in characteristic and instability study of the pin-on-disc system", Bosch NVH Symposium and Grand Opening, Feb. 2001.
- [35] NORIYUKI I., MASAOKI N., and HIDETOSHI S., "Experimental analysis of low-frequency brake squeal noise", 14<sup>th</sup> Annual Brake Colloquium, SAE paper n. 962128, New Orleans, October, 1996.
- [36] HULTEN J., FLINT J. and NELLEMOSE T., "Mode shape of a squealing drum brake", SAE technical paper series, paper n. 972028, 1997.
- [37] FIELDHOUSE J. D., TALBOT C. and BANAWI A., "Generating 3-dimensional animations of vehicle brake noise", SAE paper series, paper n. 2000-01-2770, 2000.
- [38] MARCHI M. M., CHEN F., HARWOOD P. et al., "Holographic Interferometry and its application in brake vibration and noise analysis", Research and Vehicle Technology, Ford Motor Co., 2000.
- [39] CHEN F., SHIH C. and HARWOOD P., "In-plane mode/friction process and their contribution to disc brake squeal at high frequency", SAE paper series, paper n. 2000-01-2773, 2000.
- [40] CUNEFARE K. and RYE R., "Investigation of disc brake squeal via sound intensity and laser vibrometry", SAE paper series, paper n. 01-nvc-102, 2001.
- [41] TERREL T. R., BERGER E. J. and WYNN, R. H., "A dynamometer for automobile brake squeal study", SAE paper series, paper n. 2001-01-1599, 2001.
- [42] BLASCHKE P., ABDELHAMID M. K., WANG A. et al., "An overview of brake noise and vibration problems", Bosch NVH Symposium and Grand Opening, Feb. 2001.

- [43] "Shock and vibration handbook", 4<sup>th</sup> edition, edited by Cyril M. Harris, Mc Graw-Hill, 1996.
- [44] Software for data reduction and nomogram generation, Ahid Nashif / MSC Engineered Material and Solutions Group.
- [45] TRICHÊS Jr. M., "Uma metodologia para análise de ruído e vibrações em sistemas de freio a disco", Thesis Project, Universidade Federal de Santa Catarina, Brasil, April, 2002.
- [46] HU Y and NAGY L., "Brake squeal analysis by using nonlinear transient finite element method", SAE paper series, paper n. 971510, 1997.
- [47] BELL L. H., "Industrial Noise Control – Fundamentals and Applications", Ed. Marcel Dekker Inc., 1982.
- [48] MEIROVITCH L., "Fundamental of Vibrations", Ed. Mc Graw-Hill, New York, 2001.
- [49] STAR System, Copyright 1997, version 5.23.32, Spectral Dynamics Inc., 1997.
- [50] AUWERAER H. V der, DEBLAUWE F., "Advances in industrial modal analysis", SAE paper series, paper n. 2001-01-3832, SAE Brasil Congress, São Paulo, 2001.
- [51] CROCKER M. J. and JACOBSEN F., "Encyclopedia of Acoustics – Chapter 156", John Wiley & Sons Inc., 1997.
- [52] GADE S., "Sound intensity (Part I – Theory)", B&K Technical Review No. 3, 1982.
- [53] GINN K. B., "Active and reactive intensity measurements using the dual channel real-time frequency analyzer 2133", B&K Application Note.
- [54] GADE S., "Sound intensity (Part II – Instrumentation and applications), B&K Technical Review No. 4, 1982.
- [55] GADE S., "Validity of intensity measurements", B&K Technical Review No. 4, 1985.
- [56] "Sound power determination", Hewlett Packard publication, 1992.
- [57] ISO Standard 9614 "Acoustics – Determination of sound power levels of noise sources using sound intensity", 1<sup>st</sup> edition, 1993.
- [58] SMITH R., "Changing the effective mass to control resonance problems", Sound and Vibration Magazine, May, 2001.
- [59] BLOEMHOF H., "Optimization of damping treatment in the car design process using advanced simulation techniques", SAE paper series, paper n. 951265, 1995.
- [60] HIRABAYASHI T., REBANDT R., SAHA P. et al., "Application of noise control and heat insulation materials and devices in the automotive industry", SAE paper series, paper n. 951375, 1995.

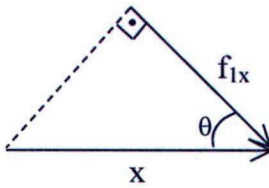
**APPENDIX 1**

**Equations of Motion for the Modal Coupling Model and Implementation in Mathcad®**



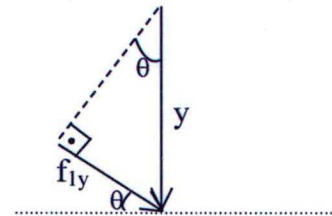
① Considering the forces acting at spring 1:

Displacement on X-axis



$$f_{1x} = K_1 \cdot x \cdot \cos\theta$$

Displacement on Y-axis

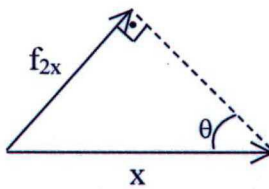


$$f_{1y} = K_1 \cdot y \cdot \sin\theta$$

$$f_1 = K_1(x \cdot \cos\theta - y \cdot \sin\theta)$$

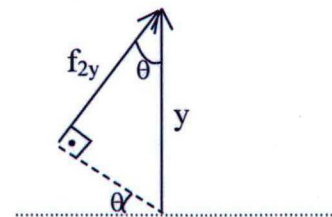
② Considering the forces acting at spring 2:

Displacement on X-axis



$$f_{2x} = K_2 \cdot x \cdot \sin\theta$$

Displacement on Y-axis



$$f_{2y} = K_2 \cdot y \cdot \cos\theta$$

$$f_2 = K_2(x \cdot \sin\theta + y \cdot \cos\theta)$$

Dynamic equation on direction x:

$$f_1 \cos \theta + f_2 \sin \theta + \mu N + M \ddot{x} = 0$$

$$K_1(x \cos \theta - y \sin \theta) \cos \theta + K_2(x \sin \theta + y \cos \theta) \sin \theta - \mu N + M \ddot{x} = 0$$

$$xK_1 \cos^2 \theta - yK_1 \sin \theta \cos \theta + xK_2 \sin^2 \theta + yK_2 \cos \theta \sin \theta - \mu N + M \ddot{x} = 0$$

$$x(K_1 \cos^2 \theta + K_2 \sin^2 \theta) + y \sin \theta \cos \theta (K_2 - K_1) - \mu N + M \ddot{x} = 0$$

The normal force N is given by:

$$N - f_1 \sin \theta + f_2 \cos \theta = 0 \Rightarrow N = f_1 \sin \theta - f_2 \cos \theta$$

$$N = -K_1(x \cos \theta - y \sin \theta) \sin \theta + K_2(x \sin \theta + y \cos \theta) \cos \theta$$

$$N = x \sin \theta \cos \theta (K_2 - K_1) + y (K_1 \sin^2 \theta + K_2 \cos^2 \theta) //$$

Dynamic equation on direction y:

$$-f_1 \sin \theta + f_2 \cos \theta + M \ddot{y} = 0$$

$$-K_1(x \cos \theta - y \sin \theta) \sin \theta + K_2(x \sin \theta + y \cos \theta) \cos \theta + M \ddot{y} = 0$$

$$-xK_1 \sin \theta \cos \theta + yK_1 \sin^2 \theta + xK_2 \sin \theta \cos \theta + yK_2 \cos^2 \theta + M \ddot{y} = 0$$

$$x \sin \theta \cos \theta (K_2 - K_1) + y (K_2 \cos^2 \theta + K_1 \sin^2 \theta) + M \ddot{y} = 0$$

Back to Equation (1):

$$x(K_1 \cos^2 \theta + K_2 \sin^2 \theta) + y \sin \theta \cos \theta (K_2 - K_1) - \mu x \sin \theta \cos \theta (K_2 - K_1)$$

$$- \mu y (K_2 \cos^2 \theta + K_1 \sin^2 \theta) + M \ddot{x} = 0$$

Therefore, the equations of motions are:

$$x [K_1 \cos^2 \theta + K_2 \sin^2 \theta + \mu \sin \theta \cos \theta (K_2 - K_1)]$$

$$+ y [\sin \theta \cos \theta (K_2 - K_1) - \mu (K_2 \cos^2 \theta + K_1 \sin^2 \theta)] + M \ddot{x} = 0$$

$$x [\sin \theta \cos \theta (K_2 - K_1)] + y (K_2 \cos^2 \theta + K_1 \sin^2 \theta) + M \ddot{y} = 0$$

Considering

$$K_{11} = K_1 \cos^2 \theta + K_2 \sin^2 \theta + \mu \sin \theta \cos \theta (K_2 - K_1)$$

$$K_{22} = K_1 \sin^2 \theta + K_2 \cos^2 \theta$$

$$K_{12} = (K_2 - K_1) \sin \theta \cos \theta - \mu (K_1 \sin^2 \theta + K_2 \cos^2 \theta)$$

$$K_{21} = (K_2 - K_1) \sin \theta \cos \theta$$

The dynamic equation can be written as

$$\begin{bmatrix} K_{11} & K_{12} \\ K_{21} & K_{22} \end{bmatrix} \begin{Bmatrix} x \\ y \end{Bmatrix} - \omega^2 \begin{bmatrix} M & 0 \\ 0 & M \end{bmatrix} \begin{Bmatrix} x \\ y \end{Bmatrix} = \begin{Bmatrix} 0 \\ 0 \end{Bmatrix}$$

or

$$\begin{bmatrix} K_{11} - \omega^2 M & K_{12} \\ K_{21} & K_{22} - \omega^2 M \end{bmatrix} \begin{Bmatrix} x \\ y \end{Bmatrix} = \begin{Bmatrix} 0 \\ 0 \end{Bmatrix}$$

and the characteristic equation becomes

$$K_{11}K_{22} - K_{11}\omega^2 M - K_{22}\omega^2 M + \omega^4 M^2 - K_{12}K_{21} = 0$$

with coefficients

$$a = \omega^4 M^2$$

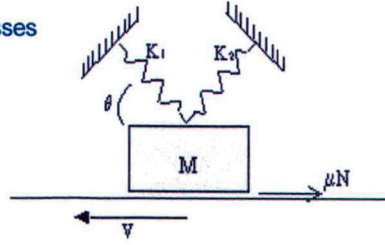
$$b = M(K_{11} + K_{22})$$

$$c = K_{11}K_{22} - K_{12}K_{21}$$

### SELF EXCITED VIBRATIONS OF A 2DOF SYSTEM

t := 0, 0.001 2    Δ := 1    Initial Displacement of the block  
 m := 1    Mass    k1 := 600(1 + 0.i)    k2 := 1000(1 + 0.i)    Stiffnesses

μ := .5    θ :=  $\frac{\pi}{3}$   
 k11 := k1 cos(θ)<sup>2</sup> + k2 sin(θ)<sup>2</sup> + μ sin(θ) cos(θ) (k2 - k1)  
 k22 := k1 sin(θ)<sup>2</sup> + k2 cos(θ)<sup>2</sup>  
 k12 := (k2 - k1) sin(θ) cos(θ) - μ (k1 sin(θ)<sup>2</sup> + k2 cos(θ)<sup>2</sup>)  
 k21 := sin(θ) cos(θ) (k2 - k1)



a := k11k22 - k12k21    b := m(k11 + k22)    c := m<sup>2</sup>

$$K := \begin{bmatrix} k11 & k12 \\ k21 & k22 \end{bmatrix}$$

$$M := \begin{bmatrix} m & 0 \\ 0 & m \end{bmatrix}$$

k11 = 986.603

k22 = 700

k12 = -176.795

k21 = 173.205

$$v := \begin{bmatrix} a \\ 0 \\ b \\ 0 \\ c \end{bmatrix}$$

b<sup>2</sup> = 2.84510<sup>6</sup>

4 a c = 2.88510<sup>6</sup>

b<sup>2</sup> - 4 a c = -4.03510<sup>4</sup>

λ := eigenval(MK)

$$\lambda = \begin{bmatrix} 843.304 + 100.432i \\ 843.304 + 100.432i \end{bmatrix}$$

Roots of Characteristic equation    roots := polyroots(v)

roots<sub>0</sub> = -1.726 - 29.091i

roots<sub>1</sub> = -1.726 - 29.091i

roots<sub>2</sub> = 1.726 + 29.091i

roots<sub>3</sub> = 1.726 + 29.091i

Eigenvectors

v := eigenvc(MK)

$$v = \begin{bmatrix} 0.711 & 0.711 \\ 0.576 - 0.404i & 0.576 + 0.404i \end{bmatrix}$$

B11 = 0

B12 = 0

B21 =  $\frac{\Delta}{2}$

B22 =  $\frac{\Delta}{2}$

α 1 := Re(roots<sub>2</sub>)

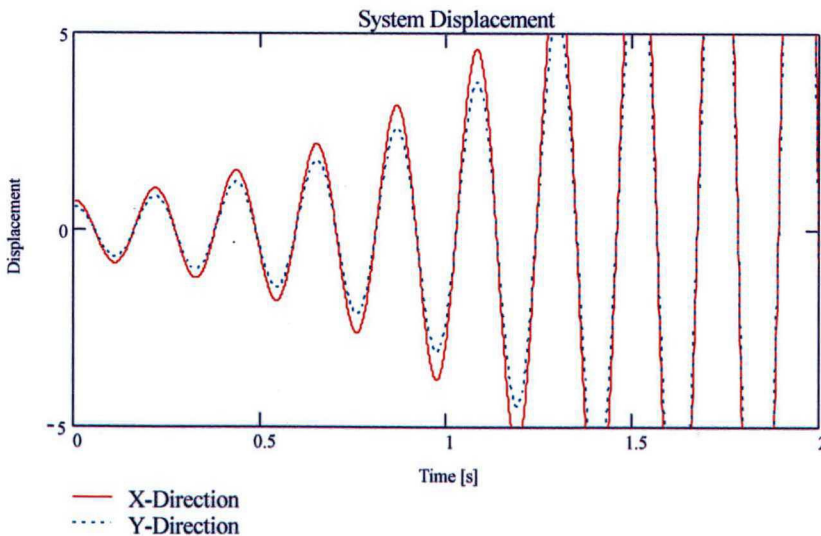
ω 1 := Im(roots<sub>2</sub>)

α 2 := Re(roots<sub>3</sub>)

ω 2 := Im(roots<sub>3</sub>)

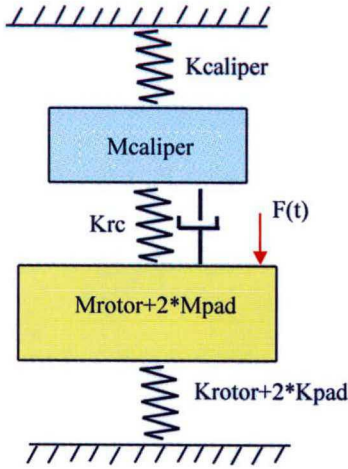
qx(t) := e<sup>α1 t</sup> [ |v<sub>0,0</sub>| [ (B11 sin(ω 1 t - arg(v<sub>0,0</sub>))) + B21 cos(ω 1 t - arg(v<sub>0,0</sub>))) ] ] + e<sup>α2 t</sup> [ |v<sub>0,1</sub>| [ (B12 sin(ω 2 t - arg(v<sub>0,1</sub>))) + B22 cos(ω 2 t - arg(v<sub>0,1</sub>))) ] ]

qy(t) := e<sup>α1 t</sup> [ |v<sub>1,0</sub>| [ (B11 sin(ω 1 t - arg(v<sub>1,0</sub>))) + B21 cos(ω 1 t - arg(v<sub>1,0</sub>))) ] ] + e<sup>α2 t</sup> [ |v<sub>1,1</sub>| [ (B12 sin(ω 2 t - arg(v<sub>1,1</sub>))) + B22 cos(ω 2 t - arg(v<sub>1,1</sub>))) ] ]



## APPENDIX 2

### Equations of Motion of the 2 Degrees-of-Freedom System Used for Parametric Analysis of Rubber Coat Damping Mechanism and Implementation of Routine in Matlab



$K_{rotor}$ ,  $K_{pad}$ ,  $K_{caliper}$  and  $K_{rc}$  are the stiffness of rotor, pad, caliper and rubber coat, respectively

$M_{rotor}$ ,  $M_{pad}$ ,  $M_{caliper}$  and  $M_{rubbercoa}$  are the mass of rotor, pad, caliper and rubber coat, respectively

Considering

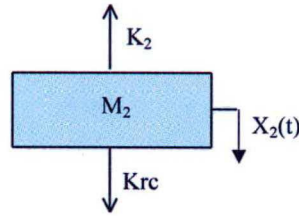
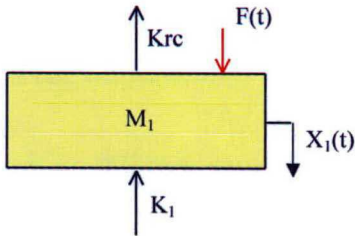
$$M_1 = M_{rotor} + M_{pad}$$

$$M_2 = M_{caliper}$$

$$K_1 = K_{rotor} + K_{pad}$$

$$K_2 = K_{caliper}$$

Free body diagrams



Dynamic equations

$$(1) \quad M_1 \ddot{x}_1 + K_1 x_1 + K_{rc} (x_1 - x_2) = F$$

$$(2) \quad M_2 \ddot{x}_2 + K_2 x_2 + K_{rc} (x_1 - x_2) = 0$$

Considering

$$x_1(t) = \hat{x}_1 e^{i\omega t} \quad x_2(t) = \hat{x}_2 e^{i\omega t} \quad \text{and} \quad F(t) = F e^{i\omega t}$$

$$(1) \quad -\omega^2 M_1 x_1 + K_1 x_1 + K_{rc} (x_1 - x_2) = F$$

$$(2) \quad -\omega^2 M_2 x_2 + K_2 x_2 + K_{rc} (x_1 - x_2) = 0$$

Isolating  $X_2$  in equation (2):

$$x_2(-\omega^2 M_2 + K_2 + K_{rc}) - K_{rc} x_1 = 0$$

$$x_2 = \frac{K_{rc} x_1}{(-\omega^2 M_2 + K_2 + K_{rc})}$$

Substituting in equation (1)

$$-\omega^2 M_1 x_1 + K_1 x_1 + K_{rc} x_1 - \frac{-K_{rc}^2 x_1}{(-\omega^2 M_2 + K_2 + K_{rc})} = F$$

$$\frac{x_1}{F} = \frac{1}{-\omega^2 M_1 + K_1 + K_{rc} - \frac{-K_{rc}^2}{(-\omega^2 M_2 + K_2 + K_{rc})}}$$

Obs.

$K_{rotor}$ ,  $K_{pad}$ ,  $K_{caliper}$  and  $K_{rc}$  are complex values:

$$K_{rotor}(1+i\eta_{rotor})$$

$$K_{pad}(1+i\eta_{pad})$$

$$K_{caliper}(1+i\eta_{caliper})$$

$$K_{rc}(1+i\eta_{rc})$$



```

% SCRIPT FILE TO PLOT INERTANCE (a/F) OF A DAMPED 2DOF SYSTEM
% CONSIDERING GROUND//PAD+ROTOR//RUBBER COAT//CALIPER//GROUND
echo off;
clear all, clc, clf
Krotor=1.06*6.8e9;           %Rotor Stiffness
Mrotor=2.786;               %Rotor Mass
LFrotor=0.00254;           %Loss Factor of Rotor
Kpad= 1.5*6.388e8;         %Pad Stiffness
Mpad=0.369;                %Pad Mass
LFpad=0.0143;              %Loss Factor of Pad
% Rotor and Pad properties are set to have the same ressonance frequencies
Kcaliper = 4.725e9;
Mcaliper = 1.225;

Aload = 0.00252;           % Loaded Area;
t = 1*0.000102;           % Rubber Thickness
Grc = 4.826e7;             % Rubber Shear Modulus
LFrc = .63;                % Rubber Loss Factor

Erc = 3*Grc;               % Rubber Young Modulus
Krc = ((Erc*Aload)/t)*(1+i*LFrc); % Complex Rubber Stiffness

K1 = Krotor*(1+i*LFrotor) + 2*Kpad*(1+i*LFpad);
M1 = Mrotor + 2*Mpad;
K2 = Kcaliper;
M2 = Mcaliper;

wn1 = sqrt(K1/M1);
fn1 = wn1/(2*pi);
wn2 = sqrt(K2/M2);
fn2 = wn2/(2*pi);

K1,K2,Krc
fmin=3000;                  % Range of Frequency Analysis
fmax = 25000;
inc=1;
w = 2*pi*(fmin:inc:fmax);
FRFX1 = (-w.^2)./(-M1*w.^2+K1+Krc-(Krc.^2./(-M2*w.^2+K2+Krc)));
subplot(2,1,1);
FRFX2 = (Krc./(-M2*w.^2+K2+Krc)).*FRFX1;
loglog((w./(2*pi)),abs(FRFX1)), axis([fmin fmax 1E-1 1e6]), grid on
title('FRF for a 2 DOF System')
ylabel ('FRF (-w^2*X1 / Fo)')
ii=1;
while abs(FRFX1(ii+1)) >= abs(FRFX1(ii)) %Frequency of 1st peak
    ii=ii+1;
    FRFmax1 = FRFX1(ii);
    freq1=w(ii)/(2*pi);
end
FRFrms1=abs(FRFmax1)/sqrt(2); %Loss Factor Routine for 1st Peak
iii=ii;
while abs(FRFX1(ii)) >= FRFrms1 %Calculate 3dB lower frequency
    if FRFX1(ii)==FRFrms1
        finf1=w(ii)/(2*pi);
    else
        finf1=((w(ii)+w(ii-1))/2)/(2*pi);
    end
    ii=ii-1;
end
FRFaux = abs(FRFX1(iii));
while FRFaux >= FRFrms1 %Calculate 3dB higher frequency

```

```

if FRFaux == FRFrms1
    fsup1=w(iii)/(2*pi);
    FRFaux=FRFrms1/10;
else
    if iii > 2*ii
        fsup1 = 2*freq1-finfl;
        FRFaux=FRFrms1/10;
    else
        fsup1=((w(iii)+w(iii+1))/2)/(2*pi);
        iii=iii+1;
        FRFaux=abs(FRFX1(iii));
    end
end
end
lossfactor1=(fsup1-finfl)/freq1; %End of 1st peak loss factor
Routine
jj=length(w);
while abs(FRFX1(jj-1))>= abs(FRFX1(jj)) %Frequency of 2nd peak
    jj=jj-1;
    FRFmax2 = FRFX1(jj);
    freq2=w(jj)/(2*pi);
end
FRFrms2=abs(FRFmax2)/sqrt(2); %Loss Factor of 2nd peak Routine
jjj=jj;
while abs(FRFX1(jj)) >= FRFrms2 %Calculate 3dB lower frequency
    if FRFX1(jj)==FRFrms2
        finf2=w(jj)/(2*pi);
    else
        finf2=((w(jj)+w(jj-1))/2)/(2*pi);
    end
    jj=jj-1;
end
FRFaux = abs(FRFX1(jjj));
while FRFaux >= FRFrms2 %Calculate 3dB higher frequency
    if FRFaux==FRFrms2
        fsup2=w(jjj)/(2*pi);
        FRFaux=FRFrms/2;
    else
        if jjj==length(w)
            fsup2=w(jjj)/(2*pi);
            FRFaux=FRFrms2/2;
        else
            fsup2=((w(jjj)+w(jjj+1))/2)/(2*pi);
            jjj=jjj+1;
            FRFaux=abs(FRFX1(jjj));
        end
    end
end
end
lossfactor2=(fsup2-finf2)/freq2;
subplot(2,1,2);
semilogx((w./(2*pi)),angle(FRFX1./FRFX2)*180/pi,axis([fmin fmax -200 200])
title('Phase Angle Between X1 and X2')
xlabel ('Frequency (Hz)')
text(fmin,-20,'f1 = ')
text(fmin*1.25,-20,num2str(freq1))
text(fmin,-60,'f2 = ')
text(fmin*1.25,-60,num2str(freq2))
text(fmax*.5,-20,'LF1 = ')
text(fmax*.6,-20,num2str(lossfactor1,3))
text(fmax*.5,-60,'LF2 = ')
text(fmax*.6,-60,num2str(lossfactor2,3))

```